Boundary-Layer Transition on a Slender Cone in Hypervelocity Flow with Real Gas Effects
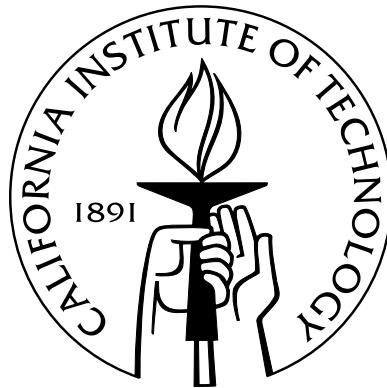
Thesis by

Joseph Stephen Jewell

In Partial Fulfillment of the Requirements

for the Degree of

Doctor of Philosophy

California Institute of Technology

Pasadena, California

2014

(Defended May 15, 2014)

For Poppy

Abstract

The laminar to turbulent transition process in boundary layer flows in thermochemical nonequilibrium at high enthalpy is measured and characterized. Experiments are performed in the T5 Hypervelocity Reflected Shock Tunnel at Caltech, using a 1 m length 5-degree half-angle axisymmetric cone instrumented with 80 fast-response annular thermocouples, complemented by boundary layer stability computations using the STABL software suite. A new mixing tank is added to the shock tube fill apparatus for premixed freestream gas experiments, and a new cleaning procedure results in more consistent transition measurements. Transition location is nondimensionalized using a scaling with the boundary layer thickness, which is correlated with the acoustic properties of the boundary layer, and compared with parabolized stability equation (PSE) analysis. In these nondimensionalized terms, transition delay with increasing CO_2 concentration is observed: tests in 100% and 50% CO_2, by mass, transition up to 25% and 15% later, respectively, than air experiments. These results are consistent with previous work indicating that CO_2 molecules at elevated temperatures absorb acoustic instabilities in the MHz range, which is the expected frequency of the Mack second-mode instability at these conditions, and also consistent with predictions from PSE analysis. A strong unit Reynolds number effect is observed, which is believed to arise from tunnel noise. N_{Tr} for air from 5.4 to 13.2 is computed, substantially higher than previously reported for noisy facilities. Time- and spatially-resolved heat transfer traces are used to track the propagation of turbulent spots, and convection rates at 90%, 76%, and 63% of the boundary layer edge velocity, respectively, are observed

for the leading edge, centroid, and trailing edge of the spots. A model constructed with these spot propagation parameters is used to infer spot generation rates from measured transition onset to completion distance. Finally, a novel method to control transition location with boundary layer gas injection is investigated. An appropriate porous-metal injector section for the cone is designed and fabricated, and the efficacy of injected CO_2 for delaying transition is gauged at various mass flow rates, and compared with both no injection and chemically inert argon injection cases. While CO_2 injection seems to delay transition, and argon injection seems to promote it, the experimental results are inconclusive and matching computations do not predict a reduction in N factor from any CO_2 injection condition computed.

Acknowledgements

Joe Shepherd, my advisor, deserves credit for his careful guidance, expertise, and substantial patience over the years. I returned to Caltech specifically to work with him after getting my first real research experience in his lab group as a summer SURF student in 2002, and have since only grown in my appreciation for this exceptional scientist and educator. Ivett Leyva of the Air Force Research Laboratory went above and beyond any reasonable expectation as a collaborator and committee member, regularly making the drive to Pasadena to discuss our work in person and advise on research and writing. The other members of my committee are Hans Hornung, Tony Leonard (who was also my undergraduate Aeronautics advisor), and Guillaume Blanquart, each of whom not only read the thesis but provided careful review of early drafts for a substantial portion of this work. Warren Brown (who was also my undergraduate Medieval History advisor) advised me on the coursework for the History minor.

The collaboration of Ross Wagnild at Sandia National Laboratories was critically important to the success of this thesis, both in the complementary computations he made personally and in his support of our local work with the Fujii code and especially with the STABL software suite, which Nick Parziale successfully installed and debugged on a Caltech computer with Ross' guidance. Nick's help with running T5 was appreciated, and his dogged determination in hunting down and mitigating sources of particulate contamination in the shock tube deserves special mention. Discussions with Nick in lab were invariably both useful and entertaining, and his

Other members of the Shepherd group, including Phil Boettcher, Sally Bane, Angie Capece, Stephanie Coronel, Greg Smetana, and Remy Mevel each provided advice, support, and friendship.

I am also indebted to Christopher Brennen, whose courses were my formal introduction to fluid mechanics and have subsequently been instrumental to my efforts in the field. Chris also advised me and John Meier on the most interesting and fruitful side project I pursued during this work.

My parents, Suzanne and Stephen Jewell, along with my grandparents Dorothy Kramer and the late Charles and F. Kathryn Jewell, have been the basis for all of my success. My grandfather, Richard M. Kramer, to whose memory this thesis is dedicated, gave me my earliest experiences of engineering in his basement workshop, and remained an enthusiastic and curious supporter of my work for the rest of his life.

My wife Katie's patient love and support has been critical to the completion of this work. I simply do not deserve her. Finally, thanks be to God for perseverance and fortitude: "O give thanks unto the LORD; for he is good: for his mercy endureth forever."[1]

---

[1]Psalm 136:1 (KJV)

Contents

List of Figures

List of Tables

Chapter 1

Introduction

1.1 Motivation

> So, yes, this Nation remains fully committed to America's space program.
> We are going forward with our shuttle flights. We are going forward to
> build our space station. And we are going forward with research on a new
> Orient Express that could, by the end of the next decade, take off from
> Dulles Airport and accelerate up to 25 times the speed of sound, attaining
> low-earth orbit or flying to Tokyo within two hours. (Reagan, 1986)

In the time since President Reagan delivered the 1986 State of the Union Address,
the Space Shuttle flew 110 additional missions and was retired, and the International
Space Station has been completed and stands occupied on orbit, but the latter-day
Orient Express—the National Aerospace Plane, the only project to which Reagan
attached a timeline—has failed to materialize. Twenty-eight years later, the goal of
air-breathing, manned hypervelocity flight seems scarcely closer than it was then. Several obstacles persist[1] and are the subject of vigorous research, including the issue of
supersonic mixing and fuel-air combustion. One of the most significant aerodynamic
challenges, however, remains the problem of boundary layer transition and turbulence

---

[1]See Barber et al. (2009) for an overview of the current technical deficiencies in hypersonic
applications.

at hypervelocity (Malik, 2003).

When a vehicle's boundary layer transitions from laminar to turbulent flow, the heat flux through the surface increases in magnitude. This challenge is exacerbated for air-breathing hypersonic vehicles, which must cruise at low enough altitudes to ingest sufficient oxygen to sustain efficient combustion (Bertin, 1994) in contrast to, for example, the Space Shuttle, which experienced peak heating during only about 10 minutes of the re-entry process (Alber, 2012). Drag, skin friction, and other flow properties are also significantly impacted. At hypersonic speeds—generally taken to be above Mach 4—much higher thermal loads, by half an order of magnitude or more, result from the increased heat transfer due to turbulent flow (van Driest, 1952). In this flow regime, heat transfer and thermal management are dominant design considerations, and more massive thermal protection systems, required to safely dissipate the heat from turbulent flow, impose significant mass and efficiency penalties (Anderson, 2006). Measuring, understanding, and if possible controlling the path from laminar to turbulent flow is thus a critical process for hypervelocity vehicle design and operation, and many recent computational, experimental, and flight efforts have pursued these goals (Fedorov, 2011a).

1.2 Boundary Layer Instability and Transition

Instability and transition at subsonic speeds have been topics of significant interest in fluid mechanics for over a century. Lord Rayleigh published several papers on fluid instability beginning with Rayleigh (1879), and Reynolds (1883) first documented the "sinuous" nature of certain pipe flows evolving from previously smooth motion. Reynolds noticed that fluid particles that initially move at constant speed in parallel streamlines eventually exhibit transverse motion with respect to their original paths, as orderly flow breaks down and a strong fluid mixing effect occurs. Interest in tran-

sition within the boundary layer, as opposed to pipe flow, came later, with an early overview of boundary layer transition given by Lees (1947), and the first measurements of instability waves in flow over a flat plate taken by Schubauer and Skramstad (1948). An excellent historical overview of the progression of subsonic instability and transition theory and experiments, advancing into compressible investigations, is given in Part III of Schlichting and Gersten (2001).

The study of hypersonic instability and transition is more recent. Demetriades (1960) performed the first hypersonic stability experiment, using hot wire anemometry to measure the amplification rates of small disturbances in a Mach 5.8 boundary layer. Reshotko (1976) provides a review of stability and transition with significant focus on supersonic and hypersonic flows, and transition prediction methods. Stetson and Kimmel (1992) compared experiments with theory to examine the effects of parameters including nose-tip bluntness, wall temperature, angle of attack, unit Reynolds number, and Mach number on hypersonic stability. Most recently the excellent review of Fedorov (2011a), focusing on slender bodies at zero angle of attack, surveyed studies with an emphasis on qualitative features of high-speed boundary layer instability, including the receptivity of the boundary layer to the disturbance environment.

More focused surveys of the literature are included in the introductory material for the chapters constituting this thesis. These include: Section 2.1 on T5 design and operation, Section 4.2 on the development of the semi-empirical e^N method and Section 4.2.2 for applications of the same, Section 5.1 on hypersonic boundary layer transition onset in ground and flight experiments, Section 5.2.2.1 on the unit Reynolds number effect, Section 6.1 on turbulent spot observations and Section 6.3 on turbulent spot theory and modeling, and Section 7.1 on transition experiments with injection and blowing.

1.3   Motivation For High-Enthalpy Transition Study

In hypervelocity flow over cold, slender bodies, the most significant instability mechanism is the so-called second or Mack mode. These flows are characteristic of atmospheric re-entry and air-breathing hypersonic vehicles, and were the target conditions for which high-enthalpy facilities like the T5 shock tunnel at Caltech were developed. Section 4.3.2 presents a more thorough discussion of Mack's second mode, as well as computations demonstrating that this mode is present and unstable for T5 conditions. A second mode disturbance depends on the amplification of acoustic waves trapped in the boundary layer, as described by Mack (1984). Another potential disturbance is the first mode, which is the high speed equivalent of the viscous Tollmien–Schlichting instability (Malik, 2003). However, at high Mach number (> 4) and for cold walls, the first mode is damped and higher modes are amplified, so that the second mode would be expected to be the only mechanism of linear instability leading to transition for a slender cone at zero angle of attack.

1.3.1   Damping of Acoustic Disturbances by Vibrational Relaxation

By assuming that the boundary layer acts as an acoustic waveguide for disturbances (see Fedorov (2011a) for a schematic illustration of this effect), the frequency of the most strongly amplified second-mode disturbances in the boundary layer may be estimated as Equation (1.1), as shown in Stetson (1992) with a different coefficient[2].

$$f \approx 0.7 \frac{U_{\mathrm{e}}}{2\delta_{99}} \tag{1.1}$$

Here δ_{99} is the boundary layer thickness defined by the height above the surface

---

[2]Stetson (1992) reports 0.8; in the present work 0.7 is found to more closely match STABL computations for most-amplified frequency.

where the local velocity is 99% of the freestream velocity, and U_e is the velocity at the boundary layer edge. For a typical T5 condition in air, with enthalpy of 10 MJ/kg and reservoir pressure of 50 MPa, the boundary layer thickness is on the order of 1.5 mm by the end of the cone and the edge velocity is 4000 m/s. This indicates that the most strongly amplified frequencies are in the 1 MHz range. This is broadly consistent with the results of Fujii and Hornung (2001).

Kinsler et al. (1982) provide a good general description of the mechanisms of attenuation of sound waves in fluids due to molecular exchanges of energy within the medium. The relevant exchange of energy for carbon dioxide in the boundary layer of a thin cone at T5-like conditions is the conversion of molecular kinetic energy (*e.g.*, from compression due to acoustic waves) into internal vibrational energy. In real gases, molecular vibrational relaxation is a nonequilibrium process, and therefore irreversible. This absorption process has a characteristic relaxation time.

The problem of sound propagation, absorption, and dispersion in a dissociating gas has been treated from slightly different perspectives by Clarke and McChesney (1964), Zeldovich and Raizer (1967), and Kinsler et al. (1982). However, in nonequilibrium flows when the acoustic characteristic time scale and relaxation time scale are similar, some finite time is required for molecular collisions to achieve a new density under an acoustic pressure disturbance. This results in a work cycle, as the density changes lag the pressure changes. The area encompassed by the limit cycle's trajectory is related to energy absorbed by relaxation. Energy absorbed in this way is transformed into heat and does not contribute to the growth of acoustic waves (Leyva et al., 2009b).

1.3.2 Relevant Properties of Air, N_2, and CO_2

In order to damp acoustic vibrations within the boundary layer, energy must be transferred into the gas molecules' internal modes, the energy content of which depends upon vibrational specific heat. Vincenti and Kruger (1965) present Equation (1.2)

for vibrational specific heat, where Θ_i is the characteristic vibrational temperature of each mode of the gas molecule, and R is the molecule's gas constant. The exponential factors dominate the vibrational contribution from each mode, and indicate that an increase in temperature causes an increase in both total specific heat and the contribution to specific heat from each vibrational mode.

$$C_{v_{\text{vib}}} = R \sum_i \left\{ \left(\frac{\Theta_i}{T} \right)^2 \frac{e^{\Theta_i/T}}{\left(e^{\Theta_i/T} - 1 \right)^2} \right\} \tag{1.2}$$

Specifically, as Θ_i/T becomes large (for small T), the summand tends to zero, which means there is no contribution to the vibrational specific heat from that vibrational mode. As Θ_i/T becomes small (for large T), the summand tends to unity, and the maximum contribution from a given vibrational mode is therefore R. As temperature increases within the boundary layer, each mode becomes more fully excited and capable of exchanging more energy from acoustic vibrations. The temperature of the boundary layer increases with enthalpy. See Figure 5.7 in Chapter 5 for an illustration of the dependence upon reservoir enthalpy of T^*, a characteristic boundary layer reference temperature, for each experiment.

Carbon dioxide, a linear molecule, has four normal vibrational modes. The first two, which correspond to transverse bending, are equal to each other, and have characteristic vibrational temperatures $\Theta_1 = \Theta_2 = 959.66$ K. The third mode, corresponding to symmetric longitudinal stretching, has $\Theta_3 = 1918.7$ K, and the fourth mode, corresponding to asymmetric longitudinal stretching, has $\Theta_4 = 3382.1$ K.

Camac (1966) assumed that the four vibrational modes for carbon dioxide could be modeled as relaxing at the same rate due to inter-mode coupling, and proposed a single formula, Equation (1.3), to calculate vibrational relaxation times for all four modes, which was reproduced in Fujii and Hornung (2001).

$$\ln \left(A_4 \tau_{\text{CO}_2} P \right) = A_5 T^{-1/3} \tag{1.3}$$

Here A_4 and A_5 are constants given by Camac for carbon dioxide as $A_4 = 4.8488 \times 10^2 \, \text{Pa}^{-1} s^{-1}$ and $A_5 = 36.5 \, \text{K}^{1/3}$. Using the constants suggested by Camac, with $P = 35$ kPa and $T = 1500$ K, which are consistent with a typical T5 condition with reservoir enthalpy 10 MJ/kg and reservoir pressure 50 MPa, we find vibrational relaxation time τ_{CO_2} $= 1.43 \times 10^{-6}$ s, which indicates that frequencies around 700 KHz should be most strongly absorbed at these conditions. This is broadly similar to the results of Fujii and Hornung (2001), who computed absorption curves at 1000 K and 2000 K with peaks bracketing 700 kHz.

1.3.3 Gas in Chemical Nonequilibrium at Rest

The method of Fujii and Hornung (2001) for estimating the absorption of acoustic waves perturbing high temperature gas is used to compute sample absorption curves for several conditions from the present study, chosen to match the reference temperature of the boundary layer and the computed most-amplified frequency at transition for each case. One condition each is computed for an air, N_2, and 50% CO_2 experiment. Figure 1.1 presents the results of these computations. In the relevant frequency range, the computed acoustic absorption per wavelength for 50% CO_2 is more than 3 orders of magnitude larger than the air case at similar conditions, and about 5 orders of magnitude larger than the N_2 case.

Thus, in a flow of gas that absorbs energy most efficiently at frequencies similar to the most strongly amplified frequencies implied by the geometry of the boundary layer, laminar to turbulent transition is expected to be delayed. Using computational techniques described in Chapter 4, we show that the flow of carbon dioxide/air mixtures over a slender cone at T5 conditions allows for such a match in frequencies and a significant effect on the predicted stability properties of the boundary layer. We then perform a series of experiments to confirm this effect for transition onset, the results of which are presented in Chapter 5.
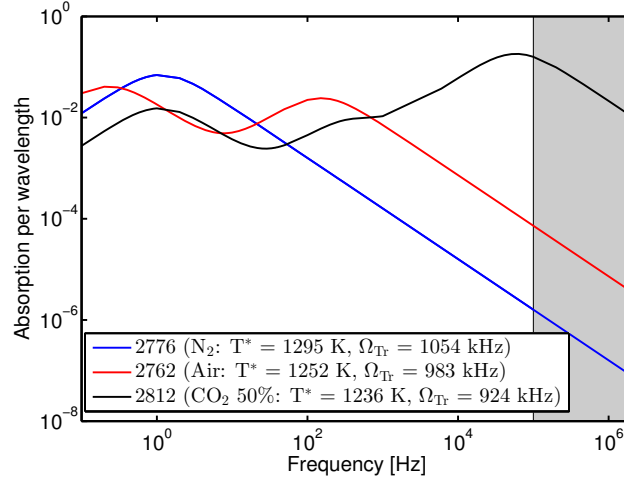
Figure 1.1: Fujii acoustic absorption per wavelength for air, N_2, and 50% CO_2 calculated at similar conditions. The area of the graph highlighted in gray, which extends from 100 kHz to 2 MHz, is the most relevant frequency range for the present study and encompasses the predicted most amplified frequencies at transition for all of the included cases. In this range, the computed acoustic absorption per wavelength for 50% CO_2 is more than 3 orders of magnitude larger than the air case.

1.4   Instability and Transition Studies

1.4.1   T5 Studies on Slender Cones with Sharp Tips

Parametric studies in air and CO_2 in the T5 hypervelocity reflected shock tunnel by Germain (1993) and Adam and Hornung (1997) on smooth 5-degree half-angle cones at zero angle of attack showed an increase in the reference Reynolds number Re^* (see Equation 3.17 on page 53) at the onset of transition as reservoir enthalpy h_{res} increased. Germain and Adam also observed that flows of CO_2 transitioned at higher values of Re^* than flows of air for the same h_{res} and P_{res}. Johnson et al. (1998) studied this effect with a linear stability analysis focused on the chemical composition of the flow, and found an increase in transition Reynolds number with increasing freestream total enthalpy, and further found the increase to be greater for gases with lower dissociation energies and multiple vibrational modes, such as CO_2. In fact, with the assumption of

a transition N factor[3] of 10 that was made at the time, none of the CO_2 cases computed by Johnson et al. predicted transition at all. These effects led Fujii and Hornung (2001) to further investigate their hypothesis that the delay in transition was due to the damping of acoustic disturbances in nonequilibrium relaxing gases by vibrational absorption. Fujii and Hornung estimated the most strongly amplified frequencies for representative T5 conditions and found that these agreed well with the frequencies most effectively damped by nonequilibrium CO_2. This suggests that the suppression of the second mode through the absorption of energy from acoustic disturbances through vibrational relaxation is the dominant effect in delaying transition for high-enthalpy carbon dioxide flows. Most recently, Parziale (2013) studied the second mode instability using a differential interferometric technique. Parziale measured disturbance frequencies of about 1 MHz for wavepackets observed propagating in the boundary layer, and found amplitude growth accompanied by a drop in frequency consistent with the second mode instability for measurements at different locations downstream from the tip of the cone.

1.4.2 Studies on Transition Delay

Numerous studies have been made on inhibiting the second mode, and therefore preventing or delaying transition through the suppression of acoustic disturbances within the boundary layer; see Fedorov et al. (2001) for a computational study and Rasheed et al. (2002) for experimental work focused on absorbing acoustic energy using porous walls, which was performed in T5. Kimmel (2003) surveys a variety of potential control methods to induce hypervelocity boundary layer transition delay, including wall heat transfer, nose-tip bluntness, and passive porosity. Kimmel's review, while presenting a limited computational basis for the use of boundary layer

---

[3]See Section 4.2 for more details on the computation of the N factor, which is a measure of instability growth rate.

suction in hypersonic transition control, did not cover any gas injection experiments or computations. Schneider (2010) reviewed experimental blowing studies for a range of geometries and gases[4], but found that boundary layer injection generally was an effective method for promoting, rather than inhibiting, transition in hypersonic boundary layers. Notably, none of the reviewed studies involved carbon dioxide injection, or considered the potential for hypersonic transition control through the exploitation of vibrational relaxation in any species.

1.5   Scope of the Present Study

The present approach to suppression of the pressure waves that lead to transition centers around altering the chemical composition within the boundary layer to include species capable of absorbing acoustic energy at the appropriate frequencies. Efforts in this area have included preliminary experimental work on mixed freestream flows (*e.g.*, Beierholm et al. (2008)) and computations (*e.g.*, Wagnild et al. (2010) and Wagnild (2012)). The present aim is to confirm and extend these studies both computationally and experimentally by considering transition within a hypervelocity boundary layer on a 5-degree half-angle cone in air, nitrogen, carbon dioxide, and freestream mixtures of air and carbon dioxide. The problem is analyzed, and relevant computational techniques for both mean flow and stability described, in Chapter 4. Experimental measurements of transition onset in air, nitrogen, carbon dioxide, and mixtures are presented, and compared to matching boundary layer stability computations, in Chapter 5. Measurements of turbulent spot propagation and merging are presented in Chapter 6, and inferences about turbulent spot generation rate in different gas mixtures are made through comparison with a simple model.

This work has been motivated in part by preliminary experiments with promis-

---

[4]Further details on the experiments reviewed by Schneider are found in Section 7.1.

ing but inconclusive results that used direct injection of absorptive gases into the boundary layer, (*viz.*, Jewell et al. (2011)), which found significant differences in the observed transition location for boundary layers with carbon dioxide injection *versus* argon injection and tests without injection tests at the same conditions. This work is further detailed in Chapter 7. Furthermore, the present work provides a set of well-characterized experimental results which explore boundary layer transition onset on a slender cone within a significant portion of the T5 performance envelope, and pairs those results with modern computational analysis of mean flow and stability properties. This dataset is intended both to be a resource for future computational stability and transition work on high-enthalpy flows, and to serve as a baseline result for future stability and transition work in T5.

Chapter 2

Facility

2.1 Description and Test Procedure

The facility used for all experiments in the present study is the T5 Hypervelocity Reflected Shock Tunnel located at the Graduate Aerospace Laboratories of the California Institute of Technology; see Hornung (1992) and Hornung and Belanger (1990) for details on the design and operation of this facility, a rendering of which is presented in Figure 2.1. For a good explanation of the basic principles underlying piston-driven reflected shock tunnels, see Section 16.2 in Tropea et al. (2007).

2.1.1 Overview

Figure 2.2 is a labeled schematic diagram of the relevant T5 components. Prior to each experiment, atmospheric air is compressed up to a maximum of 4500 psi into holding tanks outside the laboratory. A stainless steel diaphragm, scored to an empirically determined depth to burst at a given pressure differential, is inserted in the primary diaphragm position between the compression tube and the shock tube. A thin Mylar diaphragm is placed in the secondary diaphragm position between the shock tube and the nozzle. A 120 kg aluminum piston is loaded into the piston space, which is at the end of the compression tube just downstream of the junction with the secondary reservoir. All sections of the tunnel are evacuated with vacuum pumps.
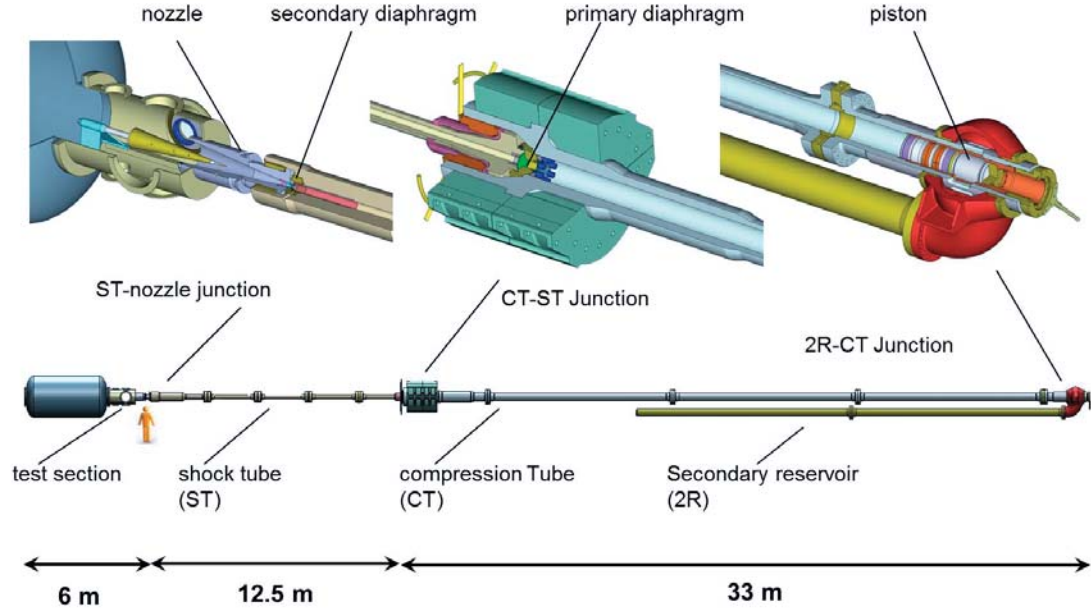
Figure 2.1: Rendering of the T5 Hypervelocity Shock Tunnel. (Based on drawings prepared by Bahram Valiferdowsi.)
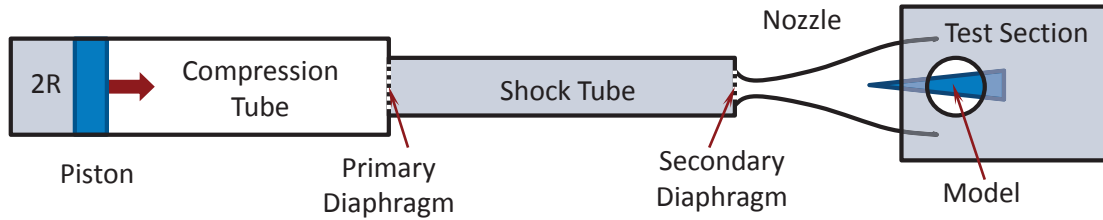
Figure 2.2: Simplified schematic diagram of the T5 Hypervelocity Shock Tunnel. The section labeled "2R" is the secondary reservoir. See also Figure 2.5.

At the beginning of the experiment, the shock tube is filled with the desired test gas; in the present experiments, this is always N_2, air, CO_2, or a mixture of CO_2 and air premixed in the tank described and pictured in Section 2.1.2. The compression tube is filled sequentially with a mixture of He and Ar, and the secondary reservoir is filled with pressurized atmospheric air from the external holding tanks.

The piston is released and propelled down the compression tube by the compressed air in the secondary reservoir, in turn adiabatically compressing and heating the He and Ar mixture behind the primary diaphragm. When the burst pressure of the

primary diaphragm is reached, it fails quasi-instantaneously and a strong shock wave is created at the contact surface between high-pressure driver gas and lower-pressure test gas in the shock tube. This shock wave propagates through the shock tube, accelerating, compressing, and heating the test gas, and is reflected off the end wall, simultaneously vaporizing the Mylar secondary diaphragm. The reflected shock wave propagates back through the already-shocked gas, further compressing and heating it, and also bringing it to rest. This stagnant, high-temperature, high-pressure slug of test gas serves as the reservoir for a contoured 100:1 area ratio converging-diverging nozzle, which accelerates the test gas to hypervelocity before it flows over the model. Chapter 3 provides a further description of the test article and its instrumentation, and Section 2.5 presents analysis of the uncertainty in flow conditions at the end of the nozzle and over the test article.

2.1.2   Gas Premixing Tank

To ensure complete mixture in the shock tube for air and CO_2 mixture experiments, a mixing tank was constructed from an internally cleaned and wire-brush polished former combustion vessel of approximately 400 L volume. The mixing tank has connections for two standard gas bottles and is attached to the T5 shock tube fill manifold. The tank is pictured in its position next to the shock tube in Figure 2.3. The vessel is rated to 612 psi or 4.22 MPa. However, the maximum pressure rating for the M-30 compressed air filter, which is attached to the tank, is 125 psi or 862 kPa, so the system should not in any case be operated at a higher pressure. This filter is located in between the tank and the shock tube manifold, and is designed to remove particulates, moisture, and oil aerosol contaminants down to 0.01 µm from the mixed gas. The pressure gauge currently attached to the tank has a full-scale value of 100 psig or 690 kPa. The highest fill pressure used for the mixing tank in any of the present work was 45 psia or 207 kPa. As the volume of the shock tube is about

76 L, and fill pressures for most cases are rarely higher than 100 kPa, this quantity of premixed gas is usually sufficient for at least five experiments.
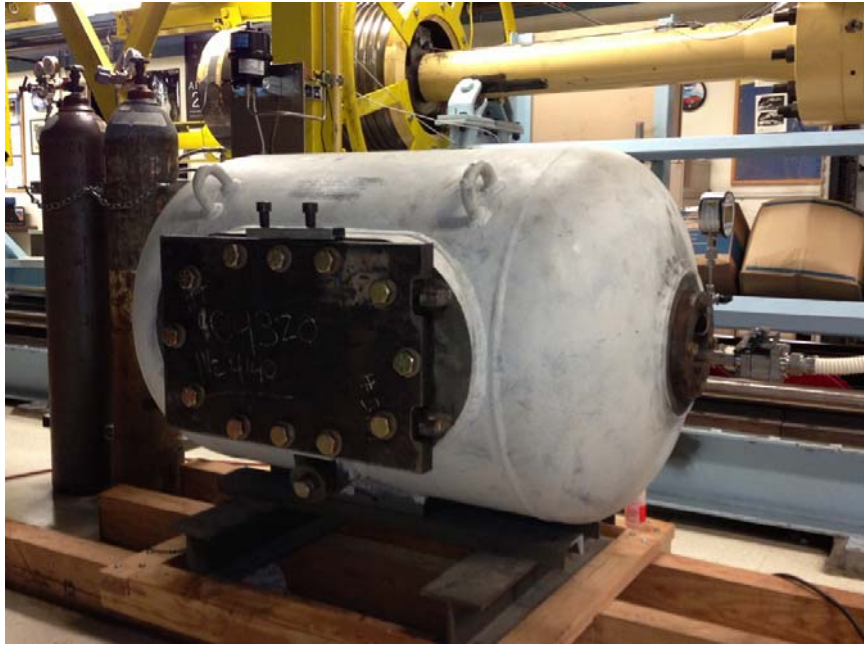
Figure 2.3: Gas premixing tank.

In the present series of tests, the mixing tank was filled sequentially to the desired partial pressure of each gas several hours prior to any experiments. To ensure complete mixing and a uniform distribution of gas species, two 120 mm 12 VDC brushless computer fans were installed in the mixing tank and are run continuously prior to the experiment. These fans, pictured in Figure 2.4, are wired in parallel to an external transformer through a switch located on the mixing tank control panel.

For safety, a CO_2 alarm that triggers at 5000 ppm, meeting OSHA specifications, is positioned near the tank.

Figure 2.4: Gas premixing tank internal fans.

2.1.3   Shock Tube Cleaning Procedure

At the conclusion of each experiment, care must be taken to thoroughly clean the shock tube, nozzle, and model, each of which is to a varying degree coated with soot and other small particles carried in the driver gas. This cleaning step is especially critical for work on laminar to turbulent transition, as particulates in the freestream can destabilize the boundary layer and can lead to early instability (Fedorov and Koslov, 2011, Fedorov, 2013), including intermittent broad-band density disturbances as described in Parziale (2013) and transition to turbulence.

Prior to shot 2703, the standard T5 cleaning procedure consisted of pulling a bundle of clean white towels through the length of the shock tube once or twice, and propelling a bucket covered in towels down the length of the compression tube test section. This procedure was eventually found to be insufficient for performing repeatable experiments, in that inconsistent stability and transition results were sometimes obtained, and clouds consisting of dark particulate contamination were sometimes observed in schlieren movies during the test time. Both of these results were more likely in the next experiment performed after a shot with CO_2 present in the shock tube. A variety of more ambitious cleaning procedures, involving solvents, abrasives, power tools, and multiple passes, were tested in an attempt to reduce particulate contamination. We observed that soot-like dust was present primarily in the shock

tube, and secondarily in the compression tube near its junction with the shock tube. We also determined that the most important segment of the tunnel to clean was the end of the shock tube immediately before the nozzle, where the "slug" of reservoir gas resides.

The cleaning procedure stabilized by shot 2760, and consists of the following steps: first, the final 2 m of the compression tube is dry polished with a wire wheel mounted on an electric drill, prior to propelling the towel-covered bucket through the length of the compression tube. Next, using an appropriate ventilator, gloves, and goggles, the final 2.1 m of the shock tube is polished with a wire wheel around which is wrapped a fresh 3M ScotchBrite Ultra-Fine Hand Pad (#7448) moistened with acetone, with additional acetone sprayed directly into the end of the tube. Over several polishing cycles, black, soot-laden solvent flows out of the end of the shock tube and is collected in a towel placed under the mouth. Next, a fresh towel is wrapped around a mop mounted at the end of a length of 1 in diameter aluminum conduit pipe, with a total pole length of 4 m. This towel is sprayed with acetone and, while twisting the pole, pushed into and then pulled out of the final 4 m of the shock tube. This is repeated at least eight times, inverting each towel once and then replacing it so that a clean surface is always exposed, until the towels return clean. Next, a bundle of several towels is rolled, sprayed with acetone, and pulled with a rope down the length of the shock tube from the nozzle end to the primary diaphragm end (so that any debris is drawn further away from the already cleaned test gas stagnation region). This process is repeated with fresh towel surfaces until the towels come through the tunnel clean, which usually takes at least 20 cycles. Finally, clean towels sprayed with denatured ethyl alcohol are pulled through the shock tube twice in the same manner in an effort to remove any acetone residue, and a single, balled dry towel is pulled through with a shop vacuum.

In addition to the extensive effort devoted to cleaning the shock tube (a total

of ∼3 man-hours per experiment was devoted to cleaning), the primary diaphragm holder is cleaned with acetone and denatured ethyl alcohol. The test article, throat, and nozzle also accumulate dark soot-like dust, although not to the same degree as the shock tube, and are cleaned with Kimwipes sprayed with denatured ethyl alcohol.

Rather than using standard "Industrial"-quality gas bottles to fill the shock tube, as had been the previous practice, reduced-contaminant "Breathing Air" was used from shot 2739. Finally, only Air Liquide "ALPHAGAZ" research-quality gas bottles were used from shot 2757, for all gas types. In this line of gas bottles, the supplier specifies tight tolerances on the O_2 vs. N_2 partial pressure ($\pm 0.5\%$) for air, and total hydrocarbon contamination is less than 0.05 ppm. All of these measures, taken together, were successful in mitigating the effects of particulate contamination and resulted in more consistent, clean, repeatable transition measurements. It is recommended that these cleaning and contaminant minimization measures be maintained for all future T5 experiments where flow purity, optical measurements, and avoiding particulate contamination are important.

2.2 Measured Tunnel Quantities
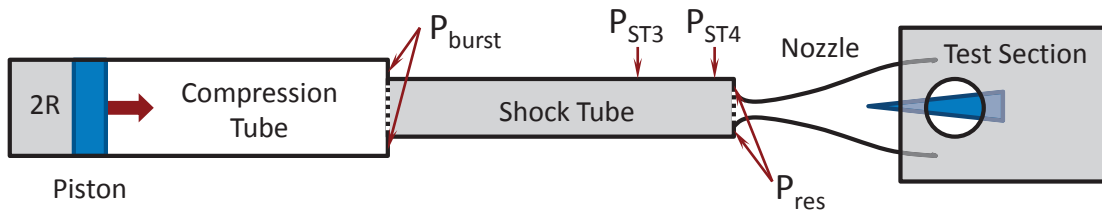
Figure 2.5: Simplified schematic diagram of the T5 Hypervelocity Shock Tunnel with labeled pressure transducers at the diaphragm burst location, stations 3 and 4 (located 4.8 m and 2.4 m, respectively, from the end of the shock tube), and at the shock tube reservoir. See also Figure 2.2.

The piston path is chosen such that the driver gas is maintained at approximately constant pressure P_{burst} during the test time. Burst pressure is measured by two trans-

ducers mounted at the primary diaphragm station. See Figure 2.5 for the transducer location and Figure 2.6 for an example of the burst pressure traces with the burst pressure level indicated. Together with the known shock tube fill pressure P_1, and the composition of the driver gas and test gas, this measurement defines the diaphragm pressure ratio. Taking gas 1 as the unshocked test gas and gas 4 as the high-pressure (P_{burst}) driver gas, as is common in the literature, we can write (*e.g.*, as in Thompson (1972)) the perfect gas relationship:

$$\frac{P_4}{P_1} = \frac{2\gamma_1 \mathrm{M}_{\mathrm{s}}^2 - (\gamma_1 - 1)}{\gamma_1 + 1} \left[1 - \frac{\gamma_4 - 1}{\gamma_1 + 1} \frac{c_1}{c_4} \left(\mathrm{M}_{\mathrm{s}} - \frac{1}{\mathrm{M}_{\mathrm{s}}} \right) \right]^{\frac{-2\gamma_4}{\gamma_4 - 1}} \tag{2.1}$$

This equation may be solved for the shock Mach number M_{s} at a given diaphragm pressure ratio, and converted to shock speed U_{s} using the known properties of gas 1. Real gas properties and numerical methods can be used as discussed in Browne et al. (2008) to compute M_{s} without making the perfect gas assumption. In practice M_{s} is calculated from the measured U_{s} and Equation (2.1) is used to check the consistency of the data.

The primary shock speed is measured experimentally by two time of arrival pressure transducers, at shock tube stations 3 and 4, mounted 2.402 m apart near the end of the shock tube. See Figure 2.5 for the transducer locations and Figure 2.7 for an example of the time of arrival pressure transducer traces with incident and reflected shocks marked.

The calculated value from Equation (2.1) is representative of the initial shock speed after the diaphragm bursts. The shock slows as it propagates through the shock tube and the boundary layer grows inside the tube. Hornung and Belanger (1990) hypothesized that the shock may also slow due to geometric imperfections at the junction of the shock tube with the compression tube. Results show that a good correlation for a measured final shock speed between stations 3 and 4 is ∼90%
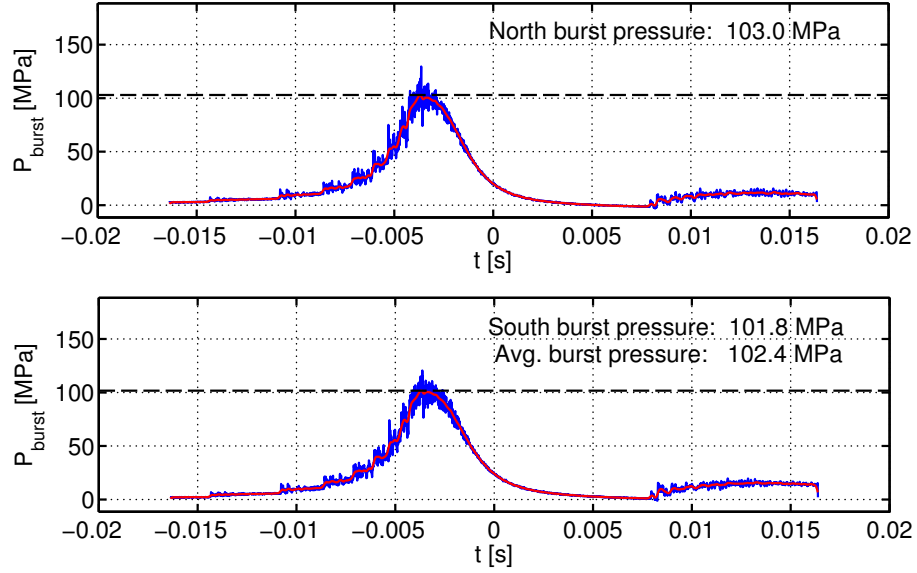
Figure 2.6: Raw (blue) and smoothed (red) pressure traces from the north and south burst pressure transducers for shot 2742, mounted in the primary diaphragm holder at the end of the compression tube (see Figure 2.5). The peak value of the smoothed signal is marked with a dashed line.
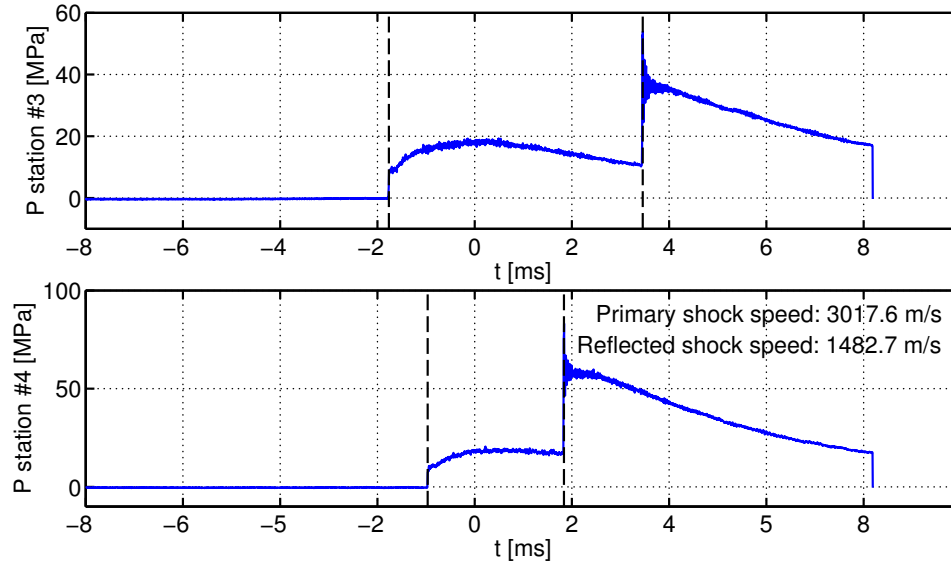
Figure 2.7: Pressure traces from pressure transducers mounted at stations 3 and 4 on the shock tube (see Figure 2.5) for shot 2742, showing time of arrival signals at each station, from which are calculated the primary and reflected shock speeds at the end of the shock tube.

of the initial shock speed computed from Equation (2.1), which agrees with direct measurements of the shock speed decay from time of arrival gauges at stations 1 and

2 during past experiments in T5 with air (Hornung, 1991).

2.3   Reservoir Condition Calculation

The reservoir pressure, P_{res}, is directly measured by two pressure transducers mounted
at the shock tube end wall, immediately upstream of the nozzle throat. See Figure 2.5
for the transducer locations and Figure 2.8 for an example of the reservoir pressure
transducer traces with the period of relatively steady constant pressure supply to the
nozzle conservatively indicated. This indicated period corresponds to the temporal
extent of the experiment (allowing an additional period, $\sim$0.3 ms, to account for the
gas flow time through the nozzle from the throat to the tip of the test article) and
is selected individually from the reservoir pressure plot for each experiment. While
P_{res} remains relatively constant for several milliseconds for some conditions in the
present study, the work of Sudani and Hornung (1998) indicates that the useful test
time for the present enthalpy range is limited to $\sim$1 ms due to driver gas contamina-
tion. As Sudani et al. (2000) recommend, undertailored (discussed subsequently in
Section 3.2.1) conditions are used to minimize contamination.

The measured incident shock speed, U_{s}, from Section 2.2 and the shock tube fill
pressure P_1 are used with the `reflected_eq` routine from the Cantera (Goodwin,
2003; Goodwin, 2009) Shock and Detonation Toolbox (Browne et al., 2008) with CO_2
reaction rates taken from Smith et al. (1999) to calculate the equilibrium thermody-
namic state of the gas after processing by the incident and reflected shock. The test
gas is then isentropically expanded from the computed reservoir pressure state to the
measured P_{res} from the transducers, which adjusts for the effects of wave reflections
between the shock tube end wall and the contact surface between driver and test gas.
This gas state is taken as the input for both one-dimensional nozzle calculations and
the axisymmetric nozzle code described in Section 2.4.2.
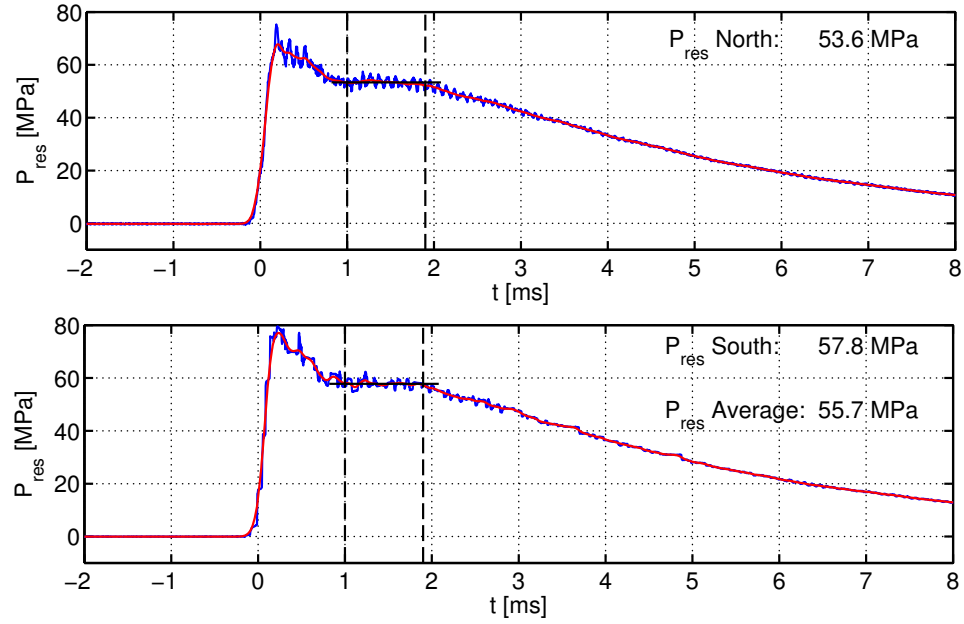
Figure 2.8: Raw (blue) and smoothed (red) pressure traces from the north and south reservoir pressure transducers for shot 2742, mounted at the shock tube end wall just upstream of the nozzle throat (see Figure 2.5). The steady test time, here about 0.9 ms long, is highlighted with dashed lines. This example is undertailored, as an expansion wave at the shock wave/contact surface interface is seen to lower the reservoir pressure prior to the useful test time (Tropea et al., 2007).

2.4   Nozzle Flow Calculation

2.4.1   1-D Nozzle Calculation

Section 3.3.2 of Beierholm et al. (2008) developed a set of four differential equations for mass, momentum, energy, and species describing flow through a one-dimensional nozzle based on sonic conditions at the throat and a given area change with x-

displacement, defined by the physical nozzle geometry $A(x)$:

$$\begin{aligned}
\frac{\mathrm{d}U}{\mathrm{d}x} &= \frac{1}{\eta}\left[\dot{\sigma} - \frac{U}{A}\frac{\mathrm{d}A}{\mathrm{d}x}\right] \\
\frac{\mathrm{d}P}{\mathrm{d}x} &= -\frac{\rho U}{\eta}\left[\dot{\sigma} - \frac{U}{A}\frac{\mathrm{d}A}{\mathrm{d}x}\right] \\
\frac{\mathrm{d}\rho}{\mathrm{d}x} &= \frac{\rho}{U\eta}\left[\dot{\sigma} - \mathrm{M}^2\frac{U}{A}\frac{\mathrm{d}A}{\mathrm{d}x}\right] \\
\frac{\mathrm{d}y_i}{\mathrm{d}x} &= \frac{W_i\dot{\omega}_i}{\rho U}
\end{aligned}$$

The thermicity, $\dot{\sigma}$, is defined as:

$$\dot{\sigma} \equiv \sum_{i=1}^{k}\left(\frac{W}{W_i} - \frac{h_i}{C_p T}\right)U\frac{\mathrm{d}y_i}{\mathrm{d}x}$$

The production rate, molar mass, mole fraction, and mass fraction of species i are, respectively, $\dot{\omega}_i$, W_i, χ_i, and y_i. $\eta \equiv (1 - \mathrm{M}^2)$ is the sonic parameter.

The solution to these four coupled differential equations is implemented, for convenience and backwards compatibility, with a similar nozzle format as that used by NENZF (Lordi et al., 1966), the previous nozzle flow solver. Beierholm et al. (2008) developed non-Cantera MATLAB subroutines that interface with the Cantera package to solve for nozzle flow equations, including `oneDflow`, `areafun`, `non-ideal_eq_soundspeed`, `nonideal_soundspeed`, and `isenfun`. Coupled with Cantera routines for computing net production rates, species, entropy, and enthalpy, these MATLAB functions are implemented in a new nozzle flow solver, which takes as its gas state inputs the reservoir conditions described in Section 2.3, and evolves a Cantera gas object down the length of the defined nozzle geometry. The chemical kinetics models used are described in Smith et al. (1999) and Gupta et al. (1990).

The results of these computations for the nozzle exit (*i.e.*, 100 cm downstream from the throat) are labeled as "1D 100 cm" in, for example, Table 2.14 (for freestream properties), Table 2.15 (for freestream species mass fractions), and throughout Ap-

pendix B. Dissociated species mass fractions "freeze" during nozzle expansion when the density and temperature become too low to sustain collisions frequent enough for recombination and vibrational energy transfer. This effect leaves a greater fraction of dissociated, vibrationally excited species present in the mean flow than would be the case for equilibrium flows, or the comparable free flight conditions (Stalker, 1989).

2.4.2 Axisymmetric Nozzle Flow Simulations

In order to obtain more accurate values for the flow properties over the test cone than are possible with the simple one-dimensional calculation described in Section 2.4.1, including a more accurate accounting of vibrational nonequilibrium, we begin with the same reservoir conditions computed with the procedure described in Section 2.3 and tabulated in Appendix A. Gas at each reservoir condition is computationally expanded through the nozzle using the CFD solver described below, rather than the one-dimensional calculation previously used in T5 studies, which is described in Lordi et al. (1966).

We simulate the flow through the nozzle by solving the chemically reacting, vibrationally active, axisymmetric, two-dimensional Navier-Stokes equations with a structured-grid CFD solver developed at the University of Minnesota (Candler, 2005), as described in Wagnild (2012). The solver uses an excluded-volume equation of state in order to model molecular size effects on gas properties at high pressure. The inviscid fluxes are calculated using the modified Steger-Warming flux vector splitting method (Steger and Warming, 1981) and are second-order accurate with a MUSCL limiter as the total variation dimishing scheme (van Leer, 1979). The viscous fluxes are second-order accurate. The time advancement method is the implicit, first-order DPLR method (Wright et al., 1998). The turbulent boundary layer flow is modeled using the one-equation, Spalart-Allmaras (Spalart and Allmaras, 1992) model with the Catris-Aupoix (Catris and Aupoix, 2000) correction for compressibility. The noz-

zle flow is calculated on a single-block, structured grid with dimensions 492 cells by 219 cells in the streamwise and wall-normal directions, respectively (see Figure 2.9). The grid, used originally by Wagnild (2012), is clustered near the nozzle wall in order to sufficiently resolve the boundary layer for both laminar and turbulent cases.

This nozzle computation is performed for every experiment in the present study, and provides the input conditions for the boundary layer calculations described in Section 4.1.2. For most of the current computational analyses, it is assumed that the boundary layer on the nozzle walls becomes turbulent in the reservoir and remains in this state for the remainder of the nozzle, but the effect of a potentially laminar boundary layer on the nozzle wall on nozzle conditions is one of the variables examined in Section 2.6. In all cases the wall temperature for the nozzle is taken to be 297 K.
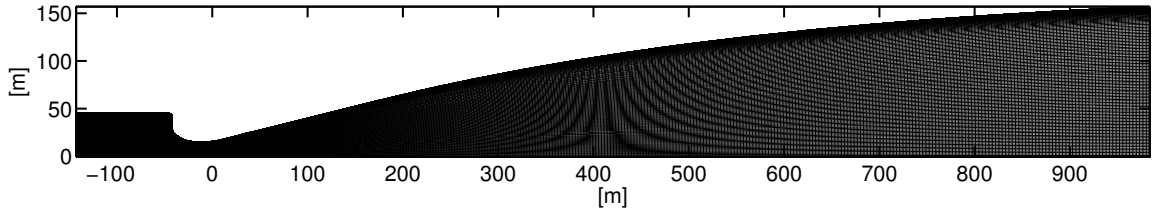
Figure 2.9: Axisymmetric grid of 492 cells by 219 cells in the streamwise and wall-normal directions, respectively, used for nozzle flow computations.

2.5 Run Conditions and Uncertainty Estimates

2.5.1 Overview

The shock speed is measured by two time of arrival pressure transducers with a known physical displacement along the axial direction of the shock tube, as discussed in Section 2.2. These transducers have an approximate measurement uncertainty of 8×10^{-6} s. The uncertainty in the shock speed measurement thus increases as the measured time of arrival difference decreases, based on the time scale that the data acquisition system can resolve. At a shock speed of 3000 m/s, typical for the

present study, the uncertainty is ∼30 m/s. The shock tube fill pressure uncertainty is ∼0.25 kPa, and the measured reservoir pressure uncertainty, based upon recorded pressure traces such as those presented in Figure 2.8, is typically ∼4 MPa. The measured uncertainties are presented in Table 2.1.

Uncertainties on the calculated quantities are estimated by perturbing Cantera Shock and Detonation Toolbox condition computations, similar to those described in Section 2.3, within the range of the uncertainties on the measured shock speed, reservoir pressure, and initial shock tube pressure. Only experiments with measured shock speeds that fall within the uncertainty for the adjusted shock speed curve[1] predicted by the shock jump conditions from the primary diaphragm burst pressure, driver gas composition, and initial shock tube conditions are included in the present data set.

There are a number of other potential sources of measurement error, including nonideal gas behavior in the reservoir due to the high pressure, the extrapolation of the shock speed (which decays as it propagates down the shock tube) to the end wall, nonuniformity of reservoir conditions due to nonideal shock reflection, and the method of correcting flow conditions from the ideal reflected-shock pressure to measured reservoir pressure using an isentropic expansion. Furthermore, the one-dimensional contoured nozzle computation, described in Section 2.4.1, does not account for boundary layer growth within the nozzle, off-design operation conditions that lead to flow nonuniformity, or vibration-translation nonequilibrium and freezing within the nozzle, which is particularly significant for the N_2 cases. However, the axisymmetric nozzle computations described in Section 2.4.2, which provide the input conditions for boundary layer analysis, do include these nozzle effects.

Run conditions and uncertainty estimates for three typical T5 conditions taken from low enthalpy (2649), mid-range enthalpy (2645), and high enthalpy (2788) shots

---

[1]See Figure 3.13 for an example from the present study.

Measurement	Symbol	Uncertainty	Units
Shock Speed	U_s	±13–53	m/s
Shock Tube Fill Pressure	P_1	±0.25	kPa
Reservoir Pressure	P_{res}	±2–4	MPa

Table 2.1: Estimated uncertainty of measured quantities, all shots.

are made below. Computed boundary layer edge condition uncertainties are estimated at the edge of the cone boundary layer using a Taylor-Maccoll solution from the nozzle exit conditions.

The fluid properties of greatest interest in the present work are typically those near the surface of the conical test article, after the conical shock at the boundary layer edge (see Tables 2.4, 2.7, and 2.10), since those quantities define the boundary layer's properties. For typical conditions from a wide range of enthalpies, the greatest uncertainty at the boundary layer edge in percentage terms is found to be the edge pressure. This is a result of the relatively uncertain measurement of reservoir conditions at the end of the shock tube. The smallest uncertainty is found in the Mach number and edge velocity.

2.5.2 Uncertainty Estimates (Low Enthalpy, Shot 2649)

Experiment 2649 had a computed enthalpy of 4.78 MJ/kg. Uncertainty values for the measured tunnel quantities, computed thermal quantities, and computed boundary layer edge quantities are presented in Tables 2.2, 2.3, and 2.4, respectively.

Measurement	Symbol	Value	Uncertainty	Units	Percent
Shock Speed	U_s	2256	±17	m/s	0.8
Shock Tube Fill Pressure	P_1	90.0	±0.25	kPa	0.3
Reservoir Pressure	P_{res}	22.2	±2	MPa	9.1

Table 2.2: Estimated uncertainty of measured quantities, shot 2649.

Computed Quantity	Symbol	Value	Uncertainty	Units	Percent
Reservoir Enthalpy	h_{res}	4.78	± 0.14	MJ/kg	3.0
Reservoir Temperature	T_{res}	3785	± 78	K	2.0
Reservoir Density	ρ_{res}	20.1	± 1.5	kg/m^3	7.4
Freestream Temperature	T_∞	604	± 23	K	3.8
Freestream Density	ρ_∞	0.0438	± 0.0066	kg/m^3	8.5
Freestream Pressure	P_∞	7.63	± 1.7	kPa	11.3
Freestream Velocity	U_∞	2923	± 40	m/s	1.4
Freestream Mach Number	M_∞	5.97	± 0.03	-	0.5

Table 2.3: Estimated uncertainty of computed thermal quantities, shot 2649.

Computed Quantity	Symbol	Value	Uncertainty	Units	Percent
Edge Temperature	T_{e}	678	± 25	K	3.6
Edge Density	ρ_{e}	0.0596	± 0.0041	kg/m^3	6.9
Edge Pressure	P_{e}	11.7	± 1.1	kPa	9.3
Edge Velocity	U_{e}	2895	± 39	m/s	1.4
Edge Mach Number	M_{e}	5.58	± 0.02	-	0.4

Table 2.4: Estimated uncertainty of computed boundary layer edge quantities, shot 2649.

2.5.3   Uncertainty Estimates (Mid-Range Enthalpy, Shot 2645)

Experiment 2645 had a computed enthalpy of 9.96 MJ/kg. Uncertainty values for the measured tunnel quantities, computed thermal quantities, and computed boundary layer edge quantities are presented in Tables 2.5, 2.6, and 2.7, respectively.

Measurement	Symbol	Value	Uncertainty	Units	Percent
Shock Speed	U_{s}	3209	± 35	m/s	1.1
Shock Tube Fill Pressure	P_1	85.35	± 0.25	kPa	0.3
Reservoir Pressure	P_{res}	54.3	± 4	MPa	7.4

Table 2.5: Estimated uncertainty of measured quantities, shot 2645.

Computed Quantity	Symbol	Value	Uncertainty	Units	Percent
Reservoir Enthalpy	h_{res}	9.96	± 0.32	MJ/kg	3.3
Reservoir Temperature	T_{res}	6166	± 150	K	2.5
Reservoir Density	ρ_{res}	27.5	± 2.2	kg/m^3	7.9
Freestream Temperature	T_{∞}	1485	± 61	K	4.1
Freestream Density	ρ_{∞}	0.0588	± 0.0043	kg/m^3	7.4
Freestream Pressure	P_{∞}	25.7	± 2.5	kPa	9.9
Freestream Velocity	U_{∞}	4043	± 62	m/s	1.5
Freestream Mach Number	M_{∞}	5.33	± 0.03	-	0.5

Table 2.6: Estimated uncertainty of computed thermal quantities, shot 2645.

Computed Quantity	Symbol	Value	Uncertainty	Units	Percent
Edge Temperature	T_{e}	1616	± 65	K	5.2
Edge Density	ρ_{e}	0.0768	± 0.0056	kg/m^3	7.4
Edge Pressure	P_{e}	36.4	± 3.5	kPa	9.6
Edge Velocity	U_{e}	4002	± 61	m/s	1.5
Edge Mach Number	M_{e}	5.06	± 0.02	-	0.5

Table 2.7: Estimated uncertainty of computed boundary layer edge quantities, shot 2645.

2.5.4 Uncertainty Estimates (High Enthalpy, Shot 2788)

Experiment 2788 had a computed enthalpy of 13.1 MJ/kg. Uncertainty values for the measured tunnel quantities, computed thermal quantities, and computed boundary layer edge quantities are presented in Tables 2.8, 2.9, and 2.10, respectively.

Measurement	Symbol	Value	Uncertainty	Units	Percent
Shock Speed	U_{s}	3707	± 46	m/s	1.3
Shock Tube Fill Pressure	P_1	65.0	± 0.25	kPa	0.4
Reservoir Pressure	P_{res}	54.7	± 4	MPa	7.3

Table 2.8: Estimated uncertainty of measured quantities, shot 2788.

Computed Quantity	Symbol	Value	Uncertainty	Units	Percent
Reservoir Enthalpy	h_{res}	13.1	± 0.46	MJ/kg	3.5
Reservoir Temperature	T_{res}	7375	± 180	K	2.4
Reservoir Density	ρ_{res}	21.9	± 1.8	kg/m^3	8.2
Freestream Temperature	T_{∞}	1932	± 79	K	4.1
Freestream Density	ρ_{∞}	0.0469	± 0.0039	kg/m^3	8.4
Freestream Pressure	P_{∞}	27.3	± 2.5	kPa	9.4
Freestream Velocity	U_{∞}	4550	± 73	m/s	1.6
Freestream Mach Number	M_{∞}	5.19	± 0.03	-	0.5

Table 2.9: Estimated uncertainty of computed thermal quantities, shot 2788.

Computed Quantity	Symbol	Value	Uncertainty	Units	Percent
Edge Temperature	T_{e}	2095	± 84	K	4.0
Edge Density	ρ_{e}	0.0606	± 0.0050	kg/m^3	8.3
Edge Pressure	P_{e}	38.4	± 3.5	kPa	9.1
Edge Velocity	U_{e}	4504	± 72	m/s	1.6
Edge Mach Number	M_{e}	4.94	± 0.02	-	0.5

Table 2.10: Estimated uncertainty of computed boundary layer edge quantities, shot 2788.

2.6   Cone-Nozzle Position Study

A series of computations were carried out to determine the sensitivity of computed boundary layer freestream and edge conditions to assumptions about the flow in the nozzle, the location of the cone tip, and the effect of vibrational-translational relaxation modeling. See Section 4.3.3 for a discussion of the sensitivity of computed N factors (Table 4.1) to these same assumptions.

The conditions from three air experiments (2742, 2764, and 2823); two N_2 experiments (2776 and 2778); two CO_2 experiments (2793 and 2808); and two CO_2/air mixture experiments (2817 and 2821) were chosen for analysis. The detailed analysis of experiment 2742, an air case performed in T5 on 19 July 2012, is presented below. The remaining eight cases analyzed are recorded in Appendix B.

2.6.1 Geometry

The test article was a 1 m 5-degree half-angle cone with a sharp tip. The initial shock tube composition was 100% air. Reservoir temperature, density, and composition are computed from the measured shock speed and shock tube initial conditions using a Cantera-based reflected-shock model adjusted for measured reservoir pressure.

2.6.2 Measured Quantities

Measurement	Symbol	Value	Units
Shock Speed	U_{s}	3020	m/s
Shock Tube Fill Pressure	P_1	110.50	kPa
Reservoir Pressure	P_{res}	55.7	MPa

Table 2.11: Measured quantities, shot 2742

2.6.3 Computed Reservoir Conditions

Computed Quantity	Symbol	Value	Units
Reservoir Temperature	T_{res}	5623	K
Reservoir Density	ρ_{res}	31.81	kg/m^3
Reservoir Enthalpy	h_{res}	8.64	MJ/kg

Table 2.12: Computed reservoir conditions, shot 2742

$Y_{\mathrm{N_2}}$	$Y_{\mathrm{O_2}}$	$Y_{\mathrm{CO_2}}$	Y_{NO}	Y_{CO}	Y_{N}	Y_{O}
6.99×10^{-1}	7.14×10^{-2}	0	1.40×10^{-1}	0	2.24×10^{-3}	8.68×10^{-2}

Table 2.13: Computed reservoir species mass fractions, shot 2742

2.6.4 Effect of Nozzle Position and Nozzle Wall Transition

The edge quantities are computed using the UMNAEM nozzle code, described in Section 2.4.2, with turbulent (unless otherwise stated) or laminar nozzle boundary layer assumptions, and the DPLR/STABL suite taking averaged input freestream

conditions representing the tip of the cone at five different positions in the nozzle for turbulent wall conditions, and one position in the nozzle for laminar wall conditions, designated by the five black boxes in Figure 2.10, and the single black box in Figure 2.11. The results are compared to the results of the one-dimensional Cantera-based nozzle code at the nozzle exit. Freestream (input) conditions and mass fractions for each case are presented in Tables 2.14 and 2.15. Conditions after the shock at the edge of the cone's boundary layer edge are presented in Tables 2.16 and 2.17. The "1D 100 cm" line in these latter two tables is computed from the one-dimensional nozzle exit conditions with a Taylor-Maccoll shock from the cone tip.

The study indicates that variation in the cone/nozzle relative position, and the assumption about whether the nozzle boundary layer is laminar or turbulent, are not very important in terms of the resulting computed edge conditions, which vary by $\pm 5\%$ or less in most cases for all edge parameters with ± 5 cm variation in cone/nozzle relative position (the exception is edge pressure, which varies up to 9% in a few cases). However, the position 72 cm from the nozzle throat matches the best measurement of the experimental geometry, and stability solutions for the laminar nozzle wall, frozen, and equilibrium cases are computed from input conditions at this position in Section 4.3.2.

	U_∞	T_∞	Tv_∞	M_∞	P_∞	ρ_∞	Unit Re_∞
	m/s	K	K	-	kPa	kg/m^3	1/m
1D 100 cm	3808	1274.0	1274.0	5.44	25.2	0.068	5.34×10^6
100 cm	3803	1221.7	1223.4	5.40	23.3	0.066	5.32×10^6
Lam 72 cm	3787	1272.3	1277.8	5.27	27.8	0.075	5.90×10^6
82 cm	3780	1294.4	1292.5	5.21	29.7	0.079	6.13×10^6
77 cm	3778	1301.6	1301.4	5.20	30.4	0.081	6.21×10^6
72 cm	3782	1287.4	1294.1	5.23	29.1	0.078	6.04×10^6
67 cm	3791	1259.1	1270.6	5.30	26.6	0.073	5.77×10^6
62 cm	3795	1246.0	1251.6	5.33	25.4	0.070	5.61×10^6

Table 2.14: Computed freestream conditions at 62, 67, 72, 77, 82, and 100 cm downstream of the nozzle throat with turbulent nozzle wall assumptions, 72 cm with laminar nozzle wall assumptions, and 100 cm for a one dimensional nozzle expansion, shot 2742. For the equivalent experiment, the tip of the cone was 72 cm downstream of the nozzle throat.

	Y_{N_2}	Y_{O_2}	Y_{CO_2}	Y_{NO}	Y_{CO}	Y_N	Y_O
1D 100 cm	7.38×10^{-1}	1.88×10^{-1}	0	6.14×10^{-2}	0	6.46×10^{-10}	1.19×10^{-2}
100 cm	7.33×10^{-1}	1.87×10^{-1}	0	7.40×10^{-2}	0	4.26×10^{-10}	6.30×10^{-3}
Lam 72 cm	7.33×10^{-1}	1.87×10^{-1}	0	7.39×10^{-2}	0	8.44×10^{-10}	6.37×10^{-3}
82 cm	7.33×10^{-1}	1.87×10^{-1}	0	7.39×10^{-2}	0	9.86×10^{-10}	6.40×10^{-3}
77 cm	7.33×10^{-1}	1.87×10^{-1}	0	7.39×10^{-2}	0	1.11×10^{-9}	6.38×10^{-3}
72 cm	7.33×10^{-1}	1.87×10^{-1}	0	7.39×10^{-2}	0	9.86×10^{-10}	6.36×10^{-3}
67 cm	7.33×10^{-1}	1.87×10^{-1}	0	7.39×10^{-2}	0	7.36×10^{-10}	6.34×10^{-3}
62 cm	7.33×10^{-1}	1.87×10^{-1}	0	7.39×10^{-2}	0	5.94×10^{-10}	6.33×10^{-3}

Table 2.15: Computed freestream species mass fractions at 62, 67, 72, 77, 82, and 100 cm downstream of the nozzle throat with turbulent nozzle wall assumptions, 72 cm with laminar nozzle wall assumptions, and 100 cm for a one dimensional nozzle expansion, shot 2742. For the equivalent experiment, the tip of the cone was 72 cm downstream of the nozzle throat.

	U_e	T_e	$T\text{v}_\text{e}$	M_e	P_e	ρ_e	Unit Re$_\text{e}$
	m/s	K	K	-	kPa	kg/m^3	1/m
1D 100 cm	3771	1391.5	1391.5	5.15	36.2	0.089	6.57×10^6
100 cm	3740	1396.9	1396.4	4.97	33.9	0.084	5.98×10^6
Lam 72 cm	3725	1445.5	1445.0	4.86	39.9	0.095	6.66×10^6
82 cm	3717	1467.0	1466.6	4.82	42.5	0.100	6.93×10^6
77 cm	3714	1475.9	1475.5	4.80	43.4	0.102	7.02×10^6
72 cm	3718	1461.0	1458.8	4.83	41.7	0.099	6.92×10^6
67 cm	3727	1436.4	1435.9	4.88	38.4	0.092	6.47×10^6
62 cm	3732	1421.5	1421.1	4.91	36.7	0.089	6.30×10^6

Table 2.16: Computed boundary layer edge conditions with the freestream input conditions taken from 62, 67, 72, 77, 82, and 100 cm downstream of the nozzle throat with turbulent nozzle wall assumptions, 72 cm with laminar nozzle wall assumptions, and 100 cm for a one dimensional nozzle expansion, shot 2742. For the equivalent experiment, the tip of the cone was 72 cm downstream of the nozzle throat.

	Y_{N_2}	Y_{O_2}	Y_{CO_2}	Y_{NO}	Y_{CO}	Y_{N}	Y_{O}
1D 100 cm	7.38×10^{-1}	1.88×10^{-1}	0	6.14×10^{-2}	0	6.46×10^{-10}	1.19×10^{-2}
100 cm	7.33×10^{-1}	1.87×10^{-1}	0	7.40×10^{-2}	0	2.67×10^{-9}	5.97×10^{-3}
Lam 72 cm	7.33×10^{-1}	1.88×10^{-1}	0	7.39×10^{-2}	0	4.00×10^{-9}	5.96×10^{-3}
82 cm	7.33×10^{-1}	1.88×10^{-1}	0	7.39×10^{-2}	0	4.76×10^{-9}	5.95×10^{-3}
77 cm	7.33×10^{-1}	1.88×10^{-1}	0	7.39×10^{-2}	0	5.08×10^{-9}	5.91×10^{-3}
72 cm	7.33×10^{-1}	1.88×10^{-1}	0	7.39×10^{-2}	0	4.51×10^{-9}	5.92×10^{-3}
67 cm	7.33×10^{-1}	1.88×10^{-1}	0	7.39×10^{-2}	0	3.72×10^{-9}	5.95×10^{-3}
62 cm	7.33×10^{-1}	1.88×10^{-1}	0	7.39×10^{-2}	0	3.28×10^{-9}	5.96×10^{-3}

Table 2.17: Computed boundary layer edge species mass fractions with the freestream input conditions taken from 62, 67, 72, 77, 82, and 100 cm downstream of the nozzle throat with turbulent nozzle wall assumptions, 72 cm with laminar nozzle wall assumptions, and 100 cm for a one dimensional nozzle expansion, shot 2742. For the equivalent experiment, the tip of the cone was 72 cm downstream of the nozzle throat.
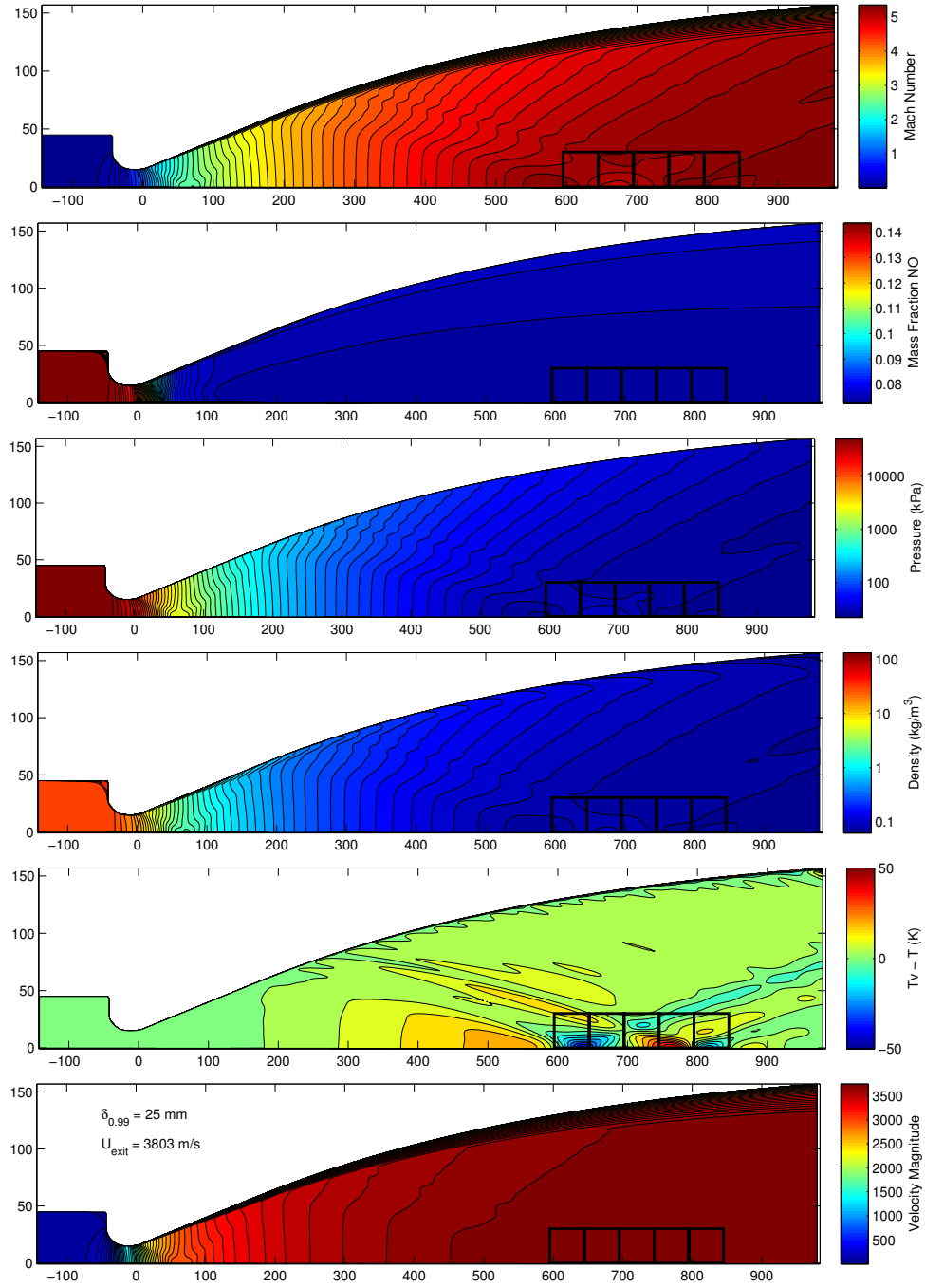
Figure 2.10: Nozzle flow computed with the Spalart-Allmaras turbulence model for the wall, shot 2742. The black boxes highlights the averaged regions used to create STABL/DPLR inputs. The nozzle velocity boundary layer thickness, δ_{99}, is an order of magnitude larger for the turbulent case here than for the laminar case in Figure 2.11.
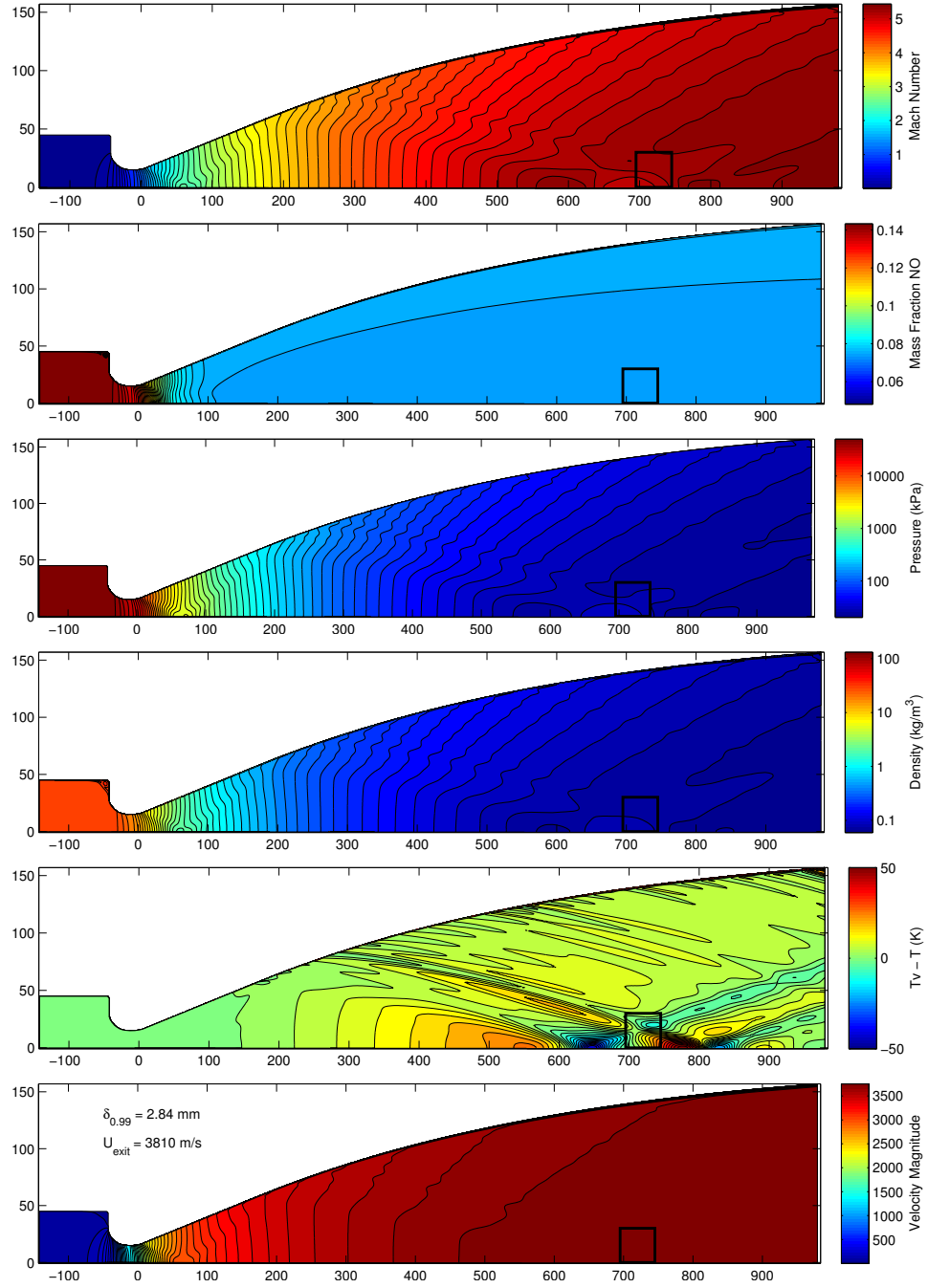
Figure 2.11: Nozzle flow computed with laminar boundary layer growth for the wall, shot 2742. The black box highlights the averaged region used to create STABL/DPLR inputs. The nozzle velocity boundary layer thickness, δ_{99}, is an order of magnitude smaller for the laminar case here than for the turbulent case in Figure 2.10.

Chapter 3

Test Methods and Conditions

3.1 Test Article

The model is a smooth 5-degree half-angle aluminum cone similar to that used in a number of previous experimental studies in T5, 1 m in axial length, and is composed of three sections: a sharp tip fabricated of molybdenum, an interchangeable mid-section which may contain a porous gas-injector section (in the present experiments this section is a smooth, solid piece of plastic), and the main body. The conical model geometry was chosen because of the wealth of experimental and numerical data available with which to compare the results from this program. Two photographs of the cone model are shown in Figure 3.1. The model is axially centered and mounted at angle of attack and yaw of no more than $\pm 0.10°$ with the T5 nozzle axis, such that the tip of the cone protrudes about 280 mm into the nozzle at run time, in order to maximize the linear extent of the cone within the test rhombus defined by the expansion fan radiating from the nozzle's edge.

The molybdenum tip for all experiments detailed in this thesis had a radius ~ 0.175 mm or less (see Figure 3.2). Karl et al. (2011) computationally confirmed that the theoretical entropy layer swallowing distance developed in Rotta (1966) and Stetson (1983) effectively defines the length from a blunted tip beyond which a cone's surface pressure and heat flux distributions do not vary from the sharp tip values.

This swallowing length depends upon Mach number, Reynolds number, cone angle, and tip radius. Using values for the entropy layer swallowing distance parameter in Figure 5 of Stetson (1983), for $M_\infty = 6$ and a tip with radius ~ 0.175 mm, the swallowing distance for a flow with unit Re $= 10.0 \times 10^6$ m^{-1}, at the upper end of values in this study, is calculated to be 53 mm. For a flow with unit Re $= 3.0 \times 10^6$ m^{-1}, at the lower end of values in this study, the swallowing distance is calculated to be 36 mm. As the first row of thermocouples is located at $x = 220.9$ mm from the tip, the cone is effectively sharp over the study's entire range of Reynolds numbers from the standpoint of the heat transfer measurements. The same conclusion is reached for the porous injector for the injection cases in Chapter 7, as the leading edge of the injector is located 132.6 mm from the tip (See Figure 7.1). For all experiments considered in the present work, the flow around the cone has effectively "forgotten" the small nose tip bluntness[1].
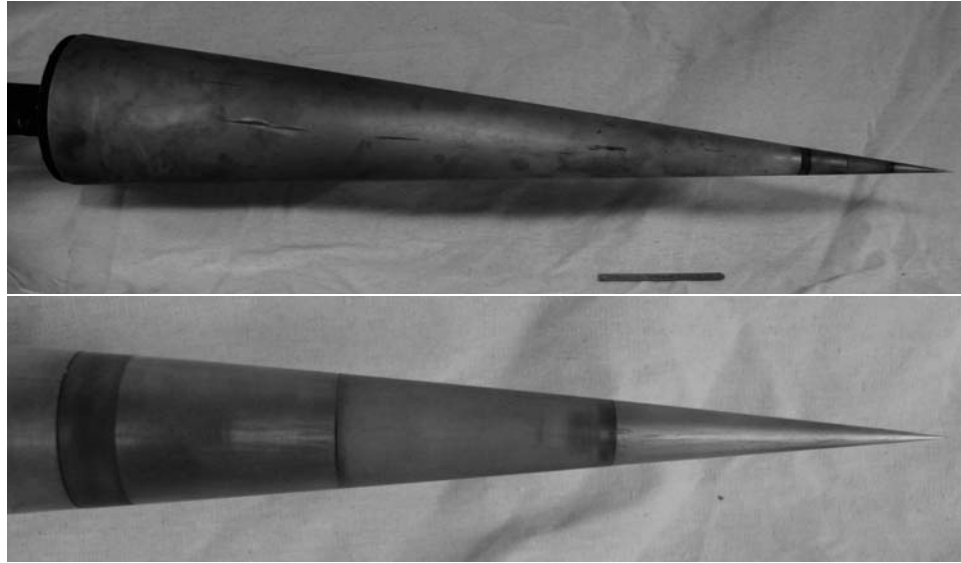
Figure 3.1: Top: Aluminum cone, 1 m in length, instrumented with 80 thermocouples in 20 rows. Bottom, from right to left: molybdenum tip, plastic holder, 316L sintered stainless steel 10 μm porous section, plastic mating section, cone.

---

[1]This conclusion would be true even for the "end of life" tip shown in Figure 3.2, which has a swallowing distance of 92 mm for the high Reynolds number condition. However, at no point during the present work was a tip this blunt used.
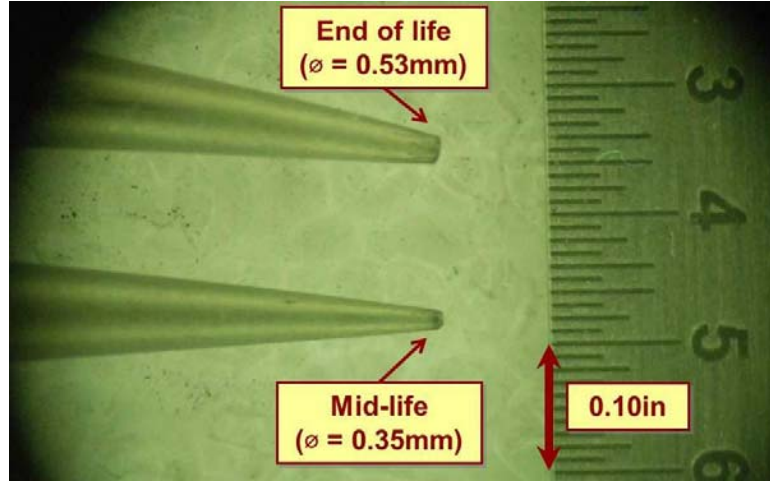
Figure 3.2: Molybdenum cone tips with measured diameters at typical (bottom) and end-of-life (top) states. The end-of-life tip was not used in the present work, but can be considered the extreme limiting case, as it is the most blunt extant example of discarded cone tips from past T5 test campaigns.

The main body of the cone consists of two halves, with polished seams extending radially from the tip section to the aft part of the cone. For the non-injection cases constituting the bulk of the present work, there are two main circumferential seams, depicted in a dimensional drawing in Figure 3.3. The forward of these two seams, where the molybdenum tip attaches to the rest of the assembly and the boundary layer is thinner, is the most significant potential source of roughness-based instability on the cone. There is a second seam aft of the tip joint where the plastic holder is joined to the cone frustum. Both seams are sanded and polished for fit after cone assembly, and the potential remaining isolated step roughness height, k, is estimated at no more than 500 μin.

A Reynolds number based on roughness height k, following the notation of Reda (2002), may be used to correlate the effect of roughness elements of various sizes and in different flow regimes on boundary layer stability and transition:

$$\mathrm{Re}_{kk} = \frac{\rho_k u_k k}{\mu_k} \tag{3.1}$$

Virtual sharp 39.423

32.222
32.662
34.282
36.429
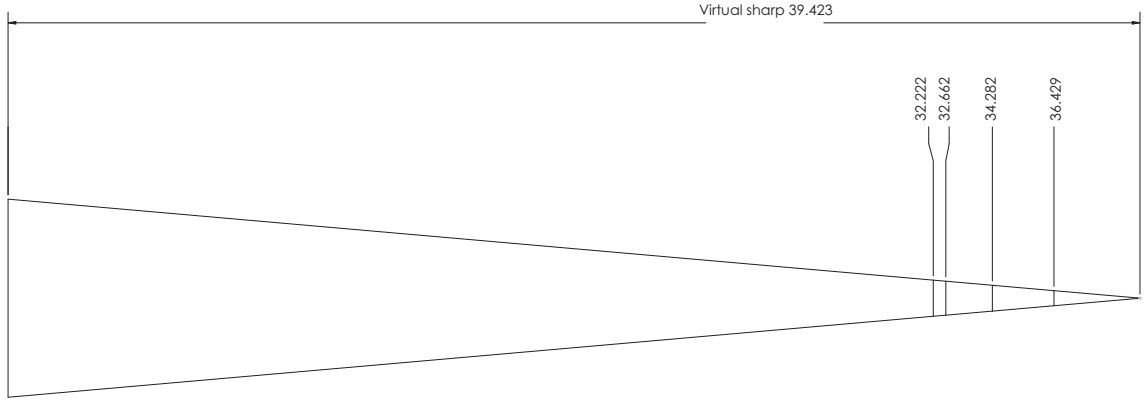
Figure 3.3: Dimensional drawing of 1 m cone (dimensions notated in inches from the base) with the location of the joint between the main cone frustum and the plastic holder noted at 32.222 in. (182.9 mm from the tip) and the joint between the plastic holder and the molybdenum tip noted at 36.429 in. (76.0 mm from the tip). The intermediate joints, associated with a sintered stainless steel porous section, were only present for the injection tests discussed in Chapter 7.

In Equation 3.1 all fluid properties are evaluated at the location equivalent to the height of the roughness element k in an undisturbed laminar boundary layer[2]. Schneider (2008b) notes that "there is almost no data for the effect of roughness on transition at high-enthalpy conditions with chemistry", but since that review a handful of relevant studies have been performed, primarily in the NASA Ames Research Center hypersonic ballistic range. Reda et al. (2010) studied transition on hemispheres with isolated roughness elements in both air at Mach 12 and CO_2 at Mach 15, and Reda et al. (2012) studied the effect of distributed roughness elements on blunt cones of 30° half-angle in air at Mach 10. Reda et al. (2012) report critical Re_{kk} of 600–800 for CO_2 experiments and 750–850 for air experiments for isolated roughness elements. Reda et al. (2010) report critical $Re_{kk} \approx 250$ for roughness elements distributed over the entire blunt cone frustum.

---

[2]A Reynolds number with length scale k, but with the fluid properties evaluated at the boundary layer edge may also be constructed, and is often designated Re_k or Re_{ke}, although Reda (2002) and Schneider (2008b) agree that Equation 3.1 is the more effective correlation. As the edge Reynolds number calculation does not require a detailed boundary layer solution, Re_k appears more often in older work, but has also been used more recently to describe roughness elements which are large relative to the boundary layer height, as in Iyer and Mahesh (2013). Confusingly, some authors (*e.g.* Schneider (2008b)) have used Re_k to designate the quantity specified here in Equation 3.1 as Re_{kk}.

At lower enthalpy (but more similar geometry) Casper et al. (2011) describe adiabatic wall tests at Mach 6 in the Purdue Quiet Tunnel with isolated roughness elements on a slightly blunt ($r_N = 1.19$ mm) 7° half-angle cone at zero angle of attack, and report critical Re_{kk} as low as 100–200 for noisy flow, noting that larger values are necessary to provoke transition under quiet conditions.

Equation 3.1 is used to calculate Re_{kk} based on $k = 500$ µin., with the mean flow and boundary layer solutions computed as described in Section 4.1.2. Results for three typical T5 conditions taken from low enthalpy (2649), mid-range enthalpy (2645), and high enthalpy (2788) shots are presented in Figure 3.4, with the location of the two seams indicated and the region around the nose tip detailed. Note that the surface finish is even smoother than the value of k assumed here for the seams, and so these Re_{kk} are an upper bound for the distributed roughness effects due to the surface, as well.

Figure 3.5 presents Re_{kk} and Re_k for all experiments in the present data set. While there is no exact analogue to the type of roughness element that the cone seams may create in the literature (isolated, not distributed, step roughness at high enthalpy on a slender, sharp cone with a cold wall), the calculated values of Re_{kk} for the present experiments are less than all of the critical values which are available and summarized above, by about a factor of two or more. Note also that a number of fully laminar experiments were observed. Furthermore, the values of Re_{kk} in Figure 3.5 imply that for roughness-dominated transitional flows, the N_2 cases (which have relatively lower Re_{kk}) in the present data set ought to transition later and at higher disturbance amplification N factors, and the CO_2-containing cases (which have relatively higher Re_{kk}) ought to transition earlier and at lower disturbance amplification N factors. In fact, as shown in Chapter 5, exactly the opposite trends are observed. Therefore, it may be reasonably inferred that roughness is not an important factor in the measured transition locations discussed in Chapters 5, 6, and 7.

(a) $h_{\mathrm{res}} = 4.78$ MJ/kg, $P_{\mathrm{res}} = 22.2$ MPa (2649)

(b) $h_{\mathrm{res}} = 9.96$ MJ/kg, $P_{\mathrm{res}} = 54.3$ MPa (2645)

(c) $h_{\mathrm{res}} = 13.15$ MJ/kg, $P_{\mathrm{res}} = 54.7$ MPa (2788)
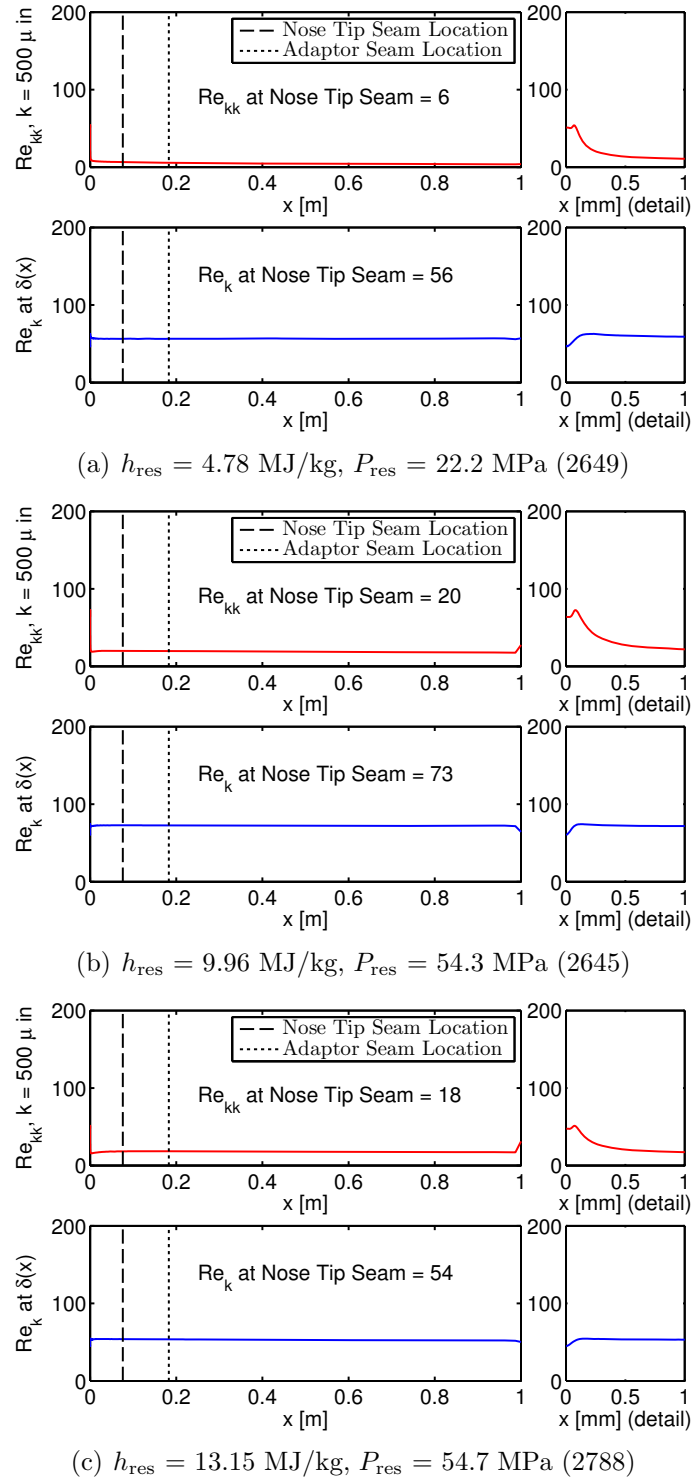
Figure 3.4: Re_{kk} distribution for three sample T5 experiments at low, mid-range, and high enthalpy conditions in air, with Re_k also included for reference to facilitate comparison to older data. The locations of the two seams, associated with the molybdenum tip and the plastic adapter section, are indicated on each plot. The region around the nose tip is detailed in the right subplots of each set.
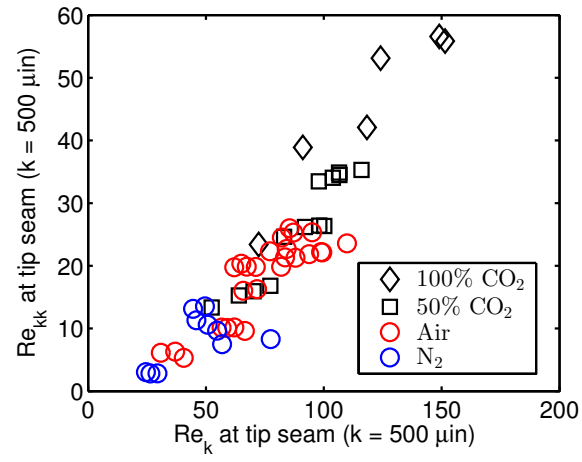
Figure 3.5: Re_{kk} vs. Re_k for all shots in the present data set.

3.1.1 Instrumentation

The main body of the cone is instrumented with a total of 80 flush-mounted thermocouples evenly spaced at 20 lengthwise locations, beginning at 221 mm along the surface from the tip of the cone, with each row located 38 mm in the lengthwise direction from the last (see Table 3.1 for details). These thermocouples, developed by Sanderson and Sturtevant (2002), have a response time on the order of a few microseconds (Marineau and Hornung, 2009) and have been successfully used for boundary layer transition determination in Adam and Hornung (1997) and Rasheed et al. (2002). The instrumentation layout by thermocouple number is presented graphically on a developed cone surface in Figure 3.6. Note that the offset axial spacing pattern of the thermocouples results in eight rays of 10 sensors each generated from the tip of the cone. This arrangement is useful for tracking the propagation of turbulent spots where they occur along one of the sensor rays, as described in Chapter 6.

TC	x mm	$\theta°$	TC	x mm	$\theta°$	TC	x mm	$\theta°$	TC	x mm	$\theta°$
1	220.9	0	2	220.9	180	3	220.9	90	4	220.9	270
5	258.8	45	6	258.8	225	7	258.8	135	8	258.8	315
9	296.8	0	10	296.8	180	11	296.8	90	12	296.8	270
13	334.7	45	14	334.7	225	15	334.7	135	16	334.7	315
17	372.7	0	18	372.7	180	19	372.7	90	20	372.7	270
21	410.6	45	22	410.6	225	23	410.6	135	24	410.6	315
25	448.6	0	26	448.6	180	27	448.6	90	28	448.6	270
29	486.5	45	30	486.5	225	31	486.5	135	32	486.5	315
33	524.5	0	34	524.5	180	35	524.5	90	36	524.5	270
37	562.5	45	38	562.5	225	39	562.5	135	40	562.5	315
41	600.4	0	42	600.4	180	43	600.4	90	44	600.4	270
45	638.4	45	46	638.4	225	47	638.4	135	48	638.4	315
49	676.3	0	50	676.3	180	51	676.3	90	52	676.3	270
53	714.3	45	54	714.3	225	55	714.3	135	56	714.3	315
57	752.2	0	58	752.2	180	59	752.2	90	60	752.2	270
61	790.2	45	62	790.2	225	63	790.2	135	64	790.2	315
65	828.1	0	66	828.1	180	67	828.1	90	68	828.1	270
69	866.1	45	70	866.1	225	71	866.1	135	72	866.1	315
73	904.0	0	74	904.0	180	75	904.0	90	76	904.0	270
77	942.0	45	78	942.0	225	79	942.0	135	80	942.0	315

Table 3.1: Thermocouple locations.
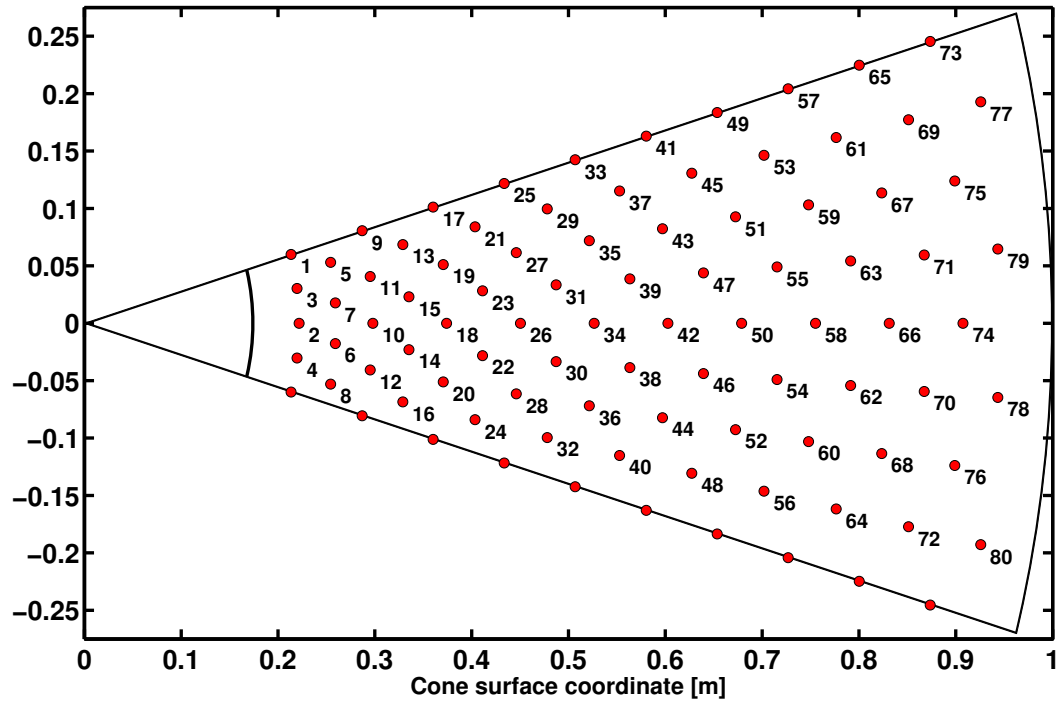
Figure 3.6: Instrumentation layout by thermocouple number. The lowest (unlabeled) ray on this diagram is the same set of thermocouples as the top ray. The cone is aligned in the test section such that the half containing odd-numbered thermocouples faces up.

3.1.2 Data Reduction

All thermocouple traces were sampled at 200 kHz. This is sufficient to capture the motion of turbulent spots, which propagate at speeds less than the boundary layer edge velocity. At a thermocouple streamwise distance of 38 mm and a nominal edge velocity of 4000 m/s, which is in the upper range for expected edge velocities in the present study, the relevant flowtime assuming that the propagation speed is 95% of the freestream velocity is 10 μs, which is equivalent to 100 kHz. However, the thermocouples have insufficient time response to detect the MHz-range instabilities that are the precursors to turbulent breakdown.

Similar thermocouples have a substantial history of use in T5. There are several methods for calculating heat flux from recorded thermocouple signals. The "direct" method of heat flux calculation, from Schulz and Jones (1973) integrates the temperature trace time rate of change directly with Equation (3.2), with the assumption that the test time is short compared to the characteristic heat transfer time, allowing the surface to be modeled as semi-infinite.

$$\dot{q}(t) \; = \; \sqrt{\frac{\rho c k}{\pi}} \int_0^t \frac{\mathrm{d}T(\tau)}{\mathrm{d}\tau} \frac{\mathrm{d}\tau}{\sqrt{t - \tau}} \tag{3.2}$$

As Schulz and Jones (1973) note, this form uses the differential of the surface temperature, a noisy measurement, which will tend to make the calculation difficult. Germain (1993) and Adam (1997) used the so-called "indirect" method to calculate the heat flux by first obtaining the fluence or integrated heat flux time history from Equation (3.3), which is obtained by integrating Equation (3.2) by parts, and can be discretized in finite difference form as Equation (3.4) and then differentiated to find heat flux in Equation (3.5).

$$Q(t) \; = \; \sqrt{\frac{\rho c k}{\pi}} \int_0^t \frac{T(\tau)}{\sqrt{t - \tau}} \, \mathrm{d}\tau \tag{3.3}$$

$$Q(t_n) \;=\; \sqrt{\frac{\rho c k}{\pi}} \sum_{i=1}^{n} \frac{T(t_i) \;-\; T(t_{i-1})}{\sqrt{t_n - t_i} \;+\; \sqrt{t_n - t_{i-1}}} \,(t_n - t_{n-1}) \qquad (3.4)$$

$$\dot{q}(t_n) \;=\; \frac{\mathrm{d}Q(t_n)}{\mathrm{d}t} \;=\; \frac{1}{40(t_n - t_{n-1})}(-2Q_{n-8} - Q_{n-4} + Q_{n+4} + 2Q_{n+8}) \qquad (3.5)$$

This approach avoids differentiation of the temperature data, and therefore the associated noise.

In the present work, following the analysis of Sanderson (1995), Davis (1999), and Rasheed (2001), a spectral deconvolution method, which makes use of fast Fourier transforms, is used to compute heat flux. This method allows for finer control over the signal smoothing and noise filtering than is permitted by the "indirect" method outlined above. This advantage is particularly important for attempting to resolve time-dependent phenomena, including individual turbulent spots. The convolution integral for the temperature change with time, which defines the transient solution of the system, is:

$$\Delta T(y,t) = \int_0^t g(y, t - \tau)\dot{q}(\tau)\mathrm{d}\tau$$

The unit impulse response function, for $t > 0$, is:

$$g(y,t) = \sqrt{\frac{\alpha}{\pi k^2 t}} \exp\left(\frac{-y^2}{4\alpha t}\right)$$

Fast Fourier transform techniques described in Rasheed (2001) are used to compute $\dot{q}(t)$, with the following more accurate values for thermal diffusivity α, thermal conductivity k, and junction depth y, for chromel and constantan, informed by the work of Marineau and Hornung (2009): $\alpha = 5.47 \times 10^{-6}$ m^2/s, $k = 20.55$ W/m°C, and $y = 5.0 \times 10^{-6}$ m. The maximum heat flux values measured in the present study, for turbulent flows at high enthalpy, were around 5 MW/m^2. For comparison, this is roughly ten times the peak heat flux experienced by the Space Shuttle during re-entry

(Alber, 2012).

The heat-flux data were nondimensionalized by Stanton number, which is (*e.g.*, in Anderson (2007)) defined as:

$$\text{St} = \frac{\dot{q}(x)}{\rho_e U_e (h_{aw} - h_w)} \tag{3.6}$$

The quantities in the denominator are computed as follows. The enthalpies[3] are calculated using MATLAB Cantera routines for the reservoir, edge, and wall conditions, and by expressing the adiabatic wall enthalpy as:

$$h_{aw} = h_e + r(h_{res} - h_e) \tag{3.7}$$

where r is the recovery factor, and neglecting any rise in wall temperature due to the extremely short test time, a simplified form for the Stanton number is obtained.

$$\text{St} = \frac{\dot{q}(x)}{\rho_e U_e [h_{res} - \frac{1}{2} U_e^2 (1 - r)]} \tag{3.8}$$

Equation (3.7) is also the basis for calculating the adiabatic wall temperature. This is done by iteratively solving Equation (3.7) with Cantera for the computed h_{res} and h_e with the known pressure and guessed values of T_{aw}. It is also necessary to know the species composition of the gas. Two assumptions for the gas composition are relatively straightforward to make and result in different values for T_{aw}. If the temperature is assumed to be sufficiently high, then the reactions will take place quickly enough that the gas will be in equilibrium. If the temperature is relatively low, the gas composition is frozen and will not change significantly from the boundary layer edge to the wall. Figure 3.7 presents the dependence of the two values for T_{aw}

[3]The standard enthalpy of formation for both N_2 and O_2 is zero at 298 K, while the standard enthalpy of formation of CO_2 is -393.5 kJ/mol. For consistency, all CO_2 results in this thesis are expressed taking the enthalpy at 298 K as zero, as has been done for past CO_2 work in T5 (*e.g.*, Adam (1997)).

on each other for the present test series. The frozen and equilibrium T_{aw} bracket the true value, which may be obtained by running a more sophisticated boundary layer solver, such as STABL-DPLR, with adiabatic wall assumptions.
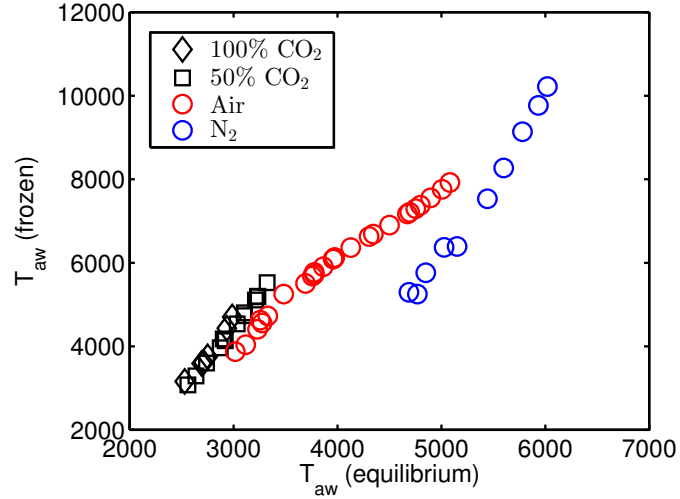
Figure 3.7: Adiabatic wall temperatures calculated with Cantera for frozen and equilibrium gas composition assumptions.

The Prandtl number (Pr) depends on changing gas composition with pressure and temperature and is evaluated using Eucken's approximation, Equation (3.9), as found in Thompson (1972), evaluated using γ at the boundary layer edge. The Prandtl numbers for each experiment in the present transition study are presented in Figure 3.8.

$$\mathrm{Pr} = \frac{4\gamma}{9\gamma - 5} \tag{3.9}$$

For laminar flows, $r_{\mathrm{lam}} = \sqrt{\mathrm{Pr}}$ and for turbulent flows $r_{\mathrm{turb}} \approx \sqrt[3]{\mathrm{Pr}}$ (Anderson, 1990). Equation (3.8) with r_{lam} is used to calculate the Stanton number for the heat transfer data points on each St-Re plot (*e.g.*, Figure 3.9), as well as the laminar correlation described in Section 3.1.2.1, while r_{turb} is used to calculate the turbulent correlation described in Section 3.1.2.2.

Displacement along the cone's surface is nondimensionalized by Reynolds num-
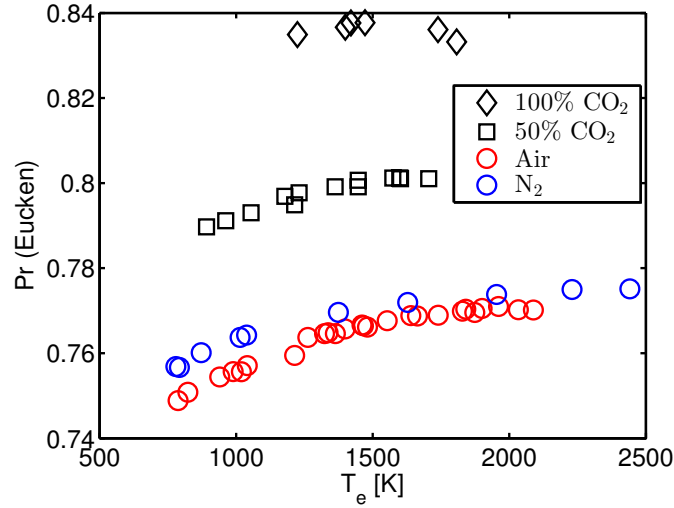
Figure 3.8: Prandtl number *vs.* edge temperature for the conditions in the present transition study. Prandtl number is calculated using Eucken's approximation, Equation (3.9), with γ at the boundary layer edge conditions.

ber. The Reynolds number evaluated at boundary layer edge conditions is defined in Equation (3.10), with Wilke's method used to calculate the dynamic viscosity, μ, of the gas. For consistency, the St-*vs.*-Re plots used to determine transition location (*e.g.*, Figure 3.9) all use Re_x evaluated at the boundary layer edge.

$$Re_x = \frac{\rho_e u_e x}{\mu_e} \tag{3.10}$$

It is possible to correlate Stanton number with Reynolds number for both laminar and turbulent flow conditions. The edge Reynolds number is a standard boundary layer parameter, and the laminar and turbulent heat flux correlations described in Sections 3.1.2.1 and 3.1.2.2 all use Equation (3.10). This is not, however, the only or necessarily the best Reynolds number for transition *location* correlations in high-enthalpy cold-wall flows, which is explored further in Chapter 5.

3.1.2.1 Laminar Heat Flux Correlation

Following the analysis in Adam (1997) and Rasheed (2001) we begin from the standard Blasius solution for the boundary layer on an incompressible flat plate, as taken from White (1991), and modify it for the case of compressible, chemically frozen, conical flow. Assuming self-similarity and a high-speed boundary layer, the Reynolds analogy relates the Stanton number St to the skin friction coefficient C_f as:

$$\text{St} \approx \frac{1}{2}C_f\text{Pr}^{-2/3} \tag{3.11}$$

The skin friction coefficient is the normalized wall shear stress:

$$C_f(x) = \frac{\tau_{\text{w}}(x)}{\frac{1}{2}\rho_{\text{e}}U_{\text{e}}^2} \tag{3.12}$$

For a two-dimensional incompressible boundary layer with no pressure gradient, the numerical solution is the classic flat plate Blasius solution, from which may be obtained the incompressible C_f:

$$C_{f_{\text{inc}}}(x) \approx \frac{0.664}{\sqrt{\text{Re}_x}} \tag{3.13}$$

where Re_x is the Reynolds number based on the surface distance x. This may be adapted approximately to include compressibility effects by introducing a correction factor $\sqrt{C_{\text{w}}}$, where $C_{\text{w}} = \rho_{\text{w}}\mu_{\text{w}}/\rho_{\text{e}}\mu_{\text{e}}$ is the Chapman-Rubesin parameter at wall conditions:

$$C_{f_{\text{comp}}}(x) \approx \frac{0.664}{\sqrt{\text{Re}_x}}\sqrt{C_{\text{w}}} \tag{3.14}$$

Within a hypervelocity boundary layer, strong temperature gradients between the wall and the freestream result in strong gradients in fluid properties. To define a single representative Reynolds number, it is convenient to choose a single so-called reference

temperature at which to evaluate density and viscosity. In transition work, this is often the Reynolds number at the transition onset location, evaluated at boundary layer edge conditions. This Reynolds number is defined in Equation (3.15).

$$\mathrm{Re}_{\mathrm{Tr}} = \frac{\rho_{\mathrm{e}} u_{\mathrm{e}} x_{\mathrm{Tr}}}{\mu_{\mathrm{e}}} \tag{3.15}$$

However, experiments by Adam and Hornung (1997) showed that computing the Reynolds number at reference conditions as in Equation (3.17), rather than boundary layer edge conditions as in Equation (3.15), more clearly separated transition results from CO_2 experiments from pure air and N_2 data. The Dorrance (1962) reference temperature, defined in Equation (3.16) has the same form as the Eckert reference temperature but may be used for other gases as well as air.

$$\frac{T^*}{T_{\mathrm{e}}} = \frac{1}{2} + \frac{\gamma - 1}{2} \frac{\sqrt{\mathrm{Pr}}}{6} \mathrm{M}_{\mathrm{e}}^2 + \frac{1}{2} \frac{T_{\mathrm{w}}}{T_{\mathrm{e}}} \tag{3.16}$$

The Dorrance temperature is used to calculate the quantities in Equation (3.17), the Reynolds number with density and viscosity, from Wilke's method, evaluated at reference conditions.

$$\mathrm{Re}_{\mathrm{Tr}}^* = \frac{\rho^* u_{\mathrm{e}} x_{\mathrm{Tr}}}{\mu^*} \tag{3.17}$$

This expression may be used for any gas. Evaluating the Chapman-Rubesin parameter at the Dorrance reference temperature T^*, we use $C^* = \rho^* \mu^* / \rho_{\mathrm{e}} \mu_{\mathrm{e}}$, to write:

$$C_{f_{\mathrm{comp}}}(x) \approx \frac{0.664}{\sqrt{\mathrm{Re}_x}} \sqrt{C^*} \tag{3.18}$$

For axisymmetric conical geometry, the Lees-Illingworth transformation (Lees, 1956) is applied to the flat-plate solution, as described in White (1991):

$$C_{f,\mathrm{cone}} = \sqrt{3} \, C_{f,\mathrm{plate}} \tag{3.19}$$

which yields an approximate relationship between St and Re:

$$\text{St} \;\approx\; \frac{\sqrt{3}}{2}C_f\text{Pr}^{-2/3} \;\approx\; \frac{0.664\sqrt{3}}{2}\frac{\sqrt{C^*}}{\text{Pr}^{2/3}\sqrt{\text{Re}}} \tag{3.20}$$

3.1.2.2   Turbulent Heat Flux Correlation

A similar approach is used to find an approximate relationship between St and Re for the turbulent case. Beginning again from the Reynolds analogy in Equation (3.11), the following approximate expression for the incompressible turbulent skin friction on a flat plate may be used (White, 1991):

$$C_{f_{\text{inc}}} \;\approx\; \frac{0.455}{\ln^2(0.06\,\text{Re}_x)} \tag{3.21}$$

Morkovin (1962) hypothesized that if the density fluctuations within the compressible turbulent boundary layer are small, its structure does not differ qualitatively from the incompressible case. The Mach number fluctuations M′ must therefore remain small, which Morkovin predicted should hold for Mach numbers up to about 5. It is important to note both that many of the present edge Mach numbers exceed this criterion by up to about 10%, and also that many of the experimental validations of the Morkovin hypothesis have been made in low enthalpy, adiabatic wall conditions, neither of which prevail in T5. However, recent DNS studies (Martin, 2007) have shown agreement (within 10%, and in most cases much better) with skin friction predictions made using the Morkovin hypothesis for lower wall temperatures (Duan et al., 2010), higher Mach numbers (Duan et al., 2011), and higher enthalpies (Duan and Martin, 2011) which better encompass the T5 operating envelope. Assuming, therefore, that the hypothesis holds, the equation for skin friction may be written as:

$$C_{f_{\text{comp}}} \;=\; \frac{1}{F_c}C_{f_{\text{inc}}}(\text{Re}_x\,F_{\text{Re}}) \;\approx\; \frac{1}{F_c}\frac{0.455}{\ln^2(0.06\,\text{Re}_x\,F_{\text{Re}})} \tag{3.22}$$

Here F_{Re} is a "stretching" factor and F_{c} is a skin friction correction factor. Two formulations for F_{Re} and F_{c} are presented, the first from van Driest (1952) (commonly known as "van Driest II") and the second from White and Christoph (1972). The former is more widely used, but the latter provides results that correlate better with experimental results for cold wall hypersonic flow. For relevant conditions, the results of each theory are similar, and both turbulent correlations are provided for comparison with experimental results in this work (*e.g.*, in Figure 3.9). The development of these theories is treated in White (1991). For both models, F_{c} is given as:

$$F_{\mathrm{c}} \;=\; \frac{T_{\mathrm{aw}}/T_{\mathrm{e}} \;-\; 1}{(\sin^{-1} A \;+\; \sin^{-1} B)^2} \tag{3.23}$$

Here T_{e} is the temperature at the boundary layer edge and T_{aw} is the temperature for an adiabatic wall, defined here[4] as:

$$\frac{T_{\mathrm{aw}}}{T_{\mathrm{e}}} \;=\; 1 \;+\; r_{\mathrm{turb}}\frac{\gamma\;-\;1}{2}\mathrm{M}_{\mathrm{e}}^2 \tag{3.24}$$

In these equations the parameters A and B are given by:

$$\begin{aligned}
A &\;=\; \frac{2a^2 \;-\; b}{\sqrt{b^2 \;+\; 4a^2}} \\
B &\;=\; \frac{b}{\sqrt{b^2 \;+\; 4a^2}}
\end{aligned} \tag{3.25}$$

and a and b are defined as:

$$\begin{aligned}
a &\;=\; \sqrt{\frac{\gamma\;-\;1}{2}\mathrm{M}_{\mathrm{e}}^2\frac{T_{\mathrm{e}}}{T_{\mathrm{w}}}} \\
b &\;=\; \frac{T_{\mathrm{aw}}}{T_{\mathrm{w}}} \;-\; 1
\end{aligned} \tag{3.26}$$

---

[4]Section 3.1.2 presents a more sophisticated approach for calculating T_{aw}, but the standard constant γ expression is used here so that the correlation remains consistent with past results.

The Reynolds number stretching factor F_{Re} is defined differently in each theory. For van Driest II:

$$F_{\mathrm{Re}} = \frac{1}{F_c}\frac{\mu_{\mathrm{e}}}{\mu_{\mathrm{w}}}$$
(3.27)

and for White and Christoph:

$$F_{\mathrm{Re}} = \frac{1}{\sqrt{F_{\mathrm{c}}}}\frac{\mu_{\mathrm{e}}}{\mu_{\mathrm{w}}}\sqrt{\frac{T_{\mathrm{e}}}{T_{\mathrm{w}}}}$$
(3.28)

Finally, to complete the analysis, a correction for axisymmetric conical flow must be applied to the heat transfer, similar to that in Equation (3.19) for the laminar case. For the laminar case this correction is exactly $\sqrt{3}$. The corresponding transformations for turbulent conical flow, which apply to both correlations and are due to van Driest (1952), yield an equivalent correction factor of about 1.10:

$$C_{f,\mathrm{cone}} \approx 1.10\, C_{f,\mathrm{plate}}$$
(3.29)

3.1.2.3   Transition Onset Location

One example of results from the present tests, shot 2744 in air, is shown in Figure 3.9. Normalized heat-transfer results at 7.68 MJ/kg and 60.7 MPa are presented. In this figure, the laminar similarity correlation and STABL/DPLR laminar heat transfer results for this case are blue and the turbulent correlations are green. The laminar heat transfer data are slightly offset from the laminar correlation, an effect that has been observed in past T5 transition studies. Adam (1997) speculated that this effect might be due to nonequilibrium processes in the boundary layer. However, the nonequilibrium DPLR[5] laminar heat transfer result closely follows the laminar

---

[5]See Section 4.1.2 for a discussion of STABL/DPLR.
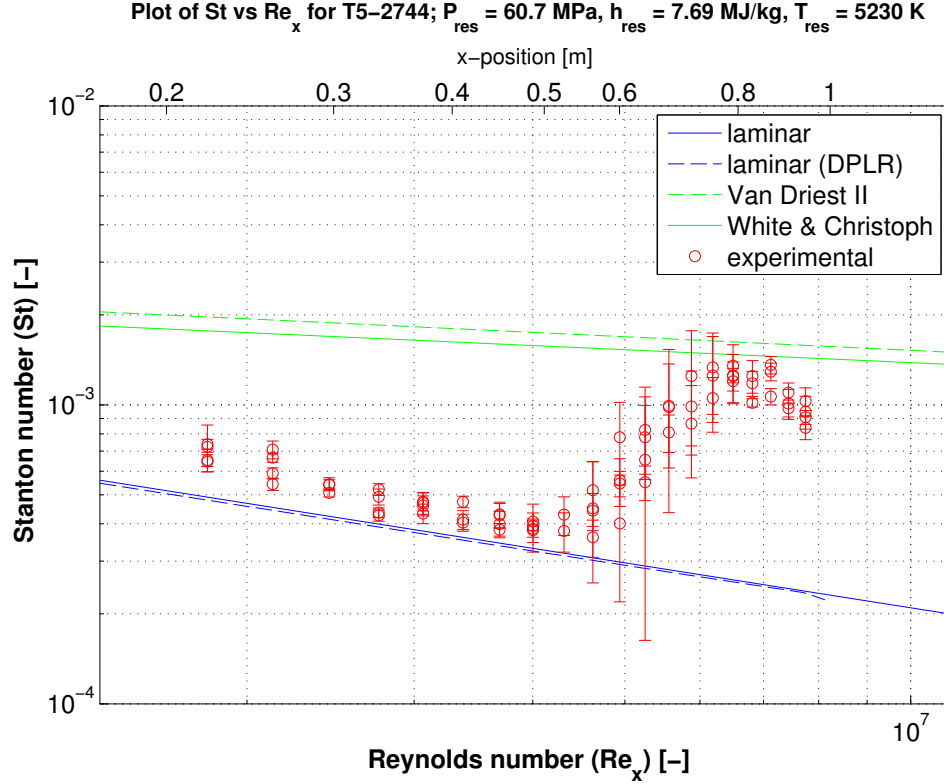
Figure 3.9: Time-averaged nondimensional plot of heat transfer results in terms of Stanton number *vs.* Reynolds number for T5 shot 2744 in 100% air, with the laminar similarity correlation and STABL/DPLR laminar heat transfer results for this case indicated in blue, and two common turbulent correlations in green. The bars on each point represent the RMS values of each thermocouple's signal, and transition onset occurs at 0.51 m from the tip of the cone.

correlation. Due to the distribution of the sensors around the circumference of the cone, in this representation of the data there are four results at each of 20 x-locations. The circles represent the time-averaged heat transfer results over the ~1 ms steady flow time, and the bars represent the root-mean-squared (RMS) values from each sensor over the steady flow time. The RMS values are initially small in the laminar zone as the heat transfer levels are consistently near the laminar correlation value, increase in size in the transitional zone as the flow becomes intermittent, and may then decrease in size again as the flow approaches the fully turbulent zone and heat transfer levels are consistently near the turbulent correlation value. A slight drop-off from the

fully turbulent value is observed in the last two rows of thermocouples, as they are positioned near the maximum extent of the T5 test rhombus and may intersect with the expansion fan emanating from the lip of the nozzle. For this experiment, transition onset is observed at 0.51 m from the tip of the cone, and transition completion, when the turbulent heat transfer value is achieved, is observed at 0.78 m from the tip of the cone. Transition onset and completion results are discussed further in Chapter 5.

An alternate transition detection algorithm is developed by analyzing the intermittency of the heat flux signals, as described in Clark et al. (1994) and implemented for similar conditions in Mee and Goyne (1996). Intermittency, γ, represents the fraction of the run time during which flow over each gauge is turbulent. Gauge signals are considered turbulent when the signal is elevated above the predicted laminar value by more than 40% of the difference between the predicted laminar and turbulent values. Gauge signals are considered laminar when the signal is elevated above the predicted laminar value by less than 20% of the difference between the predicted laminar and turbulent values. For values between 20% and 40% above the laminar correlation, the numerical intermittency meter of Mee and Goyne (1996) is employed. With this method, which applies the universal intermittency curve of Narasimha (1985), the authors suggest that data sets at sufficiently similar conditions may be combined for better intermittency determination. Sample intermittency plots for two different (individual) shots are presented in Figure 3.10. Transition location is determined from these plots by noting where the intermittency trend departs from zero.
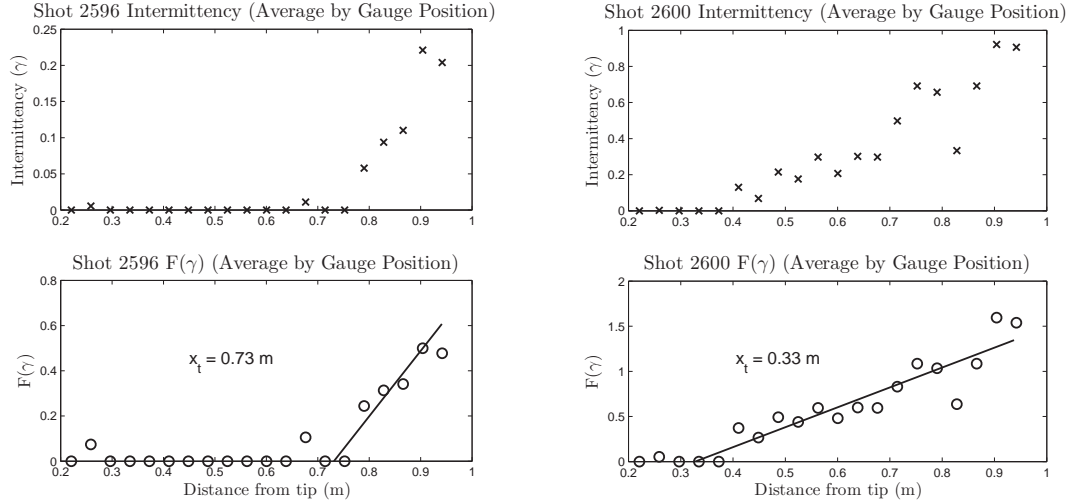
Figure 3.10: Top: Combined intermittency by gauge location. Bottom: Using the universal intermittency of Narasimha (1985) as applied in Mee and Goyne (1996), the curve is linearized with $F(\gamma)$ and then used to find transition location via the x-intercept.

3.2 Test Series

The analysis in Chapter 5 draws conclusions only from shots performed after the more intensive cleaning procedure described in Section 2.1.3 was initiated. These experiments included air (Section 3.2.2), nitrogen (Section 3.2.3), carbon dioxide (Section 3.2.4), and air-carbon dioxide mixture (Section 3.2.5) shock tube fill conditions. The injection experiments presented in Chapter 7 took place before the more intensive cleaning procedure began, and are therefore not directly comparable with results from the tests below. While a total of 129 experiments took place after the new cleaning procedure was initiated, many of these were not necessarily intended to transition as the conditions were selected to support the instability work described in Parziale (2013), which was performed in parallel to the present study, and others exhibited some transient transition features but no obvious transition onset. In all, transition sufficiently clear to establish an onset location as described in Section 3.1.2.3 was observed in 55 cases. The parameters for these tests are described below. Of these

55 cases, transition completion as described in Section 3.1.2.3 was observed in 17. A complete record of the measured tunnel parameters and calculated flow conditions for every experiment performed for this thesis is presented in Appendix A.

A supplemental report with detailed results for each experiment referenced in Appendix A is available as Jewell and Shepherd (2014).

3.2.1 Tunnel Operation

"Tailored interface" operation[6] of the shock tunnel was proposed by Wittliff et al. (1959). Tailored operation of a shock tube means selecting operating conditions so that the gas properties on each side of the contact surface, the interface between driven and driver gas that is immediately behind the shock wave, such that the interaction between the interface and the reflected primary shock wave does not generate a reflected wave. "Undertailoring" refers to conditions where the reflected wave is an expansion, while "overtailoring" refers to conditions where the reflected wave is a shock. Reddy (1971) derives an analytical expression for the tailored (denoted by subscript T) shock Mach number at this condition, which assumes perfect driver gas but real driven gas in the shock tube:

$$\mathrm{M_{sT}} = \frac{a_4}{a_1} \frac{2}{(\gamma_4 - 1)(1 - \varepsilon)} \left[\frac{\beta_4^{1/2}}{\beta_4^{1/2} + (\alpha_4 \varepsilon)^{1/2}} \right] \qquad (3.30)$$

In this equation, $\alpha \equiv (\gamma + 1)/(\gamma - 1)$, $\beta \equiv (\gamma - 1)/2\gamma$, and $\varepsilon = \rho_1/\rho_2$, where state 4 is the driver gas, state 1 is the driven gas, and state 2 is the post-shock state. ε may be determined with a real gas solution for a given $\mathrm{M_s}$ and P_1, such as that provided by the `PostShock_eq` routine from the Cantera (Goodwin, 2003; Goodwin, 2009) Shock and Detonation Toolbox (Browne et al., 2008). For each shock tube composition and fill pressure P_1, Equation (3.30) may then be tabulated to find

---

[6]In practice, the conditions selected in the present study are actually slightly undertailored; see Section 2.3.

a_4/a_1, as presented in Figure 3.11 for the four gas mixtures used in the present study, calculated for $P_1 = 100$ kPa. P_4/P_1 is measured and T_4/T_1 is computed based on adiabatic compression of the driver gas. When the driver gas composition is specified[7] the sound speed in the driver gas, a_4, may also be calculated. The sound speed in the driven gas, a_1, is calculated from the known initial fill conditions of the shock tube.

Figure 3.12 presents the pressure ratio P_4/P_1 necessary to produce a given reservoir enthalpy for three values of P_1 for each of the four shock tube gas mixtures. Figure 3.12(a) is calculated for a 100% He driver, used in high-enthalpy cases, and Figure 3.12(b) is calculated for an 84% He, 16% Ar (by mass) driver, commonly used for midrange enthalpy cases, including many in the present study. For each P_4/P_1, there is one value of a_4/a_1 which results in tailored operation. While it is often inconvenient to adjust the compression ratio to change P_4/P_1, tailored operation may be achieved over a range of reservoir enthalpies by adjusting the ratio of Ar to He in the driver gas.
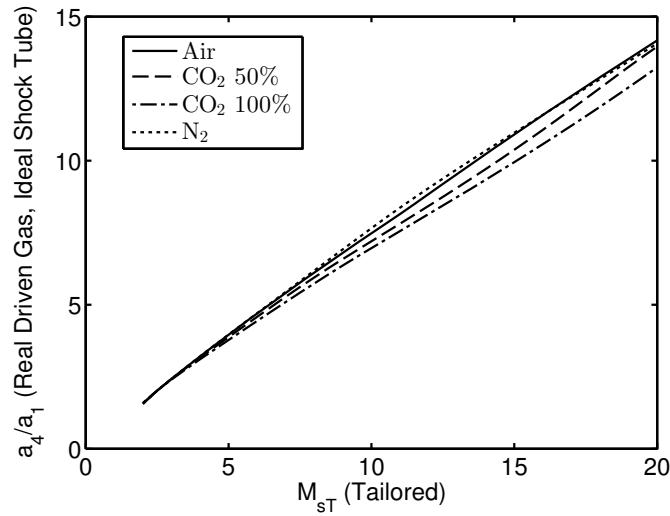
Figure 3.11: a_4/a_1 *vs.* M_s for ideal tailored operation of a reflected shock tunnel

In practice the shock speed is observed to decrease with increasing distance from

---

[7]We have thus far assumed only $\gamma = 5/3$ for the driver, true for both He and Ar, but to calculate the speed of sound the molecular weights are necessary.

(a) 100% He driver (b) 84% He, 16% Ar driver
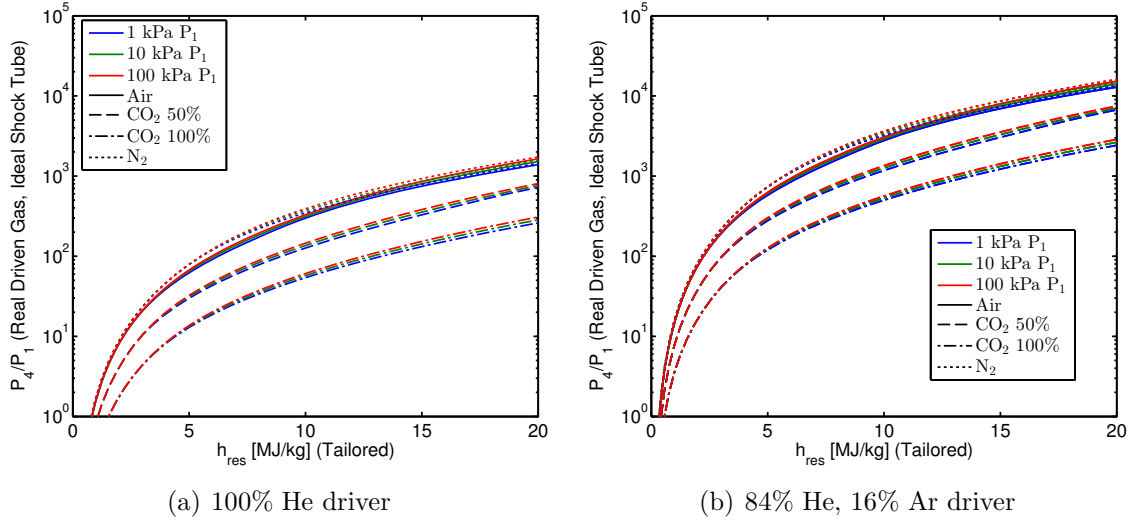
Figure 3.12: (a) P_4/P_1 vs. h_{res} for ideal tailored operation, 100% He driver; (b) P_4/P_1 vs. h_{res} for ideal tailored operation, 84% He, 16% Ar driver. All cases are calculated for four driver gas mixtures at shock tube fill pressure values P_1 of 1, 10, and 100 kPa.

the primary diaphragm due to the interaction between the boundary layer wave and the mean flow behind the shock (Hornung and Belanger, 1990). This is not accounted for by the idealized shock tube model used by Reddy (1971) in deriving Equation (3.30). For the T5 shock tube, $L/d = 130$, which makes these nonideal effects more important in T5 than in shorter reflected shock tunnels and further reduces the velocity of the incident shock as compared to the ideal value, which results in a reduction of the reservoir enthalpy (Belanger and Hornung, 1994). Figure 3.13 documents the measured shock speed decrement in air for a set of experiments from the present study, all with 84% He, 16% Ar driver and burst pressure $P_4 \approx 100$ MPa. The results are approximate due to the small number of pressure transducers available for determining arrival time and inferring shock speed. The shock speed measured between the last two transducers in the shock tube is about 92.5% the shock speed calculated from `PostShock_eq` in the Cantera Shock and Detonation Toolbox. Previous results in T5 (Belanger and Hornung, 1994) indicate that the shock wave is continuously decelerating as it travels through the tube. In the present study, this effect is neglected and shock speeds based on shock arrival times at the last two sta-

tions at 4.8 and 2.4 m from the end wall are used to calculate all reflected shock and reservoir conditions.
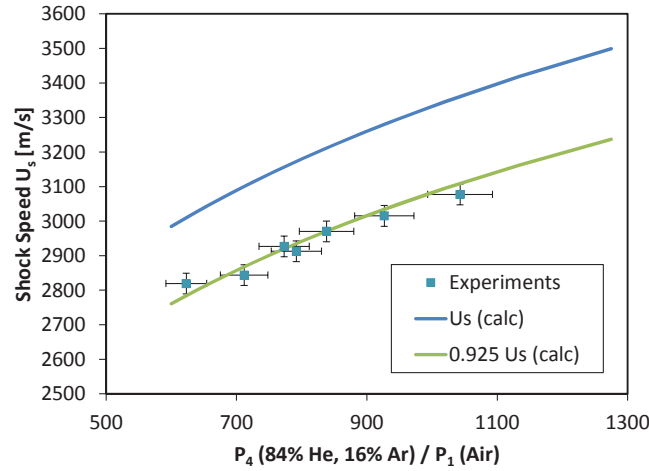
Figure 3.13: Shock speed decay in air for a set of experiments all with 84% He, 16% Ar driver and burst pressure $P_4 \approx 100$ MPa. The shock speed measured between the last two transducers in the shock tube is about 92.5% the shock speed calculated from PostShock_eq in the Cantera Shock and Detonation Toolbox.

Page and Stalker (1983) considered the effects of tunnel geometry and compression ratio (the ratio of initial to final volumes of the driver gas) on the P_{res}/P_4 ratio, finding that measured compression ratios for a given P_4 were as much as two to three times higher than calculations based upon isentropic processes in the compression tube, and that losses for "plateau pressure" (P_{res}) correlated with increasing L/d of the shock tube across different facilities[8]. Page and Stalker (1983) did not consider the effect of tailored tunnel operation.

For the present set of slightly undertailored experiments, a correlation between P_{res} and P_5 is observed, where P_5 is calculated from the measured, not theoretical, shock speed U_{s}. As Morgan (2001) observes, "In practice, free-piston shock tunnels have been found to deliver less reflected shock pressure than the theoretical values". This is illustrated in Figure 3.14. The average P_{res}/P_5 ratio for the air tests is 0.63,

---

[8]Belanger and Hornung (1994) observed a similar effect in T5, with P_{res}/P_4 averaging about 0.7 for conditions with $h_{\text{res}} < 12.5$ MJ/kg, but it is unclear if the empirical correlation provided in Page and Stalker (1983) holds for all cases.

0.62 for N_2, 0.41 for 50% CO_2, and 0.34 for 100% CO_2.
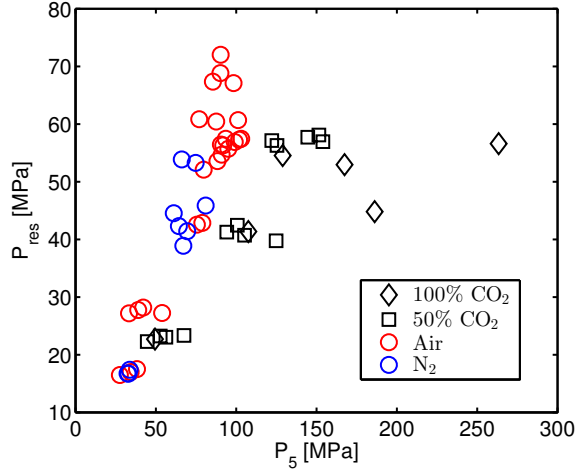
Figure 3.14: P_{res} *vs.* P_5 for the present set of transition experiments.

Using the empirical Belanger and Hornung (1994) average value of 0.7 for P_{res}/P_4 for T5 conditions with $h_{\text{res}} < 12.5$ MJ/kg, and assuming a typical T5 driver of 84% He, 16% Ar, the relationships presented in Figure 3.12(b) for tailored P_4/P_1 can be used to find the dependence of P_{res} on h_{res} and fill pressure P_1 for a given shock tube gas mixture:

$$P_{\text{res}} = \frac{P_{\text{res}}}{P_4} P_1 \frac{P_4}{P_1} \approx 0.7 P_1 \frac{P_4}{P_1} \tag{3.31}$$

While this relationship should correctly portray the general trend of reservoir pressure and enthalpy increasing together under tailored conditions when initial fill pressure and composition are held constant, it is not a reliable quantitative prediction for the relationship, which is highly empirical. In particular, the modeled P_{res}-h_{res} curves calculated for several values of P_1 in Sections 3.2.2–3.2.4 below would in practice require different and facility-dependent values for P_1 to produce the equivalent conditions. This is discussed in Hornung and Belanger (1990); Morgan (2001) summarizes the situation as follows: "Real gas effects in the test gas do not change the performance insofar as the post-shock pressure is concerned. However, they seriously alter the filling pressure (P_1) required to achieve the required flow speed." The con-

sequences for T5 are shown by comparing the modeled and experimental P_{res}-h_{res} results in Sections 3.2.2–3.2.4.

3.2.2 Air

Transition onset was observed for a total of 26 experiments in air, which had reservoir enthalpies between 5.3 MJ/kg and 11.9 MJ/kg and reservoir pressures between 16.5 MPa and 72.0 MPa. Equation (3.31) is used with the air values for P_4/P_1 from Figure 3.12(b) to plot an empirical relationship for P_{res} *vs.* h_{res} for four shock tube fill pressures (25, 50, 100, and 200 kPa). This is presented in Figure 3.15(a), next to the tunnel parameters for each air experiment presented in Figure 3.15(b). These tunnel conditions resulted in boundary layer edge pressures between 9.1 kPa and 59.6 kPa and Dorrance reference temperatures between 1120 K and 2180 K.

(a) 84% He, 16% Ar driver, P_1 air   (b) Experimental air conditions
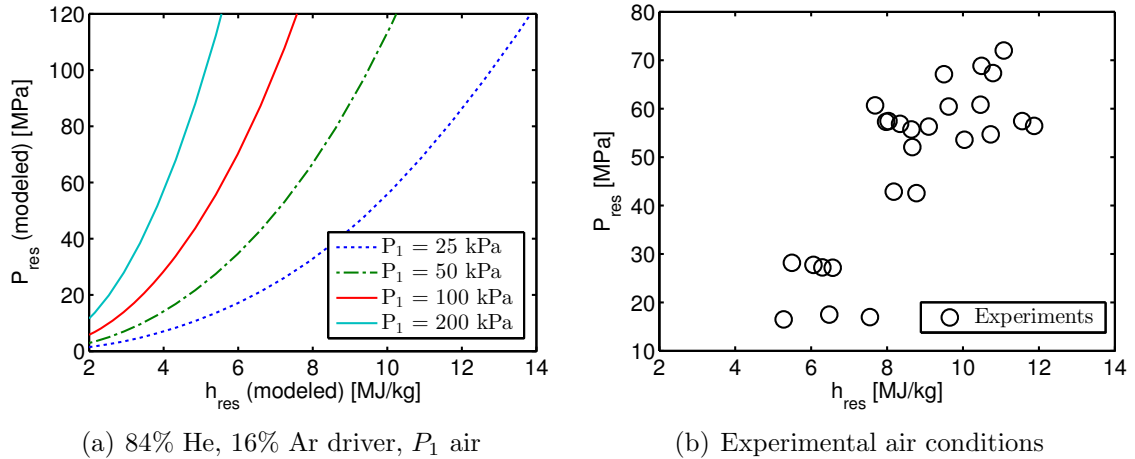
Figure 3.15: Tunnel parameters for air (a) modeled for several shock tube fill pressures P_1, all with a 84% He, 16% Ar driver; and (b) as calculated for the present air experiments.

3.2.3 Nitrogen

Transition onset was observed for a total of 10 experiments in N_2, which had reservoir enthalpies between 7.2 MJ/kg and 15.9 MJ/kg and reservoir pressures between

16.7 MPa and 53.9 MPa. Equation (3.31) is used with the N_2 values for P_4/P_1 from Figure 3.12(b) to plot an empirical relationship for P_{res} *vs.* h_{res} for four shock tube fill pressures (25, 50, 100, and 200 kPa). This is presented in Figure 3.16(a), next to the tunnel parameters for each N_2 experiment presented in Figure 3.16(b). These tunnel conditions resulted in boundary layer edge pressures between 5.2 kPa and 38.0 kPa and Dorrance reference temperatures between 1280 K and 2640 K.

(a) 84% He, 16% Ar driver, P_1 N_2 (b) Experimental N_2 conditions
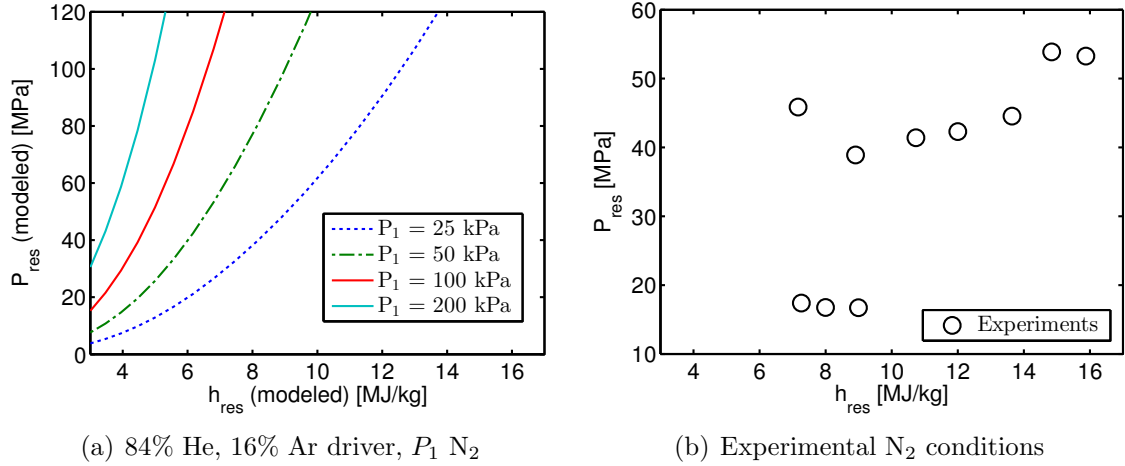
Figure 3.16: Tunnel parameters for N_2 (a) modeled for several shock tube fill pressures P_1, all with a 84% He, 16% Ar driver; and (b) as calculated for the present N_2 experiments.

3.2.4 Carbon Dioxide

Transition onset was observed for a total of 6 experiments in CO_2, which had reservoir enthalpies between 4.6 MJ/kg and 7.7 MJ/kg and reservoir pressures between 22.7 MPa and 56.6 MPa. Equation (3.31) is used with the CO_2 values for P_4/P_1 from Figure 3.12(b) to plot an empirical relationship for P_{res} *vs.* h_{res} for four shock tube fill pressures (25, 50, 100, and 200 kPa). This is presented in Figure 3.17(a), next to the tunnel parameters for each CO_2 experiment presented in Figure 3.17(b). These tunnel conditions resulted in boundary layer edge pressures between 23.6 kPa and 63.4 kPa and Dorrance reference temperatures between 1060 K and 1480 K.

(a) 84% He, 16% Ar driver, P_1 CO_2 (b) Experimental CO_2 conditions
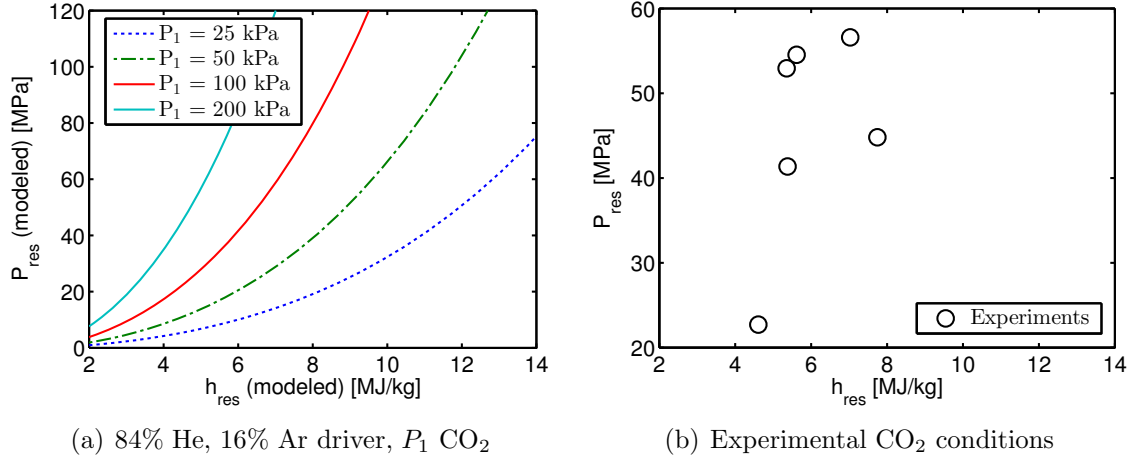
Figure 3.17: Tunnel parameters for CO_2 (a) modeled for several shock tube fill pressures P_1, all with a 84% He, 16% Ar driver; and (b) as calculated for the present CO_2 experiments.

3.2.5 Air-Carbon Dioxide Mixtures

Transition onset was observed for a total of 13 experiments in 50% air, 50% CO_2 mixtures by mass, which had reservoir enthalpies between 4.1 MJ/kg and 8.5 MJ/kg and reservoir pressures between 22.3 MPa and 58.1 MPa. Equation (3.31) is used with the 50% air, 50% CO_2 values for P_4/P_1 from Figure 3.12(b) to plot an empirical relationship for P_{res} vs. h_{res} for four shock tube fill pressures (25, 50, 100, and 200 kPa). This is presented in Figure 3.18(a), next to the tunnel parameters for each 50% air, 50% CO_2 experiment presented in Figure 3.18(b). These tunnel conditions resulted in boundary layer edge pressures between 18.7 kPa and 53.8 kPa and Dorrance reference temperatures between 970 K and 1600 K.
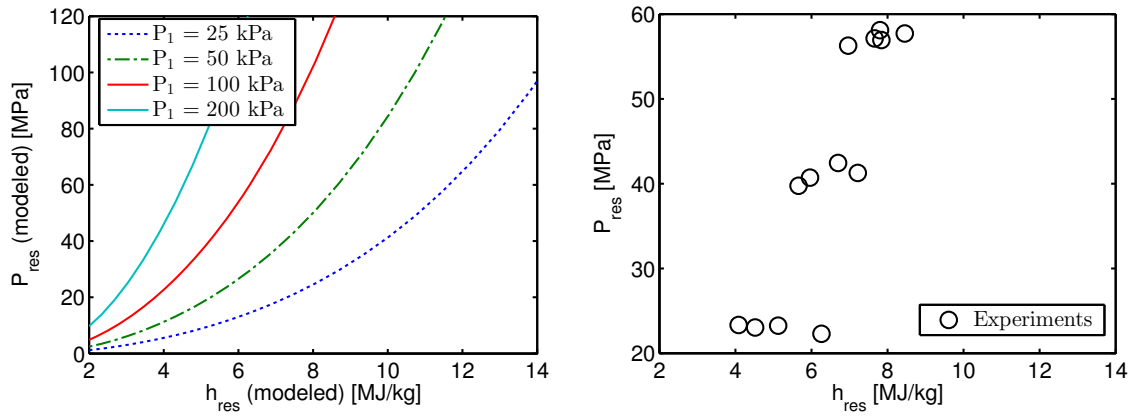
(a) 84% He, 16% Ar driver, P_1 50% air, 50% CO_2 (b) Experimental 50% air, 50% CO_2 conditions

Figure 3.18: Tunnel parameters for 50% air, 50% CO_2 (a) modeled for several shock tube fill pressures P_1, all with a 84% He, 16% Ar driver; and (b) as calculated for the present 50% air, 50% CO_2 experiments.

Chapter 4

Analysis

4.1 Hypersonic Boundary Layer Mean Flow

To apply the e^N method[1], the hypersonic boundary layer mean flow must first be computed. Two approaches to doing so are presented in this section. Section 4.1.1 presents similarity assumptions and frozen boundary layer composition to derive simplified boundary layer relationships and arrive at an approximate solution, and Section 4.1.2 uses an axisymmetric reacting-flow CFD solver as implemented in STABL.

4.1.1 Similarity Solution

The planar, two-dimensional, steady boundary layer equations for a compressible fluid are derived by White (1991). Continuity:

$$\frac{\partial}{\partial x}(\rho u) + \frac{\partial}{\partial y}(\rho v) = 0$$

x-momentum:

$$\rho \left(u\frac{\partial u}{\partial x} + v\frac{\partial u}{\partial y} \right) = -\frac{\partial p_e}{\partial x} + \frac{\partial}{\partial y}\left(\mu\frac{\partial u}{\partial y} \right)$$

---

[1]See Section 4.2 for a description of the e^N method.

y-momentum:

$$\frac{\partial p}{\partial y} = 0$$

Energy:

$$\rho \left(u\frac{\partial h}{\partial x} + v\frac{\partial h}{\partial y} \right) = u\frac{\partial p_\mathrm{e}}{\partial x} + \frac{\partial}{\partial y}\left(k\frac{\partial T}{\partial y} \right) + \mu\left(\frac{\partial u}{\partial y} \right)^2$$

Where the fluid enthalpy is $h = e + p/\rho$, and both temperature and enthalpy depend upon pressure and density only: $T = T(p, \rho)$ and $h = h(p, \rho)$. This formulation can be used for fully mixed gas mixtures, such as atmospheric air.

White (1991) Chapter 7 provides an expression for a similarity solution in compressible flow which uses the transformation of the arbitrary two-dimensional equations above. Illingworth (1950), quoted in White, separated the effects of viscosity and density into similarity variables ξ and η, respectively, for a flat plate:

$$\xi(x) = \int_0^x \rho_\mathrm{e}(x)U_\mathrm{e}(x)\mu_\mathrm{e}(x)\mathrm{d}x \tag{4.1}$$

$$\eta(x, y) = \frac{U_\mathrm{e}(x)}{\sqrt{2\xi}} \int_0^y \rho\,\mathrm{d}y \tag{4.2}$$

Lees (1956) performed a transformation of this flat-plate solution for axisymmetric laminar compressible boundary layers on a cone with less than $55°$ half-angle, for which the shock wave remains attached to the vertex of the cone, and flow at the cone surface may be assumed to have constant temperature, velocity, and pressure:

$$\xi(x) = \int_0^x \rho_\mathrm{e}(x)U_\mathrm{e}(x)\mu_\mathrm{e}(x)r_0^{2j}(x)\mathrm{d}x \tag{4.3}$$

$$\eta(x, y) = \frac{\rho_\mathrm{e}U_\mathrm{e}(x)r_0^j(x)}{\sqrt{2\xi}} \int_0^y \frac{\rho}{\rho_\mathrm{e}}\mathrm{d}y \tag{4.4}$$

Here $j = 0$ for flow over a flat plate and $j = 1$ for axisymmetric flow, and the

body surface radius is $r_0 = bx$ with $b = \arctan 5°$ for the laminar boundary layer of a 5° half-angle cone. This modification is analogous to the Mangler transformation for incompressible flow, as described in White (1991) Chapter 4. Equations 7-80 from White (1991)[2] reproduce the Lees solution:

$$\xi = \frac{\rho_e U_e \mu_e b^2 x^3}{3} \tag{4.5}$$

$$d\eta_{cone} = \left(\frac{3U_e}{2x\rho_e\mu_e} \right)^{1/2} \rho \, dy \tag{4.6}$$

For the axisymmetric conical geometry, the following equations for momentum and energy, respectively, are given by White (1991), where $f(\eta) = u/u_e$ is a shape function normalized by the velocity at the boundary layer edge, and $g(\eta) = h/h_e$ is a shape function normalized by enthalpy at the boundary layer edge. The right hand side of the second equation constitutes the viscous dissipation term. Primes represent differentiation by η (the variable accounting for density effects):

$$(Cf'')' + ff'' = 0 \tag{4.7}$$

$$(Cg')' + \Pr fg' = -\Pr C(\gamma - 1) M_e^2 f''^2 \tag{4.8}$$

Here C is the Chapman-Rubesin parameter, defined as the ratio of the products of density and viscosity at a location within the boundary layer to the products of density and viscosity at the edge. If the boundary layer profile is indeed self-similar, then the Chapman-Rubesin parameter will also be a function of η:

---

[2]Equations 7-80 in the Second Edition of White (1991) are incorrect for $d\eta_{cone}$. The relationship is stated correctly here.

$$C = \frac{\rho\mu}{\rho_{\mathrm{e}}\mu_{\mathrm{e}}} \approx C(\eta)$$

The gas flow in the boundary layers of the present experiments is hot but at low pressure. This means that the gas can be treated as ideal ($P = \rho RT$), but the composition may not be constant due to chemical reaction and transport processes within the boundary layer. In general, the enthalpy is a function of both species and temperature, and vibrational nonequilibrium and relaxation within the boundary layer may be significant in some cases. These important issues cannot be treated within the framework of self-similar solutions and are addressed in the present study by use of numerical solutions of the boundary layer equations as discussed in Section 4.1.2.

Nevertheless, in many cases it is possible to neglect the effect of composition changes and vibrational nonequilibrium and use the self-similar solutions as an approximation to the actual boundary layer flow. As first suggested by Chapman and Rubesin, the dependence of $C(\eta)$ can be determined through correlation with other thermodynamic properties. The first step is to relate the density within the boundary layer to temperature, making the standard assumption of constant pressure across the boundary layer and applying the ideal gas relationship for a fixed composition. Instead of temperature, it is made convenient to use enthalpy as a variable, motivated by the case of constant heat capacity, and density is further approximated with a power-law dependence on enthalpy:

$$\frac{\rho_{\mathrm{e}}}{\rho(y)} = \frac{T(y)}{T_{\mathrm{e}}} = \frac{h(y)}{h_{\mathrm{e}}}$$

Therefore, assuming a power-law relationship between viscosity ratio and temperature ratio, C can be expressed in terms of the enthalpy ratio only:

$$C = \frac{\rho}{\rho_{\mathrm{e}}}\frac{\mu}{\mu_{\mathrm{e}}} \approx \frac{h_{\mathrm{e}}}{h}\left(\frac{T}{T_{\mathrm{e}}}\right)^{n} \approx \left(\frac{h}{h_{\mathrm{e}}}\right)^{n-1} = g(\eta)^{n-1}$$

For air, $n \approx {}^2\!/_3$ and thus $C \approx g^{-1/3}$ (White, 1991). For non-zero wall temperature, assuming constant pressure across the boundary layer, an ordinary differential equation with the following five boundary conditions may be defined:

From the no-slip condition:

$$f(0) = f'(0) = 0$$

From free stream velocity:

$$f'(\infty) = 1$$

From free stream enthalpy:

$$g(\infty) = 1$$

From constant wall temperature:

$$g(0) = \frac{C_{p_{\mathrm{w}}} T_{\mathrm{w}}}{C_{p_{\mathrm{e}}} T_{\mathrm{e}}} = \frac{T_{\mathrm{w}}}{T_{\mathrm{e}}}$$

This ODE may be solved numerically using (for example) the MATLAB $\mathtt{bvp4c}$ routine. The boundary conditions at infinity are incorporated numerically by specifying them at a relatively large number for η, then confirming that using successively larger values of η for "infinity" does not change the solution. Figure 4.1(a) demonstrates this asymptotic effect for five values of η from 15 to 20. In each case, $\mathrm{d}f/\mathrm{d}\eta \to 1$ within machine precision.

The expression for $\mathrm{d}\eta_{\mathrm{cone}}$ in Equation (4.6) is numerically integrated to find the relationship between η and y, and solutions for $u/U_{\mathrm{e}} = f(y)$, $T/T_{\mathrm{e}} = g(y)$, and $\rho/\rho_{\mathrm{e}} = 1/g(y)$ are computed. Examples of these solutions at conditions corresponding to one T5 experiment in air, shot 2742 ($h_{\mathrm{res}} = 8.64$ MJ/kg, $P_{\mathrm{res}} = 55.7$ MPa) are presented in Figure 4.1. Similarity solutions of this form are computationally inexpensive and useful as a guide to the general properties of the compressible boundary layer on a 5° half-angle cone. However, a more sophisticated approach, detailed in Section 4.1.2, is

necessary to model the nonsimilar and nonequilibrium properties.

(a) Asymptotic behavior as $\eta \to \infty$

(b) Density

(c) Temperature
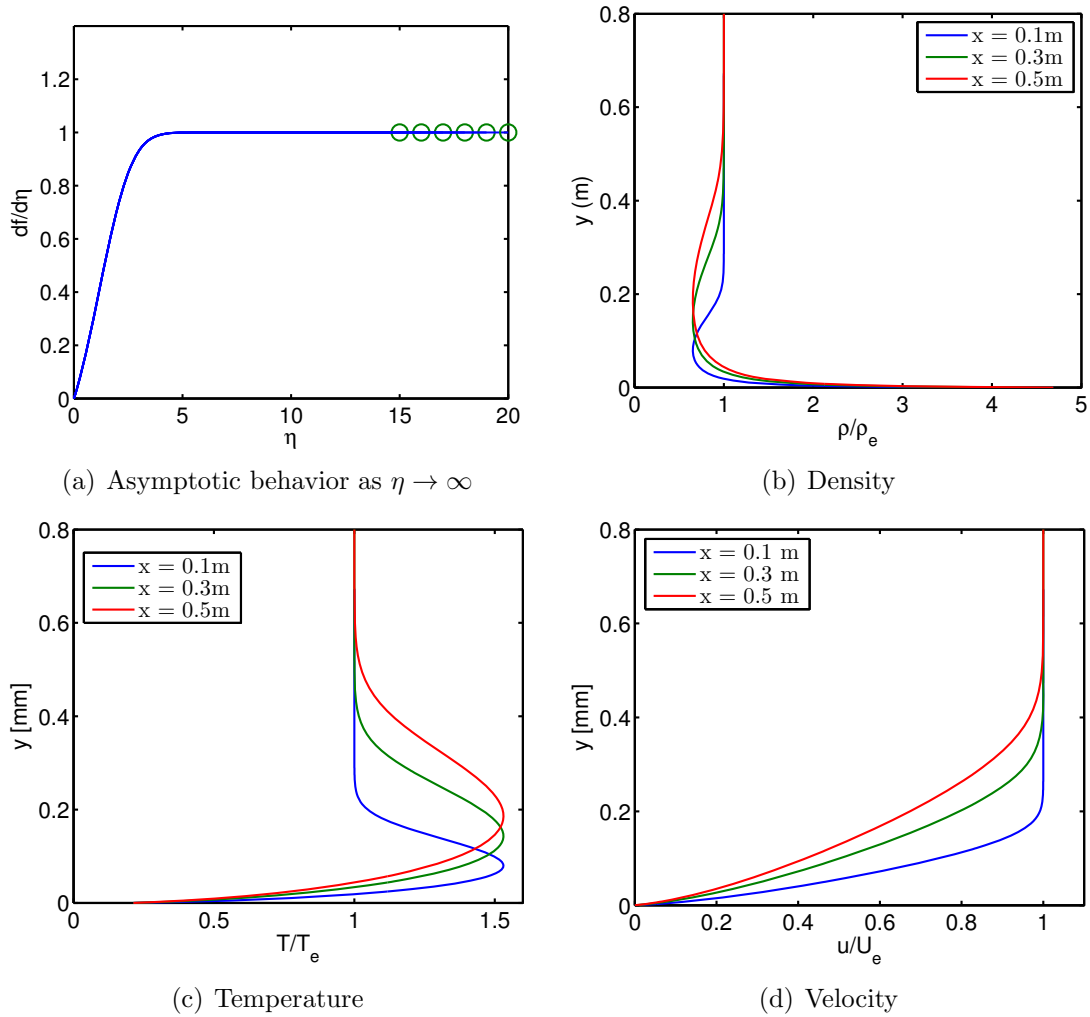
(d) Velocity

Figure 4.1: Similarity solution convergence and profiles for density, temperature, and velocity, normalized by the boundary layer edge conditions, at three x-locations along the surface of the cone. For clarity, since the five $df/d\eta$ curves in (a) are nearly identical, a circle indicates the η at which the boundary conditions at "infinity" were imposed for each curve. As the curves do not vary with increasing η from 15 to 20, the boundary conditions have been enforced at a sufficiently large value of η.

4.1.2 STABL: DPLR[3]

In order to treat chemical reactions, vibrational nonequilibrium, and relaxation, a numerical solution of the boundary layer that does not assume self-similarity is re-

[3]Portions of this section and Section 4.3.1 are adapted from Jewell et al. (2013c).

quired. For the present study, this was done using the software package STABL, developed by the Candler group at the University of Minnesota. The outer flow for the boundary layer was determined by the nozzle flow simulations that were described in Section 2.4.2. The freestream properties over the cone are approximated by averaging the nozzle flow within a notional box of gas positioned around the tip of the cone, and are held constant over the length of the cone. This is a simplifying approximation, because in the experiment the freestream properties vary over the length of the cone due to the nonuniformity of the actual flow created by off-design operation of the nozzle and the large extent (1 m in length) of the test article, resulting in some portions interacting with the expansion waves created at the nozzle exit. These effects are ignored in the present computations; the effect of the expansion waves are obvious in the experimental data observed on the final 10 cm of the cone for some conditions (Wagnild, 2012), as observed previously in Germain (1993) and Adam (1997). In all cases the wall temperature for the nozzle and cone walls is assumed to be 297 K due to the short flow time ($\sim$1 ms). The cone's nose has been approximated as spherical with a radius of 0.0125 mm. See Section 3.1 for the details justifying this approximation.

The mean flow for the stability analysis is computed using a structured-grid, axisymmetric CFD solver, which solves the reacting Navier-Stokes equations and is part of the STABL software suite (Johnson, 2000). This flow solver is also based on the finite-volume formulation and is similar to the one used to simulate the nozzle flow with the exception of the excluded volume equation of state. This specialized equation of state is not necessary for the boundary layer solver because the static pressure over the cone is sufficiently low (typically, 10–50 kPa) that the gas can be treated as ideal. The mean flow is computed on a single-block, structured grid (see Figure 4.2) with dimensions of 361 cells by 361 cells in the streamwise and wall-normal directions, respectively.
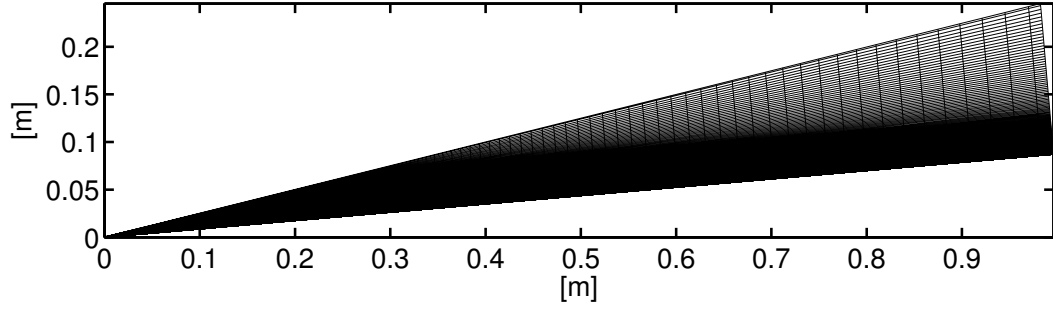
Figure 4.2: Axisymmetric grid of 361 cells by 361 cells in the streamwise and wall-normal directions, respectively, used for STABL-DPLR mean flow computations.

The wall-normal span of the grid increases down the length of the cone, from 0.3 mm at the tip to 159 mm at the base, allowing for the shock to be fully contained within the grid for all cases tested. The grid is clustered at the wall as well as at the nose in order to capture the gradients in these locations. The Δy^+ value for the grid, extracted from the DPLR solution for each case, is everywhere less than 1, where Δy^+ is a measure of local grid quality at the wall in the wall-normal direction defined as:

$$\Delta y^+ \equiv \frac{(y_1 - y_0)\, u_\tau}{\nu}$$

Here, the so-called friction velocity u_τ is:

$$u_\tau = \sqrt{\nu \frac{\partial u}{\partial n}}$$

and u is the velocity component parallel to the wall.

4.2   Semi-Empirical e$^{\mathrm{N}}$ Method

Smith and Gamberoni (1956) and van Ingen (1956) proposed a boundary layer transition prediction method, initially for the low-speed, incompressible case, based upon calculating the relative amplification of disturbances present in the boundary layer.

Further historical background on this method was reviewed by the latter author in van Ingen (2008). For an overview of the method's subsequent application to high-speed compressible boundary layers, see Herbert (1997).

4.2.1 Overview

The e^N method is based on the observation that laminar boundary layers are unstable and small disturbances can be amplified to the point that nonlinearity results in the breakdown of laminar flow and transition to turbulence. The critical amplitude of linear disturbances is a highly simplified view of transition and is one of many mechanisms by which transition may occur. The growth rates σ of the instabilities are obtained from solutions of the small disturbance equations obtained by linearizing the Navier-Stokes equations for small perturbations around the mean flow in the boundary layer as discussed in Schlichting and Gersten (2001). In the most simplified type of linear instability analysis, assuming parallel flow and temporal growth at a fixed frequency, all disturbances are assumed to vary with time and distance with amplitude

$$A \sim \phi(y) \exp(i(\alpha x - \omega t)) \tag{4.9}$$

where $\omega = 2\pi f$ is the temporal frequency of oscillation, $-\mathrm{Im}(\alpha)$ is the spatial growth rate and ϕ is an eigenfunction describing the shape of the perturbation at a given downstream location. The solution of the eigenvalue problem for ϕ and α as a function of location within the boundary layer can be used to predict the growth in amplitude $A(x)$ of disturbances in pressure, velocity, density and temperature with downstream distance in terms of the ratio $A/A(x)$, where the disturbance propagates within the initial laminar boundary layer in the x-direction and A_0 is an arbitrary initial amplitude of the disturbance. The critical value of the amplitude is linked to transition onset location by empirical observation with a critical value of N at the transition

location, where $e^{N_{Tr}} \approx A_{Tr}/A_0$. The critical value of N is determined empirically, as discussed subsequently, and is known to be a strong function of factors such as the freestream turbulence level, wall roughness, and pressure gradient. As described in Johnson (2000) Chapter 5, N represents the integrated growth rate of boundary layer disturbances and is defined as:

$$N(f, x) = \ln\left(\frac{A}{A_0}\right) = \int_{x_0}^{x} \sigma \, dx$$

where f is the disturbance frequency, x represents distance along the surface of interest (x_0 is the location of instability onset) and the disturbance growth rate σ is:

$$\sigma(f, x) = -\text{Im}(\alpha(\omega, x)) + \frac{1}{2E}\frac{dE}{dx}$$

where α is the complex wave number, computed at each streamwise location, and E is the kinetic energy of the disturbance, integrated over the spatial variable in the normal direction to the flow, n:

$$E = \int_{n} \bar{\rho}\left(|u'|^2 + |v'|^2 + |w'|^2\right) dn$$

The amplification rate α and the disturbance amplitudes u', v' and w' are computed either with a linear stability analysis (LST) assuming locally parallel flow in the boundary layer or else the parabolized stability equations (PSE) that approximately account for the non-parallel development of the flow; see Johnson (2000) for how this is implemented in the STABL software.

The change in σ and N with distance along the boundary layer reflects the underlying stability characteristics. At a given downstream location boundary layers are only unstable over a narrow range of frequency or spatial wavelength (see Figure 4.6 and associated discussion). The center of the band of unstable frequencies shifts downward

as the boundary layer becomes thicker with increasing distance downstream. Starting from the leading edge and progressing downstream, a disturbance is initially stable ($\sigma < 0$) and damped, becomes unstable ($\sigma > 0$) when the neutral stability boundary is crossed at x_0 and grows, then again becomes stable and damped. This results in amplitudes A and N factors that increase with increasing downstream distance (after reaching the neutral stability boundary), reach a maximum value, then decrease. The maximum value of N increases with increasing downstream distance due to the longer distance available for positive growth. Figure 4.3, calculated for shot 2742 from the present study, illustrates this behavior in a series of N factor curves at fixed frequency along the surface of a five-degree half-angle cone. The overall N factor curve is taken to be the envelope of these individual curves. See Wagnild (2012) Chapter 3 for a more detailed description of the implementation of the e^N method used in the present study.

The chief weakness of the e^N method is that it does not account for the amplitude of the initial disturbance from which N derives, but only the subsequent growth rate of disturbances. Thus, the most useful comparisons can only be made between experiments performed in very similar flow environments (*i.e.*, the same geometry in the same facility), for which boundary layer receptivity characteristics may be reasonably assumed to be similar (Saric et al., 2002). The e^N method also does not account for bypass transition mechanisms. However, within these limitations and with the caveat that computations become much more challenging as conditions proceed away from the two-dimensional incompressible flows for which the theory was originally developed, the e^N method is currently considered the most reliable technique available for estimating transition location given a repeatable freestream turbulence level and a streamlined body with a relatively smooth surface. In particular, it provides a means of relating boundary layer characteristics across different geometries, thermochemical models, and freestream conditions. For "noisy" tunnels, as some authors, including
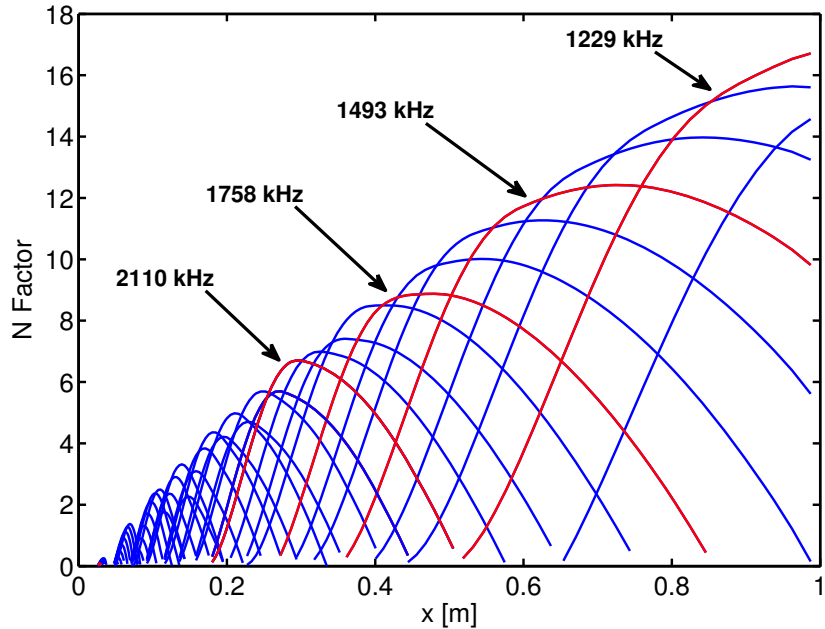
Figure 4.3: Computed N factor at selected frequencies along the surface of a 5° half-angle cone, from shot 2742. Four individual N factor results, in red, are labeled with their frequencies to illustrate the frequencies contributing to the maximum N factor at different positions on the cone.

Schneider (2001), have characterized Caltech's T5 facility, the N factors at transition are around 4 to 7 (Johnson, 2000). For so-called "quiet" tunnels, the characteristic transition N factors may be 8 to 9, extending all the way up to N factors equivalent to free flight of 10 to 11 (Schneider, 2008a). For N~20 and above, the effects of Brownian motion alone are enough to cause transition (Fedorov, 2011b). The critical value of N is empirical and depends, among other factors, on the disturbance environment; therefore, N_{Tr} must be calibrated for a particular wind tunnel facility.

4.2.2   Past Work

Historically, many computational studies on hypersonic boundary layer instability with the e^N method have been based upon linear stability theory (LST), which neglects the nonparallel nature of a the boundary layer as well as non-linear effects.

Malik and Anderson (1991), for example, used this approach to demonstrate that first-mode instabilities were suppressed, and second-mode instabilities amplified, for real-gas hypersonic flows at Mach 10 and Mach 15. Johnson et al. (1998) used LST to examine the effects of freestream total enthalpy and chemical composition on transition onset location for T5 flows. Reed et al. (1996) review the application of LST to boundary layers. For an overview of hypersonic boundary layer stability in the context of transition prediction methods, see Fedorov (2011a).

The e^N method implemented with parabolized stability equations (PSE) has become popular in recent decades as a more accurate representation of boundary layer instabilities than that available from LST (Herbert, 1997). Malik (2003) used PSE methods to analyze second-mode growth and transition in two flight experiments, including Reentry-F (Zoby and Wright, 1977). More recently, Wagnild et al. (2012) and Gronvall et al. (2014) applied the e^N method as implemented in STABL/PSE-Chem to a notional cone at Mach 12, and used the same software to analyze transition data from cones at Mach 6.7–7.7 in the Japan Aerospace Exploration Agency's free-piston High Enthalpy Shock Tunnel, respectively. As part of the present study, Wagnild et al. (2010) used the e^N method to evaluate the effect of gas injection into a conical boundary layer on transition onset location, and Jewell et al. (2013c) examined the effect of freestream gas mixtures with the same geometry.

4.3   Stability Computation

4.3.1   STABL: PSE-Chem

The stability analyses are performed using the PSE-Chem solver, which is also part of the STABL software suite. PSE-Chem (Johnson and Candler, 2005) solves the reacting, two-dimensional, axisymmetric, linear parabolized stability equations (PSE) to predict the amplification of disturbances as they interact with the boundary layer.

The PSE-Chem solver includes finite-rate chemistry and translational-vibrational energy exchange. The parabolized stability equations predict the amplification of disturbances as they interact with the boundary layer. Both the mean flow and stability analysis solvers in STABL are capable of selectively freezing both chemical reactions and molecular vibration, allowing for the determination of internal molecular effects on boundary layer disturbances.

A seven-species chemistry model including CO_2, CO, N_2, O_2, NO, N, and O is used to simulate the flow through the nozzle as well as over the cone for all conditions tested. In all computations, a finite-rate chemical reaction model is used, with reaction rates based on Park et al. (1994) and Bose and Candler (1996, 1997). The equilibrium coefficients are calculated from fits based on Park (1990) and McBride et al. (2002). It is assumed that the vibrational-vibrational energy exchanges occur on a relatively short time scale, allowing for a single temperature governing all vibrational modes. It is also assumed that rotation and translation are coupled and governed by the translational temperature. The translational-vibrational energy exchanges are governed by the Landau-Teller model for the simple harmonic oscillator, following Candler and MacCormack (1991). The vibrational relaxation times are governed by the Millikan and White model with several empirical corrections given in Camac (1966) and Park et al. (1994). The viscosity for each species is calculated using Blottner fits and the mixture quantities are calculated using Wilke's semi-empirical mixing law.

The role of vibration-translational relaxation can be examined by adjusting the inputs to STABL. For example, the vibrational energy can be "frozen" by halting vibrational rate processes by setting the relevant Millikan and White parameter for all rate processes to a value several orders of magnitude higher than the physical case, which means that the rate processes are given characteristic times much longer than the relevant flow times. This technique has been used previously for T5 cases

in Wagnild (2012) and Jewell et al. (2013c), and is used later in the present work in Section 5.2.1. A similar technique can be used to produce quasi-equilibrium cases, by setting the relevant Millikan and White parameter for all rate processes to a value several orders of magnitude lower than the physical case, which means that the rate processes are given characteristic times much shorter than the relevant flow times. These comparisons allow the isolation of the effect of vibrational rate processes on the damping of boundary layer disturbances and the stability characteristics of the boundary layer, and their implications for transition to turbulence based on the N factor approach.

4.3.2   Discussion of Instability Computations

The PSE-Chem/STABL suite is used to perform stability analysis on the nine test cases (three air, two N_2, two CO_2, and two CO_2/air mixture experiments) described in Section 2.6 and Appendix B. As in that section, the details of one air case, shot 2742 (h_{res} = 8.64 MJ/kg, P_{res} = 55.7 MPa), are presented below as an example. The remaining eight cases analyzed are recorded in Appendix B.

Eigenfunctions of pressure and density from PSE-Chem computations at the conditions of shot 2742 are presented in Figure 4.4. The results are for x = 0.505 m and 1550 kHz, which is an unstable frequency at that location. Mack (1984) (p. 3-37) used the following nomenclature for referring to unstable boundary layer modes: "...the number of zeroes in [the pressure eigenfunction $\beta(y)$] is one less than the mode number n. For example, the second mode has one zero, and $\beta(0)$ is 180° out of phase with $\beta(\delta)$ [δ is the boundary layer thickness]; the third mode has two zeroes and $\beta(0)$ is in phase with $\beta(\delta)$. The number of zeroes in $\beta(y)$ is the surest identification of the mode under consideration."

Therefore, for Mack's so-called "second mode" disturbances, the pressure eigenfunction's phase should shift by approximately 180° somewhere in the boundary layer

(*cf.* Mack (1969) Chapter 11 and Figure 11.10)[4]. Furthermore, the real part of the eigenfunction amplitude should have one zero (*cf.* Mack (1984) Chapter 9 and Figure 9.5). These characteristics identified by Mack have also been used for second-mode identification in recent studies including Hudson et al. (1997), Johnson (2000), Gronvall (2012) and Gronvall et al. (2014). All of these behaviors are present in the present results for shot 2742 at $x = 0.505$, indicating that the 1550 kHz instability at this location is the second mode.

The spatial evolution for the region up to 10 cm downstream of the pressure and density eigenfunction given in Figure 4.4 is shown in Figure 4.5. For the chosen parameters and spatial region explored, the growth rates are all positive and that is reflected by the increase in amplitude with increasing downstream distance. The evolution of the eigenfunction shapes as a function of downstream distance is a result of the non-parallel nature of the mean flow in the boundary layer.

---

[4]This result, given by Mack for the inviscid case, was also shown to hold for the real-gas viscous case in Malik and Anderson (1991).
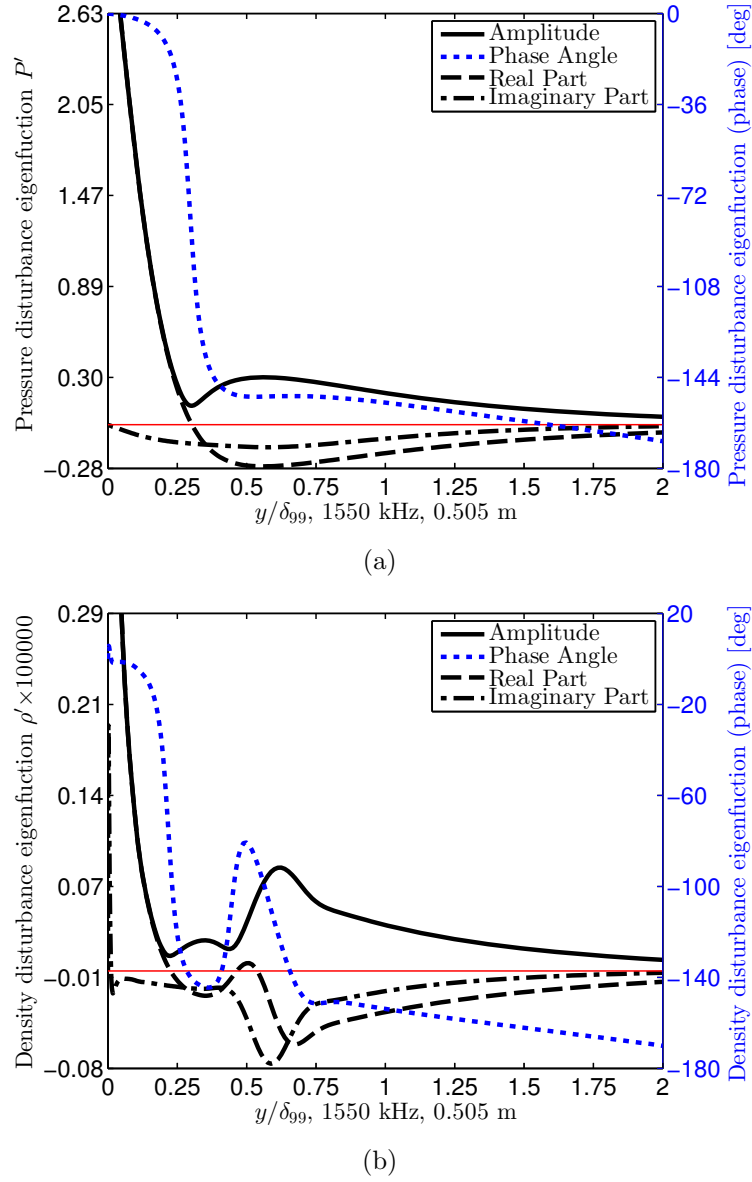
Figure 4.4: Representative pressure (a) and density (b) disturbance eigenfunctions calculated by PSE-Chem for an unstable frequency from shot 2742, 1550 kHz at $x = 0.505$ m. Amplitude and phase are presented along with the real and imaginary components for each eigenfunction. The eigenfunction shapes are typical of trapped acoustic waves in the boundary layer and indicate that most of the disturbance is contained within δ_{99}. The red line represents zero on the left-hand axis.
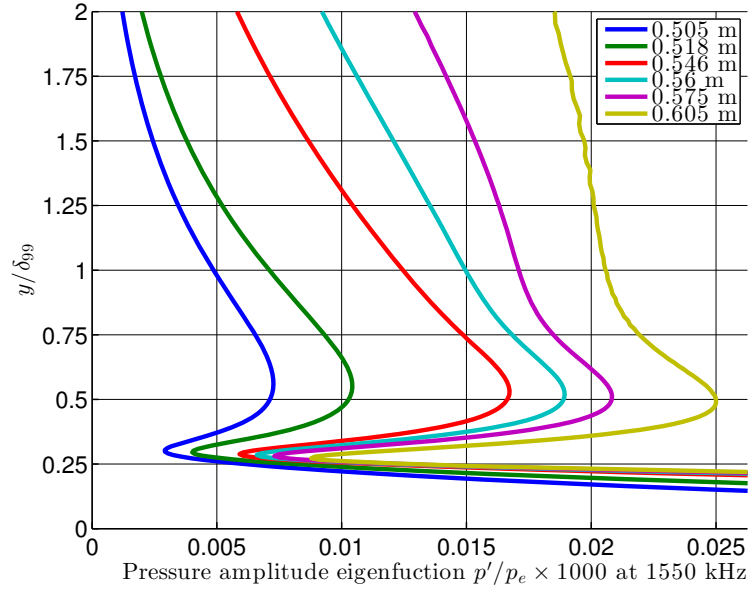
(a)
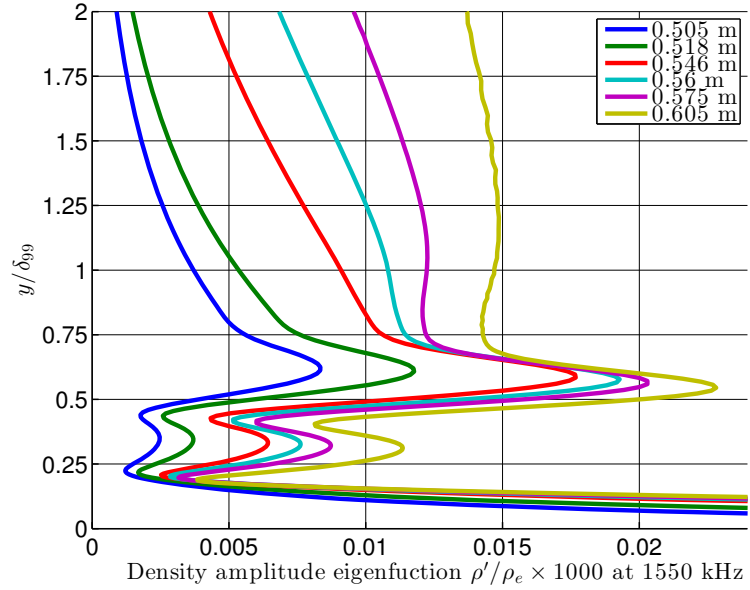
(b)

Figure 4.5: Growth of pressure (a) and density (b) disturbance eigenfunctions calculated by PSE-Chem for shot 2742 at 1550 kHz, at several locations downstream from $x = 0.505$ m. Only amplitude is presented on these plots.

4.3.2.1 Most Amplified Frequency

The band of amplified frequencies within the boundary layer is presented on contour plots in terms of amplification $-\alpha_i$ in Figure 4.6. Three models of vibrational relaxation are examined. The model labeled "vib" corresponds to using the Landau-Teller model with realistic values of the relaxation time parameters. The model labeled "frozen" corresponds to setting the relaxation times to very long values which freezes the vibrational energy and eliminates any vibrational-translation energy exchange. The model labeled "equilibrium" sets the relaxation times to very small values, which results in rapid equilibration between vibrational and translational energy. The most amplified frequency predicted by the simple model based on edge velocity and boundary layer thickness in Equation 1.1 is also plotted for each case, and shows generally good agreement with the detailed computations. Spatial amplification $-\alpha_i$ as a function of the frequency at the experimentally observed transition onset location is shown in Figure 4.7. The inclusion of the vibrational relaxation slightly decreases the amplification rate (increases the damping rate) as compared to cases with either very slow relaxation (frozen) or extremely fast relaxation (equilibrium). The explanation for this effect is that vibrational-translational relaxation is only effective at damping the boundary layer instabilities if there is the potential for energy exchange on the same scale as the period of the fluid instabilities. If the relaxation time scale is too long, then there is no possibility of energy exchange. If the relaxation time scale is too short, then the vibrational and translational energy change in phase and there is no damping effect. When significant energy exchange can happen within a time comparable to the period of fluid instability oscillations, and the two modes are out of phase, then damping can occur. This is discussed at length by Vincenti and Kruger (1965) for the case of propagating acoustic waves.
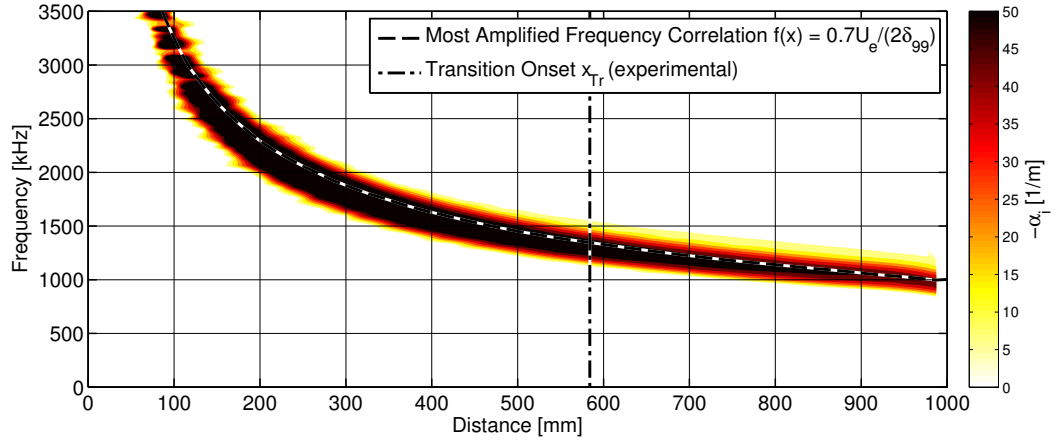
(a) "vib": realistic relaxation time parameters
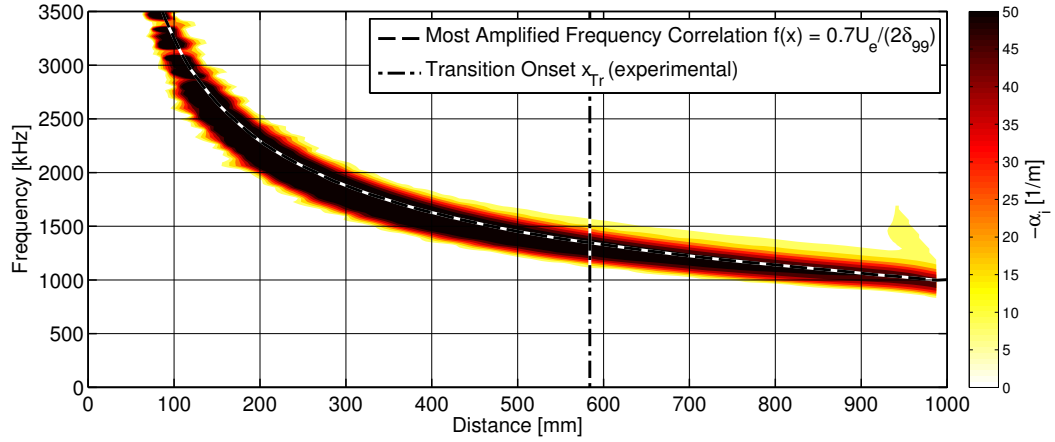
(b) "frozen": very long relaxation time parameters
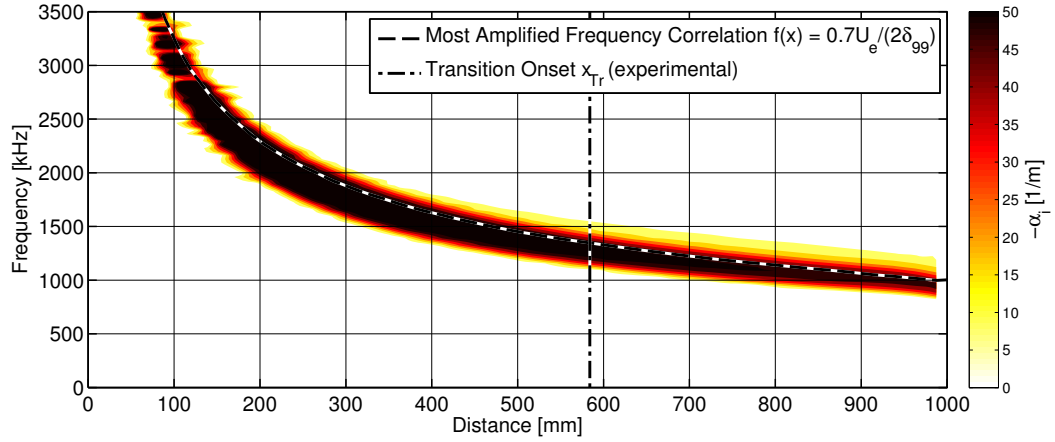
(c) "equilibrium": very short relaxation time parameters

Figure 4.6: Contours of growth rates for three models of vibrational relaxation as discussed in the text, shot 2742 in air. Dashed line indicates $0.7U_{\mathrm{e}}/(2\delta_{99})$; dot-dashed line is the transition onset location.
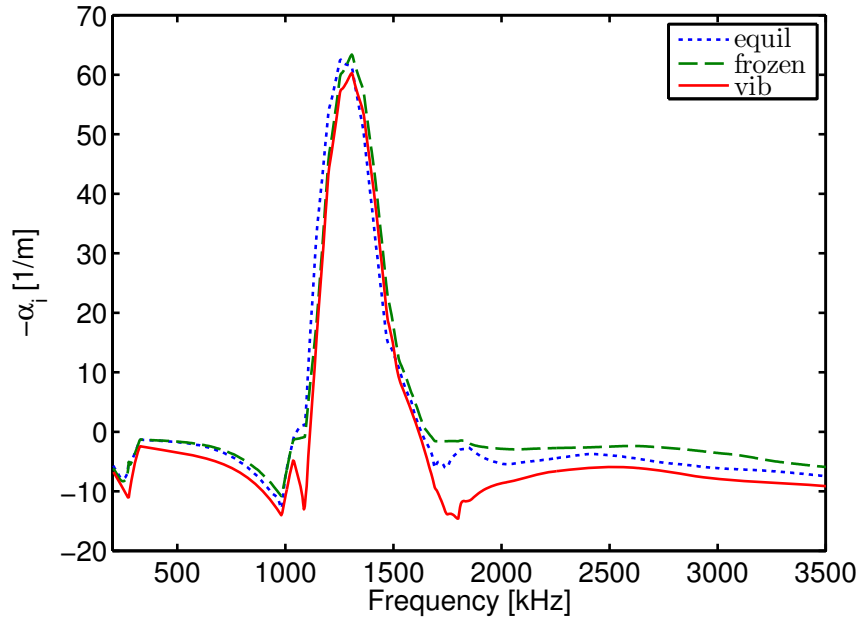
Figure 4.7: Spatial amplification rate $-\alpha_i$ as a function of frequency calculated at $x = x_{\text{Tr}}$, with physically modeled vibrational relaxation rates (labeled "vib"), frozen vibrational energy, *i.e.*, no transfer to or from translation (labeled "frozen"), and complete equilibrium between vibrational and translational energy (labeled "equil"), shot 2742 in air.

4.3.2.2 Largest Growth Frequency and N Factor

The N factor (see Section 4.2 for details) for a given frequency is found by the integration of the linear growth rate, shown in Figures 4.6 and 4.7, from the tip of the cone up to the relevant location:

$$N(f, x) = \int_0^x -a_i(f, \xi) d\xi$$

This quantity is presented on contour plots in Figure 4.8 for realistic/vibrational, frozen/no vibration, and equilibrium vibrational energy transfer assumptions. The computed frequency of largest growth at each location is also plotted. The N factor as a function of frequency at the transition onset location shows that the case with realistic relaxation rates, where vibrational relaxation contributes to acoustic absorption, has slightly lower amplification rates than the equilibrium and frozen vibration cases (Figure 4.9). The effect is very modest for flows in air, because as discussed subsequently in Chapter 5, the time scales for vibrational relaxation in air are much slower than the characteristic boundary layer oscillation periods. The envelope of maximum N factors for all computed frequencies at each location is presented in Figure 4.10. The equilibrium and frozen curves are quite similar and both are larger than the physically modeled case by about $\Delta N = 1$ at the experimentally observed transition onset location. For this case, N_{Tr} is 12, which is much higher than the expected value for noisy tunnels. This issue is explored in more detail in Chapter 5.
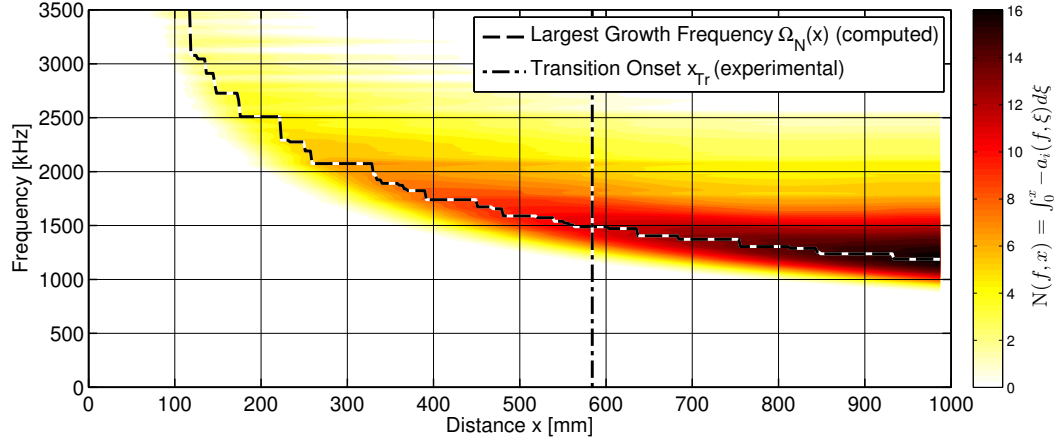
(a) "vib": realistic relaxation time parameters
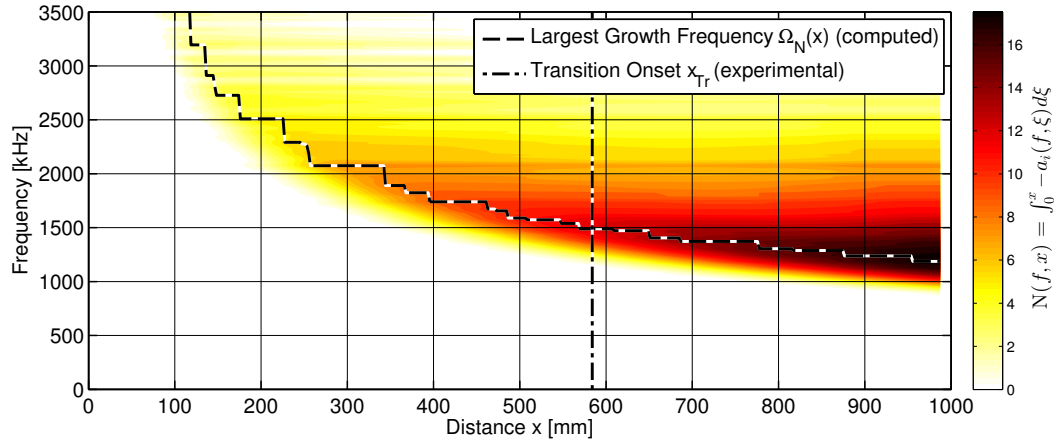
(b) "frozen": very long relaxation time parameters
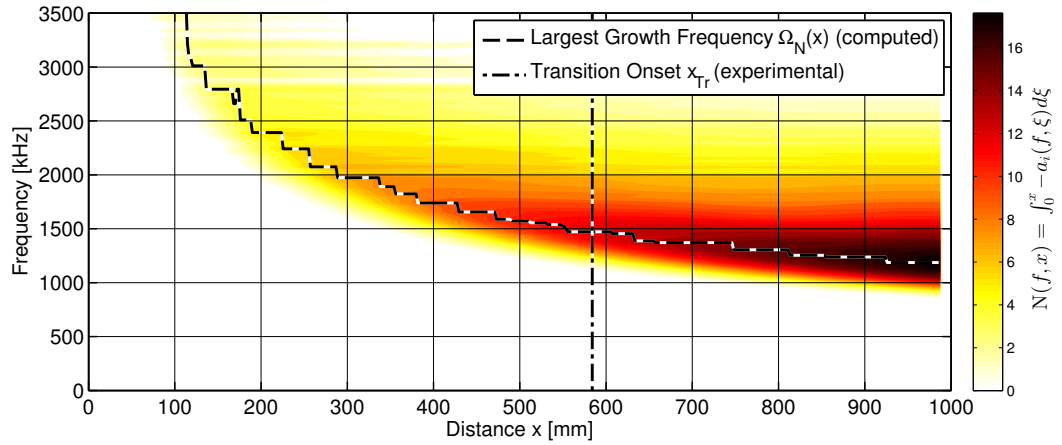
(c) "equilibrium": very short relaxation time parameters

Figure 4.8: Largest (integrated) growth frequency for three models of vibrational relaxation as discussed in the text, shot 2742 in air. Dashed line indicates the computed frequency of largest growth at each x-location; dot-dashed line is the transition x-location.
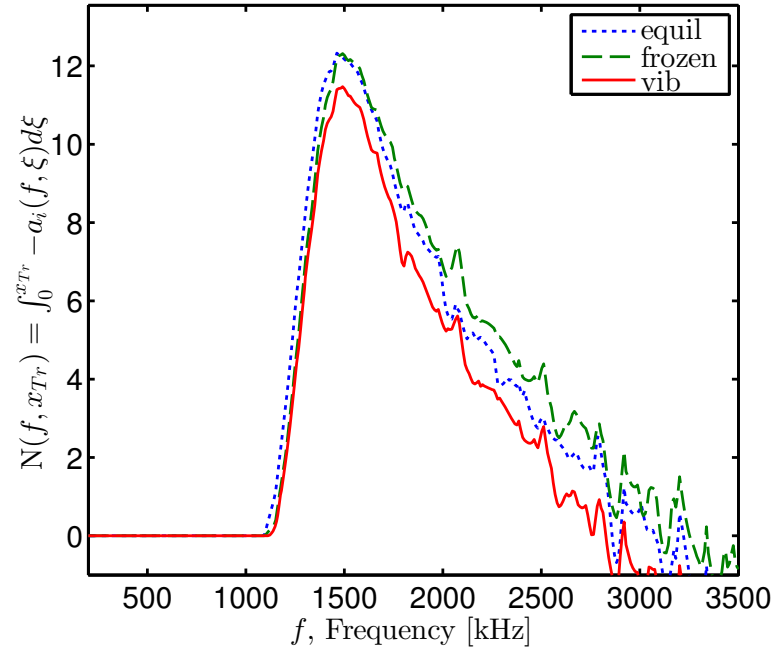
Figure 4.9: $N(f, x) = \int_0^x -a_i(f, \xi)d\xi$ calculated at $x = x_{\text{Tr}}$ as a function of frequency, for three models of vibrational relaxation as discussed in the text, shot 2742 in air.
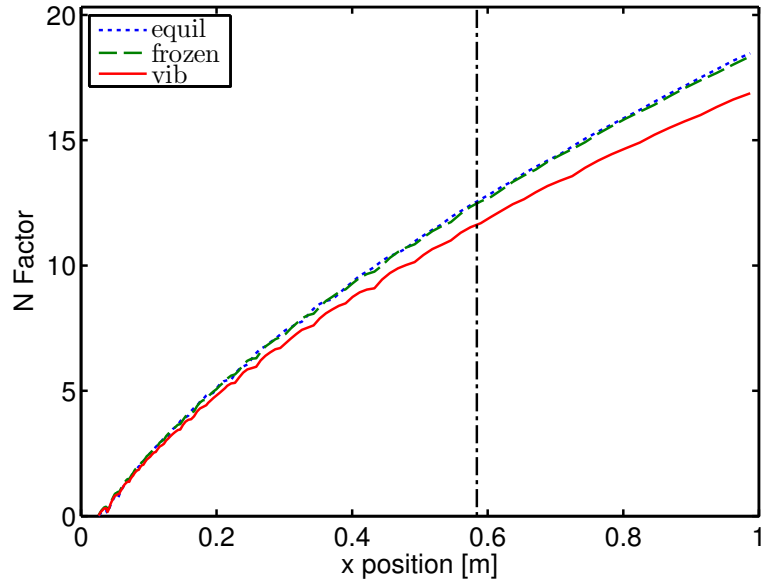
Figure 4.10: Locus of maximum N factor as a function of distance for for three models of vibrational relaxation as discussed in the text, shot 2742 in air. The dot-dashed line indicates the experimentally measured transition onset location. The vibrational result, in red, is equivalent to the envelope of maximum N factor for all of the frequencies shown in Figure 4.3.

4.3.3 Nozzle and Nonequilibrium Effects on Instability Prediction

A series of computations were carried out to determine the sensitivity of computed N factors to assumptions about the flow in the nozzle, the location of the cone tip, and the effect of vibrational-translational relaxation modeling. See Section 2.6 for a discussion of the sensitivity of computed freestream and boundary layer edge conditions to these same assumptions.

The conditions from three air experiments (2742, 2764, and 2823); two N_2 experiments (2776 and 2778); two CO_2 experiments (2793 and 2808); and two CO_2/air mixture experiments (2817 and 2821) were chosen for analysis. The results of detailed analysis of experiment 2742, an air case performed in T5 on 19 July 2012, are presented below in Table 4.1. The results of sensitivity studies for the eight other chosen tests are documented in detail in Appendix B, but selected results are discussed below.

	x_{Tr}	Re_{Tr}	N_{Tr}	Ω_{Tr}	Ω_{NTr}	δ_{99Tr}	$(x/\delta_{99})_{Tr}$	$Re_{\delta_{99Tr}}$
	m	-	-	kHz	kHz	mm	-	-
100 cm	0.584	$3.49{\times}10^6$	10.57	1312	1326	1.056	553	6312
Lam 72 cm	0.584	$3.89{\times}10^6$	11.50	1438	1462	0.991	589	6602
82 cm	0.584	$4.05{\times}10^6$	11.81	1514	1491	0.963	606	6678
77 cm	0.584	$4.10{\times}10^6$	12.00	1514	1530	0.955	611	6705
72 cm	0.584	$4.08{\times}10^6$	11.69	1514	1491	0.972	601	6719
67 cm	0.584	$3.78{\times}10^6$	11.27	1432	1462	1.003	582	6489
62 cm	0.584	$3.68{\times}10^6$	10.99	1374	1394	1.023	571	6443
Frozen 72 cm	0.584	$4.08{\times}10^6$	12.56	1514	1491	0.972	601	6719
Equil. 72 cm	0.584	$4.08{\times}10^6$	12.64	1480	1462	0.972	601	6719

Table 4.1: Boundary layer stability characteristics at experimentally observed transition onset location, shot 2742

In addition to the nozzle position study, which was performed for only these nine total cases, stability computations with both "vibrational" (realistic values for the relaxation time parameters) and nonvibrational or "frozen" (very long values for the

relaxation time parameters), as described in Section 4.3.2.1, were carried out for every experiment performed in the present study. These and other selected results for all tests are given in Appendix A.

4.3.3.1 Effect of Nozzle Boundary Layer Assumptions

The effect of modeling the nozzle boundary layer as laminar or turbulent was quite small in terms of the mean flow and edge conditions in all cases. As Table 2.14 and Table 2.16 showed, for shot 2742 all recorded freestream and boundary layer edge properties varied by less than 4% for both laminar and turbulent assumptions, except for the freestream and boundary layer edge pressures, which varied by less than 5%. The effects on boundary layer stability in terms of N factor at the observed transition location were likewise small, varying by 1.7% for shot 2742. The largest effect for any of the nine experiments chosen for detailed study was found for shot 2764 in air (see Appendix B), which had $N_{Tr} = 5.4$ for the turbulent nozzle assumption and $N_{Tr} = 4.9$ for the laminar nozzle assumption, a 10% difference. For all four of the 100% and 50% CO_2 cases, the difference was less than 2%.

4.3.3.2 Effect of Cone Position

The effect of taking the input conditions for DPLR at 62, 67, 72, 77, 82, and 100 cm downstream of the nozzle throat (all with turbulent nozzle wall assumptions) was relatively large for the most extreme cases, but for the central 67, 72, and 77 cm cases, all within 5 cm of the expected 72 cm cone-nozzle position setting, the variation was small. As Table 2.14 and Table 2.16 show, for shot 2742 mean flow and boundary layer edge properties varied by up to 28% for freestream pressure and edge pressure across the whole range of computed cone positions. The largest effect was found for shot 2776 in N_2 (see Appendix B), which varied up to 41% with cone position for freestream pressure. There were, likewise, relatively large variations in computed N_{Tr}

for DPLR input conditions selected at different locations downstream from the nozzle throat, with the largest stability effect also found for shot 2776 in N_2, for which N_{Tr} varied by 25%.

However, for the central 67–77 cm positions, the variation for all properties was less than 13% for shot 2742, and the largest effect for any of the nine experiments chosen for detailed study were found for shot 2764 in air, and shot 2817 in 50% air, 50% CO_2, which both varied up to 17% in freestream pressure across this range of positions. The largest stability effects were also smaller for the central positions, ranging up to only 11% variation for shot 2764, the largest case, and less than 5% in most cases. This central ± 5 cm range is larger than the expected uncertainty due to recoil variation and measurement imprecision.

4.3.3.3 Effect of Vibrational-Translational Relaxation Models

Depending upon gas composition, significant variation was found in N_{Tr} for each of the vibrational-translational relaxation models. Two boundary layer stability cases ("vib" or realistic vibration and "frozen" or no vibration) were computed for every experiment in the present study[5], and the N factor results at the experimentally observed transition location are tabulated in Appendix A.3. While almost no effect on stability was observed for any N_2 condition, which is typical for T5-like flows as the N_2 is effectively vibrationally frozen even for physical vibration parameters at the pressures and temperatures achieved in the boundary layer, N_{Tr} increased by up to 17% for high-enthalpy air cases (see shot 2789, page 257), 254% for pure CO_2 cases (see shot 2719, page 257), and 93% for air/CO_2 mixture cases (see shot 2729, page 257). These differences are explored further in Chapter 5.

---

[5]The "equil" cases, which used very short relaxation time parameters, produced similar results to the "frozen" cases for air, CO_2, and 50% CO_2, but for the N_2 cases did not yield meaningful results due to the large amount of thermal nonequilibrium present in the N_2 boundary layer, and are therefore omitted for that gas.

Chapter 5

Results: Transition Onset

5.1 Introduction

The usual approach for representing boundary layer transition onset is in terms of a transition location Reynolds number, for example, $\mathrm{Re}^*_{\mathrm{Tr}}$ or $\mathrm{Re}_{\mathrm{Tr}}$. This has been true even for hypersonic studies (*e.g.*, Schneider (1999), Schneider (2001), and Schneider (2004)), and previous analysis of T5 transition data has also used this approach (*e.g.*, Germain and Hornung (1997) and Adam and Hornung (1997)). However, in hypervelocity flow over a cold wall, the principal boundary layer instability mechanism is the predominantly inviscid acoustic or Mack mode (see Section 4.3.2 for a more thorough discussion of Mack's second mode and computations demonstrating that this mode is present and unstable for T5 conditions). Unlike the viscous instability of low-speed boundary layers (see, *e.g.*, the seminal experiments of Schubauer and Skramstad (1948)), in the hypervelocity flow regime the role of viscosity is therefore primarily in determining the mean flow. The properties of the acoustic instability are determined by the local boundary layer thickness[1] and profiles of velocity and thermodynamic properties. This suggests the approach of correlating transition distance with x/δ_{99} and the computed stability of the boundary layer rather than a Reynolds number. As

---

[1]For example, the frequency of the instability scales with $\delta_{99}/U_{\mathrm{e}}$, as shown earlier in Figure 4.6.

the boundary layer thickness δ_{99} scales[2] as:

$$\delta_{99} = \frac{x}{\sqrt{\mathrm{Re}_x}} F\left(\mathrm{M}, \mathrm{Pr}, \frac{T_\mathrm{w}}{T_\mathrm{aw}}, \frac{T_\mathrm{w}}{T_\mathrm{e}}, \gamma, ...\right)$$

it is expected that $(x/\delta_{99})_\mathrm{Tr}$ and a relevant transition Reynolds number will also scale together. This is shown to be the case for $\mathrm{Re}_\mathrm{Tr}^*$ and Re_Tr in Section 5.2.2.

More recently, assessments of hypersonic boundary layer transition onset location, including the present study, have relied upon computations of disturbance amplification using the semi-empirical e^N method described in Chapter 4. Schneider (2004) reports N factor agreement for hypersonic free flight experiments where the transition Reynolds numbers differed by an order of magnitude, but exhibited transition N factors of 9 to 11. For "noisy" air tunnels, as some authors, including Schneider (2001), have characterized Caltech's T5 facility, the N factors at transition have been reported to be around 4 to 7 (Johnson, 2000). For so-called "quiet" tunnels, the characteristic transition N factors may be 8 to 10 or higher (Schneider, 2008a, Gronvall, 2012).

Comparisons between computed N factors and experimentally measured transition locations have been made by a number of previous researchers for cones at zero angle of attack. Gronvall et al. (2014) computed four cases from experiments performed on a 7° half-angle cone[3] in the High Enthalpy Shock Tunnel (HIEST) facility, with $h_\mathrm{res} = 6.5 - 7.7$ MJ/kg and P_res held constant near 30 MPa, and reported $\mathrm{N}_\mathrm{Tr} = 8.0$. Gronvall et al. (2010) computed two T5 cases from the 5° cone experiments of

---

[2]A good discussion of boundary layer scaling may be found in Chapter 2 of Schlichting and Gersten (2001).

[3]The HIEST 7° cone, which is 1100 mm long, had a 2.5 mm diameter tip. While this is "sharp" in the sense that the swallowing length is less than any reported transition locations, which ranged from 660 mm to 926 mm, the entropy layer swallowing length calculated using the parameter in Figure 5 of Stetson (1983), as was done for the present experiments in Section 3.1, is 420 mm for the case that transitioned at 660 mm. By contrast, the swallowing length for the present work is no more than 53 mm for a cone of similar length.

Adam and Hornung (1997) and found[4] $N_{Tr} = 5.0$ for shot 1157 ($h_{res} = 5.83$ MJ/kg, $P_{res} = 47.2$ MPa) and $N_{Tr} = 6.5$ for shot 1156 ($h_{res} = 7.80$ MJ/kg, $P_{res} = 48.0$ MPa). Johnson et al. (1998) found values for N_{Tr} between 3.1 and 6.6 for a wider range of experiments from the same data set. MacLean et al. (2008) compared stability computations to reflected shock tunnel experiments with a 7° half-angle cone with $h_{res} = 2.5$ and 5 MJ/kg, and found N factors ranging from 4.9 to 6.8 with an average of 5.7.

Stability computations also exist for atmospheric flight tests on slender cones, though as Schneider (1999) points out the results of many flight tests are not available in the open literature. Test data from suborbital rocket flights have the additional complication that the test vehicle is often at an angle of attack and precessing or "coning" due to the difficulty of precisely controlling the attitude of the vehicle resulting from the pitching maneuver used to orient the vehicle axis to the flight path. Malik (2003) analyzed the 5° half-angle Reentry-F conditions described in Zoby and Wright (1977) at 100,000 ft altitude[5] and found $N_{Tr} = 8.1$ (for quasi-parallel flow assumptions) or $N_{Tr} = 9.5$ (for nonparallel flow assumptions) for finite rate chemistry. Li et al. (2011) computed the boundary layer stability properties of the 7° half-angle HIFiRE-1 flight test (Kimmel et al., 2007) and reported $N_{Tr} = 13.5$ for the portion of the ascent phase analyzed[6].

---

[4]Values taken from Figure 8 in Gronvall et al. (2010).

[5]The reason given by Malik (2003) for choosing this altitude for analysis was to minimize the nose radius and therefore bluntness effects, since ablation up to this point in the flight trajectory should have been minimal.

[6]HIFiRE-1 remained within approximately 0.5° of 0° angle of attack during the relevant portion of the ascent phase. During the re-entry phase, N_{Tr} between 9.5 and 14 were reported by Li et al. (2011), but these data are less relevant for comparison with the present study as the angle of attack was estimated at more than 6°.

5.2   Boundary Layer Transition Correlations

5.2.1 e^N Results and Damping Due to Vibrational Relaxation

The relative effects of vibrational rate processes in each experiment may be predicted by comparing frozen or "no vibration" and physically modeled or "vibration" PSE-Chem stability analyses for each case, as described in Section 4.3.1. For convenience, the following descriptors are used in reporting stability computation results in this chapter:

vibration (N_{Tr})
> These perturbation computations are intended to model the physical vibrational rate processes of the gas. Relaxation times are governed by the Millikan and White (1963) model with several empirical corrections for CO_2 given in Camac (1966) and Park et al. (1994). Specifically, the vibrational modes of CO_2 are modeled as a single degenerate vibrational mode with Camac (1966) rates. The STABL input files for the modified vibrational parameters are available in Appendix C of Wagnild (2012).

no vibration ($N_{TrNovib}$)
> These perturbation computations are intended to "freeze" the vibrational rate processes of the gas, as discussed in Section 4.3.1. The relevant Millikan and White parameter for each modeled rate process is set to a value several orders of magnitude higher than the physical case, which means that the rate processes are given characteristic times much longer than the relevant flow times. This technique has been used previously for T5 cases in Wagnild (2012) and Jewell et al. (2013c), and for investigating the role of vibrational relaxation in other high enthalpy transition experiments in Gronvall et al. (2014).

vibrational effects ($\Delta N_{Tr} = N_{TrNovib} - N_{Tr}$)
> ΔN_{Tr} is the difference between $N_{TrNovib}$ (computed with the "no vibration" model above) and N_{Tr} (computed with the "vibration" model above). ΔN_{Tr} is a measure of the contribution of vibrational relaxation to the computed stability for a given experiment. This metric has been used previously in Wagnild et al. (2012).

All computations discussed in this chapter use the finite-rate STABL chemistry models described in Appendix C of Wagnild (2012) and Section 4.3.1 of the present work for both the mean flow and the perturbations, to model the dissociated gas

flows typical of T5. Furthermore, all of the cases discussed in this chapter use the "vibration" model to compute the mean flow in DPLR, even when the "no vibration" model is used to compute the boundary layer stability in PSE-Chem. The "no vibration" model is used only to make perturbation stability computations for comparison to "vibration" stability computations.[7]

An example of this comparison is found in Jewell et al. (2013c), which presents computed N factor curves for a fully reacting boundary-layer stability analysis and a chemically reacting but vibrationally frozen boundary layer stability analysis for each case in a set of notional 10 MJ/kg, 50 MPa T5 conditions with freestream mixtures of air and CO_2. A reacting and vibrationally active ("vibration") mean flow computation was used in both cases. The vibrationally frozen ("no vibration") stability analysis predicted that adding carbon dioxide to the freestream should increase the N factor at every x-position along the surface of the cone, leading to earlier transition. When the vibrational rate processes were included in the stability analysis, Jewell et al. (2013c) found that the N factor at each x-position decreased with the addition of CO_2, and thus the predicted transition location x_{Tr} assuming a constant N_{Tr} moved further down the cone, due to carbon dioxide's ability to damp boundary layer disturbances at the relevant unstable frequencies. By calculating the change in expected transition location, the effectiveness of disturbance damping due to vibrational relaxation at each condition was determined. From these data, it was predicted that the damping ability of carbon dioxide should be most effective for higher enthalpy cases, while the addition of carbon dioxide for lower-enthalpy, lower-temperature ($h_{\mathrm{res}} \approx 5$ MJ/kg, $T^* \approx 1000$ K) cases should have a smaller effect on the N factor, and therefore the predicted transition location. In the latter case, there are two effects. The optimum disturbance damping frequency of carbon dioxide is no longer similar to the

---

[7]The "equilibrium" model discussed in Section 4.3.1 is not used in the present chapter, because it was found to produce similar stability results to the "no vibration" frozen model for the case in Section 4.3.1 and the cases in Appendix B.

boundary layer disturbance frequencies, and the degree of vibrational excitation of the molecules decreases with decreasing temperature. The relatively small effect of vibrational damping shown in Wagnild et al. (2012), which used the same method to compare the vibration and no vibration cases, is similarly due to the relatively low reservoir enthalpy of the flow considered in their study, approximately 4.5 MJ/kg.

(a) $N_{TrNovib}$ *vs.* $(x/\delta_{99})_{Tr}$

(b) N_{Tr} *vs.* $(x/\delta_{99})_{Tr}$
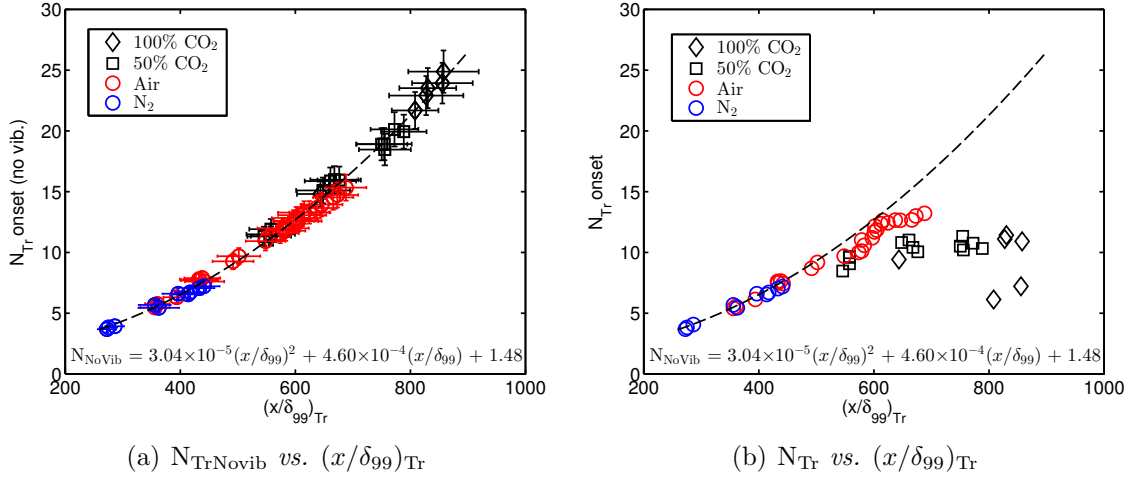
Figure 5.1: (a) N factor at transition computed with the no vibration model, with a fit of the data; (b) N factor at transition computed with the vibration model, with the no vibration fit repeated to highlight the difference and therefore the relative effect of vibrational relaxation on the stability and nondimensional transition length. The difference in N_{Tr} is large for CO_2, smaller for air, and insignificant for N_2.

Figure 5.1 presents results from the present study, in terms of computed N factor (N_{Tr}) at the experimentally measured transition onset location (x_{Tr}), from reacting boundary layer stability computations performed with PSE-Chem with physically modeled and frozen vibrational properties, plotted against $(x/\delta_{99})_{Tr}$. Figure 5.1(a) includes error bars based on the uncertainty in boundary layer transition onset location x_{Tr} and the calculated boundary layer thickness δ_{99}. Since δ_{99} is the length used to normalize the transition onset length, cases with thinner boundary layers have larger uncertainty in $(x/\delta_{99})_{Tr}$. The uncertainty on N factor at transition onset is an estimate based upon the variability in N factor observed for varying mean flow assumptions, discussed in Section 4.3.3. In subsequent plots in this chapter the error

bars are omitted for clarity, but the substantial uncertainty due to the intrinsically statistical nature of transition distance, as well as the issues discussed above, must be noted.

The data for all gas types collapse onto one curve for the no vibration case due to the inviscid nature of the instability and the relative unimportance of chemical reactions for stability in this regime. The results of Figure 5.1(a), computed without vibrational damping, predict values of $N_{Tr} > 12$ at the observed transition onset location when $(x/\delta_{99})_{Tr}$ exceeds 600, with values up to 25 at the extreme. These values are quite extraordinary and unprecedented; according to the results of Fedorov and Averkin (2010), calculated for cold-flow shock tunnel conditions at Mach 6.8, transition N factor values over 15 are inconsistent with physical reality as unavoidable kinetic fluctuations provide a noise floor even for an "absolutely quiet" free stream. With the inclusion of vibrational damping in Figure 5.1(b), the maximum values of N_{Tr} are now limited to much more realistic, although still large, values of 10–13. These results provide strong evidence of the essential role of vibrational relaxation in damping instabilities not only in carbon dioxide but also air.

The present approach differs from that of Johnson (2000), who compared vibration cases with cases that were frozen in terms of *both* vibration and chemistry, finding large effects in CO_2 cases and much smaller effects in air cases. The present approach is intended to isolate the effects of translational-vibrational energy exchange. A fit of the vibrationally frozen curve is also reproduced on the plot with vibrational effects. The departure from this curve for each data point is an indication of the relative importance of vibrational effects for each case.

The computed transition N factors vary widely, from 3.7 to 13.2. The range for air is $N_{Tr} = 5.4$–13.2, the lower end of which agrees with previous computations of T5 conditions, including Johnson et al. (1998) and Gronvall et al. (2010), but the upper range of which exceeds any previously computed shock tunnel transition results. One

possible explanation for the very high transition N factor results, which are more typical of "quiet" tunnels (Schneider, 2008a), is the strong unit Reynolds number effect discussed below in Section 5.2.2.1. This may be linked with the mismatch between the strongest noise frequencies in the T5 freestream and the second mode frequencies preferentially amplified by the boundary layer. Laser differential interferometry performed recently by Parziale et al. (2014) indicated that RMS density fluctuations in the T5 freestream are as high as 3.3% for typical conditions with a bandpass filter with a short cutoff of 700 µm and a long cutoff of 100 mm. However, with a bandpass filter with a short cutoff of 700 µm and a long cutoff of 10 mm, much more relevant for the range of wavelengths preferentially amplified by the hypervelocity boundary layer in the present study, RMS density fluctuations not greater than 0.5% (with a minimum of 0.26%) were observed in all cases. For comparison, Juliano and Schneider (2010) report fluctuations of 3.0% as typical for conventional tunnels, 0.05% for free flight, and 0.10% as the upper threshold for "quiet" tunnels.

It it is observed that all of the N_2 points and many of the air points are similarly insensitive to vibrational energy exchange, while most of the 50% CO_2 cases and all of the 100% CO_2 cases show large vibrational damping effects. In nondimensionalized terms this effect extends the maximum observed $(x/\delta_{99})_{\text{Tr}}$ to 858 for CO_2, which is 25% higher than the maximum air $(x/\delta_{99})_{\text{Tr}}$ of 688. This CO_2 case, in the absence of vibrational effects, would have had $N_{\text{Tr}} = 25$ at the measured transition onset location, which as noted earlier is physically impossible (Fedorov and Averkin, 2010, Fedorov, 2011b). The maximum observed $(x/\delta_{99})_{\text{Tr}}$ was 789 for 50% CO_2, which is 15% higher than the maximum for air.

Figure 5.2(a) demonstrates that the difference between vibrational and non-vibrational computed N factor depends strongly upon the Dorrance reference temperature, T^*, as well as the type of molecule. This can be understood by considering the effects of molecular composition and temperature on the damping due to vibrational relax-

(a) ΔN_{Tr} *vs.* T^*

(b) Fujii absorption *vs.* T^*
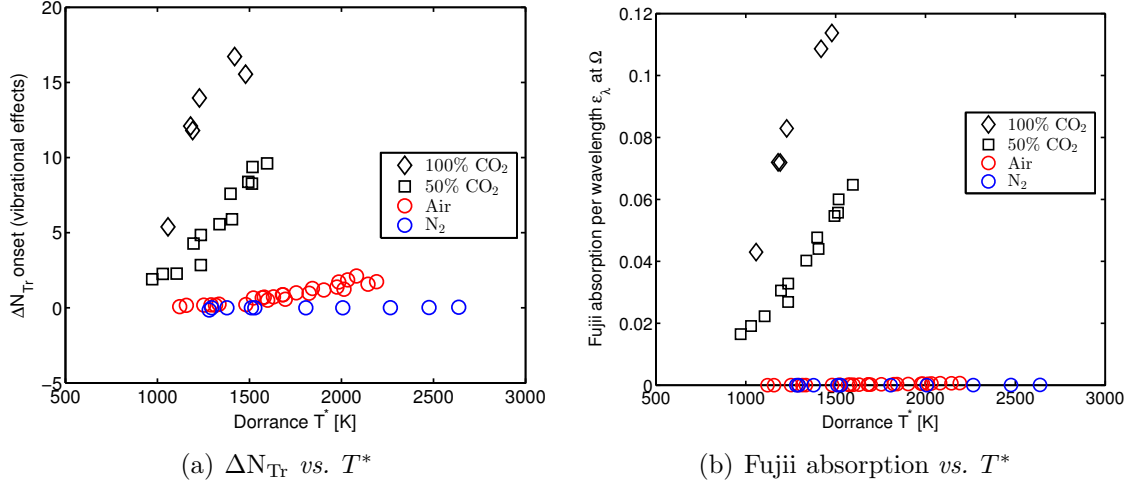
Figure 5.2: (a) The difference in N factor at transition between PSE-Chem computations made with the vibration and no vibration models, plotted against the Dorrance reference temperature; (b) Acoustic absorption rate (per wavelength) due to vibrational relaxation of Fujii and Hornung (2001), computed at T^* for the PSE-Chem-predicted most-amplified frequency Ω at transition for each case, plotted against the Dorrance reference temperature.

ation. The damping due to vibrational relaxation was calculated using the method of Fujii and Hornung (2001) and is shown in Figure 5.2(b). The absorption per unit wavelength due to vibrational-translational relaxation was evaluated at the Dorrance reference conditions for acoustic wave propagation in stationary gas.

The present results are consistent with those of Wagnild (2012). Wagnild showed that for T5 conditions, CO_2 and air boundary layers exhibit some degree of vibrational damping, with more damping present in CO_2 due to a substantial fraction of vibrationally excited CO_2 molecules for all the cases examined. Wagnild found that the relaxation times τ associated with N_2 are much too long to affect the stability characteristics of the boundary layer on a 1 m cone, since they are on the order of 10 cone flow times. Therefore Wagnild found essentially no effect for N_2 boundary layers up to 5000 K. For air and nitrogen, damping is negligible as compared to mixtures with carbon dioxide (Figure 5.2(b)). As a consequence, at comparable reference temperatures, there is a much stronger effect of vibrational relaxation on

N_{Tr} (Figure 5.2(a)) for CO_2 than for N_2 and air. The effect of molecular composition can be understood as being due to the two main effects important to damping processes: occupation of molecular vibration states and the characteristic time for translational-vibrational relaxation. At a given temperature, air and N_2 have much lower vibrational populations than CO_2 due to the higher characteristic vibrational temperatures of air and N_2 in comparison to CO_2. Therefore, at a given pressure and temperature, the vibration relaxation times in air and N_2 are much longer than those of CO_2 and most importantly, much longer than the characteristic periods of the second mode oscillations.

The procedure of Fujii and Hornung (2001) for estimating the absorption of acoustic waves perturbing high temperature gas is used to compare stationary gas absorption per wavelength to ΔN_{Tr}, as previously implemented in Wagnild (2012). The Fujii code is run with the composition and pressure at the edge of the boundary layer as computed by DPLR, but with all of the fluid properties and rates evaluated at the Dorrance reference temperature. The mean flow in the boundary layer is therefore in chemical nonequilibrium[8] (*i.e.*, the gas is in the highly dissociated state computed by DPLR). The mean flow is also assumed to be in thermal equilibrium (*i.e.*, $T = T_v$, with both set at T^*) which, as shown in Section 2.6 and Appendix B, may be a reasonable assumption for CO_2 and air conditions but is very inaccurate for N_2 cases.

Rate processes for chemical reaction and vibrational-translational energy exchange are both modeled in the absorption calculation. Following Fujii and Hornung (2001), the chemical model used is that of Lordi et al. (1966), which is given in Table 5.1. The vibrational-translational exchange rates are calculated as suggested by Millikan and White (1963) for air species and Camac (1966) for CO_2. The vibrational-translational model constants are given in Table 5.2.

---

[8]Note that all of the results presented in Fujii and Hornung (2001) are for gases with a mean flow state of chemical equilibrium. However, Fujii's code may also be used for chemically frozen gas by changing one variable. This more closely approximates both the physical experiment and the STABL/PSE-Chem computations.

| Third body | C_f | η_f | Θ_f |
	$\mathrm{m^3/mol \cdot s}$		K
N$_2$ case			

$N_2 \rightleftharpoons 2N$			
N$_2$	2.30×10^{23}	-3.5	113261.
N	8.50×10^{19}	-2.5	113261.

Air case			

$N_2 \rightleftharpoons 2N$			
N$_2$	2.30×10^{23}	-3.5	113261.
N	8.50×10^{19}	-2.5	113261.
the others	9.90×10^{14}	-1.5	113260.
$O_2 \rightleftharpoons 2O$			
O$_2$	3.60×10^{15}	-1.5	59390.
O	2.10×10^{12}	-0.5	59390.
the others	1.20×10^{15}	-1.5	59390.
$NO \rightleftharpoons N + O$			
all species	5.20×10^{15}	-1.5	75500.
$O_2 + N \rightleftharpoons O + NO$			
none	1.00×10^6	0.5	3625.
$N_2 + O \rightleftharpoons N + NO$			
none	5.00×10^7	0.0	38020.
$N_2 + O_2 \rightleftharpoons 2NO$			
none	9.10×10^{18}	-2.5	65010.

CO$_2$ case			

$CO_2 \rightleftharpoons CO + O$			
all species	2.88×10^5	0.5	37655.
$2CO \rightleftharpoons CO_2 + C$			
none	2.33×10^3	0.5	65694.
$CO + O_2 \rightleftharpoons CO_2 + O$			
none	1.60×10^7	0.0	20640.
$CO \rightleftharpoons C + O$			
CO	1.76×10^{24}	-3.52	128751.
O	1.29×10^{25}	-3.52	128751.
the others	8.79×10^{23}	-3.52	128751.
$O_2 \rightleftharpoons 2O$			
O$_2$	2.75×10^{13}	-1.0	59754.
O	2.10×10^{12}	-0.5	59382.
the others	2.55×10^{12}	-1.0	59754.
$CO + O \rightleftharpoons O_2 + C$			
none	2.73×10^5	0.5	69520.

Table 5.1: Chemical reaction rate model from Lordi et al. (1966), as implemented and more fully described in Fujii and Hornung (2001). The air/CO$_2$ mixture computation combined the models for those gases.

	MW	$\sigma\Theta_{\text{rot}}$	h_f^o	g_{v}	Θ_{v}	g_{e_o}	g_{e_i}	ϵ_{e}
	g/mol	K	J/mol		K			J/mol
N_2	28.016	5.79	0.0	1	3353.2	1	3	6.015×10^5
							6	7.136×10^5
							1	7.342×10^5
O_2	32.000	4.16	0.0	1	2239.0	3	2	9.225×10^4
							1	1.579×10^5
							3	4.320×10^5
							3	5.960×10^5
N	14.008	—	4.713×10^5	—	—	4	6	2.301×10^5
							4	2.308×10^5
							6	3.452×10^5
							12	9.971×10^5
O	16.000	—	2.468×10^5	—	—	5	3	1.903×10^3
							1	2.717×10^3
							5	1.899×10^5
							1	4.044×10^5
							5	8.829×10^5
NO	30.008	2.45	8.990×10^4	1	2699.2	4	2	5.262×10^5
							4	5.496×10^5
CO_2	44.011	1.13	-3.933×10^5	2	960.1	1		
				1	1992.5			
				1	3380.2			
CO	28.011	2.78	-1.139×10^5	1	3082.0	1	6	5.824×10^5
							3	6.687×10^5
							6	7.453×10^5
							2	7.785×10^5

Table 5.2: Vibrational-translational model as suggested by Millikan and White (1963) for air species and Camac (1966) for CO_2, as implemented and more fully described in Fujii and Hornung (2001).

The frequency chosen for the Fujii analysis is Ω_{Tr}, which is the most amplified frequency computed by PSE-Chem at the transition onset location for each case. The results are presented in Figure 5.2(b), and also in Figure 5.3, which shows a near-monotonic trend in ΔN_{Tr} with Fujii absorption per wavelength, and also in T^* within each gas type. This is consistent with the hypothesis that the varying boundary layer stability properties for each gas type in this flow regime are primarily due to vibrational relaxation.

(a) ΔN_{Tr} *vs.* Fujii absorption   (b) T^* *vs.* Fujii absorption
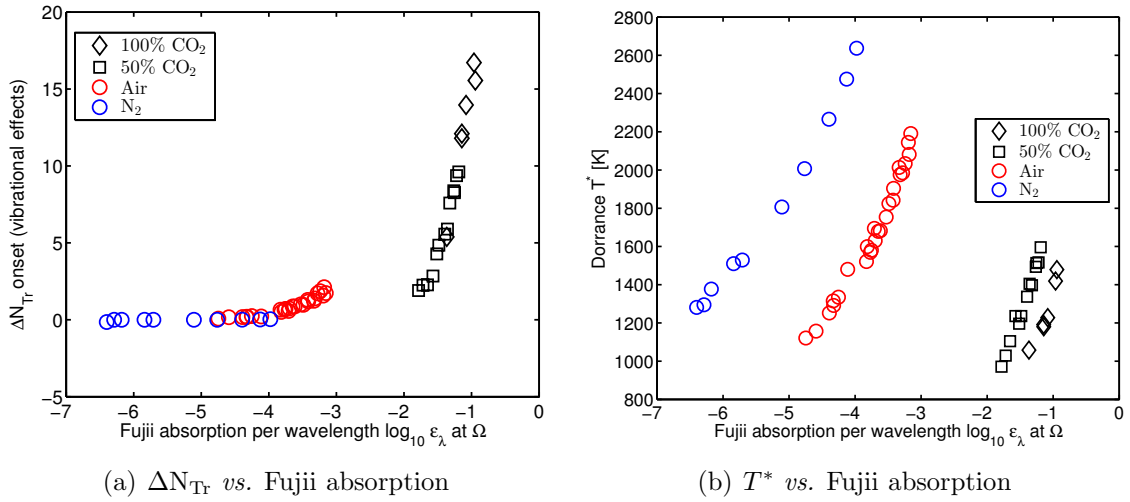
Figure 5.3: Fujii and Hornung (2001) absorption per wavelength computed at the PSE-Chem-predicted most amplified frequency at transition Ω_{Tr} for each condition in the present study, compared with (a) ΔN_{Tr}; and (b) T^*. Note the log scale on the abscissa: while absorption per wavelength increases monotonically with reference temperature for all gas types, the magnitude of the absorption for air and N_2 is still two or more orders of magnitude lower than the absorption predicted for the CO_2 and 50% CO_2 cases.

5.2.2 Reynolds Numbers

It is desirable to make a brief comparison of the present results with the more traditional correlations of transition location with Reynolds numbers that have been used in previous T5 studies and other hypersonic transition experiments. An in-depth statistical evaluation of the present results in these terms, and a re-evaluation of past T5

studies by the same method, follows below in Sections 5.3.1 and 5.3.2, respectively.

White (1991) Equation 7-45 provides a semi-empirical formula relating the nondimensional boundary layer thickness on a flat plate with edge Mach number, edge Reynolds number, ratio of specific heats, adiabatic wall temperature ratio, and the Chapman-Rubesin parameter $C_\mathrm{w} = \rho_\mathrm{w}\mu_\mathrm{w}/\rho_\mathrm{e}\mu_\mathrm{e} \approx (T_\mathrm{w}/T_\mathrm{e})^{-1/3}$. Including a factor of $\sqrt{3}$ to adapt the solution to axisymetric conical flow and rearranging for x/δ_{99} yields:

$$\frac{x}{\delta_{99}} \approx \frac{\sqrt{3}\sqrt{\mathrm{Re}_x}}{\sqrt{C_\mathrm{w}}\left[5.0 + (0.2 + 0.9T_\mathrm{w}/T_\mathrm{aw})(\gamma - 1)\,\mathrm{M}_\mathrm{e}^2\right]} \tag{5.1}$$

This relationship is plotted against $(x/\delta_{99})_\mathrm{Tr}$ in Figure 5.4. White comments that the accuracy of Equation (5.1) "is adequate, if unspectacular". It appears that for the present set of T5 cases, the relationship is improved by including an additional coefficient of $\sim 1/0.59$:

$$\frac{x}{\delta_{99}} \approx \frac{\sqrt{3}\sqrt{\mathrm{Re}_x}}{0.59\sqrt{C_\mathrm{w}}\left[5.0 + (0.2 + 0.9T_\mathrm{w}/T_\mathrm{aw})(\gamma - 1)\,\mathrm{M}_\mathrm{e}^2\right]} \tag{5.2}$$

Here, $T_\mathrm{w}/T_\mathrm{aw}$ is the equilibrium adiabatic wall temperature calculated with Cantera as described in Section 3.1.2.

$(x/\delta_{99})_\mathrm{Tr}$ correlates with both $\mathrm{Re}_\mathrm{Tr}^*$ (calculated at Dorrance reference conditions) and Re_Tr (calculated at boundary layer edge conditions), as shown in Figure 5.5. A power law fit of the results, using the MATLAB fit function, yields an exponent of 0.71 (95% confidence interval: 0.67 to 0.75) for Re_Tr and 0.42 (95% confidence interval: 0.41 to 0.44) for $\mathrm{Re}_\mathrm{Tr}^*$. The latter value is quite close to the exponent of 0.5 predicted by Equation (5.1). Past studies, including Adam and Hornung (1997) and Germain (1993), have reported results in terms of reservoir enthalpy, h_res, finding delays with increasing enthalpy and greater delays for carbon dioxide than air. Instead of reservoir enthalpy, we use the Dorrance reference temperature as a measure of the flow energy. In Figure 5.6 the dependence of $\mathrm{Re}_\mathrm{Tr}^*$ and $(x/\delta_{99})_\mathrm{Tr}$ on T^* are presented. As anticipated
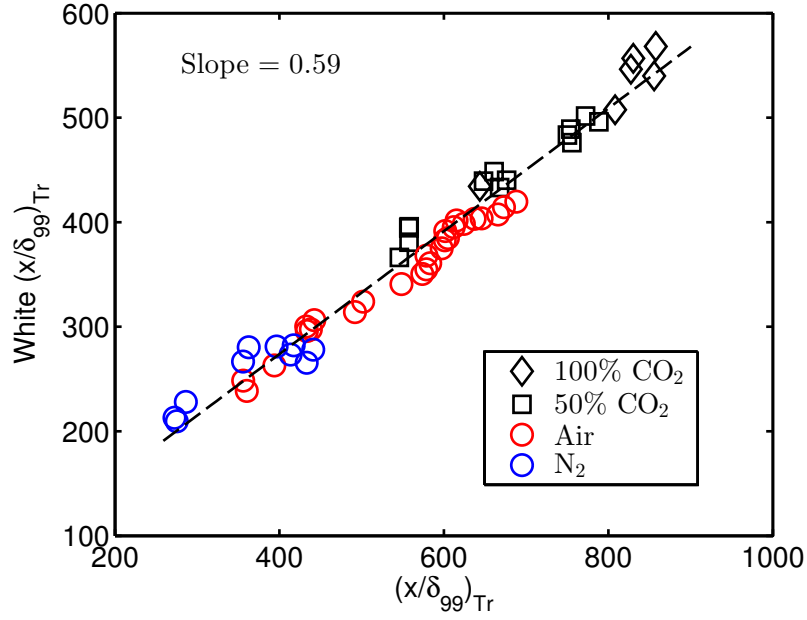
Figure 5.4: Comparison of $(x/\delta_{99})_{\mathrm{Tr}}$ with Equation (5.1), the semi-empirical nondimensional boundary layer thickness from White (1991). The linear fit has a slope of 0.59.

from the previous discussion on damping, the gas type has the most profound influence on the values of the boundary layer parameters at transition, and the correlation with T^* is relatively weak. As shown in Figure 5.7, T^* varies linearly with h_{res} across all gas types, so this comparison is comparable to previous presentations reported in terms of reservoir enthalpy.
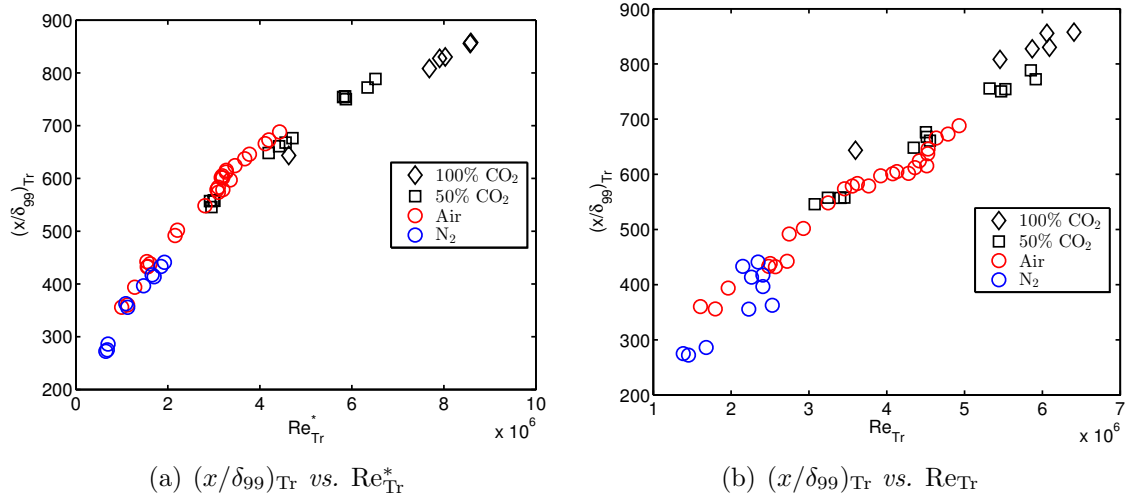
Figure 5.5: $(x/\delta_{99})_{\mathrm{Tr}}$ is an increasing function of (a) $\mathrm{Re}_{\mathrm{Tr}}^*$; and (b) $\mathrm{Re}_{\mathrm{Tr}}$.
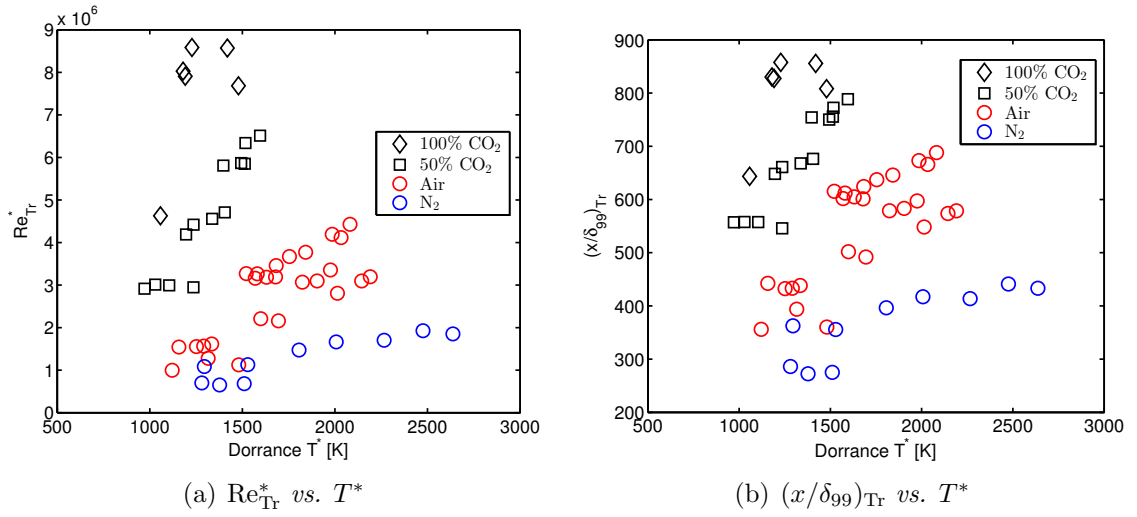
Figure 5.6: (a) $\mathrm{Re}_{\mathrm{Tr}}^*$; and (b) $(x/\delta_{99})_{\mathrm{Tr}}$ values for the experimental data in terms of T^*. As T^* varies linearly with h_{res} across all gas types, as shown in Figure 5.7, this relationship is similar to past results presented in terms of enthalpy, including those of Adam and Hornung (1997) and Germain (1993).
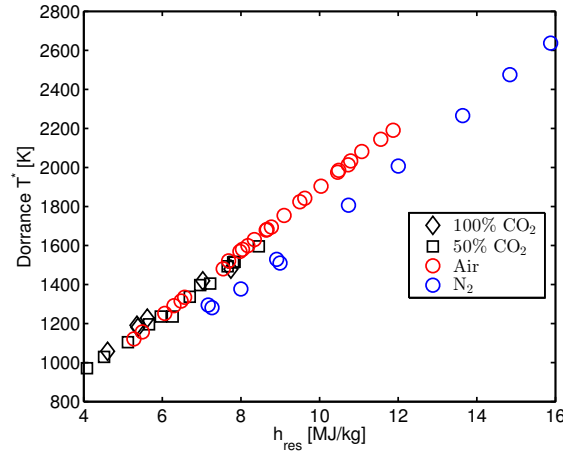
Figure 5.7: T^* has a linear relationship with h_{res} that holds across all gas types. The apparent discrepancy for N_2 is due to the way T^* is calculated, using only the translational temperature of the gas. For the air and CO_2 cases, this is similar to the vibrational temperature, but as shown in Appendix B, N_2 flows in T5 boundary layers have a significant degree of vibrational nonequilibrium, with the vibrational energy being much higher than the value it have in equilibrium due to freezing of vibrational-translational relaxation in the nozzle. As a consequence, the calculated Dorrance reference temperature is lower than would be expected at a given reservoir enthalpy and this is reflected in the lower values of T^*.

5.2.2.1 Unit Reynolds Number Effect

Past investigators have identified a so-called "unit Reynolds number effect", which is the name given to variations in the nondimensional parameter $\mathrm{Re}_{\mathrm{Tr}}$ observed in ground testing facilities. This effect makes it difficult to compare between results acquired in different facilities as well as to extrapolate to atmospheric flight conditions. Morkovin (1988) points out that this "pernicious nonconstancy of $\mathrm{Re}_{\mathrm{Tr}}$" is not in general the result of any single phenomenon, but rather the cumulative effect of the nonideal aspects of wind-tunnel experiments, with contributors including sound radiated from supersonic nozzles and sidewalls, freestream disturbances, roughness, and leading-edge geometry. Schneider (2001) reviews the disparate unit Reynolds number effects found in the literature from a number of supersonic and hypersonic experiments, and hypothesizes that the major contributor to the effect in this flow regime is radiated noise from turbulent boundary layers on the nozzle wall. Schneider (2008a) proposed that tunnels specially designed to eliminate this radiated noise might mitigate the unit Reynolds number effect.

Like most hypersonic ground-test transition data, the present results reveal a strong unit Reynolds number effect on the transition Reynolds number (see Pate (1971), Schneider (2001), and more recently Wagner et al. (2011) and Wagner et al. (2013)). These results are presented in Figure 5.8(a). This effect is also present for other relevant transition parameters, including $(x/\delta_{99})_{\mathrm{Tr}}$ (Figure 5.9(a)) and N_{Tr} (Figure 5.10(a)), and is also observed if the data are plotted in terms of unit Re^{*} (Figures 5.8(b), 5.9(b), and 5.10(b)). There is a small variation of x_{Tr} observed in the present study (0.389 to 0.758 m), limited by the geometry of the cone, the test conditions, and the selection of conditions with clear transition onset. The cone was instrumented only between 0.221 and 0.942 m (see Table 3.1). The maximum and minimum observable values of $\mathrm{Re}_{\mathrm{Tr}}$ based upon these limits are included in Figure 5.8(a). A linear fit indicates that the the transition Reynolds number is proportional to the

unit Reynolds number with a constant of proportionality of 0.57 (95% confidence interval: 0.50 to 0.63).

Schneider (2001) observed that quiet tunnel results should show less dependence on unit Re through reduction of the noise radiated from the nozzle wall. However, whether this effect holds for high enthalpy flows with vibrationally relaxing CO_2 is unknown. No comparable results for CO_2 were found in the literature, and the freestream noise measurements of Parziale et al. (2014), discussed above with respect to air, did not include any CO_2 or 50% CO_2 cases.

(a) Re_{Tr} vs. unit Re

(b) Re_{Tr}^* vs. unit Re^*
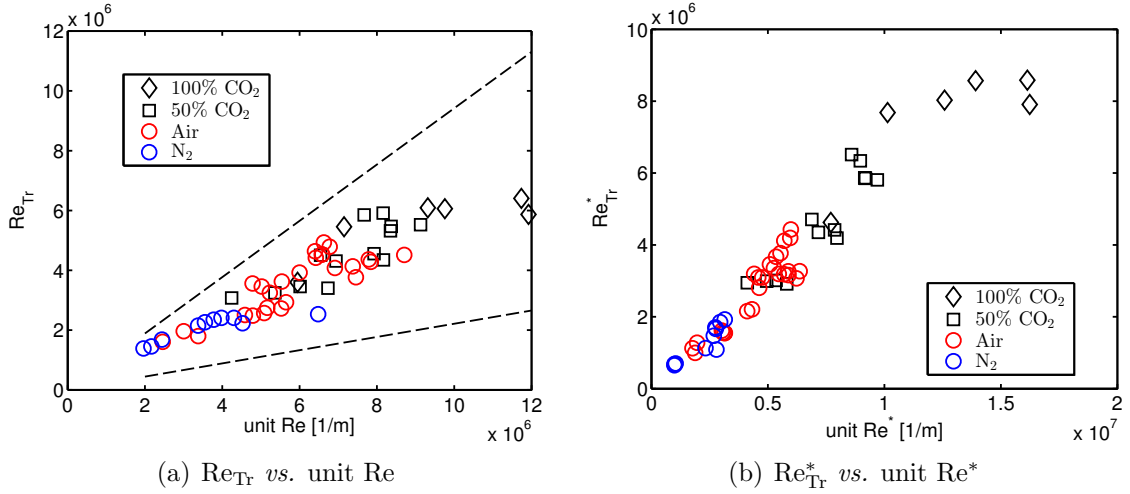
Figure 5.8: The unit Reynolds number effect on transition onset Reynolds number is identified in the present study both when physical properties are evaluated at (a) the boundary layer edge; and (b) Dorrance reference conditions.

It is widely thought (Pate and Schueler, 1969, Schneider, 2001) that an important driver of the unit Reynolds number effect is noise radiated from the boundary layer which forms on the wall of a supersonic nozzle, and the present data are consistent with this conclusion. Figure 5.11(a) presents the most amplified frequency (Ω_{Tr}) computed by STABL at the observed point of transition in terms of the boundary thickness δ_{99} at the same location. Thicker boundary layers result in a lower most amplified second mode frequency, as predicted by Equation (1.1). Figure 5.11(b) shows the relationship between Ω_{Tr} and nondimensionalized transition onset length,

(a) $(x/\delta_{99})_{\rm Tr}$ vs. unit Re

(b) $(x/\delta_{99})_{\rm Tr}$ vs. unit Re*
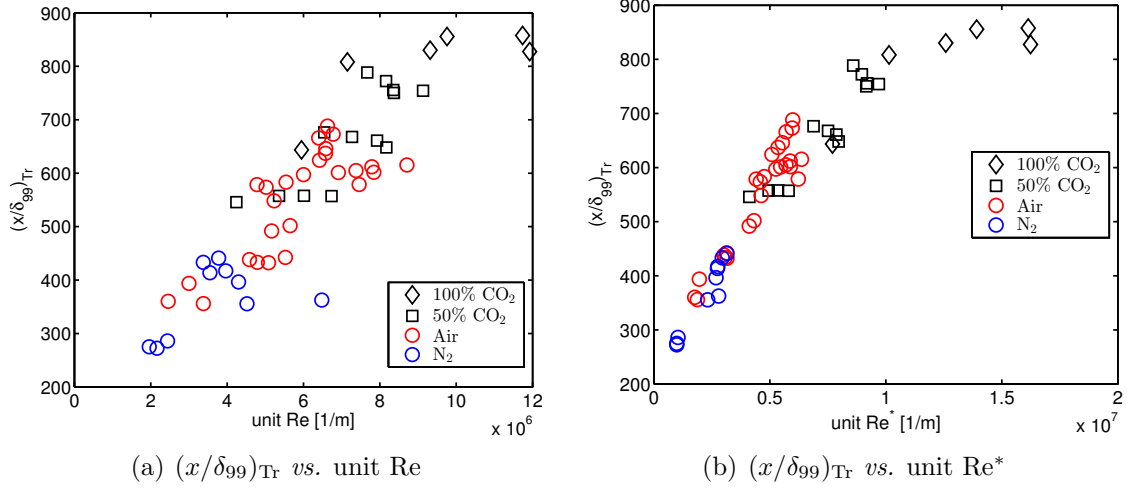
Figure 5.9: The unit Reynolds number effect on nondimensionalized transition onset length $(x/\delta_{99})_{\rm Tr}$ is identified in the present study both when physical properties are evaluated at (a) the boundary layer edge; and (b) Dorrance reference conditions.

(a) $N_{\rm Tr}$ vs. unit Re

(b) $N_{\rm Tr}$ vs. unit Re*
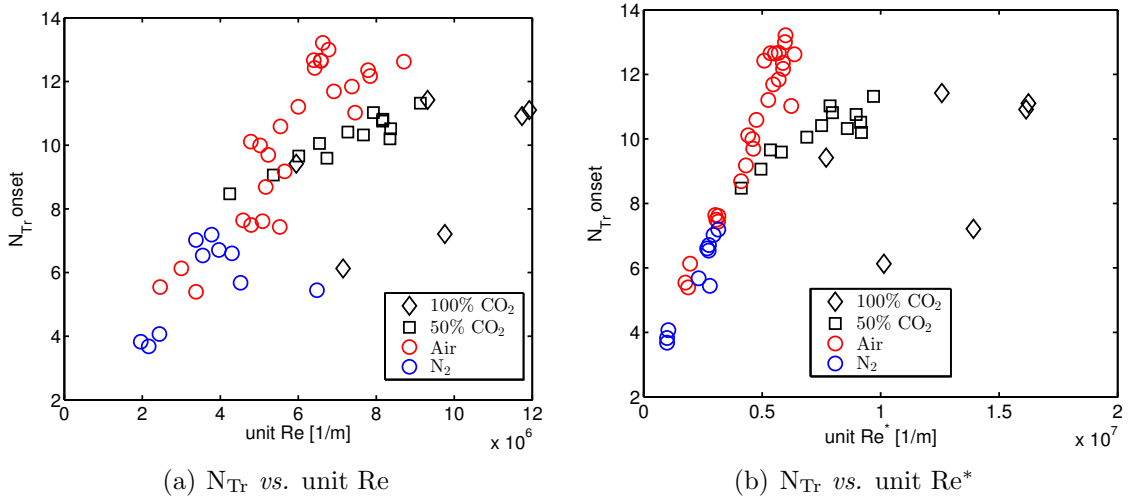
Figure 5.10: The unit Reynolds number effect on disturbance amplification rate at transition onset, $N_{\rm Tr}$, as computed by PSE-Chem, is identified in the present study both when physical properties are evaluated at (a) the boundary layer edge; and (b) Dorrance reference conditions.

$(x/\delta_{99})_{\rm Tr}$. With similar $\Omega_{\rm Tr}$, the normalized transition onset position is further downstream for CO_2 cases than it is for air or N_2 experiments. Parziale et al. (2014) showed that most of the noise in the T5 freestream is at relatively low frequencies (< 500 kHz), and observed a decrease in RMS density fluctuations with increasing frequency. This observation is consistent with the present results, which show a shorter

nondimensional transition onset length for lower computed most amplified frequencies at transition, Ω_{Tr}.

(a) Ω_{Tr} *vs.* $\delta_{99\text{Tr}}$ (b) $(x/\delta_{99})_{\text{Tr}}$ *vs.* Ω_{Tr}
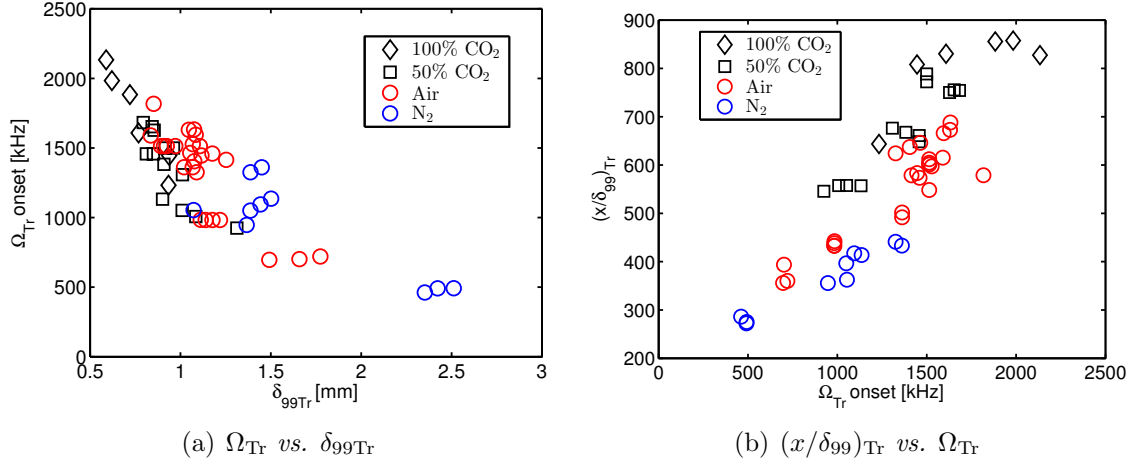
Figure 5.11: (a) Most amplified frequency (Ω_{Tr}) computed by STABL at the observed point of transition in terms of the boundary layer thickness at transition; and (b) the relationship between normalized transition onset length, $(x/\delta_{99})_{\text{Tr}}$, and most amplified frequency (Ω_{Tr}). Most amplified frequency varies inversely with boundary layer thickness as predicted by Equation (1.1). For equivalent values of Ω_{Tr}, experiments in both 100% and 50% CO_2 tend to transition later than air or N_2 experiments in terms of nondimensionalized transition onset distance $(x/\delta_{99})_{\text{Tr}}$.

5.3 Analysis for Comparison with Past Studies[9]

5.3.1 Statistical Analysis

Multivariable linear regression analysis is performed on the present data sets with the MATLAB Statistics Toolbox, taking $\bar{P}_{\text{res}}$ and $\bar{h}_{\text{res}}$ (normalized by each data set's maximum pressure and enthalpy) as the possible predictor variables and the measured values of x_{Tr} (normalized by the length of the cone, 1 m), Re^*_{Tr} and Re_{Tr} (normalized by the respective maximum unit Reynolds numbers) as the modeled variables:

$$x_{\text{Tr}} \sim x_{\text{Tr}}(\bar{P}_{\text{res}}, \bar{h}_{\text{res}})$$

$$\bar{\text{Re}}^*_{\text{Tr}} \sim \bar{\text{Re}}^*_{\text{Tr}}(\bar{P}_{\text{res}}, \bar{h}_{\text{res}})$$

$$\bar{\text{Re}}_{\text{Tr}} \sim \bar{\text{Re}}_{\text{Tr}}(\bar{P}_{\text{res}}, \bar{h}_{\text{res}})$$

We use a significance level of 5% (*i.e.*, requiring a *p*-value less than 0.05 to reject the null hypothesis that a given coefficient is zero). The linear model coefficients that result from this analysis, along with their respective *p*-values, are presented in Tables 5.3 and 5.4.

---

[9]Portions of this section are adapted from Jewell et al. (2013a) and Jewell et al. (2013b).

	x_{Tr}	$\bar{\mathrm{Re}}^*_{\mathrm{Tr}}$	$\bar{\mathrm{Re}}_{\mathrm{Tr}}$
P_{res} coefficient	**-0.45396**	**0.30819**	**0.29023**
p-value	1.20×10^{-5}	5.88×10^{-6}	7.89×10^{-7}
$\bar{h}_{\mathrm{res}}$ coefficient	**0.55527**	-0.02805	**-0.26922**
p-value	2.36×10^{-5}	0.44139	1.02×10^{-5}

Table 5.3: Multivariable linear regression analysis for N_2 results ($n = 10$) from the present study. P_{res} and h_{res} are normalized by their respective maximum values. The coefficients found to be statistically significant ($p < 0.05$) are in bold print.

	x_{Tr}	$\bar{\mathrm{Re}}^*_{\mathrm{Tr}}$	$\bar{\mathrm{Re}}_{\mathrm{Tr}}$
P_{res} coefficient	-0.13756	**0.58589**	**0.54234**
p-value	0.1017	6.40×10^{-10}	2.55×10^{-10}
$\bar{h}_{\mathrm{res}}$ coefficient	**0.5395**	-0.03401	**-0.28113**
p-value	1.84×10^{-4}	0.7000	0.00132

Table 5.4: Multivariable linear regression analysis for air results ($n = 26$) from the present study. P_{res} and h_{res} are normalized by their respective maximum values. The coefficients found to be statistically significant ($p < 0.05$) are in bold print.

	x_{Tr}	$\bar{\mathrm{Re}}^*_{\mathrm{Tr}}$	$\bar{\mathrm{Re}}_{\mathrm{Tr}}$
P_{res} coefficient	**-0.32302**	0.35653	0.33112
p-value	6.40×10^{-10}	0.03906	0.05035
$\bar{h}_{\mathrm{res}}$ coefficient	**0.63747**	0.04081	-0.04116
p-value	0.01711	0.80118	0.80495

Table 5.5: Multivariable linear regression analysis for CO_2 results ($n = 6$) from the present study. P_{res} and h_{res} are normalized by their respective maximum values. The coefficients found to be statistically significant ($p < 0.05$) are in bold print. Due to the small sample size for this set of results, the overall F-statistic p-values for the $\bar{\mathrm{Re}}^*_{\mathrm{Tr}}$ ($p = 0.056$) and $\bar{\mathrm{Re}}_{\mathrm{Tr}}$ ($p = 0.088$) models indicate that they are only marginally significant when compared against a model with coefficients of zero.

	x_{Tr}	$\bar{\mathrm{Re}}^*_{\mathrm{Tr}}$	$\bar{\mathrm{Re}}_{\mathrm{Tr}}$
$\bar{P}_{\mathrm{res}}$ coefficient	**-0.34698**	**0.44541**	**0.42017**
p-value	1.67×10^{-4}	1.20×10^{-6}	7.39×10^{-7}
$\bar{h}_{\mathrm{res}}$ coefficient	**0.85361**	**0.19304**	-0.01432
p-value	3.91×10^{-6}	0.01806	0.81970

Table 5.6: Multivariable linear regression analysis for 50% CO_2 results ($n = 13$) from the present study. P_{res} and h_{res} are normalized by their respective maximum values. The coefficients found to be statistically significant ($p < 0.05$) are in bold print.

5.3.2 Statistical Comparison with Past Work

Datasets in air ($n = 22$), CO_2 ($n = 15$), and N_2 ($n = 11$) from shots referenced by Adam (1997) and Adam and Hornung (1997) are presented in Tables 5.7, 5.8, and 5.9, respectively. Some of these experiments were performed by, and first referenced in, Germain (1993) and Germain and Hornung (1997). Observed transition onset location x_{Tr} is reproduced here as reported in Adam (1997), but the other parameters have been recalculated by the present methods, described in Chapters 2 and 3, for consistency. In the case of Re^*/m for Dorrance reference conditions, δ_{99Tr}, and f_{Tr}, the parameters have been calculated here for the first time.
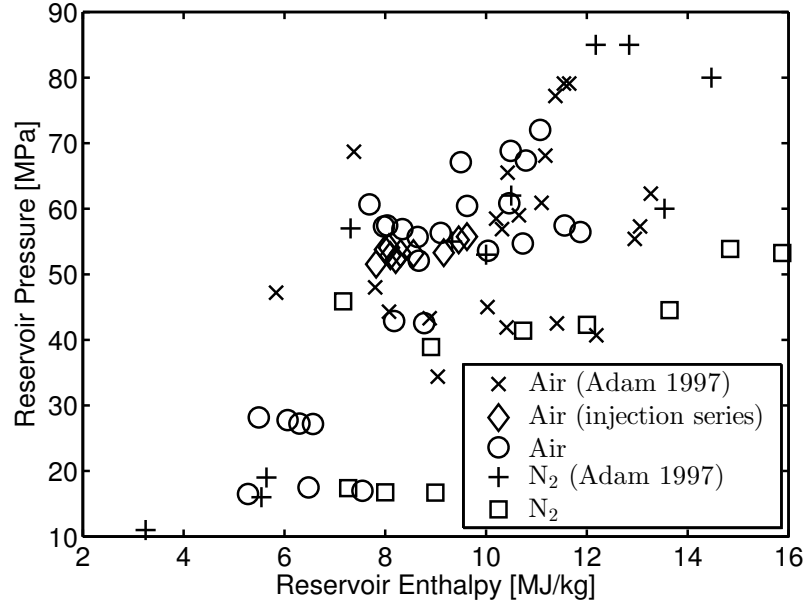
Figure 5.12: Tunnel operating parameters h_{res} and P_{res} for the present studies in air and N_2, compared with past conditions from Adam and Hornung (1997) and the injection experiments described in Chapter 7 and Jewell et al. (2011).

The tunnel parameters for which transition onset was observed during the present studies in air and nitrogen are compared with those of two past data sets in air and nitrogen in Figure 5.12. The present work both overlaps and extends the parameters of the past studies, including those performed for the injection work described in Chapter 7, especially for low pressure and enthalpy. As described in Section 3.2,

there is a significant correlation between the reservoir enthalpy and pressure for the T5 operating envelope. The R^2 values for the correlation between the two parameters are, respectively, 0.52 and 0.64 for conditions represented in the present N_2 and Air data sets, and 0.10, 0.82, and 0.59, respectively, for the Adam and Hornung (1997) air and N_2, and Jewell et al. (2011)/Chapter 7 data sets. This correlation is important to recognize because it necessitates careful statistical analysis before any trend may be attributed to h_{res} or P_{res} separately.
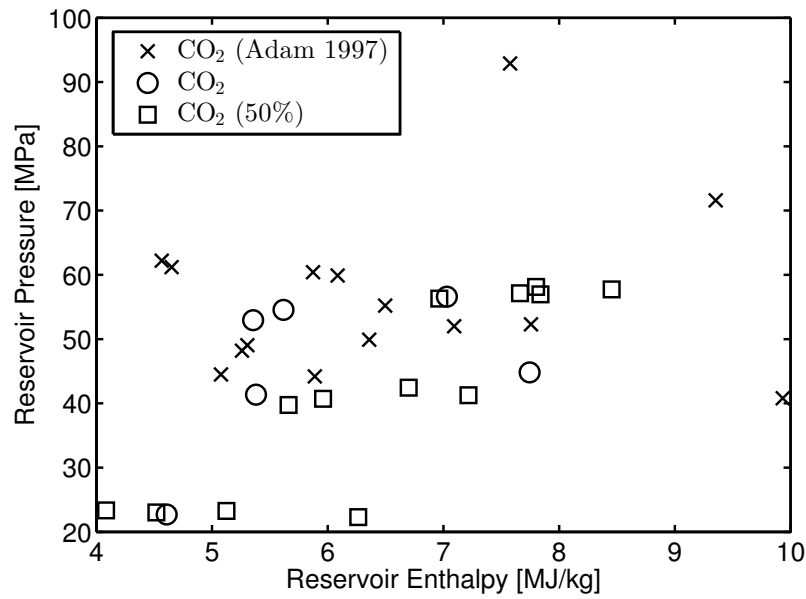
Figure 5.13: Tunnel operating parameters h_{res} and P_{res} for the present studies in CO_2 and 50% CO_2, compared with past CO_2 conditions from Adam and Hornung (1997).

The tunnel parameters for which transition onset was observed during the present studies in CO_2 and 50% air/CO_2 mixtures are compared with those of past data sets in CO_2 in Figure 5.13. The present work overlaps the past studies with the exception of the upper range of reservoir pressure and enthalpy, and extends the parameters of the past studies in the lower range of reservoir pressure. It should be noted that equivalent higher-enthalpy CO_2 tests were undertaken for the present work, as well (see Appendix A for the full list of run conditions), but no transition was observed by the end of the cone for those cases, even though transition was observed on the cone

for the equivalent historical cases. This is believed to be due to the more intensive tunnel cleaning procedure described in Section 2.1.3. The R^2 values for the correlation between the two parameters are, respectively, 0.24 and 0.77 for conditions represented in the present CO_2 and 50% air/CO_2 data sets, and 0.02 for the Adam and Hornung (1997) CO_2 data set.

For consistency with previously reported results, in these comparisons freestream conditions are taken as the conditions at the nozzle exit. The 100:1 area ratio contoured nozzle is designed to operate at Mach 6. Because the shape is optimized for a single condition, there is significant variation of the exit Mach number over the range of possible tunnel operating parameters, presented in Figure 5.14 for air over the conditions of both past and present work. The range of Reynolds numbers evaluated at the boundary layer edge and Dorrance (1962) reference temperature, which is used as representative of conditions within the boundary layer, over the same range is presented for air in Figure 5.15. The historical results from Tables 5.7, 5.8, and 5.9 are also analyzed as described above.
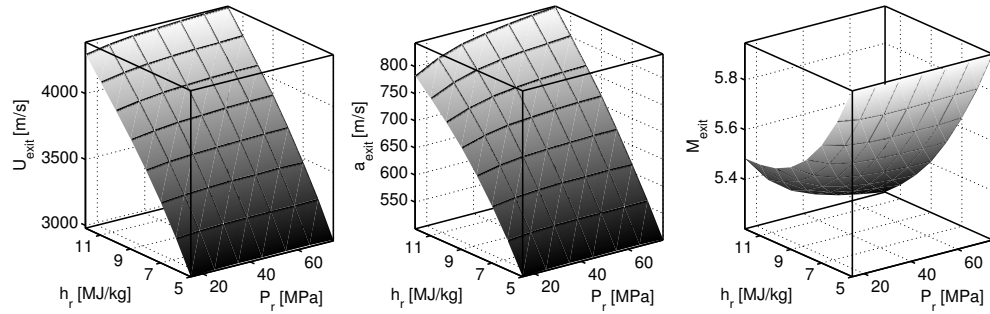
Figure 5.14: Calculated nozzle exit velocity, sound speed, and Mach number in air over a range of tunnel operating parameters h_{res} and P_{res}.

Both the present N_2 and air x_{Tr} results have a positive dependence on h_{res} (linear model coefficient 0.56 for N_2, 0.54 for air) and a negative dependence on P_{res} (-0.45 for N_2, -0.14 for air; however, the air result, with p-value $= 0.102$, is only marginally significant). The historical air data of Adam and Hornung (1997) are analyzed in the
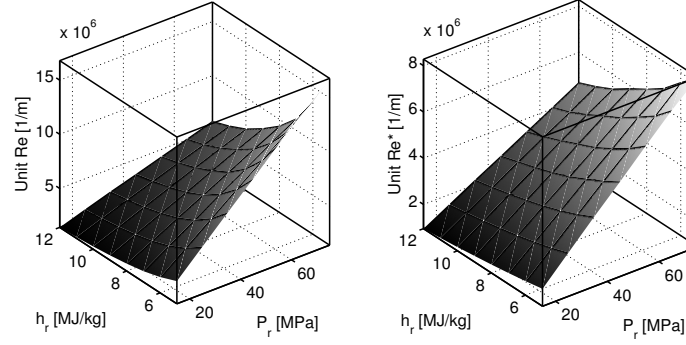
Figure 5.15: Reynolds number evaluated at the boundary layer edge in air (left) and at Dorrance reference conditions in air (right) over a range of tunnel operating parameters h_{res} and P_{res}.

same way, and likewise show a significant positive dependence of x_{Tr} on h_{res} (0.72) and negative dependence on P_{res} (-0.28). No statistically significant dependence for x_{Tr} was found in the historical N_2 data.

Both the present N_2 and air results have a positive dependence on P_{res} (linear model coefficient 0.31 for N_2, 0.59 for air) for the transition Reynolds number evaluated at Dorrance reference conditions, Re^*_{tr}, but neither have a dependence on h_{res} that is statistically significant. The historical air and N_2 data of Adam and Hornung (1997) and Germain and Hornung (1997) likewise show a significant positive dependence of Re^*_{Tr} on P_{res} (0.34 for air, 0.48 for N_2), but no statistically significant dependence on h_{res}.

No statistically significant correlation of Re^*_{Tr} with reservoir enthalpy h_{res} is observed for any data set, either in the present data or in a statistical re-examination of Germain and Hornung (1997) and Adam and Hornung (1997), except for historical CO_2 and the present 50% CO_2 results[10]. Adam and Hornung (1997) and Germain and Hornung (1997) reported an increase in Re^*_{Tr} with increasing h_{res}, but did not control for P_{res}, which varied from 10 to 85 MPa in their air experiments. In both

---

[10]The present 100% CO_2 results also show a positive correlation (linear model coefficient 0.36) of Re^*_{Tr} with reservoir enthalpy h_{res}, but the overall F-statistic p-value for the Re^*_{Tr} model was 0.088, so this result is only marginally significant.

	h_{res}	P_{res}	unit Re	unit Re*	x_{Tr}	δ_{99Tr}	$\sim f_{Tr}$
	MJ/kg	MPa	1/m	1/m	m	mm	kHz
675	10.20	58.5	5.60×10^6	4.23×10^6	0.54	1.13	1074
683	10.43	65.5	5.94×10^6	4.51×10^6	0.41	0.96	1280
684	11.10	60.9	5.25×10^6	4.09×10^6	0.46	1.07	1180
685	10.32	56.9	5.37×10^6	4.06×10^6	0.43	1.04	1178
686	12.95	55.4	4.02×10^6	3.20×10^6	0.59	1.38	974
687	13.06	57.3	4.14×10^6	3.33×10^6	0.59	1.35	1001
688	13.27	62.3	4.38×10^6	3.55×10^6	0.62	1.33	1018
689	10.65	59.0	5.34×10^6	4.09×10^6	0.54	1.15	1070
879	11.65	79.1	6.26×10^6	5.00×10^6	0.49	1.00	1289
888	11.55	79.1	6.28×10^6	4.97×10^6	0.63	1.14	1124
1113	11.37	77.2	6.34×10^6	5.04×10^6	0.48	0.98	1293
1115	7.38	68.7	9.66×10^6	6.20×10^6	0.43	0.83	1275
1151	10.03	45.0	4.46×10^6	3.29×10^6	0.57	1.32	907
1152	8.88	43.3	4.97×10^6	3.50×10^6	0.40	1.06	1076
1153	12.19	40.7	3.30×10^6	2.53×10^6	0.72	1.70	769
1155	8.08	44.3	5.66×10^6	3.80×10^6	0.45	1.09	1007
1156	7.80	48.0	6.34×10^6	4.18×10^6	0.39	0.96	1124
1157	5.83	47.2	8.94×10^6	4.90×10^6	0.23	0.67	1421
1159	11.41	42.5	3.67×10^6	2.80×10^6	0.72	1.61	788
1160	10.41	41.9	4.00×10^6	2.98×10^6	0.66	1.49	819
1162	9.04	34.4	3.91×10^6	2.74×10^6	0.60	1.48	773
1163	11.17	68.1	5.73×10^6	4.47×10^6	0.59	1.15	1094

Table 5.7: Experiments performed in air referenced in Germain and Hornung (1997) and Adam and Hornung (1997), with unit Reynolds numbers evaluated at the boundary layer edge and Dorrance reference conditions, observed transition onset location, and δ_{99} and $\sim f$ calculated at the transition onset location. Observed transition onset location x_{Tr} is as reported in Adam (1997), but the other parameters have been recalculated by the present methods for consistency, and in the case of Re*/m, δ_{99}, and f, calculated here for the first time.

present and past data, Re_{Tr}^* appears to correlate most strongly with P_{res}. The boundary layer edge pressure, and therefore the reservoir pressure, is important both in the mean flow and vibrational-translational damping processes. While the reservoir enthalpy, statistically, has been shown to be secondary to pressure, it is important to vibrational-translational relaxation due to its effect on vibrational populations, especially for CO_2. As noted above, at a given temperature, air and N_2 have much lower vibrational populations than CO_2 due to the higher characteristic vibrational temperatures of air and N_2 in comparison to CO_2.

	h_{res}	P_{res}	unit Re	unit Re*	x_{Tr}	$\delta_{99\text{Tr}}$	$\sim f_{\text{Tr}}$
	MJ/kg	MPa	1/m	1/m	m	mm	kHz
353	10.50	62	6.05×10^6	4.07×10^6	0.45	1.03	1229
361	5.64	19	3.94×10^6	1.93×10^6	0.64	1.75	548
532	10.00	53	5.49×10^6	3.60×10^6	0.45	1.10	1130
536	13.54	60	4.30×10^6	3.29×10^6	0.57	1.32	1071
540	7.31	57	8.57×10^6	4.81×10^6	0.38	0.87	1242
542	3.25	11	4.56×10^6	1.64×10^6	0.48	1.62	460
546	5.54	16	3.41×10^6	1.65×10^6	0.53	1.73	549
548	9.33	55	6.18×10^6	3.91×10^6	0.45	1.05	1148
561	12.18	85	6.84×10^6	4.95×10^6	0.57	1.07	1265
563	12.84	85	6.47×10^6	4.83×10^6	0.57	1.09	1277
565	14.47	80	5.22×10^6	4.15×10^6	0.57	1.18	1237

Table 5.8: Experiments performed in N_2 referenced in Germain and Hornung (1997) and Adam and Hornung (1997), with unit Reynolds numbers evaluated at the boundary layer edge and Dorrance reference conditions, observed transition onset location, and δ_{99} and $\sim f$ calculated at the transition onset location. Observed transition onset location x_{Tr} is as reported in Adam (1997), but the other parameters have been recalculated by the present methods for consistency, and in the case of Re*/m, δ_{99}, and f, calculated here for the first time.

	h_{res}	P_{res}	unit Re	unit Re*	x_{Tr}	$\delta_{99\text{Tr}}$	$\sim f_{\text{Tr}}$
	MJ/kg	MPa	1/m	1/m	m	mm	kHz
690	7.09	52.0	7.79×10^6	9.95×10^6	0.49	0.76	1138
1117	7.57	92.9	12.2×10^6	16.2×10^6	0.45	0.58	1537
1119	9.35	71.6	7.91×10^6	10.6×10^6	0.46	0.72	1352
1121	9.93	40.8	4.50×10^6	5.83×10^6	0.63	1.13	877
1123	6.50	55.2	8.87×10^6	11.2×10^6	0.46	0.69	1206
1124	6.06	59.9	10.1×10^6	12.7×10^6	0.39	0.60	1363
1125	4.65	61.2	13.5×10^6	16.1×10^6	0.36	0.51	1448
1126	4.56	62.2	13.8×10^6	16.4×10^6	0.37	0.51	1433
1130	5.30	49.1	9.53×10^6	11.6×10^6	0.42	0.66	1178
1131	6.36	49.9	8.21×10^6	10.3×10^6	0.43	0.70	1183
1132	7.76	52.3	7.11×10^6	9.18×10^6	0.42	0.73	1224
1133	5.26	48.2	9.49×10^6	10.5×10^6	0.37	0.61	1256
1136	5.87	60.4	10.9×10^6	13.6×10^6	0.42	0.61	1332
1148	5.89	44.2	8.07×10^6	9.95×10^6	0.45	0.73	1105
1149	5.08	44.5	9.28×10^6	11.1×10^6	0.47	0.70	1083

Table 5.9: Experiments performed in CO_2 referenced in Germain and Hornung (1997) and Adam and Hornung (1997), with unit Reynolds numbers evaluated at the boundary layer edge and Dorrance reference conditions, observed transition onset location, and δ_{99} and $\sim f$ calculated at the transition onset location. Observed transition onset location x_{Tr} is as reported in Adam (1997), but the other parameters have been recalculated by the present methods for consistency, and in the case of Re*/m, δ_{99}, and f, calculated here for the first time.

	x_{Tr}	$\bar{\mathrm{Re}}_{\mathrm{Tr}}^{*}$	$\bar{\mathrm{Re}}_{\mathrm{Tr}}$
P_{res} coefficient	**-0.28405**	**0.33725**	**0.27436**
p-value	0.01308	3.07×10^{-4}	3.24×10^{-4}
$\bar{h}_{\mathrm{res}}$ coefficient	**0.72414**	0.10048	-0.043046
p-value	1.23×10^{-5}	0.28530	0.57148

Table 5.10: Multivariable linear regression analysis for historical air results ($n = 22$) referenced in Germain and Hornung (1997) and Adam and Hornung (1997). P_{res} and h_{res} are normalized by their respective maximum values. The coefficients found to be statistically significant ($p < 0.05$) are in bold print.

	x_{Tr}	$\bar{\mathrm{Re}}_{\mathrm{Tr}}^{*}$	$\bar{\mathrm{Re}}_{\mathrm{Tr}}$
$\bar{P}_{\mathrm{res}}$ coefficient	-0.25907	**0.47606**	**0.41048**
p-value	0.18609	5.48×10^{-4}	3.75×10^{-4}
$\bar{h}_{\mathrm{res}}$ coefficient	0.36978	-0.08002	**0.30036**
p-value	0.13572	0.47584	8.69×10^{-3}

Table 5.11: Multivariable linear regression analysis for historical N_2 results ($n = 11$) referenced in Germain and Hornung (1997) and Adam and Hornung (1997). P_{res} and h_{res} are normalized by their respective maximum values. The coefficients found to be statistically significant ($p < 0.05$) are in bold print.

	x_{Tr}	$\bar{\mathrm{Re}}_{\mathrm{Tr}}^{*}$	$\bar{\mathrm{Re}}_{\mathrm{Tr}}$
P_{res} coefficient	**-0.16878**	**0.35199**	**0.44392**
p-value	0.04956	9.45×10^{-6}	4.45×10^{-5}
$\bar{h}_{\mathrm{res}}$ coefficient	**0.32474**	**-.15363**	**-0.30262**
p-value	4.06×10^{-4}	3.20×10^{-3}	3.77×10^{-4}

Table 5.12: Multivariable linear regression analysis for historical CO_2 results ($n = 15$) referenced in Germain and Hornung (1997) and Adam and Hornung (1997). P_{res} and h_{res} are normalized by their respective maximum values. The coefficients found to be statistically significant ($p < 0.05$) are in bold print.

5.4   Conclusion

An alternative nondimensionalization of the transition onset location by the local laminar boundary layer thickness $(x/\delta_{99})_{\mathrm{Tr}}$ is compared with $\mathrm{Re}_{\mathrm{Tr}}$ and $\mathrm{Re}^*_{\mathrm{Tr}}$, and used to correlate the N factor results of boundary layer stability analyses with and without vibrational effects. At the conditions examined in the present study, vibrational effects were shown to be quite large for conditions with both pure and 50% CO_2 free streams, much less significant for air, and of essentially no consequence for N_2. The maximum observed $(x/\delta_{99})_{\mathrm{Tr}}$ was 858 for CO_2, which is 25% higher than the maximum air $(x/\delta_{99})_{\mathrm{Tr}}$ of 688, and 789 for 50% CO_2, which is 15% higher than the maximum for air. The results for $(x/\delta_{99})_{\mathrm{Tr}}$ are correlated with both $\mathrm{Re}^*_{\mathrm{Tr}}$ and $\mathrm{Re}_{\mathrm{Tr}}$, which are nondimensional parameters that have been examined previously in hypersonic transition studies. Reynolds number correlations are a consequence of mean flow scaling, and acoustic instability depends on $(x/\delta_{99})_{\mathrm{Tr}}$.

The inclusion of vibrational-translational relaxation in simulations of high-enthalpy boundary layers is quite important for producing useful stability results. Relaxation was shown to limit N factors to realistic values in PSE-Chem computations, both for air and for CO_2. The largest effects were seen for CO_2 and 50% CO_2 experiments, which have a substantial fraction of vibrationally excited molecules for all the cases examined.

A strong unit Reynolds number effect on the transition Reynolds number and other relevant transition parameters has been found, consistent with a variable noise spectrum radiating from the boundary layer which forms on the nozzle wall.

Transition onset data have been correlated by performing multivariable linear regression analysis, taking P_{res} and h_{res} (normalized by each data set's maximum pressure and enthalpy) as the possible predictor variables and the measured, normalized values of x_{Tr}, $\mathrm{Re}^*_{\mathrm{Tr}}$ and $\mathrm{Re}_{\mathrm{Tr}}$ as the modeled variables. Transition onset data

reported in Germain and Hornung (1997) and Adam and Hornung (1997) have been re-analyzed in the same way to compare. Controlling for variations in P_{res}, no statistically significant dependence of Re^*_{Tr} on h_{res} was found for either the present air or N_2 data or the historical air and N_2 data. While a small but statistically significant relationship was found for the dependence of Re^*_{Tr} on h_{res} for historical CO_2 and the present 50% CO_2 results, it is negative for the former case and positive for the latter (in historical data the relationship has always been stated as positive).

Chapter 6

Results: Turbulent Spots

6.1 Introduction

Transition from laminar to turbulent flow in boundary layers occurs through the genesis, growth, and propagation of isolated local turbulence patches, known as turbulent spots. Emmons (1951) was the first to propose that laminar boundary layers break down through the convergence of spots, after observations of a water-table analogy to air flow. Spot formation and propagation has been studied extensively in subsonic and transonic flows, notably by Narasimha (1957), Dhawan and Narasimha (1958), Chen and Thyson (1971), Abu-Ghannam and Shaw (1980), Narasimha (1985), and Clark et al. (1994).

The first turbulent spots in a supersonic boundary layer were detected by James (1958) on free-launched projectiles using spark shadowgraphs with a conical light field, characterizing both propagation speed and growth rate for freestream Mach numbers from 2.7 to 10. James was able to surmise that the differences between turbulent-spot propagation in subsonic and supersonic flow were likely to be small. Fischer (1972) surveyed available supersonic and hypersonic spot studies and showed a relationship between the spreading angle of turbulent disturbances and the Mach number. Since then, a number of spot studies in supersonic and hypersonic flows have been carried out, with reviews included in Fiala et al. (2006) and Mee (2002). In all

cases, turbulent spots have been found to have roughly triangular shape in planform, as depicted in Figure 6.1, with the velocity of the leading and trailing edges each some fraction of the velocity at the boundary layer edge, U_e, and the rate at which the spot grows laterally as it progresses downstream along the surface described by a spreading angle α. As Schubauer and Klebanoff (1955) observe: "The triangular shape of the spot with vertex pointing downstream may be accounted for by the fact that the downstream end does not have the time that the upstream end has in which to grow laterally."
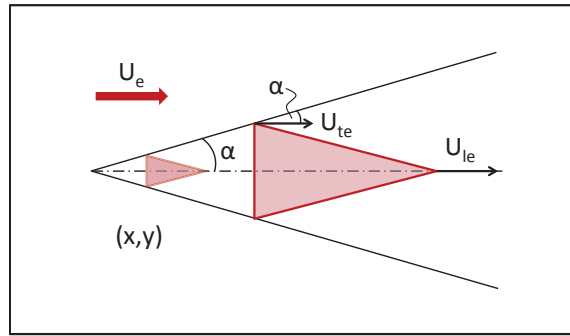
Figure 6.1: Schematic depiction of a triangular turbulent spot, with the velocities at the leading and trailing edges labeled as U_{le} and U_{te}, and the angle at which additional fluid is entrained in the spot as it moves labeled as α, the spreading angle with respect to the velocity at the boundary layer edge, U_e. Both U_{le} and U_{te} are some fraction of U_e. As U_{le} tends to be larger than U_{te}, the spot grows longitudinally as it progresses downstream. The rate at which it grows laterally is controlled by α.

6.2 Turbulent Spot Observations[1]

A method of presenting time- and spatially-resolved heat flux data has been developed and implemented, which allows the presentation of a "movie" of heat flux over the entire instrumented surface of the cone during the test time by interpolating the signals from each of 80 thermocouples. Figure 6.2 depicts four frames from the results for shot 2698, over a total time of 0.3 ms during which a turbulent spot, represented

[1]Portions of this section are adapted from Jewell et al. (2012).

by a localized region of increased heat flux, is clearly seen to propagate downstream. A similar surface heat flux method (with thin film gauges rather than thermocouples) was previously used to visualize spots in subsonic flow by Anthony et al. (2005) and in supersonic flow by Fiala et al. (2006).
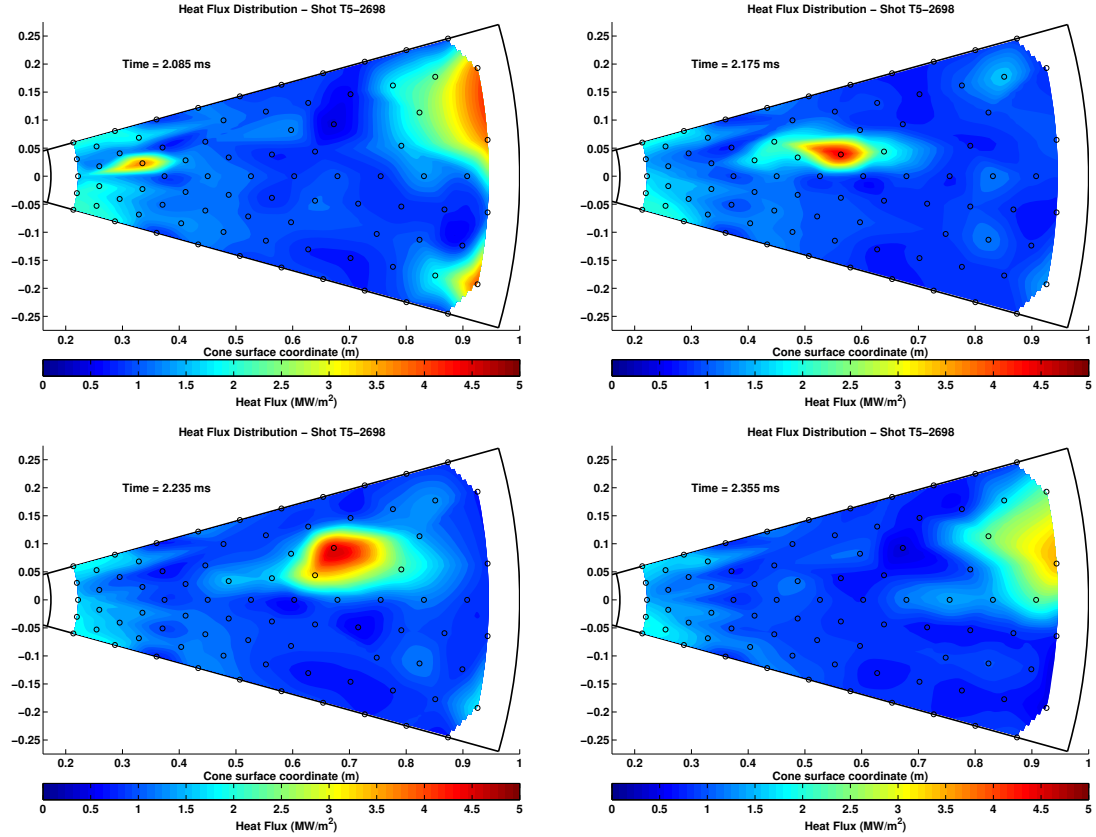
Figure 6.2: Four frames from shot 2698 covering a total time of 0.3 ms, during which a turbulent spot is observed near the tip (first frame, top left) and seen to propagate downstream and eventually off the end of the cone.

To quantitatively analyze spots, the signals from each of the eight rays of thermocouples mounted on the cone are examined individually for localized regions of elevated heat flux. Turbulent spots are seen on these heat transfer traces as well-ordered excursions above the baseline heat flux with roughly triangular form, typically passing over the gauge in about 0.1 ms, propagating downstream over the series of gauges at some fraction of the boundary layer edge velocity, and growing spatially. One example of a spot tracked down one ray of sensors, observed during shot 2700,

is presented in Figure 6.3. Clear leading edge, trailing edge, and peak heat transfer signals for the spot are observed on most of the thermocouples.
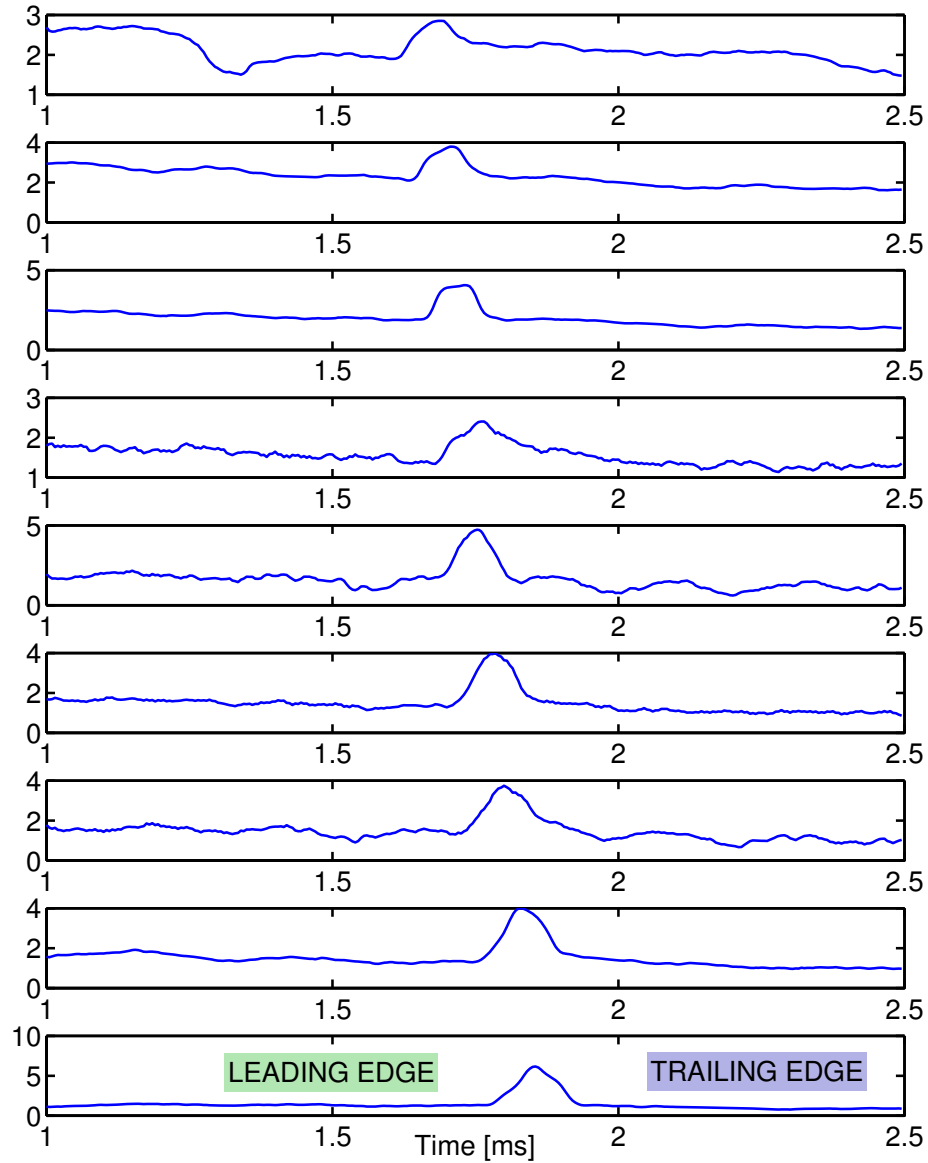
Figure 6.3: A spot observed during shot 2700, which is seen first on TC16 at about 1.7 ms after the trigger time, which is 0.3 ms into the steady test time for this experiment. The spot subsequently appears and grows over each thermocouple in sequence, eventually passing over TC80 at the end of the cone. The sides of the signal indicating the arrival and departure time at the gauge of the spot's leading and trailing edges, respectively, are indicated on the plot for TC80 at the bottom.

The traces in Figure 6.3 may be analyzed to find propagation velocities for the leading edge, trailing edge, and peak or centroid heat transfer value for each spot.

Each of these three features is tagged in each subsequent trace, and the resulting timestamps correlated with the position on the cone of each thermocouple to produce plots such as Figure 6.4. The modeled value for the slope of each set of points is taken as the velocity, and the 95% confidence interval is calculated using the MATLAB Statistics Toolbox.
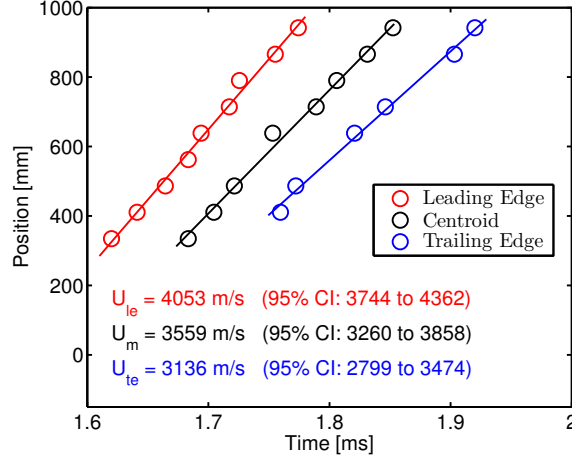
Figure 6.4: Leading edge, trailing edge, and centroid velocities for the spot observed during shot 2700, which is depicted in Figure 6.3. The modeled value for the slope of each set of points is taken as the velocity, and the 95% confidence interval is calculated using the MATLAB Statistics Toolbox. The confidence interval for the three velocities in this example is relatively small due to the large number of points in each curve.

The 29 leading edge, trailing edge, and centroid velocities measured from the present data set are shown graphically in Figure 6.5 plotted against the boundary layer edge velocity U_e. The measured velocities increase linearly with edge velocity, as expected, but no clear trend (independent of edge velocity) is observed for varying gas mixtures.

The measured spot velocities are normalized by the calculated velocity at the boundary layer edge, U_e to find appropriate values for C_{le} and C_{te} which are compared with past spot experiments and computations in Section 6.4 and used as an input in the spot propagation simulation discussed in Section 6.3. Due to the sparse number and nature of the thermocouple data, there is substantial uncertainty in defining the
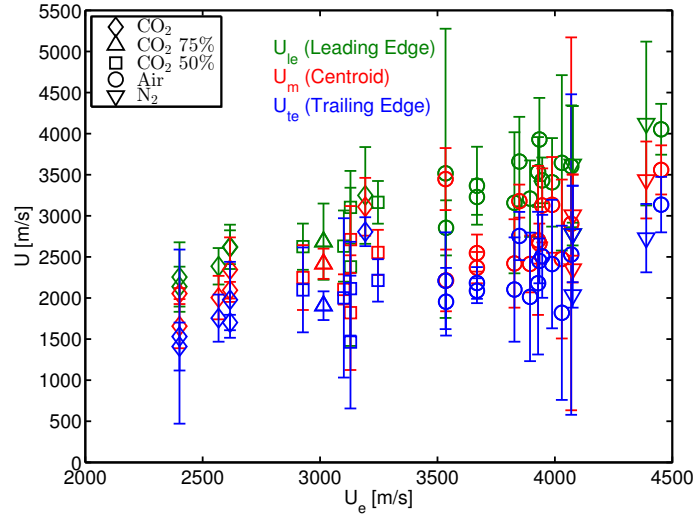
Figure 6.5: Leading edge, trailing edge, and centroid velocities for all spots during the present campaign. The velocities increase proportionally with U_e.

precise leading and trailing edges of the spot. Taking the results of all 29 isolated spot examples together, the putative leading edge propagates downstream at about $0.90U_e$ (95% confidence interval: 0.88 to 0.93), the peak or centroid at $0.76U_e$ (95% confidence interval: 0.72 to 0.80), and the trailing edge at $0.63U_e$ (95% confidence interval: 0.59 to 0.67).

Measurements for all 29 spots are presented in Table 6.1 as fractions of the respective boundary layer edge velocities, along with other relevant tunnel and boundary layer parameters for each test. The non-dimensionalized average heat flux gauge signals were examined for each of these 24 runs as Stanton number *vs.* Reynolds number plots based on the distance of the gauge from the tip of the cone. In each case, the boundary layer is on average observed to be laminar over the most of the cone for the majority of the test time, with some cases showing incipient transition near the end of the cone. Therefore, the observed spots are propagating as isolated turbulent patches within a surrounding flow field that is mainly laminar. Indeed, this relative isolation is the feature that enables tracking each event as a distinct spot over multiple gauges. The initiating events for these spots are unknown, but may be due to the
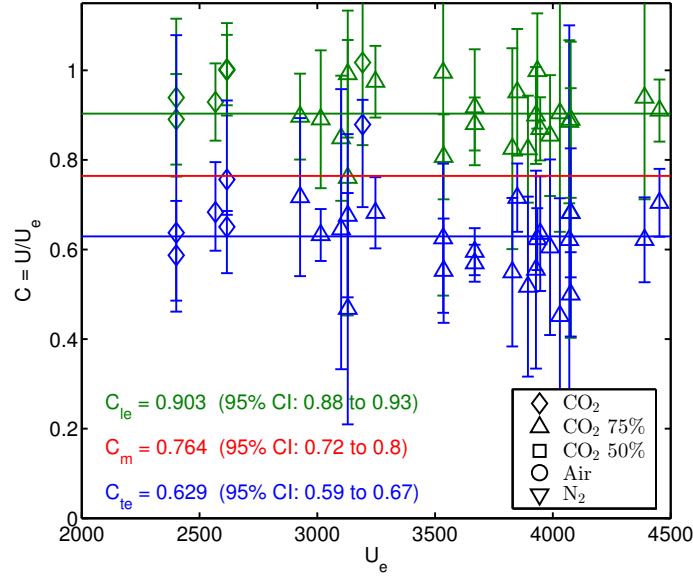
Figure 6.6: Leading edge, trailing edge, and centroid velocities for all spots during the present campaign, normalized by U_e. The reported average normalized velocities (C_{le}, C_m and C_{te}) are means weighted by the inverse standard error for each point in the data sets. In this figure, the points representing C_m are omitted for clarity, although the mean value and 95% confidence interval for that measure do appear.

nonlinear breakdown of second mode instabilities deriving from freestream acoustic disturbances (Fedorov, 2003), which have been observed within similar transitional boundary layers in T5 using recently implemented optical methods for observing low-amplitude, high-frequency density fluctuations, as described in Parziale et al. (2011) and Parziale et al. (2012). Another possible source of initiation is particulate impact on the cone's boundary layer, which is discussed in Fedorov (2013). A survey of experimental results included in Fiala et al. (2006) did not find significant differences in propagation parameters between artificially induced and naturally occurring turbulent spots. Therefore, it may reasonably be assumed that measurements of the spots observed in the present study and tabulated in Table 6.1 are relevant for the transition process in T5 regardless of whether their genesis lies in breakdown of the second mode, particulate impact, or an unknown disturbance source.

	Gas	h_{res} MJ/kg	P_{res} MPa	1st Ob. ms	TC	U_e m/s	C_{le}	C_m	C_{te}
2638	Air	7.68	54.3	1.5	24	3533	0.99 ±0.10	0.98 ±0.02	0.63 ±0.04
2642	Air	9.89	54.3	1.5	8	3933	1.00 ±0.05	0.68 ±0.03	0.62 ±0.03
2645	Air	9.96	54.3	1.4	9	3946	0.87 ±0.03	0.79 ±0.04	0.64 ±0.04
2651	Air	9.87	51.9	1.9	26	3928	0.90 ±0.03	0.69 ±0.07	0.56 ±0.07
2654	Air	10.38	74.1	1.8	26	4028	0.90 ±0.06	0.61 ±0.06	0.45 ±0.06
2667	N_2	9.95	52.2	2.1	1	4076	0.89 ±0.05	0.74 ±0.04	0.68 ±0.05
2667	N_2	9.95	52.2	1.9	30	4076	0.68 ±0.06	0.58 ±0.03	0.50 ±0.02
2677	Air	9.38	53.3	1.6	8	3848	0.95 ±0.07	0.83 ±0.04	0.72 ±0.02
2680	Air	9.19	71.2	1.6	26	3827	0.83 ±0.07	0.63 ±0.05	0.55 ±0.05
2698	Air	8.39	50.1	1.6	3	3667	0.92 ±0.07	0.69 ±0.05	0.57 ±0.05
2698	Air	8.39	50.1	2.0	15	3667	0.88 ±0.02	0.65 ±0.02	0.60 ±0.02
2700	Air	13.39	49.4	1.6	16	4452	0.91 ±0.03	0.80 ±0.03	0.70 ±0.03
2708	Air	7.70	49.6	1.7	25	3535	0.81 ±0.04	0.63 ±0.04	0.55 ±0.04
2718	Air	10.14	70.1	1.2	29	3987	0.85 ±0.05	0.79 ±0.06	0.61 ±0.06
2737	CO_2 75%	7.10	56.1	2.1	15	3015	0.89 ±0.06	0.80 ±0.02	0.63 ±0.02
2754	CO_2	9.41	53.4	1.9	24	3192	1.00 ±0.04	0.97 ±0.04	0.88 ±0.02
2759	Air	9.62	60.4	1.7	48	3894	0.82 ±0.03	0.62 ±0.03	0.52 ±0.05
2779	N_2	12.00	42.3	1.4	22	4389	0.94 ±0.05	0.78 ±0.03	0.62 ±0.02
2787	Air	10.73	54.7	1.4	29	4069	0.89 ±0.04	0.71 ±0.10	0.62 ±0.10
2793	CO_2	4.61	22.7	2.2	22	2401	0.94 ±0.04	0.86 ±0.01	0.64 ±0.03
2793	CO_2	4.61	22.7	1.5	26	2401	0.89 ±0.03	0.69 ±0.04	0.59 ±0.04
2805	CO_2	5.38	41.4	1.9	25	2568	0.93 ±0.03	0.78 ±0.04	0.68 ±0.04
2807	CO_2	5.57	54.3	1.3	4	2616	1.00 ±0.03	0.90 ±0.05	0.76 ±0.06
2807	CO_2	5.57	54.3	1.6	7	2616	1.00 ±0.04	0.80 ±0.02	0.65 ±0.01
2809	CO_2 50%	7.66	57.1	1.6	16	3247	0.97 ±0.03	0.79 ±0.04	0.68 ±0.03
2810	CO_2 50%	6.79	58.2	1.7	22	3101	0.85 ±0.04	0.68 ±0.02	0.65 ±0.07
2811	CO_2 50%	6.96	56.3	1.7	13	3129	0.99 ±0.06	0.87 ±0.05	0.68 ±0.07
2811	CO_2 50%	6.96	56.3	1.4	42	3129	0.76 ±0.07	0.58 ±0.05	0.47 ±0.02
2818	CO_2 50%	5.96	40.7	1.9	14	2927	0.90 ±0.03	0.77 ±0.05	0.72 ±0.06

Table 6.1: Individual spots observed during the present test campaign ($n = 29$) from 24 tests. Each of these spots was isolated enough to distinguish as a distinct phenomenon on the cone during the steady test time, and was observed to propagate downstream over three or more heat transfer gauges, permitting the measurement of leading edge, trailing edge, and centroid velocities. Note that there are two entries for several shots; this indicates that two individual spots were observed during these experiments. They are differentiated by time of first observation during the test, and the number of the first thermocouple their signal appears on. The uncertainties in this table are the standard errors for each measurement. For these tests, T_w/T_{aw} ranged from 0.05 to 0.12, and T_w/T_e ranged from 0.16 to 0.24.

6.3   Turbulent Spot Model and Simulations

6.3.1   Background

The transition zone length, or the distance from transition onset to completion, Δx_{Tr}, depends on spot generation or breakdown rate n, spreading angle α, and leading- and trailing-edge velocities U_{le} and U_{te} (Kimmel, 1993). The spot generation rate n depends upon the receptivity of the boundary layer and the disturbance environment of the facility; Narasimha (1985) surveyed subsonic data and found that n generally increases with freestream turbulence levels. Mee and Tanguy (2013) developed a procedure using a simple spot propagation model to infer turbulent spot initiation rates by coupling experimentally measured transition zone length with three assumptions about spot growth and development; namely, that the spot spreading angle and leading- and trailing-edge propagation speeds are known. A similar model is used for the present analysis.

The present model is based upon the code developed in Jewell (2008) for a flat plate, which was in turn an implementation in MATLAB of the spot propagation process outlined in Clark (1993). In all of these approaches, the turbulent spots are modeled, following Narasimha (1985), as triangular in planform, and assumed to be generated randomly in time and y-position at the line defined by a particular x-displacement (or in a defined distribution within a band around a particular x-displacement) from the edge or tip of the test article.

The Jewell (2008) code is adapted for conical flow by performing the calculation on a developed cone surface, as shown in Figure 6.7. In this case U_{e} is nonparallel with respect to the coordinate system of the developed surface, but emanates radially from the origin. Both U_{le} and U_{te} are some fraction of U_{e}. As U_{le} tends to be larger than U_{te}, the spot grows longitudinally as it progresses downstream. The rate at which it grows laterally is controlled by α and the angle of the cone. The spreading

angle is assumed to vary inversely with edge Mach number for each case with the empirical relationship found by Doorley and Smith (1992)[2] in the data reported by Fischer (1972).

$$\alpha \approx \frac{0.27}{M_e} \qquad (6.1)$$

This relationship is given in Equation (6.1) and was also used in the Mee and Tanguy (2013) model. C_{le} and C_{te} are taken from the mean values measured experimentally, as shown in Figure 6.6. The 95% confidence intervals for the three C values are comparable to or smaller than past reported uncertainties for these measures (*cf.* Mee (2002), who reported $\pm 10\%$ for similar conditions, and Clark et al. (1994), who reported up to $\pm 4\%$ for much slower conditions). U_e and M_e are computed by DPLR as described in Section 4.1.2.
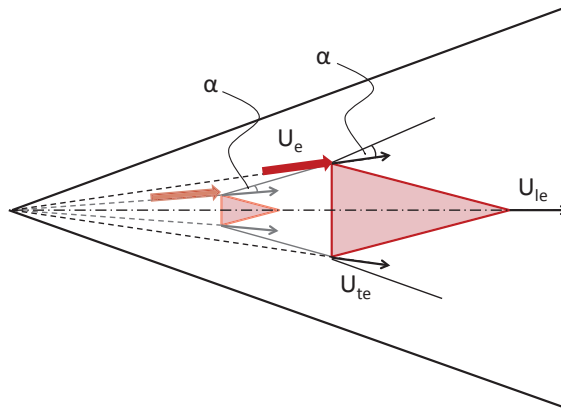
Figure 6.7: Schematic depiction of a triangular turbulent spot on the developed surface of a cone, with the velocities at the leading and trailing edges labeled as U_{le} and U_{te}, and the angle at which additional fluid is entrained in the spot as it moves labeled as α, the spreading angle with respect to the velocity at the boundary layer edge, U_e. In this frame of reference, the boundary layer edge velocity acting on the spots has a radial distribution.

6.3.2   Flat Plate and Conical Simulations and Theory

Narasimha (1957) introduced a universal intermittency curve, Equation (6.2), where γ

---

[2]Doorley and Smith (1992) give the relationship as $\alpha = 3^{-3/2}\sqrt{2}/M_e$.

is the intermittency, or fraction of the test time that the flow at a given x-displacement beyond the transition onset location, x_{Tr}, is turbulent.

$$
\gamma_{\mathrm{plate}}(x) = \begin{cases} 1 - \exp\left[-\dfrac{n\sigma}{U_{\mathrm{e}}}(x - x_{\mathrm{Tr}})^2\right] & (x \geq x_{\mathrm{Tr}}) \\[2mm] 0 & (x \leq x_{\mathrm{Tr}}) \end{cases} \tag{6.2}
$$

This concept, which was derived for the propagation of spots on a flat plate, is further developed in Narasimha (1985) and has been found to hold for both incompressible (*e.g.*, Clark et al. (1994)) and compressible (*e.g.*, Mee and Tanguy (2013)) transitional boundary layers. The relationship between γ and x depends upon edge velocity, the nondimensional spot growth (or propagation) parameter σ of Emmons (1951), and the spot generation parameter n, which is the number of spots generated per unit length and time across $x = x_{\mathrm{Tr}}$. σ incorporates both lateral and streamwise growth, and is commonly taken as in Vinod and Rama (2004):

$$
\sigma = \left[\frac{1}{U_{\mathrm{te}}} - \frac{1}{U_{\mathrm{le}}}\right] U_{\mathrm{e}} \tan\alpha \tag{6.3}
$$

The universal intermittency curve is adapted for axisymmetric conical flow in Equation (6.4), from Cebeci and Smith (1974):

$$
\gamma_{\mathrm{cone}}(x) = \begin{cases} 1 - \exp\left[-\dfrac{n\sigma}{U_{\mathrm{e}}}x_{\mathrm{Tr}}\left(\ln\dfrac{x}{x_{\mathrm{Tr}}}\right)(x - x_{\mathrm{Tr}})\right] & (x \geq x_{\mathrm{Tr}}) \\[2mm] 0 & (x \leq x_{\mathrm{Tr}}) \end{cases} \tag{6.4}
$$

In Figure 6.8, γ_{plate} and γ_{cone} from Equations (6.2) and (6.4) are compared with simulation results using the edge conditions of shot 2776 and α as defined in Equation (6.1), with $n = 4 \times 10^6$ spots/m/s. Excellent agreement is found between theory and the simulations. It is also seen that at any given x-displacement, intermittency is higher for the plate than the cone, which indicates that spots, on average, take longer to merge with their neighbors in the conical boundary layer.
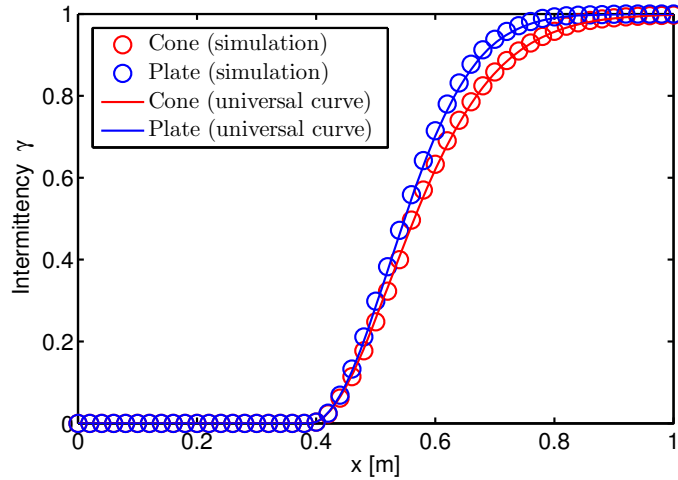
Figure 6.8: Flat plate and cone intermittency γ and curves for $n = 4 \times 10^6$ computed at shot 2776 conditions, compared with the relevant universal intermittency curves. Excellent agreement is obtained.

This effect is illustrated by comparing Figure 6.9 with Figure 6.10. Both of these figures depict the outer envelope of a single spot with spreading angle $\alpha = 2.5°$ generated along the centerline of the cone or plate at $x_{\text{Tr}} = 0.389$ as it grows while propagating down the surface. Figure 6.9 presents the spot envelope in Cartesian coordinates for a flat plate (or cylinder) in the top plot, and for a cone in the bottom plot. The physical growth of the spot is similar in both cases—in fact, due to the nonparallel edge velocity acting at the edges of the spot in the conical case, the lateral extent of the spot is actually slightly greater by the end of the 1 m cone than it as at the end of the 1 m flat plate (or equivalently, 1 m cylinder).

However, in the conical case, the surface area also increases with x, which is not the case for a plate or cylinder. Figure 6.10 presents the spot's outer envelope in angular coordinates for a flat plate (or cylinder) in the top plot, and for a cone in the bottom plot. In angular terms, the turbulent spot on the plate or cylinder covers nearly twice the circumferential fraction of the surface by the end of the body compared to the turbulent spot on the cone. This accounts for the difference in intermittency seen in Figure 6.8.
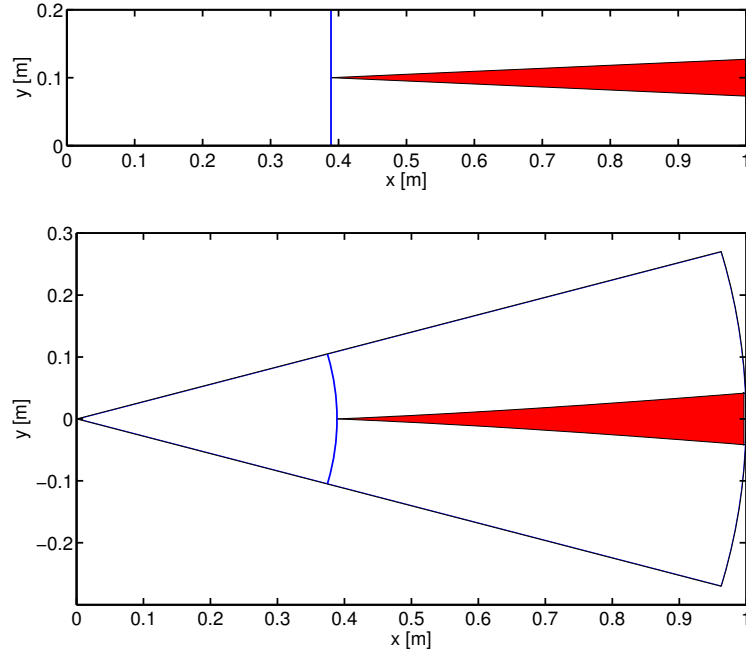
Figure 6.9: Path of a single centered spot with spreading angle $\alpha = 2.5°$ generated at $x_{\text{Tr}} = 0.389$, for a plate or cylinder (top) and an axisymmetric cone with 5° half-angle (bottom). While the growth profile of a spot in both geometries is similar, the increasing total surface area of the cone with respect to x means that each spot covers a smaller circumferential fraction of the surface, as shown in Figure 6.10.

The time-averaged intermittency at each x for this case over each of five full plate and cone simulations is presented in Figure 6.11, and linearized with the $F(\gamma)$ of Narasimha (1957) in Figure 6.12. The distance Δx_{Tr} from x_{Tr} that it takes to reach $\gamma \approx 1$ (here taken as $\gamma = 0.99$) decreases with increasing n, and for all cases the transition length is shorter for the flat plate case than the conical case with the same n, which is the same behavior seen in Figure 6.8.
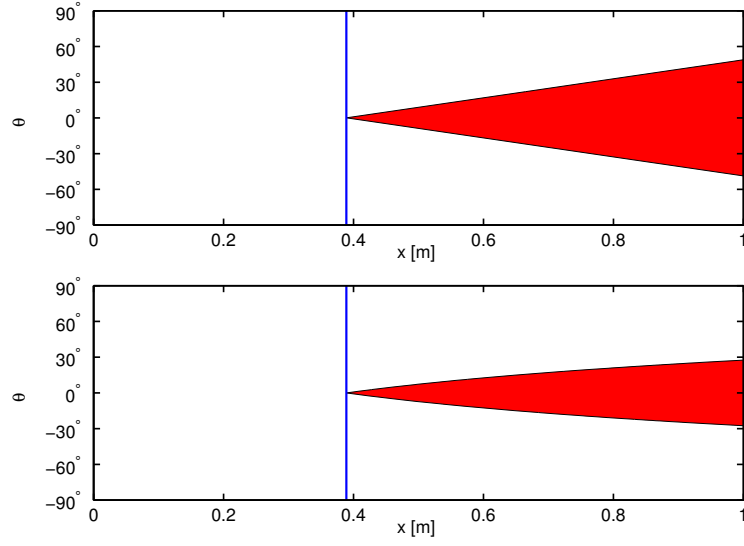
Figure 6.10: Path of a single centered spot in angular coordinates with spreading angle $\alpha = 2.5°$ generated at $x_{\mathrm{Tr}} = 0.389$, for a plate or cylinder (top) and an axisymmetric cone with 5° half-angle (bottom).
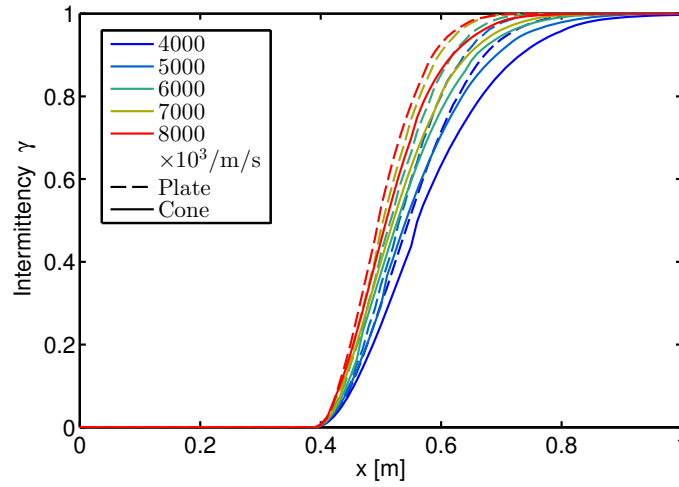
Figure 6.11: Flat plate and cone intermittency (γ) curves for several spot generation rates n computed at the conditions of shot 2776.
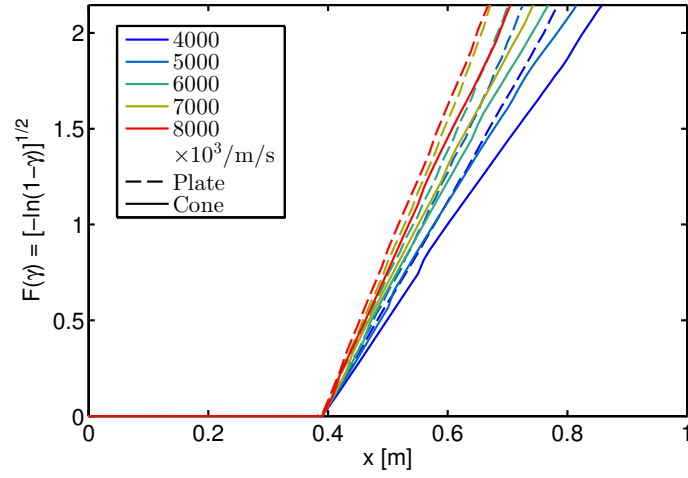
Figure 6.12: Flat plate and cone intermittency (γ) curves for several spot generation rates n computed at the conditions of shot 2776. These curves have been transformed by the Narasimha (1957) linearizing function $F(\gamma)$.

6.3.3 Correlation with Experiments

For each experiment for which both transition onset and transition completion are clearly observed, a set of conical simulations varying the spot generation parameter n are run, with spots generated randomly along the band defined by $x = x_{\text{Tr}}$ at a rate defined by the product of the circumference of that band and the input n. For each case, a total of 10 ms of test time is run (discarding the first $2(1 - x_{\text{Tr}})/U_{\text{e}}$ ms to allow time for the spots to fully develop), with a time step sufficiently small to resolve the motion of individual spots. One frame from such a simulation is presented in Figure 6.13, taken from a computation at the conditions of shot 2740 with $n = 6 \times 10^6$ spots/m/s. The long laminar region up to x_{Tr}, where $\gamma = 0$, a fully turbulent region, where $\gamma \approx 1$, and a transitional region with intermediate intermittency are all clearly discernible.
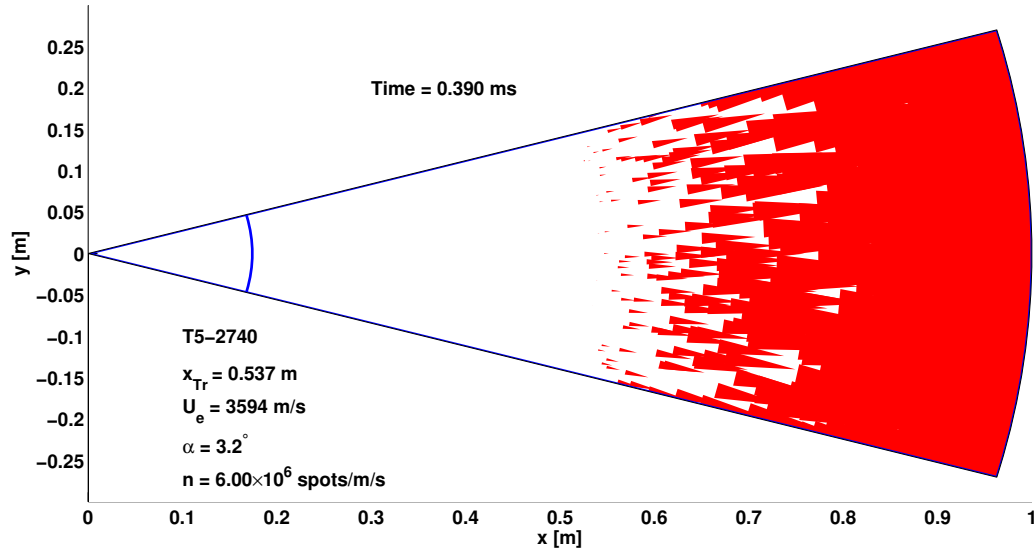
Figure 6.13: One frame from the 10 ms conical spot simulation for shot 2740.

The transition length Δx_{Tr} where $\gamma = 0.99$, taken from the linearized curves $F(\gamma)$ as in Figure 6.12, is compared with the experimentally determined transition length, shown in Figure 6.14. This measured transition length is shown with the predicted transition length for a range of n values in Figure 6.15. As in Mee and Tanguy

(2013), n is taken at the point where the computed transition length curve matches the measured transition length. The results for all 17 cases are tabulated in Table 6.2 along with relevant experimental parameters, and are plotted against unit Reynolds number, along with the replotted data of Mee and Tanguy (2013), in Figure 6.16.
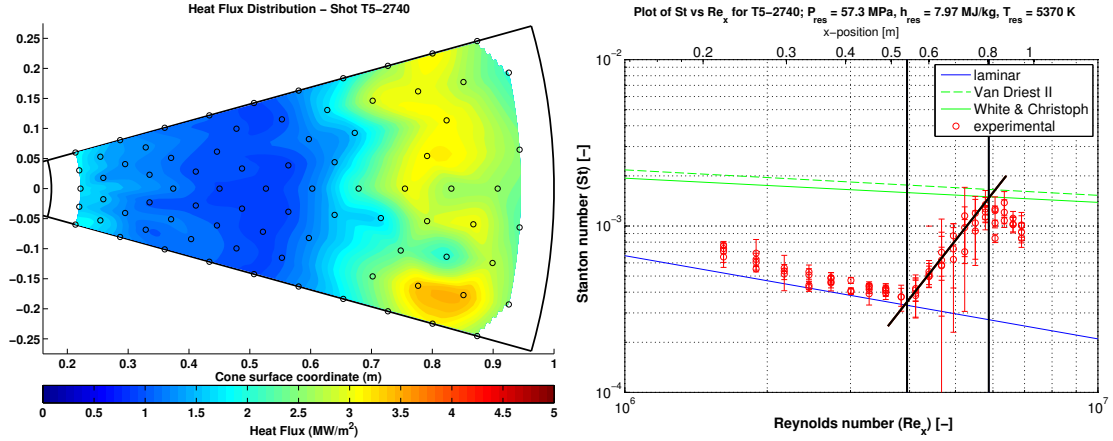
Figure 6.14: Experimentally measured distance between transition onset and transition completion for shot 2740. The contour plot at left presents the average heat flux during the test time over the surface of the cone. On the Re *vs.* St plot at right, a line is fit through the transitional region, and the transition onset location x_{Tr} is taken as the intersection of the fit with the laminar correlation. The transition completion location x_{TrComp} is taken as the intersection of the fit with the White and Christoph (1972) turbulent correlation. The distance between the two points is Δx_{Tr}.

While the data are quite scattered, it is interesting to note that the two 50% CO_2 results from the present data have spot generation rates that are only about half of those measured for the cluster of 15 air and N_2 results. This may indicate that the spot formation process or receptivity to disturbances is inhibited for CO_2-containing boundary layers compared with air and N_2. No other studies of turbulent spots in CO_2 flows[3] were found in the literature, and the matter would surely benefit from further experimental investigation.

Mee and Tanguy (2013) found a dependence of n on unit Reynolds number for

---

[3]None of the pure CO_2 experiments in the present study with clear transition onset had transition completion by the end of the cone, so these 50% CO_2 cases are the best available data on the effect of CO_2 on spot formation in the boundary layer.

air results, and the present air and N_2 data show a similar (albeit weak) dependence. While Mee's results for n are significantly lower than the present data, roughly 70% of the discrepancy can be accounted for by the fact that the Mee and Tanguy (2013) model used $C_{\text{te}} = 0.50$ as given in Mee (2002), while the present model uses $C_{\text{te}} = 0.63$ as measured in Section 6.2 (both models used $C_{\text{le}} = 0.90$, and the method of calculating α was also identical). This means that Mee's simulated spots grow more rapidly in the longitudinal dimension, and therefore each spot covers more of the surface, resulting in higher intermittency for a given spot generation rate n.

This effect is demonstrated by running one set of the present simulations (conditions matching shot 2740) with $C_{\text{te}} = 0.50$ instead of $C_{\text{te}} = 0.63$. These results are shown in Figure 6.17. Compared with the results in Figure 6.15, the matching value of n for the observed transition length drops from 7.36×10^6 spots/m/s to 3.96×10^6 spots/m/s. The value at the same unit Reynolds number for the Mee and Tanguy (2013) curve fit is 2.40×10^6 spots/m/s. While the C_{te} disparity accounts for most of the difference in the n results, the spot generation rate would not necessarily be expected to be identical in these two data sets in any case, as they were acquired in different facilities with different noise profiles and disturbance sources, as well as on different geometries: flat plates for Mee and a cone in the present work.
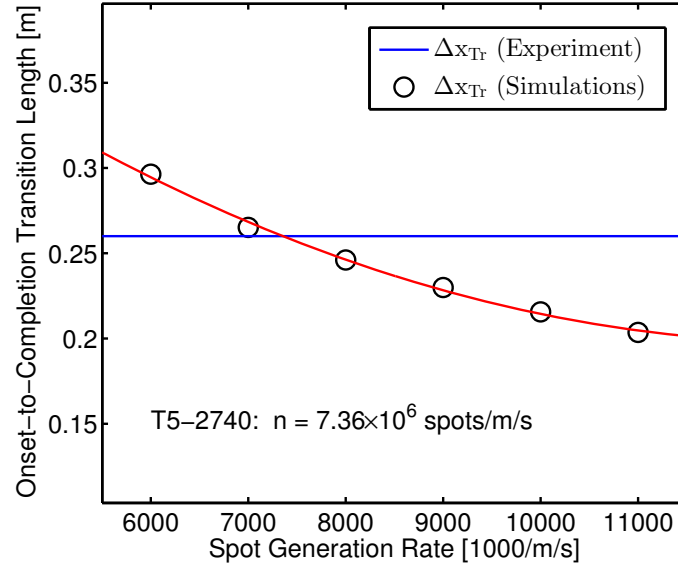
Figure 6.15: Computed and experimental transition distance Δx_{Tr} for shot 2740.

	Gas	h_{res} MJ/kg	P_{res} MPa	U_{e} m/s	$\mathrm{M_e}$	α deg	x_{Tr} m	x_{TrComp} m	unit Re 1/m	n 10^3/s/m
2714	Air	9.50	67.1	3877	4.75	3.3	0.49	0.73	7.47×10^6	9020
2739	Air	8.04	57.5	3606	4.90	3.2	0.56	0.80	7.77×10^6	8500
2740	Air	7.97	57.3	3593	4.91	3.2	0.54	0.80	7.82×10^6	7360
2741	Air	8.34	56.9	3663	4.86	3.2	0.56	0.81	7.38×10^6	8560
2744	Air	7.69	60.7	3538	4.95	3.2	0.51	0.76	8.64×10^6	8090
2760	Air	6.30	27.2	3221	5.09	3.1	0.51	0.75	4.64×10^6	8040
2761	Air	5.49	28.2	3039	5.26	3.0	0.49	0.72	5.24×10^6	8610
2762	Air	6.06	27.8	3169	5.13	3.0	0.49	0.77	4.89×10^6	5600
2763	Air	6.57	27.2	3281	5.05	3.1	0.53	0.77	4.47×10^6	8480
2764	Air	5.28	16.5	2974	5.26	3.0	0.53	0.80	3.20×10^6	6110
2776	N_2	7.17	45.9	3524	6.14	2.5	0.39	0.70	6.13×10^6	6820
2777	N_2	8.91	38.9	3876	5.90	2.6	0.49	0.79	4.44×10^6	6920
2778	N_2	10.73	41.4	4193	5.54	2.8	0.55	0.89	4.30×10^6	5950
2817	CO_2 50%	4.08	23.3	2519	4.59	3.4	0.50	0.83	6.73×10^6	3430
2819	CO_2 50%	5.66	39.8	2869	4.52	3.5	0.53	0.80	8.17×10^6	4840
2822	Air	8.18	42.9	3622	4.87	3.2	0.51	0.81	5.65×10^6	5690
2823	Air	8.77	42.6	3732	4.81	3.2	0.53	0.80	5.16×10^6	6360

Table 6.2: Spot generation rates computed for transition onset-completion length (Δx_{Tr}) during the present test campaign, taken from 17 tests for which clear transition onset (x_{Tr}) and transition completion (x_{TrComp}) locations were observed. The calculated spot spreading angle (α) and unit Reynolds number (unit Re) are included along with other relevant parameters. For these tests, $T_{\mathrm{w}}/T_{\mathrm{aw}}$ ranged from 0.05 to 0.12, and $T_{\mathrm{w}}/T_{\mathrm{e}}$ ranged from 0.18 to 0.38.
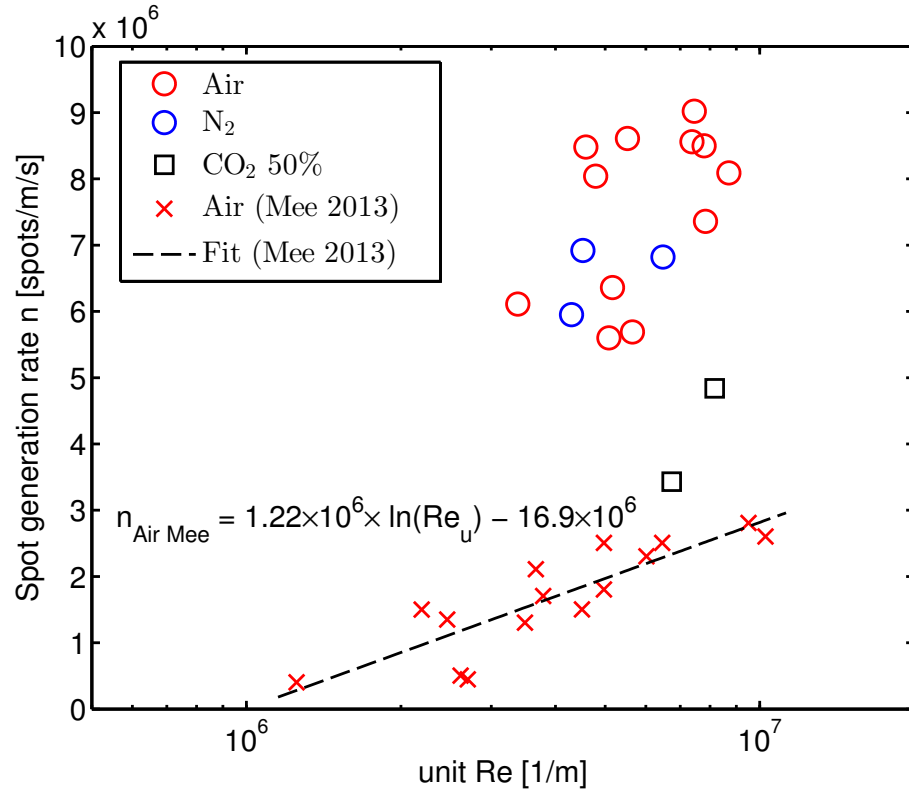
Figure 6.16: Spot generation rates for the present data compared with the results from Mee and Tanguy (2013).
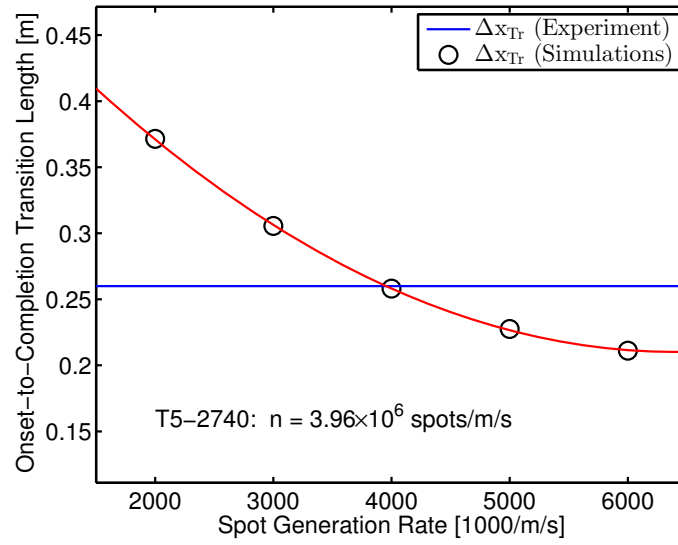
Figure 6.17: Computed and experimental transition distance Δx_{Tr} for shot 2740 with $C_{\text{te}} = 0.5$, which was the value used by Mee and Tanguy (2013). Compared with the computations in Figure 6.15, the matching value of n for the observed transition length drops by 3.4×10^6 spots/m/s. This accounts for most of the difference between the present computations and those of Mee and Tanguy (2013).

6.4   Comparison with Past Turbulent Spot Studies

6.4.1   Experimental

In addition to the results from Mee and Tanguy (2013) for the spot generation rate n, the present experimental results for C_{le}, C_{m} and C_{te} may be compared with other experimental supersonic and hypersonic results at similar and disparate boundary layer edge conditions, presented in the same format as the left four cases in Table 6.3.

Clark (1993) and Clark et al. (1994) studied the propagation of naturally occurring turbulent spots in turbine-representative flows from Mach 0.24 to Mach 1.86 using platinum thin-film heat transfer gauges to track individual spots. Clark characterized turbulent spot leading-edge, trailing-edge, and "mean" or centroid velocities, and also measured the spreading angle at several Mach numbers in this range. Clark also examined the propagation of turbulent spots in mild and strong pressure gradients both favorable and adverse.

Hofeldt, Jr. (1996) studied spots in flows from Mach 0.24 to Mach 1.86 using thin-film heat transfer gauges, examining the effect of gas-to-wall temperature ratios as well as the overhang region, in which the turbulent spot's spatial extent in the downstream direction is greater further from the plate, and observing "becalmed" regions behind turbulent spots. Hofeldt was able to show that the becalmed region behind a turbulent spot is in fact consistent with the re-establishment of a laminar boundary layer.

Mee and Goyne (1996) performed experiments to detect turbulent spots on a flat plate in free-piston shock tunnel flows of Mach 5.6 to 6.1 at low, mid-range, and high unit Reynolds numbers (unit Re_x between $1.6 \times 10^6 \text{ m}^{-1}$ and $4.9 \times 10^6 \text{ m}^{-1}$) using thin-film heat transfer gauges. They were able to detect turbulent spot activity and measure intermittency, and recommended further tests to measure convection speeds and spreading rate. Mee (2002), using the same facility as Mee and Goyne (1996)

with new instrumentation, measured the effect of using 2 mm-high boundary layer "trips" behind the leading edge of a flat plate in Mach 5.5 to Mach 6.3 flow and found them to be capable of advancing the transition location. Mee measured a spot growth angle of $3.5° \pm 0.5°$.

Fiala et al. (2006) measured turbulent spots progressing on a blunt cylindrical body with spherical nose in super/hypersonic flow (Mach 8.9 free stream; Mach 3.5 at the edge of the boundary layer) using a series of thin-film heat transfer gauges. They were able to detect clear turbulent spot activity and measure intermittency by comparing heat transfer time histories from axial gauges in the intermittent region of the body, and also visualize the passing signals from individual spots with a circumferential array of gauges.

Laurence et al. (2012) measured the propagation speed of instability waves in a hypersonic boundary layer on a 7.0° half-angle cone ($h_{res} = 3.4$ MJ/kg, $P_{res} = 28.5$ MPa, $M_e = 6.34$) and found[4] a normalized propagation velocity $C = 0.83 \pm 0.02$. While this measurement was for a wave packet rather than a turbulent spot, the propagation speed with uncertainty is close to the peak propagation velocity $C_m = 0.76 \pm 0.04$.

6.4.2 Computational

Computational studies of spot propagation in supersonic flows have been carried out by Chong and Zhong (2005), Krishnan and Sandham (2006), and Jocksch and Kleiser (2008). Most recently, Sivasubramanian and Fasel (2010) performed DNS of turbulent spot evolution on a cone in Mach 6 cold flow and observed the breakdown of two-dimensional second mode disturbances into a three-dimensional wave packet or spot. The present experimental results for C_{le}, C_m and C_{te} may be compared with

---

[4]Laurence et al. (2012) report propagation speeds between 1910 and 1995 m/s; these have been normalized to a ratio of the boundary layer edge velocity based upon reported freestream conditions and a Taylor-Maccoll solution for a 7.0° half-angle cone.

computational supersonic and hypersonic results at similar and disparate boundary layer edge conditions, presented in the same format as the right four cases in Table 6.3.

The computations of Krishnan and Sandham (2006), Jocksch and Kleiser (2008), and Sivasubramanian and Fasel (2010) are most representative of the present conditions and these authors' spot propagation speeds are reasonably consistent with our experimental results, with the exception of one trailing edge velocity from Jocksch and Kleiser (2008). This case has the $T_{\mathrm{w}}/T_{\mathrm{aw}}$ that most closely matches the present T5 results. The wall temperature and adiabatic wall temperature ratios for the present study are presented graphically in Figure 6.18.

Jocksch (2009) observes that the cold wall C_{te} is nearly equal to the trailing edge velocity for a linear wave packet at the same conditions, and hypothesizes that the cooled spot is elongated due to boundary layer linear stability properties. However, the Jocksch and Kleiser (2008) cold wall C_{te} value is much slower than any reported experimental result for this velocity, including the Fiala et al. (2006) and Mee (2002) results, which bracket Jocksch in terms of $T_{\mathrm{w}}/T_{\mathrm{aw}}$. On the other hand, the Fiala et al. (2006) and Mee (2002) C_{te} results are quite consistent with the present study. One possible explanation for this discrepancy is the structure of the simulated spots, which for the cold wall case have a long trailing edge that is only minimally elevated in terms of skin friction and Stanton number from the background values (*e.g.*, Jocksch (2009) Figures 3.51–3.54). It is quite likely that the thermocouples of the present study, and even the thin-film gauges used by Fiala et al. (2006) and Mee (2002), do not fully resolve this long tail if it exists, leading to an under-measurement for C_{te}.
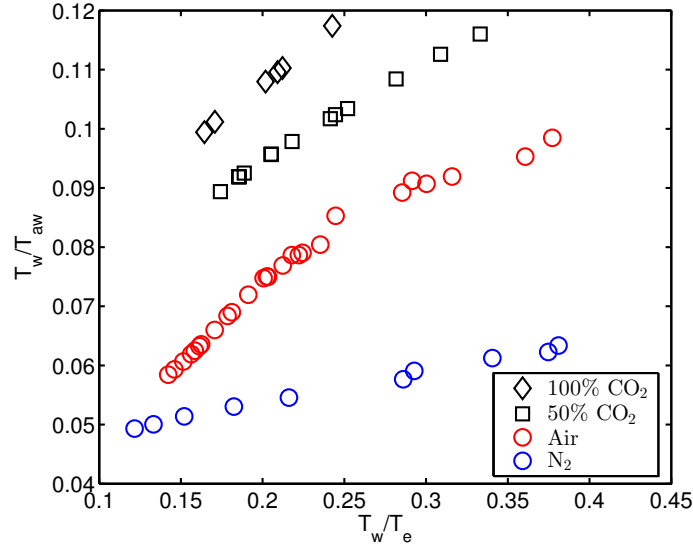
Figure 6.18: T_w/T_{aw} and T_w/T_e for the present study. These cold wall properties are far removed from the near-adiabatic conditions available in cold flow experimental hypersonic facilities and most commonly computed in the literature.

	Z&H 1996	Fiala 2006	Mee 2002	Clark 1994	K&S 2006	J&K 2008	J&K 2008	S&F 2010
Type	Exp.	Exp.	Exp.	Exp.	Comp.	Comp.	Comp.	Comp.
M_e	8.02 [b]	3.5	6.1	1.86	6	5	5	5.35
U_e [m/s]	[a]	1300 [b]	3370	580 [b]	[a]	[a]	[a]	875 [b]
unit Re [/m]	[a]	2.9×10^6	4.9×10^6	16.0×10^6	[a]	[a]	[a]	14.3×10^6
T_w/T_e	4.38 [b]	0.97 [b]	0.37 [b]	1.23 [b]	7	5.19	1	5.7
T_w/T_{aw}	0.37 [b]	0.32 [b]	0.065 [b]	0.77 [b]	0.98 [b]	1	0.19 [b]	1
C_{le}	0.98	0.81	0.90 ±0.10	0.83 ±0.04	0.89	0.96	0.89	0.91
C_m	–	0.60–0.69	–	0.64 ±0.02	0.76 [c]	–	–	–
C_{te}	0.68	0.40	0.50 ±0.10	0.53 ±0.02	0.53	0.54	0.23	0.79

[a] Value not reported.
[b] Calculated from other reported values.
[c] Spot "wing tip" convection velocity.

Table 6.3: Results from past spot propagation studies, based on supersonic and hypersonic experiments (Zanchetta and Hillier (1996), Fiala et al. (2006), Mee (2002), and Clark et al. (1994)) and computations (Krishnan and Sandham (2006), two results from Jocksch and Kleiser (2008), Jocksch (2009) and Sivasubramanian and Fasel (2010)) reported for a range of conditions and presented together in this table.

6.5 Conclusions

Time- and spatially-resolved heat transfer traces in a high-enthalpy hypervelocity flow on a 5-degree half-angle cone are measured with thermocouples. Turbulent spots are

observed propagating in both heat transfer traces and heat flux "movies" of the developed cone surface. These observations are used to calculate turbulent spot convection rates, which are compared with previous experimental and computational results. Although the present results were obtained at different conditions from past experiments, the normalized spot propagation results for the present Mach ~ 5 conditions appear to be generally consistent with past supersonic and hypersonic experiments, as well as with the computational results.

However, the flow conditions in all of the reviewed simulations are essentially nonreactive (cold flow with frozen composition), and the ratios of freestream to wall temperature, as well as adiabatic to nonadiabatic wall temperature, in the simulations are far from our experimental conditions. The flow conditions in these T5 tests are designed to simulate hypervelocity atmospheric flight and the flow over the model is hot, partially dissociated gas with some amount of chemical and vibrational nonequilibrium due to the rapid expansion process in the nozzle. The available computational results of spot propagation in hypersonic flow in the present literature survey simulated much higher wall temperature ratios T_w/T_e and adiabatic wall temperature ratios T_w/T_{aw} than actually occur in either reflected shock tunnel experiments or flight (see Table 6.3 and Figure 6.18).

At present, there are no high Mach number computational turbulent spot propagation studies in the literature which fully match the low wall-temperature ratios which are characteristic of high-enthalpy shock tunnels like T5 and T4. At lower Mach numbers, such as the results of Clark et al. (1994), the subsonic (first) mode is the dominant linear boundary layer instability mechanism. At hypersonic Mach numbers (> 4), instabilities in the second (Mack) acoustic mode dominate the boundary layer transition mechanism. For cold-wall hypervelocity flow with a hot freestream, the first mode is expected to be damped and the higher inviscid modes are amplified, so that the second mode would be expected to be the only mechanism of linear in-

stability. The present results are thus most directly comparable, in terms of Mach number and wall temperature ratio, to the flat plate T4 results of Mee (2002), and indeed are largely within the uncertainty range of Mee's measurements. Computations with realistic wall-temperature ratios would be quite valuable for comparison with the present experiments.

While the design of the experiment precludes precise measurement of spot spreading angle α, approximate bounding values for this parameter have been obtained. For example, for shot 2654, we estimate $2° < \alpha < 13°$. This result brackets the reported value of $3.5° \pm 0.5°$ of Mee (2002) for similar Mach numbers, as well as the reported value of $6.75° \pm 1.0°$ of Fiala et al. (2006) for lower Mach numbers. These are the two nearest experimental studies to the present work in terms of conditions. Both of these values are also consistent with the Mach number–spreading angle relationship, Equation (6.1), reported in Doorley and Smith (1992). More precise measurements of spreading angle would be possible with the addition of thermocouples in a more circumferentially dense pattern. The relatively small uncertainty on the spreading angle measurements in Mee (2002) and Fiala et al. (2006) is due to the use of densely packed thin film arrays extending on the test article surface in the direction orthogonal to the flow field. Mee (2002) used seven sensors at 5 mm pitch and Fiala et al. (2006) used 18 sensors at 4 mm pitch. By contrast, the present work uses rows of four sensors at pitches ranging from 19.2 mm for the first row to 82.1 mm for the last row.

With the measured parameters, a simple geometric model for the propagation of turbulent spots has been adapted from Jewell (2008) and used, following Mee and Tanguy (2013), to infer turbulent spot generation rates n from a set of 17 experimentally measured transition onset and completion distances in three different gas mixtures. The results indicate that n is significantly higher in air and N_2 boundary layers than for experiments with 50% CO_2. While spot generation rates were higher than those found by Mee and Tanguy (2013), most of the difference is accounted for by differing

model inputs for C_{te}, and the Mee results were acquired on a flat plate in a different facility.

The present results represent the first attempt to infer turbulent spot generation rate in T5, as well as the best available data on the effect of CO_2 on spot formation in a hypervelocity boundary layer. Turbulent spot generation is the outcome of the boundary layer receptivity process (Fedorov, 2003) and its characterization is therefore important for understanding both receptivity and the region of intermittent turbulence which occurs between transition onset and completion. In particular, predicting the time-resolved heat flux in this region, both for flight and for ground tests, depends upon a model for turbulent spot generation and propagation. As different tunnels have disparate acoustic spectra, particulate contamination properties, and other noise and disturbance sources, information about the spot generation rate in each facility is also important for comparing transition measurements to each other, especially the onset to completion distance.

Chapter 7

Gas Injection Study

7.1   Injector Design and Review

Chapters 3 and 5 described experiments with freestream mixtures of CO_2 and air and presented results, which indicate that under the right conditions, the presence of CO_2 in the boundary layer can be advantageous in delaying transition onset in terms of both Reynolds number and nondimensional distance. Chapter 6 further inferred that turbulent spot generation rates may be lower in boundary layers containing CO_2. However, adjusting the atmosphere through which a hypervelocity vehicle flies is usually not possible. To take advantage of the apparent transition delay mechanism, CO_2 must be inserted into the boundary layer through another mechanism. Leyva et al. (2009a) describe the present study's early efforts to devise a workable gas injector. Designs with one and four rows of 36 discrete 0.76 mm diameter holes, with a length-to-diameter ratio of 30, were both found to promote transition onset earlier on the cone than comparable smooth baseline cases. For the four-row injector geometry fully turbulent heat transfer values were observed within 5.5 cm of the last injection row for both freestream conditions examined. This effect was present for all CO_2 injection rates examined, as well as for all cases with no injection. The discrete orifices were actually found to be more effective boundary layer "trips" than protrusions of similar dimensions. Recently, Ward et al. (2013) have used similar discrete-geometry

holes in a more controlled fashion as pulsed jet perturbers to produce transition with high amplitude disturbances.
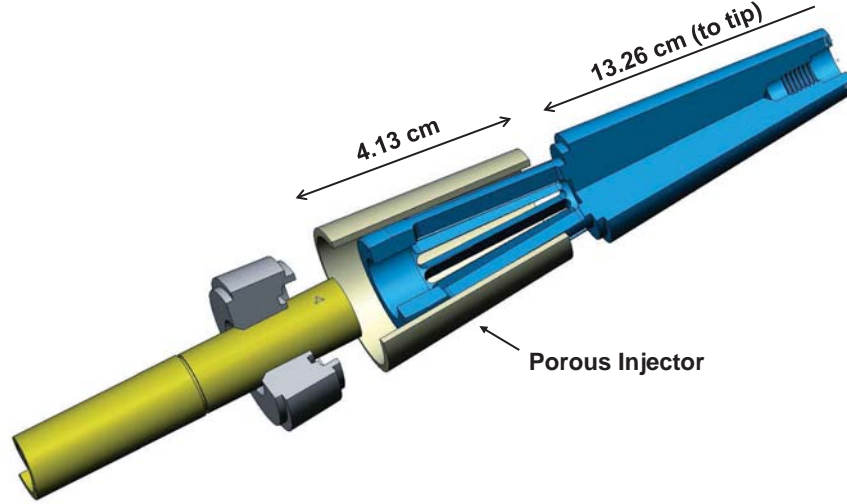
Figure 7.1: Rendering of the injector section of the cone, showing the porous injector surrounded by its plastic holder, and the pipe's position in the plenum. The replaceable molybdenum tip threads into the plastic section at upper right, and the entire apparatus is mounted to the aluminum cone with the pipe and annular mating piece at lower left. See also Figure 7.2. (Drawing by Bahram Valiferdowsi.)

Leyva et al. (2009a) also describe the earliest work with the porous injector design shown in Figure 7.1, which was intended to create more spatially uniform mass injection than is possible with macroscopic holes. The porous injector section, pictured in Figure 7.2, is 4.13 cm in length and consists of sintered 316L stainless steel. The manufacturer, Mott Corporation of Farmington, Connecticut, describes their porous material in terms of "media grade", which corresponds to the minimum restriction size in each pore. As the pore sizes are irregular, this dimension is related to, but not identical with, the pore size as observed on the surface of the injector. The injector for the present study has a media grade of 10 μm (Mott Corporation, 2010). Leyva et al. (2009a) found that for sufficiently high mass flow rates, corresponding to a boundary layer mass flow fraction of 0.48 at the injector (see Section 7.3.3 for details

158

on the calculation of boundary layer mass flow) early transition still occurred for the porous design, but the baseline case with no gas injection did not measurably affect the location of transition onset. Based on these preliminary experiments, conditions for the lower injection rate series described in Section 7.4 were selected.

Figure 7.2: Photograph of the 10 μm media grade porous injector section against a 6.35 mm grid. See also Figure 7.1.

Schneider (2010) reviewed transition experiments performed with blowing and ablation in various configurations with the goal of summarizing data suitable for validating semi-empirical transition prediction methods, including the e^N method discussed in Section 4.2. The review encompassed the interaction of transition location with both discrete (individual orifices, such as those used in Leyva et al. (2009a)), and distributed (primarily, porous sintered metal similar to that pictured in Figure 7.2) boundary-layer injection systems. For each experiment reviewed the measured transition location, after reaching a threshold, moved upstream with mass injection. This effect was observed in general for injection or ablative blowing of air, nitrogen, argon, helium, methane, ethylene, Freon-12, and paradichlorobenzene, in a variety of ground test facilities including arcjets, ballistic ranges, Ludwieg tubes, blowdown tunnels, and shock tunnels. In general, for slender non-lifting geometries (e.g., the 5° half-angle cone of the present study), lighter gases tended to move transition further upstream than heavier gases at the same mass flow rate. One study, performed

by Martellucci and Rie (1971), reported that air mass injection at low mass flow rates was destabilizing, but at higher mass flow rates the injection was stabilizing. Schneider (2010) states of that result: "The downstream movement of transition for higher blowing rates is very surprising and must be viewed skeptically unless it can be supported by additional information. It seems possible that there is some error in the inferences from the surface impact pressures." Notably, none of the reviewed studies involved carbon dioxide injection. The present study examines the impact of carbon dioxide gas injection on high enthalpy boundary layers both computationally and experimentally.

7.2   Analysis of Injector Flow Path

The steady mass flow rate for a given pressure drop through the 10 μm porous injector pictured in Figure 7.2 was measured using a Sensirion EM1 inline thermal mass flow meter accurate to 3% of the indicated value. The meter arrived with an air calibration, but was recalibrated for CO_2 and Ar using a King 7205-0061-A rotameter with dual scales for the two gases. Because the porous media would provide significant back pressure in the line, the EM1 was calibrated for several different back pressure conditions, as shown in Figure 7.3 for CO_2, and was found to be insensitive to the degree of obstruction downstream as mediated by progressively closing a needle valve.

During the injection experiments described in Section 7.4 and earlier in Jewell et al. (2011), the pressure in the injection run tank was measured with a transducer, but no mass flow meter was installed in the injection flow path. The mass flow rate out of the run tank was calculated based upon the recorded pressure drop during each experiment's run time. However, Jewell et al. (2011) failed to account for the fact that most of the gas exiting the run tank during the test time went to fill the 4 m long evacuated injection line connecting the tank to the injector, and was not in fact
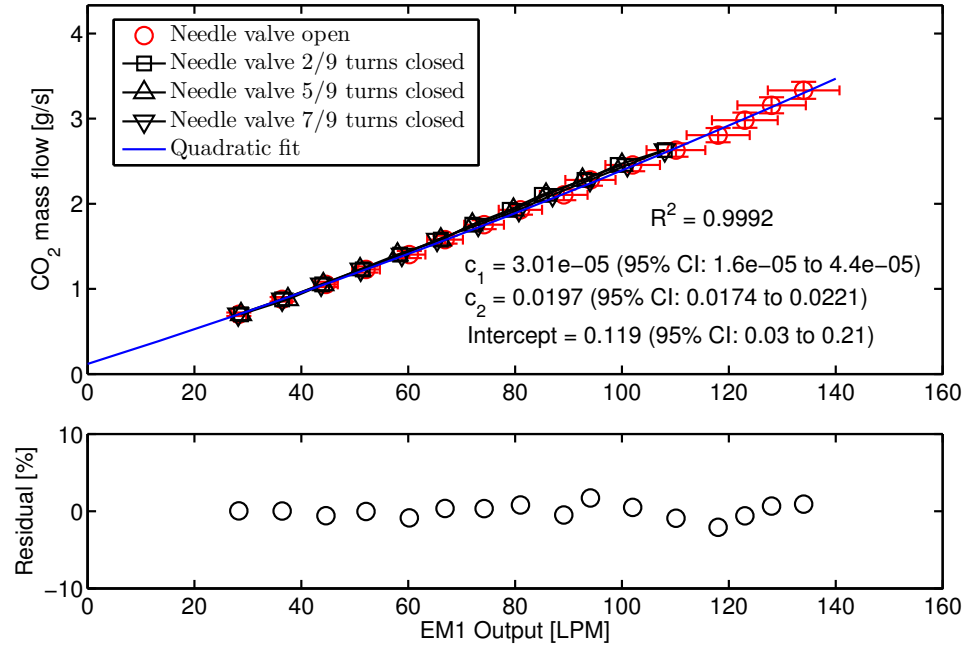
Figure 7.3: Sensirion EM1 (air) inline thermal mass flow meter calibrated against a rotameter for use in measuring CO_2 flows. The quadratic fit coefficients for the calibration are indicated as c_1 and c_2.

injected through the porous media into the boundary layer. The reported mass flow rates were therefore too high by more than an order of magnitude. To mitigate this error in any future work, the EM1 mass flow meter was selected for its small size, which would allow it to be placed directly into the flow path inside the cone, near the injector plenum. Should further injection experiments be carried out, this is recommended. However, as will be shown below, the pressure drop in the flow path between the run tank and the injector plenum is minimal for the relevant conditions, and the true mass flow rates through the injector section for the experiments in Section 7.4 may therefore be found based upon the *ex post facto* porous media calibration, using the measured run tank pressure and the calculated pressure at the boundary layer edge, P_e, to find the pressure differential upon which the mass flow rate depends.

Figure 7.4 is a schematic of the injector flow path. It will be shown that for relevant conditions, the run tank pressure $P_1{'}$ is essentially identical to the plenum pressure P_1, which implies that the correct mass flow rates may be determined from
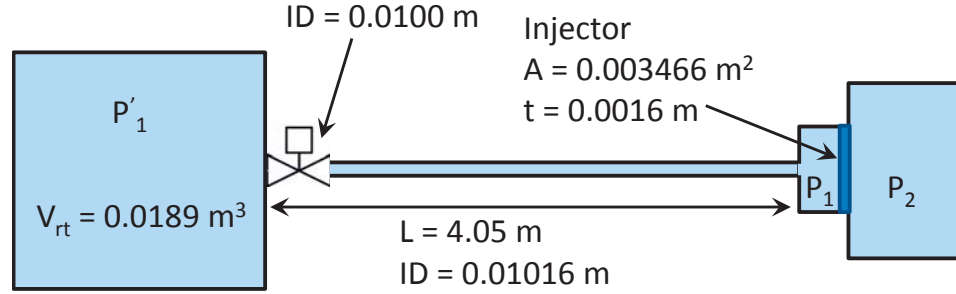
Figure 7.4: Schematic (not to scale) diagram of the injector flow path showing pipe length, on/off ball valve with an opening time of ~30 ms, sharp-edged entrance at the run tank, and sharp-edged entrance exit into the plenum behind the porous metal injector, which injects into the test section (a total of four junctions and three 90° turns between the ball valve and the plenum are omitted for clarity, but are included in the pipe analysis: see Table 7.1).

a steady-state calibration on the pressure drop from P_1 to P_2. First, assume a CO_2 mass flow rate of 0.5 g/s from the maximum tested run tank pressure $P_1' = 172$ kPa. As it happens, this is about 25% higher than the maximum mass flow rate observed in the experiments, and therefore would be expected to exceed the maximum pressure drop for any of the conditions treated below. Flow velocity at the outlet of the tank, U_1, can be calculated from the tank temperature, pressure, and the outlet area:

$$U_1 = \frac{\dot{m} R T_1}{P_1' A_{\text{pipe}}}$$

For CO_2 at the conditions described, $U_1 = 2.01$ m/s. The Reynolds number based on pipe diameter D is defined as:

$$\mathrm{Re}_D = \frac{\rho U_1 D}{\mu}$$

For the present pipe internal diameter $D = 0.01016$ m, $\mathrm{Re}_D \approx 5000$, so the flow is expected to be turbulent. For turbulent pipe flow, from Anderson (1990) equation 3.97, the effects of shear stress can be expressed in terms of a friction coefficient f, and for a calorically perfect gas the variation of the mean cross-sectional flow properties between two locations in the pipe, x_1 and x_2, can be recast in terms of the Mach

numbers M_1 and M_2 at each location to find the friction equation:

$$\int_{x_1}^{x_2} \frac{4f \mathrm{d}x}{D} = \left[-\frac{1}{\gamma M^2} - \frac{\gamma+1}{2\gamma} \ln \left(\frac{M^2}{1 + \frac{\gamma-1}{2}M^2} \right) \right]_{M_1}^{M_2} \tag{7.1}$$

Taking $x = L^*$ as the distance where $M = 1$,

$$\frac{4\bar{f}L^*}{D} = \left[\frac{1 - M^2}{\gamma M^2} + \frac{\gamma+1}{2\gamma} \ln \left(\frac{(\gamma+1)M^2}{2 + (\gamma - 1)M^2} \right) \right] \tag{7.2}$$

Here, $\bar{f}$ is an approximate average (or constant) value for the friction factor. For a Swagelok stainless steel tube, the equivalent roughness ε is about 0.0015 mm. Therefore, from $\varepsilon/D = 1.48 \times 10^{-4}$ and Re_D, the friction factor $f = 0.031$ may be found from a Moody diagram, and is used as $\bar{f}$.
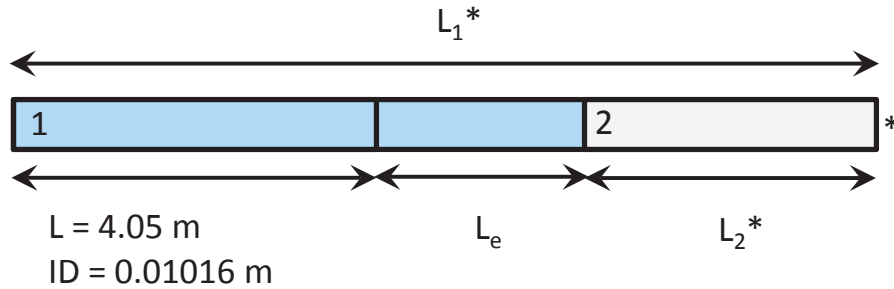
Figure 7.5: Schematic (not to scale) diagram of the physical pipe length L and total equivalent length of the fittings L_e, with notional sonic pipe lengths from stations 1 and 2 indicated as L_1^* and L_2^*. Finding the conditions at which sonic velocity is reached at station * for the two pipe lengths L_1^* and L_2^* permits the calculation of conditions at station 2.

The so-called minor losses due to pipe system components in the flow path may be represented, for approximately known conditions, as an equivalent lengthening of the tube by a quantity L_e. Numerical values for the loss coefficients of various fittings must be determined empirically; the coefficients used here are from Moran et al. (2003) and tabulated along with their computed equivalent lengths in Table 7.1. The integral on the left hand side of Equation (7.1) can be expressed with L_1^* and

Component	Quantity	Loss Coeff. K_L	Equiv. Length L_e (each) [m]
90° bend	3	0.30	0.0798
Fully open ball valve	1	0.05	0.0133
Union, threaded	4	0.08	0.0213
Entrance, sharp-edged	1	0.50	0.1330
Plenum exit, sharp-edged	1	1.00	0.2660
			Total $L_e = 0.737$ m

Table 7.1: Loss coefficients for injection system components from Moran et al. (2003), converted into equivalent pipe lengths.

L_2^* taken as the length of tube necessary for the flow to reach sonic velocity from the conditions at station 1 and station 2, respectively (see Figure 7.5).

$$\frac{4\bar{f}(L + L_e)}{D} = \frac{4\bar{f}L_1^*}{D} - \frac{4\bar{f}L_2^*}{D} \tag{7.3}$$

For a pipe of the given diameter, length, components, and assumed constant friction coefficient, we have:

$$\frac{\bar{f}(L + L_e)}{D} = 17.7$$

Equations (7.2) and (7.3) can be solved iteratively to find M_2, which is in turn used with M_1 to calculate the change in pressure and temperature from adiabatic relations:

$$\frac{T_2}{T_1} = \frac{2 + (\gamma - 1)M_1^2}{2 + (\gamma - 1)M_2^2}$$

$$\frac{P_2}{P_1} = \frac{M_1}{M_2}\sqrt{\frac{2 + (\gamma - 1)M_1^2}{2 + (\gamma - 1)M_2^2}}$$

Mach number M_1 can then be found from:

$$M_1 = \frac{U_1}{\sqrt{\gamma RT}}$$

For a CO_2 mass flow rate of 0.5 g/s and run tank pressure $P_1' = 172$ kPa, $M_1 = 0.00745$. The solution of Equations (7.2) and (7.3) is found by iteration to be

$M_2 = 0.007469$. Therefore, $P_1/P_1' = 0.9974$ and $T_1/T_1' = 0.99999996$, so there is a maximum pressure drop of less than 0.3% in the injection system, and virtually no temperature change. Therefore, the conditions in the injector plenum are assumed to be the conditions in the run tank. The resulting corrected mass flow rates are recorded as part of Table 7.4 in Section 7.4.

7.3 Calculations and Computations

7.3.1 Adaptation of Similarity Solution to Mass Injection

With new boundary conditions, the formulation in Section 4.1.1 may be extended to flows with injection (or suction), as long as the injection velocity varies with a certain profile to satisfy the laminar similarity solution. The injection profile must satisfy $v_{\mathrm{w}} \sim 1/\sqrt{x}$, where v_{w} is the wall injection velocity. This does not match the assumed physical condition of approximately constant injection per area on the injector section, but even if not exact this approach permits the exploration of trends in the boundary layer with increasing and decreasing injection. For this self-similar injection profile, the boundary conditions are:

For injection:

$$f(0) = -v_{\mathrm{w}} \neq 0$$

From the no-slip condition:

$$f'(0) = 0$$

From freestream velocity:

$$f'(\infty) = 1$$

From freestream enthalpy:

$$g(\infty) = 1$$

From constant wall temperature:

$$g(0) = \frac{C_{p_\mathrm{w}} T_\mathrm{w}}{C_{p_\mathrm{e}} T_\mathrm{e}} = \frac{T_\mathrm{w}}{T_\mathrm{e}}$$

The suction-blowing parameter may be normalized as:

$$v_\mathrm{w}^* = \frac{v_\mathrm{w}}{U} \sqrt{\mathrm{Re}_x} = \frac{-f(0)}{\sqrt{2}}$$

Results for the boundary layer profiles $f'(\eta) = u/U_\mathrm{e}$ for this injection condition are presented for several values of v_w^* in Figure 7.6. The solution does not converge beyond $v_\mathrm{w}^* \approx 0.4315$, which may represent the limiting case before the boundary layer is entirely "blown off" the surface of the cone. Solutions for $u/U_\mathrm{e} = f(y)$ and $T/T_\mathrm{e} = g(y)$, with freestream conditions corresponding to experiment 2609 ($h_\mathrm{res} = 9.62$ MJ/kg, $P_\mathrm{res} = 55.7$ MPa) and with the maximum converging value of the normalized suction-blowing parameter v_w^*, are found in Figure 7.7 next to comparison plots for the same solutions with $v_\mathrm{w}^* = 0$. Similarity solutions of this form are computationally inexpensive and useful as a guide to the general properties of the compressible boundary layer on a 5° half-angle cone with gas injection, including the distorted velocity profiles near the wall. However, a more sophisticated approach, detailed in Section 7.3.4, is necessary to model the nonsimilar and nonequilibrium stability properties of the boundary layer with injection.
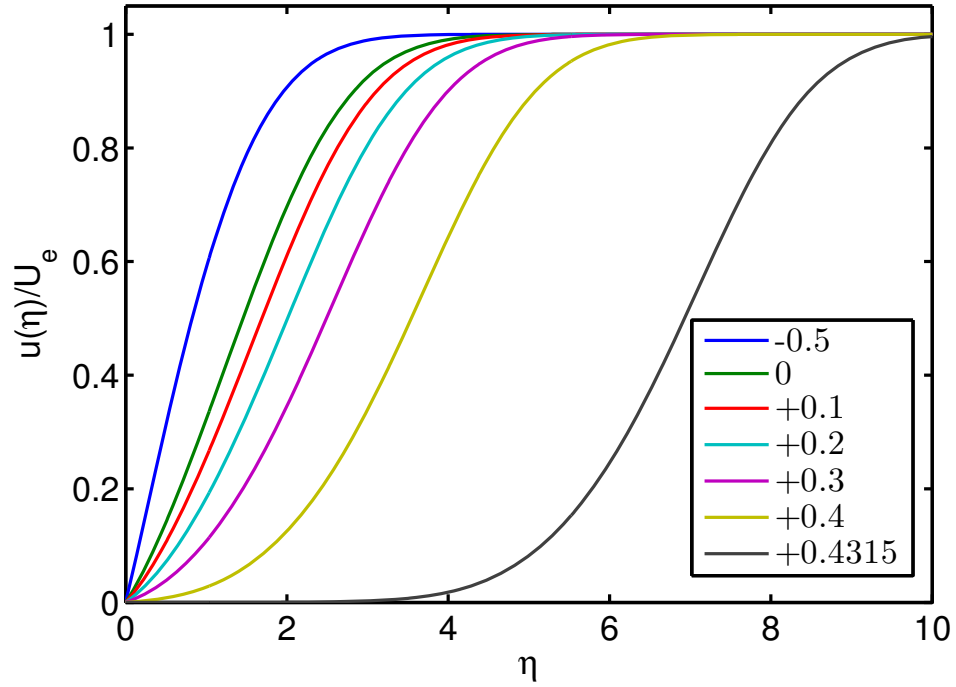
Figure 7.6: Wall-parallel velocity profiles for various values of the suction/blowing parameter v_w^* up to a limit of $v_w^* \approx 0.4315$, after which the solution breaks down and the boundary layer has been "blown off". Note the significant effect on velocity near the wall that large values of the suction/blowing parameter have as they approach the limit.
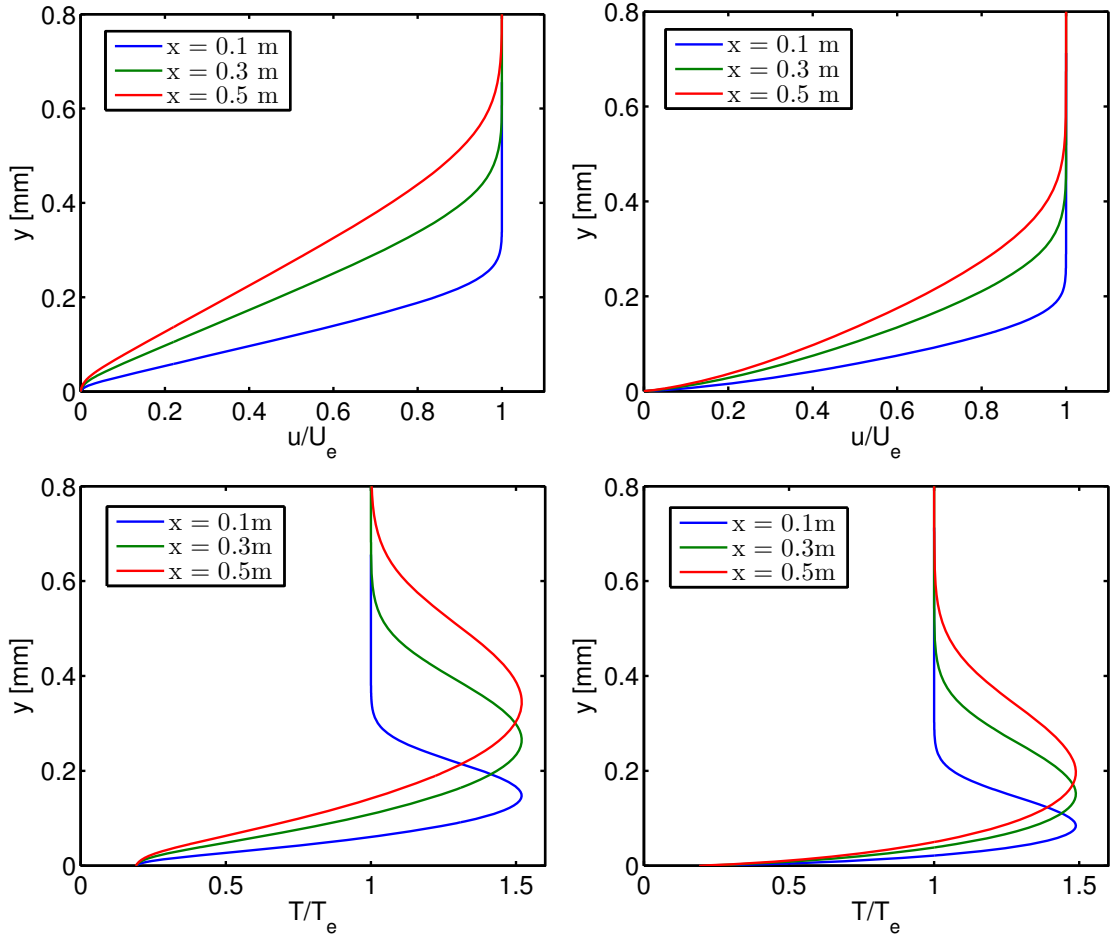
Figure 7.7: $u/U_e = f(y)$ and $T/T_e = g(y)$ with freestream conditions corresponding to experiment 2609 with maximum normalized suction-blowing parameter $v_w^* \approx 0.4315$ (left) compared to $v_w^* = 0$ (right). Blowing tends to thicken the boundary layer and also creates a layer of relatively cold, low-velocity gas near the wall.

7.3.2 Diffusion Coefficients of Carbon Dioxide and Argon

For any acoustic absorption to take place, injected CO_2 must be thoroughly mixed into the mean flow boundary layer. Assuming that the boundary layer at the point of injection is and remains laminar, turbulent mixing will not occur. A lower bound on the mixing may be found by considering only the diffusion of CO_2 into air, neglecting turbulence and convection. Following Anderson (2006) and modifying and expanding Beierholm et al. (2008), a calculation to approximate diffusion coefficients follows. First define a binary diffusion coefficient (mass diffusivity), from kinetic theory, for the diffusion of one species, designated A, into another, designated B:

$$D_{AB} = K'_D \frac{\sqrt{T^3}}{P\sigma}$$

Here P is pressure, σ is the collision cross-section for the two species, and K'_D is a constant. This quantity, with units of cm^2, may be calculated from Eq. 16.19 in Anderson (2006):

$$D_{AB} = 0.0018583 \frac{\sqrt{T^3 \left(\frac{1}{M_A} + \frac{1}{M_B}\right)}}{P d^2_{AB} \Omega_{d,AB}}$$

Here P is in atm, d_{AB} is the characteristic molecular diameter in Å, and $\Omega_{d,AB}$ is a collision integral which depends upon temperature and the characteristic energy of interaction in the form $k_1 T/\varepsilon_{AB}$, and is tabulated in Anderson (2006). The parameters d_{AB} and ε_{AB}/k_1 are associated with the Lennard-Jones model for the interaction of two molecules. The quantities ε_{AB} and d_{AB} may be taken as:

$$d_{AB} \approx \frac{1}{2}(d_A + d_B) \tag{7.4}$$

$$\varepsilon_{AB} = \sqrt{\varepsilon_A \varepsilon_B} \tag{7.5}$$

See Table 7.2 for a compilation of values necessary to calculate the binary diffusion coefficient, taken from Anderson (2006) Table 16.1.

Gas	Molecular Weight g/mol	σ Å	ε_{AB}/k_1 K
Ar	39.944	3.418	124
CO_2	44.01	3.996	190
N_2	28.02	3.681	91.5
Air	28.97	3.617	97

Table 7.2: Parameters used in the calculation of D_{AB}.

For the present experiments, the injectant gases were Ar (as a control) and CO_2, and the boundary layer mean flow gases are N_2 and air. See Table 7.3 for a compilation of values taken or interpolated from Anderson (2006) Table 16.2 and evaluated at typical T5 boundary layer conditions: boundary layer edge temperature[1] 1600 K and boundary layer edge pressure 37.0 kPa. Results of D_{AB} calculations for the four possible injectant-atmosphere combinations are also recorded in Table 7.3.

Injectant–Atmosphere	d_{AB} Å	ε_{AB}/k_1 K	$k_1 T/\varepsilon_{AB}$	$\Omega_{d,AB}$	D_{AB} cm^2/s
Ar–N_2	3.550	106.5	14.95	0.704	9.13
Ar–Air	3.518	109.7	14.52	0.707	9.17
CO_2–N_2	3.839	131.9	12.07	0.726	7.42
CO_2–Air	3.807	135.8	11.73	0.729	7.44

Table 7.3: Results of diffusion coefficient D_{AB} calculations for four relevant injectant-atmosphere gas combinations, evaluated at $T = 1600$ K.

7.3.3 Mass-Concentration Boundary Layer

First define the Schmidt number, a dimensionless number which is the ratio of momentum diffusivity, or viscosity, and mass diffusivity, calculated in the section above:

[1]Figures 7.14 and 7.15 indicate that outside the immediate region of the injector, where the injectant is near room temperature, the boundary layer temperature profile is quickly recovered, especially for lower mass flow rates. A typical T_e is therefore chosen as an illustrative example for these simple diffusion calculations.

$$\mathrm{Sc} = \frac{\mu}{\rho D_{\mathrm{AB}}}$$

While this number will change with the mixture viscosity, which of course varies based upon relative species concentration, Kays et al. (2005) suggest that the viscosity term be evaluated for the medium of diffusion (here, air or N_2). Hirschel (2005) presents Fick's first law for the molecular transport of mass in a given direction (here, into the boundary layer, with the y-direction normal to the surface) based upon density, the diffusion coefficient D_{AB} calculated above, and the mass-fraction gradient $d\xi_{\mathrm{A}}/dx$ for a given species A diffusing into a second species B. The diffusion mass fluxes are equal and opposite, and given as:

$$j_{\mathrm{A}_y} = -j_{\mathrm{B}_y} = -\rho D_{\mathrm{AB}} \frac{\mathrm{d}\xi_{\mathrm{A}}}{\mathrm{d}y}$$

We introduce a species continuity equation for species A:

$$\frac{\partial \rho_{\mathrm{A}}}{\partial t} + \underbrace{\frac{\partial \rho_{\mathrm{A}} u}{\partial x}}_{1} + \frac{\partial \rho_{\mathrm{A}} v}{\partial y} = -\left(\frac{\partial j_{\mathrm{A}_x}}{\partial x} + \underbrace{\frac{\partial j_{\mathrm{A}_y}}{\partial y}}_{2} \right) + S_{m_{\mathrm{A}}}$$

Here $S_{m_{\mathrm{A}}}$ is a source term to account for chemical reactions, and $\rho_{\mathrm{A}} = \rho \xi_{\mathrm{A}}$, where ξ_{A} is the mass fraction distribution of species A. Taking the source term as zero, the magnitudes of convective transport in the x-direction (labeled "1" on the left hand side), assuming small transverse injection compared to the boundary layer mass flux, and molecular transport in the y-direction (labeled "2" on the right hand side) can be compared to find a mass-concentration boundary layer thickness, δ_M, by combining the continuity equation with the diffusion mass flux equation and eliminating negligible terms:

$$\underbrace{\frac{\partial \rho \xi_A u}{\partial x}}_{1} + \ldots \approx \ldots + \underbrace{\frac{\partial}{\partial y}\left(\rho D_{AB}\frac{\partial \xi_A}{\partial y}\right)}_{2} + \ldots$$

Using characteristic length scales L for the length of the body in the x-direction, and δ_M for the mass-concentration boundary layer that is sought, this can be written as:F

$$\frac{\rho \xi_A u}{L} \sim \frac{\rho D_{AB}\xi_A}{\delta_M^2}$$

Where the left hand side corresponds to the convective transport terms and the right hand side corresponds to the molecular transport terms. With further manipulation and the use of the Reynolds and Schmidt numbers this becomes:

$$\frac{\delta_M}{L} \sim \sqrt{\frac{D_{AB}}{uL}} \sim \frac{1}{\sqrt{\text{Re}_L \text{Sc}}}$$

And in terms of the x-variable instead of L:

$$\frac{\delta_M}{x} \sim \sqrt{\frac{D_{AB}}{ux}} \sim \frac{1}{\sqrt{\text{Re}_x \text{Sc}}}$$

Thus the new mass-concentration boundary layer thickness can be related to the flow boundary layer thickness, since $\delta \sim x/\sqrt{\text{Re}_x}$ for a laminar boundary layer, as:

$$\frac{\delta_M}{\delta} \sim \frac{1}{\sqrt{\text{Sc}}}$$

Using the diffusion coefficients calculated above, with the viscosity for air and N_2 calculated as before for $T_e = 1600$ K and $P_e = 37.0$ kPa, values of Sc of 0.78 are obtained for both Argon injection cases, and 0.96 for both CO_2 injection cases (cf. Kays et al. (2005) for CO_2 diffusion into air, which is also reported as 0.96 even though the conditions—"approximately normal atmospheric"—are quite different). Since the

Schmidt numbers for all four cases are $\mathcal{O}(1)$, the mass-concentration boundary layer should have a thickness δ_M on the same order as the flow boundary layer thickness δ, which is an indication that the injectant gas should diffuse throughout the boundary layer. This analysis corresponds to the physical case presented schematically in Figure 7.8. However, Figure 7.9 represents the experimental case, which is slightly different as the injector area is only a subset of the cone's surface. In the latter case, injectant concentration is zero in region 1 and the boundary layer develops conventionally. In region 2, the profiles are similar to profiles for the continuous injector case. In region 3, the velocity profile recovers, injectant concentration at the wall drops as no new injectant mass is being added, and the injectant mass-concentration profile flattens through diffusion. In region 4, the velocity profile is once again self-similar, and the injectant mass-concentration profile continues to flatten through diffusion as more freestream gas is entrained in the boundary layer.
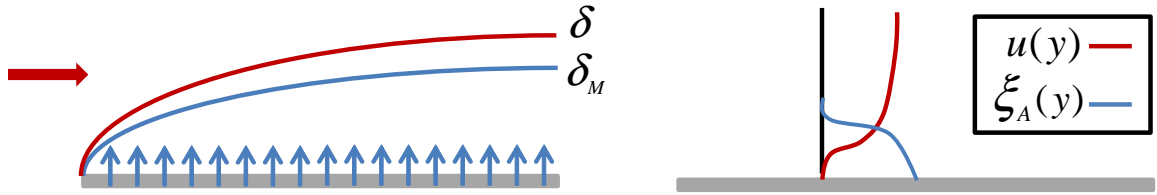
Figure 7.8: Injection distributed over the entire surface of the cone, analogous to the conditions corresponding to the present analysis. (Left) The flow boundary layer (thickness δ) and the mass flow boundary layer (thickness δ_M) develop from the same point. (Right) Possible profiles for velocity in the boundary layer $u(y)$, in red, and injectant A mass fraction in the boundary layer $\xi_A(y)$, in blue, are shown schematically at a particular x-position. These profiles will each vary with x.

If profiles for density and velocity within the boundary layer are known, the total boundary layer mass flow rate at a given x-position along the cone can be calculated in general as:

$$\dot{m} = 2\pi \int_0^\delta \rho u (x \sin\theta + y\cos\theta) \mathrm{d}y$$
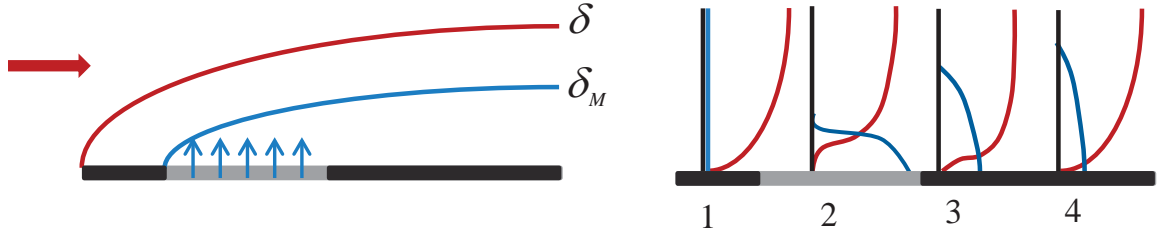
Figure 7.9: Injection distributed over only a portion of the cone's surface, analogous to real conditions. (Left) The flow boundary layer (thickness δ) develops upstream from the mass flow boundary layer (thickness δ_M). (Right) Possible profiles for velocity in the boundary layer $u(y)$, in red, and injectant A mass fraction in the boundary layer $\xi_A(y)$, in blue, are shown schematically at four particular x-positions.

where θ is the cone half-angle. The calculated mean flow boundary layer mass flow for experiment 2609 ($h_{\text{res}} = 9.62$ MJ/kg, $P_{\text{res}} = 55.7$ kPa) is presented in Figure 7.10. If, additionally, the profile for mass fraction of A within the boundary layer is known, the mass flow rate of injectant A in the boundary layer at a given x-position along the cone can be calculated as:

$$\dot{m}_A = 2\pi \int_0^\delta \rho u \xi_A (x \sin\theta + y \cos\theta) \mathrm{d}y \tag{7.6}$$
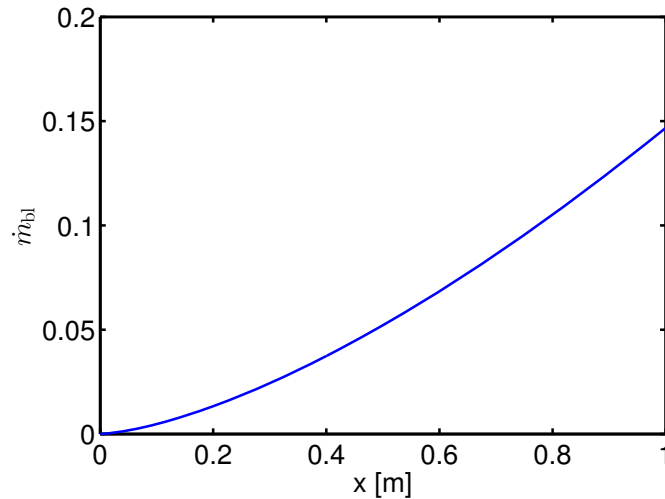
Figure 7.10: Shot 2609, $\dot{m}_{\text{bl}}$ from the similarity solution.

Since the mass injected into the boundary layer per unit time is known through

measurement of the mass flow rate, it is possible to calculate the average mass flow fraction (in other words, the mass flow fraction at every point in the boundary layer if complete mixing occurs) of the injectant through the boundary layer at any given position along the surface of the cone by assuming that the mean flow boundary layer profiles match those computed above for the conditions of shot 2609. Essentially, this approach means solving for ξ_A, which to a first-order approximation we assume to be constant with respect to y (although it is different at each x). This assumption implies complete mixing. For a typical high CO_2 mass flux of 0.011 g/cm^2/s through the surface of the porous injector (which has area 35 cm^2) the mass flow rate is 0.4 g/s. To calculate the constant-ξ_A mass flow fraction for the full-surface injector in Figure 7.8, this flow rate is assumed over the entire surface of the cone, which gives the $\dot{m}_{CO_2}$ profile presented in Figure 7.11.
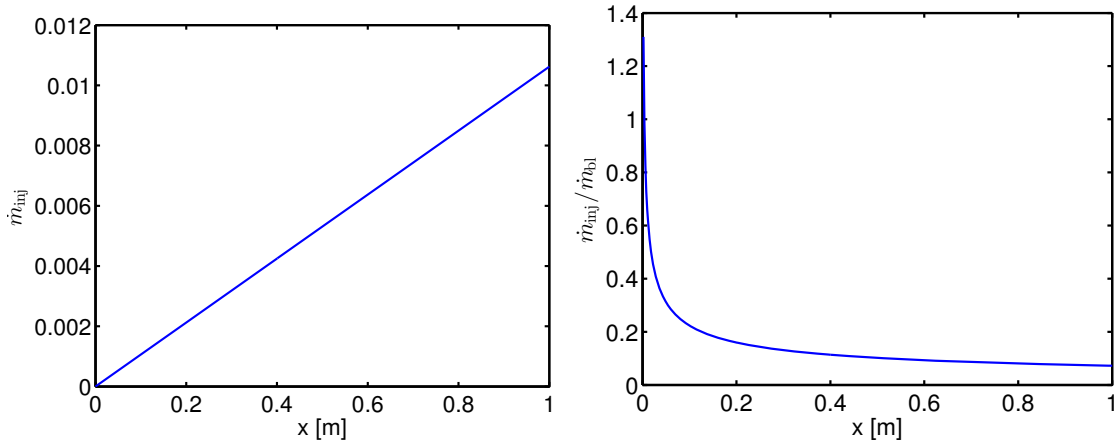
Figure 7.11: Shot 2609, full-surface injector $\dot{m}_{inj}$ (left) and $\dot{m}_{inj}/\dot{m}_{bl}$ (right) from the similarity solution.

Acoustic absorption depends in part upon the fraction of CO_2 in the boundary layer. Assuming complete mixing and constant injection over the surface of the entire cone the ratio of the mass flow of CO_2 to the mass flow of the freestream gas in the boundary layer may be calculated. This is presented in Figure 7.10. For the case matching the experiments, with an injector of limited dimensions as in Figure 7.9

but with the same mass flux, and again with complete mixing, the gas ratio distribution is presented in Figure 7.12. This procedure allows a general estimate of the cumulative dilution of CO_2 (or another injectant) in the boundary layer as additional gas is entrained from the free stream. Section 7.3.4 provides a more sophisticated computation of injectant behavior in the boundary layer.
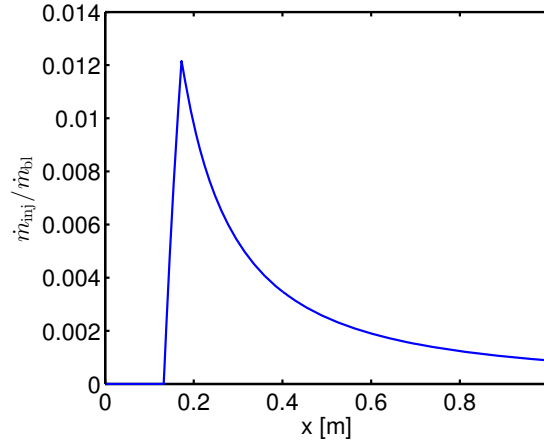
Figure 7.12: Shot 2609, partial-surface (experimental case) injector from the similarity solution, showing cumulative injectant mass fraction in the boundary layer, which rises rapidly over the surface of the injector and peaks at the end, before falling off rapidly as additional free stream gas is entrained.

7.3.4 DPLR Injection Computations

A parametric computational study was performed with the DPLR software implemented in the STABL package (see Section 4.1.2) based on the conditions of shot 2789, an air experiment with $h_{res} = 11.9$ MJ/kg and $P_{res} = 56.4$ MPa. This experiment was chosen for its relatively high enthalpy and therefore T^*, since as shown previously in Section 5.2.1, the effectiveness of CO_2 acoustic absorption, and therefore instability damping, depends upon temperature. The geometry for this experiment was a smooth cone with no injection, and transition onset was observed at $x_{Tr} = 0.725$ m. This corresponds to $\mathrm{Re}_{Tr} = 3.60 \times 10^6$ at edge conditions and $\mathrm{Re}_{Tr}^* = 3.20 \times 10^6$ at Dorrance reference conditions.

With the freestream conditions held constant, the porous CO_2 injector was modeled with an axisymmetric "top hat" injection profile over the surface of the cone from $x = 0.1326$ m to $x = 0.1739$ m (*cf.* Figure 7.1). The injection mass flow rate $\dot{m}_{\mathrm{inj}}$ was varied computationally to 11 values from 0.15 g/s to 25.0 g/s. Normalized by the boundary layer mass flow at the beginning of the injector section $\dot{m}_{\mathrm{bl}}$, the equivalent injection ratios were 0.018 to 3.1. One useful indicator of the extent of flow disturbance caused by each injection ratio is the skin friction coefficient C_f, presented in Figure 7.13. As the relative magnitude of the transverse injection increases, the wall-parallel velocity profile (and therefore the skin friction coefficient) near the wall tends to zero. In the present computations C_f did not reach zero for cases up to injection ratio 0.19, reached zero for ratios between 0.35 and 1.1, and became slightly negative in the region around the injector immediately next to the wall for ratios from 1.8 to 3.1, which was the strongest injection case simulated. Because no separation bubble is evident in the flowfield even for these large injection coefficients, it is hypothesized that the small region of negative wall-parallel velocity results from the presence of sufficient CO_2 injection pressure to overcome the pressure in the boundary layer near the wall, resulting in locally reversed flow.

Boundary layer contours for species mass concentration, both raw and normalized by the concentration at the wall, are presented for the $\dot{m}_{\mathrm{inj}}/\dot{m}_{\mathrm{bl}} = 0.018$ case in Figure 7.14 along with temperature contours. As will be shown in Section 7.3.5, beyond the region 20 cm downstream of the injector, the stability characteristics of flows with injection ratios of this magnitude are comparable to the no-injection case. The same bounday layer contours are presented for a much larger $\dot{m}_{\mathrm{inj}}/\dot{m}_{\mathrm{bl}} = 1.1$ in Figure 7.15. Flows with injection ratios of this magnitude are highly unstable compared to the no-injection case for the entire length of the 1 m cone. Figure 7.16 illustrates evolving $u(y)$ profiles for three injection rates. $\dot{m}_{\mathrm{inj}}/\dot{m}_{\mathrm{bl}} = 1.1$ creates a large, highly unstable velocity deficit, while $\dot{m}_{\mathrm{inj}}/\dot{m}_{\mathrm{bl}} = 0.018$ enters the boundary
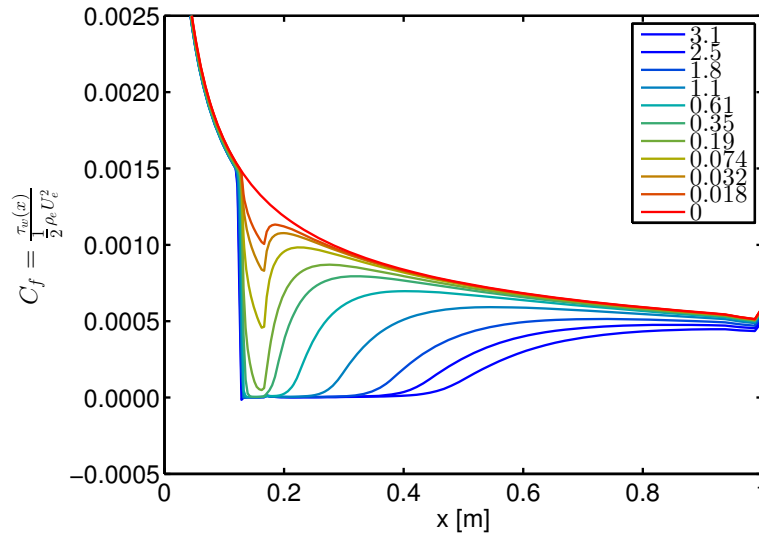
Figure 7.13: Skin friction coefficients calculated from the DPLR results for shot 2789 freestream with several values of $\dot{m}_{\mathrm{inj}}/\dot{m}_{\mathrm{bl}}$ from 0 to 3.1. Injection causes a local skin friction deficit. For the three largest values of $\dot{m}_{\mathrm{inj}}/\dot{m}_{\mathrm{bl}}$, the skin friction becomes negative near the front of the injector.

layer essentially without disturbing the self-similar velocity profile.

In each case, it is clear that the CO_2 (and CO) mass-concentration boundary layers, once they begin at the injector, grow proportionally with the δ_{99} boundary layer thickness, as was predicted in Section 7.3.3. With increasing x, as the δ_{99} boundary layer grows, the normalized mass-concentration boundary layer profile presented in Figure 7.17 approaches a constant distribution. It is important to note that the absolute CO_2 concentration must of necessity still decrease even after this constant normalized boundary layer profile is achieved, because additional freestream gas is entrained into the boundary layer as it grows both in height and in circumference, while no additional CO_2 is added beyond the injector section. Figure 7.18 presents Y_{CO_2} at the wall for three mass flow rates in logarithmic form to highlight the power-law relationship that describes the reduction in injectant concentration. After the initial injection peak, the CO_2 mass concentration decays as $Y_{CO_2} \propto 1/\delta^3$.

This power-law relationship can be shown to be expected from Equation (7.6),
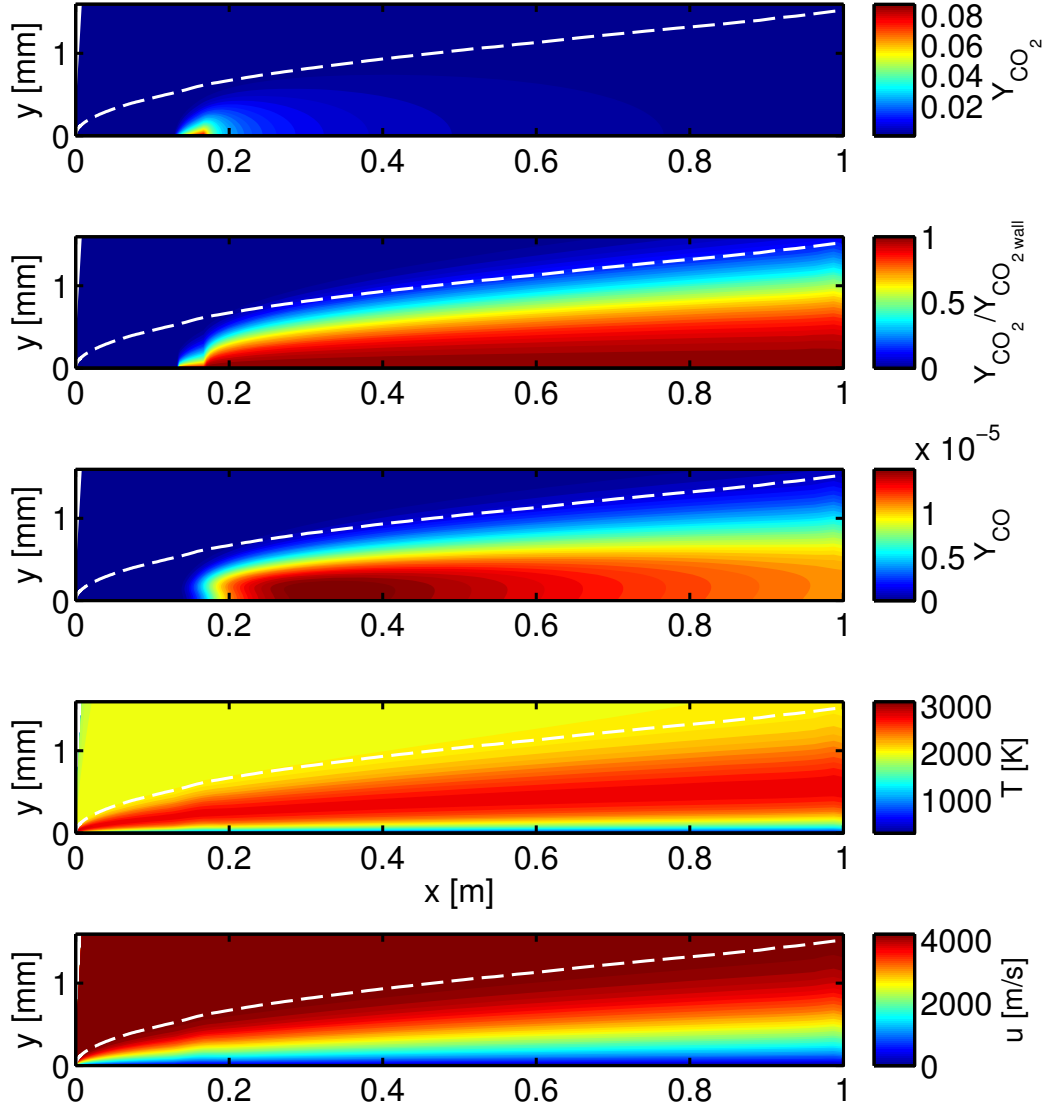
Figure 7.14: DPLR results for shot 2789 freestream with $\dot{m}_{inj}/\dot{m}_{bl} = 0.018$, including boundary layer CO_2 physical and normalized mass fraction, CO mass fraction, and temperature distribution. While the physical mass fraction of CO_2 is large only in the immediate vicinity of the injector section because more air is entrained as the boundary layer grows, the gas has mixed and approaches a steady state normalized distribution. The δ_{99} boundary layer is indicated by a white dashed line.

taking the injectant mass-concentration profile at a given x-location as $Y_{CO_2}(x, y)$. Making a small-angle approximation and noting the dependence of y' upon x alone for the radius of the cone (radius $R(y') = x' \tan \theta = x \sin \theta$, where x' and y' are defined from the tip along the cone centerline and x and y are defined from the tip along the
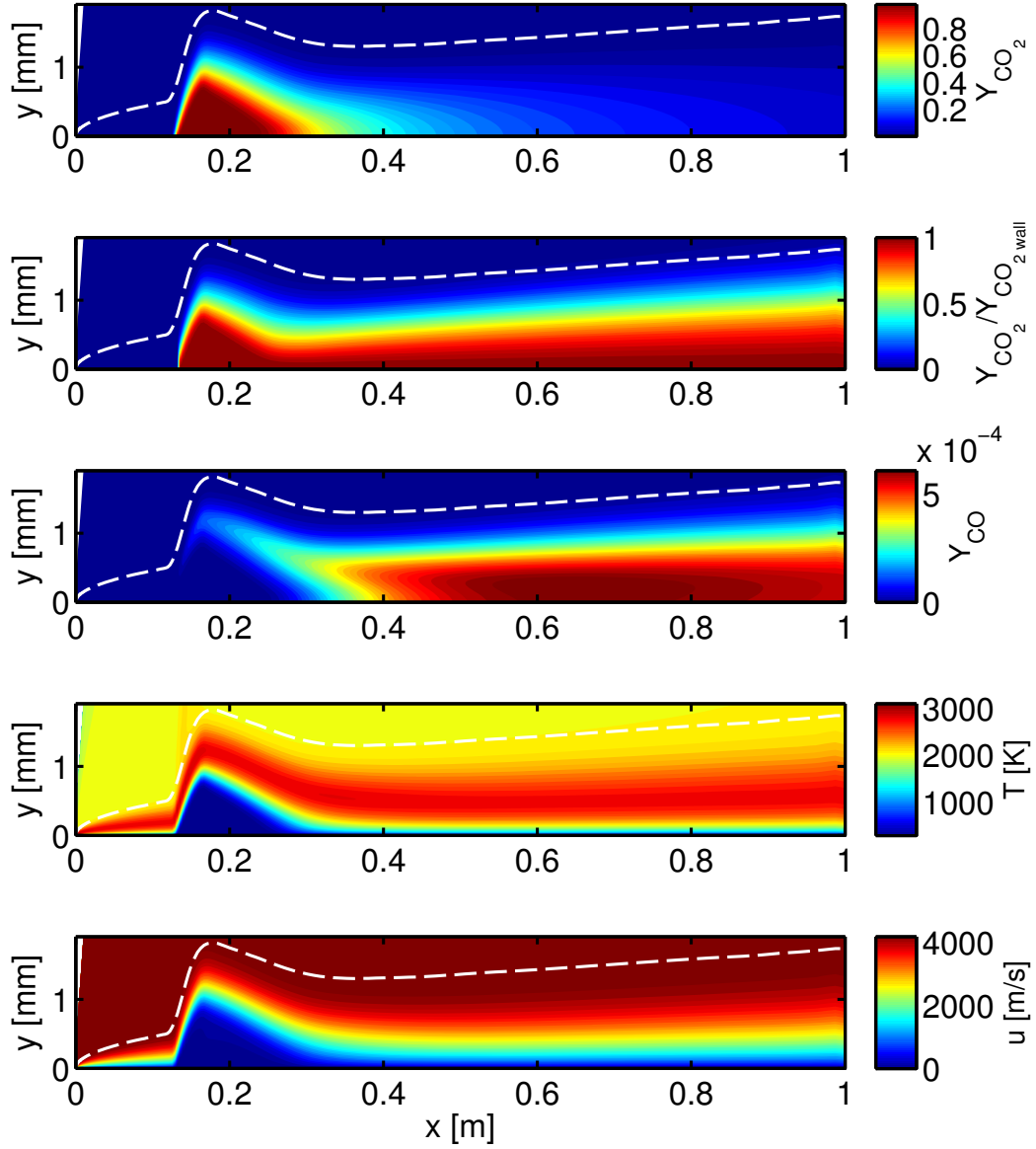
Figure 7.15: DPLR results for shot 2789 freestream with $\dot{m}_{\text{inj}}/\dot{m}_{\text{bl}} = 1.1$, including boundary layer CO_2 physical and normalized mass fraction, CO mass fraction, and temperature distribution. While the physical mass fraction of CO_2 is large only in the immediate vicinity of the injector section because more air is entrained as the boundary layer grows, the gas has mixed and approaches a steady state normalized distribution. The δ_{99} boundary layer is indicated by a white dashed line.

surface of the cone), we have:

$$\dot{m}_{CO_2} \approx 2\pi \int_0^{\delta} \rho u Y_{CO_2}(x,y)(x\sin\theta)\mathrm{d}y$$
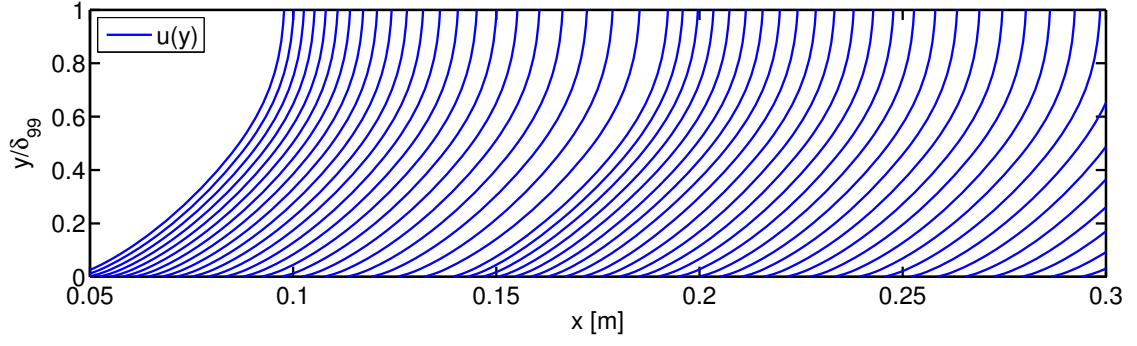
(a) $\dot{m}_{\mathrm{inj}}/\dot{m}_{\mathrm{bl}} = 0.018$
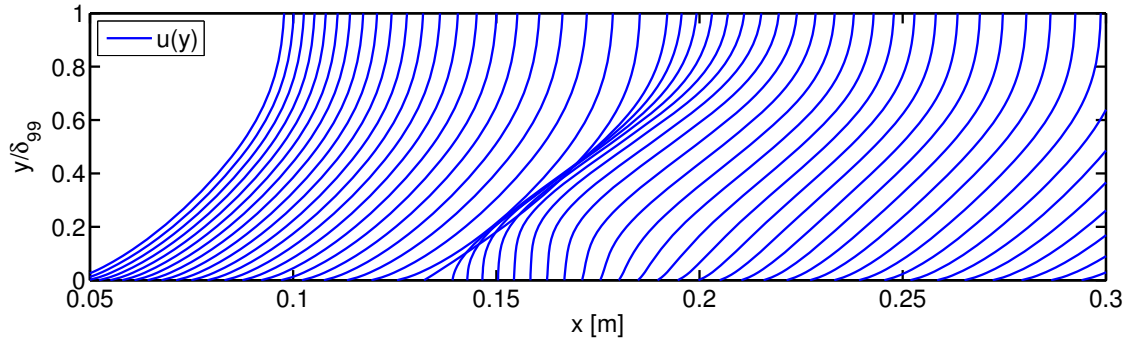
(b) $\dot{m}_{\mathrm{inj}}/\dot{m}_{\mathrm{bl}} = 0.35$
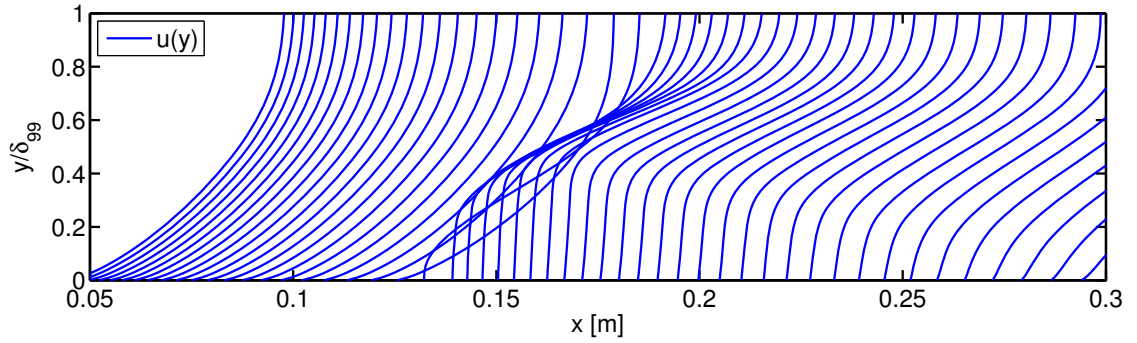
(c) $\dot{m}_{\mathrm{inj}}/\dot{m}_{\mathrm{bl}} = 1.1$

Figure 7.16: DPLR $u(y)$ results for shot 2789 freestream with (from top to bottom) $\dot{m}_{\mathrm{inj}}/\dot{m}_{\mathrm{bl}} = 0.018$, 0.35, and 1.1, presented in normalized form. $\dot{m}_{\mathrm{inj}}/\dot{m}_{\mathrm{bl}} = 1.1$ creates a large, highly unstable velocity deficit, while $\dot{m}_{\mathrm{inj}}/\dot{m}_{\mathrm{bl}} = 0.018$ enters the boundary layer essentially without disturbing the self-similar velocity.

Pulling out the variables that do not depend upon upon y:

$$\dot{m}_{\mathrm{CO_2}} \approx 2\pi(x\sin\theta)\int_0^\delta \rho u Y_{\mathrm{CO_2}}(x,y)\mathrm{d}y$$
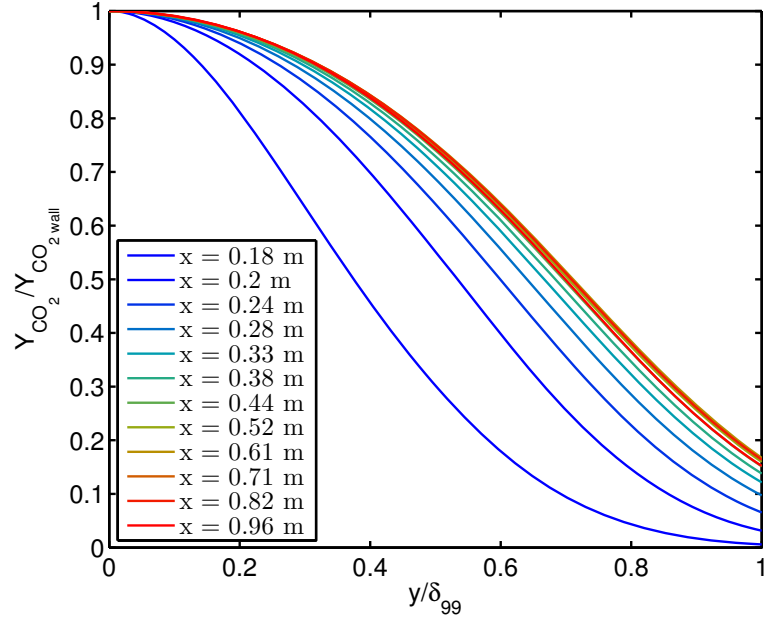
Figure 7.17: Boundary layer CO_2 mass fraction profiles at several x-locations, normalized by the CO_2 mass fraction at the surface of the cone, for the freestream conditions of shot 2789 with $\dot{m}_{\mathrm{inj}}/\dot{m}_{\mathrm{bl}} = 0.018$. The normalized mass fraction curves approach a steady state as x increases.

And changing variables to $\eta = y/\delta$, $\mathrm{d}\eta = \mathrm{d}y/\delta$ to normalize each term of the integral:

$$\dot{m}_{CO_2} \approx 2\pi x \sin\theta Y_{CO_2}(x,0)\delta\rho_e U_e \int_0^1 \frac{Y_{CO_2}(x,y)}{Y_{CO_2}(x,0)}\left(\frac{y}{\delta}\right)\frac{u}{U_e}\left(\frac{y}{\delta}\right)\frac{\rho}{\rho_e}\left(\frac{y}{\delta}\right)\frac{\mathrm{d}y}{\delta}$$

The integral then has a constant value which does not depend upon x. It is combined with the rest of the constants to yield:

$$\dot{m}_{CO_2} \approx x\delta Y_{CO_2}(x,0)C'$$

Finally, noting that after the region of the injector $\dot{m}_{CO_2}$ is constant, we solve for $Y_{CO_2}(x,0)$ and use $\delta \sim x/\sqrt{\mathrm{Re}_x} \sim \sqrt{x}$, to find that:

$$Y_{CO_2}(x,0) \approx \frac{C}{x\delta} \sim \frac{1}{\delta^3}$$
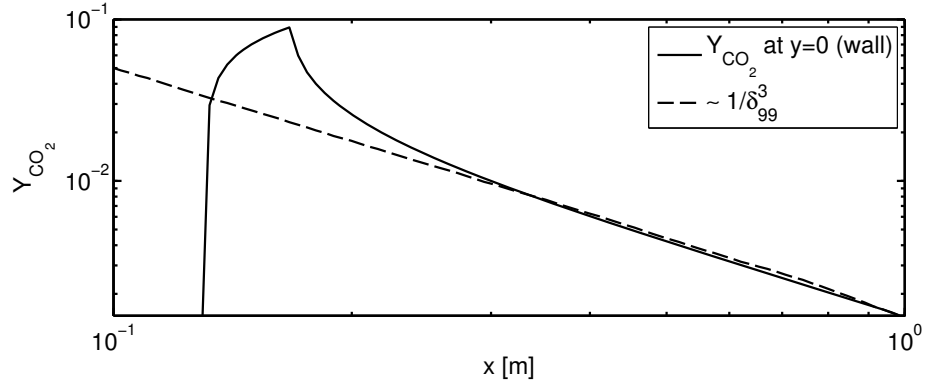
(a) $\dot{m}_{\mathrm{inj}}/\dot{m}_{\mathrm{bl}} = 0.018$
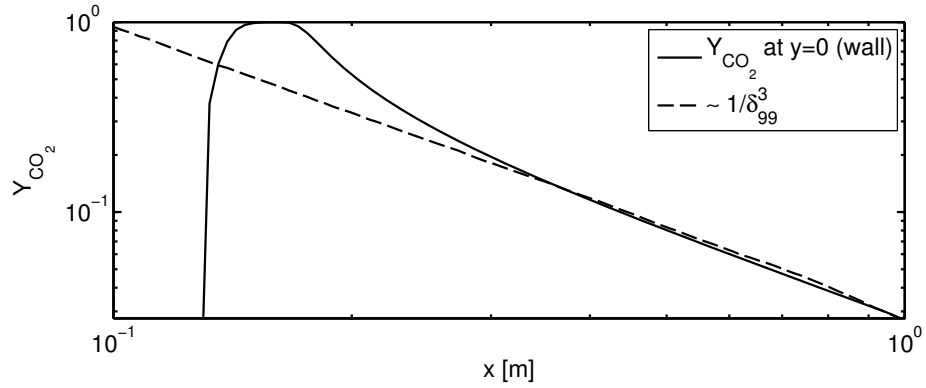
(b) $\dot{m}_{\mathrm{inj}}/\dot{m}_{\mathrm{bl}} = 0.35$
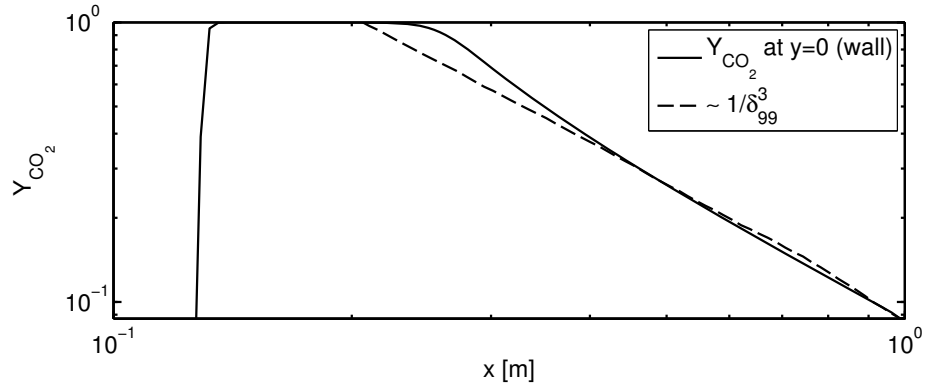
(c) $\dot{m}_{\mathrm{inj}}/\dot{m}_{\mathrm{bl}} = 1.1$

Figure 7.18: DPLR $Y_{\mathrm{CO_2}}$ at the wall ($y = 0$) results for shot 2789 freestream with (from top to bottom) $\dot{m}_{\mathrm{inj}}/\dot{m}_{\mathrm{bl}} = 0.018$, 0.35, and 1.1, presented in logarithmic form to highlight the power-law relationship that describes the the reduction in injectant concentration in each case, as the initial fixed quantity of CO_2 diffuses into a growing boundary layer. After the initial injection peak, the CO_2 mass concentration decays as $Y_{\mathrm{CO_2}} \propto 1/\delta^3$.

This is the behavior, beyond the injection region, of the wall mass concentration profiles $Y_{CO_2}(x, 0)$ for each of the three injection ratios observed in Figure 7.18, even though the injection ratios vary by nearly two orders of magnitude. The evolution of the full CO_2 boundary layer at the injector and downstream for the three cases is presented in Figure 7.19. Higher values of $\dot{m}_{inj}/\dot{m}_{bl}$ result in a bubble of near-100% CO_2 concentration near the wall around the injection section, but diffusion to the upper part of the boundary layer is not immediate. At each x-location past the injector, the CO_2 concentration profile is zero at $y = \infty$ and approaches the wall value presented in Figure 7.18 at $y = 0$, with $y'(0) = \infty$. These profiles are a more quantitative and detailed version of the schematic mass-concentration boundary layer from Figure 7.9.

As discussed in Section 1.3, absorption of acoustic waves from the conversion of molecular kinetic energy (*e.g.*, from compression) into internal vibrational energy is favorable at T5-like conditions for the CO_2 molecule. However, for this vibrational relaxation to affect the stability and transition process, the CO_2 must both mix into the boundary layer and heat up. Wagnild (2012) found computationally that injecting pre-heated CO_2 is more effective for decreasing the maximum N-factor than injecting CO_2 at room temperature, but all of the present experiments and computations have not used pre-heated CO_2. Therefore, there is a bubble of low-temperature, low-velocity gas, which is especially apparent for relatively high mass injection ratios; for example, the bottom two plots in Figure 7.15 show this bubble. This effect is much less prominent at very low mass flow rates, as demonstrated in Figure 7.14. To complement these contour profiles, Figures 7.20, 7.21, and 7.22 display quantitative plots of the velocity, temperature, and Y_{CO_2} at six x-locations beginning at the injector and proceeding downstream. It is clear from these plots that even for higher mass flow rates, the injection process results in a substantial quantity of the injected CO_2 reaching temperatures above 1000 K within about 10 cm of the end of the injector.

(a) $\dot{m}_{\mathrm{inj}}/\dot{m}_{\mathrm{bl}} = 0.018$

(b) $\dot{m}_{\mathrm{inj}}/\dot{m}_{\mathrm{bl}} = 0.35$

(c) $\dot{m}_{\mathrm{inj}}/\dot{m}_{\mathrm{bl}} = 1.1$
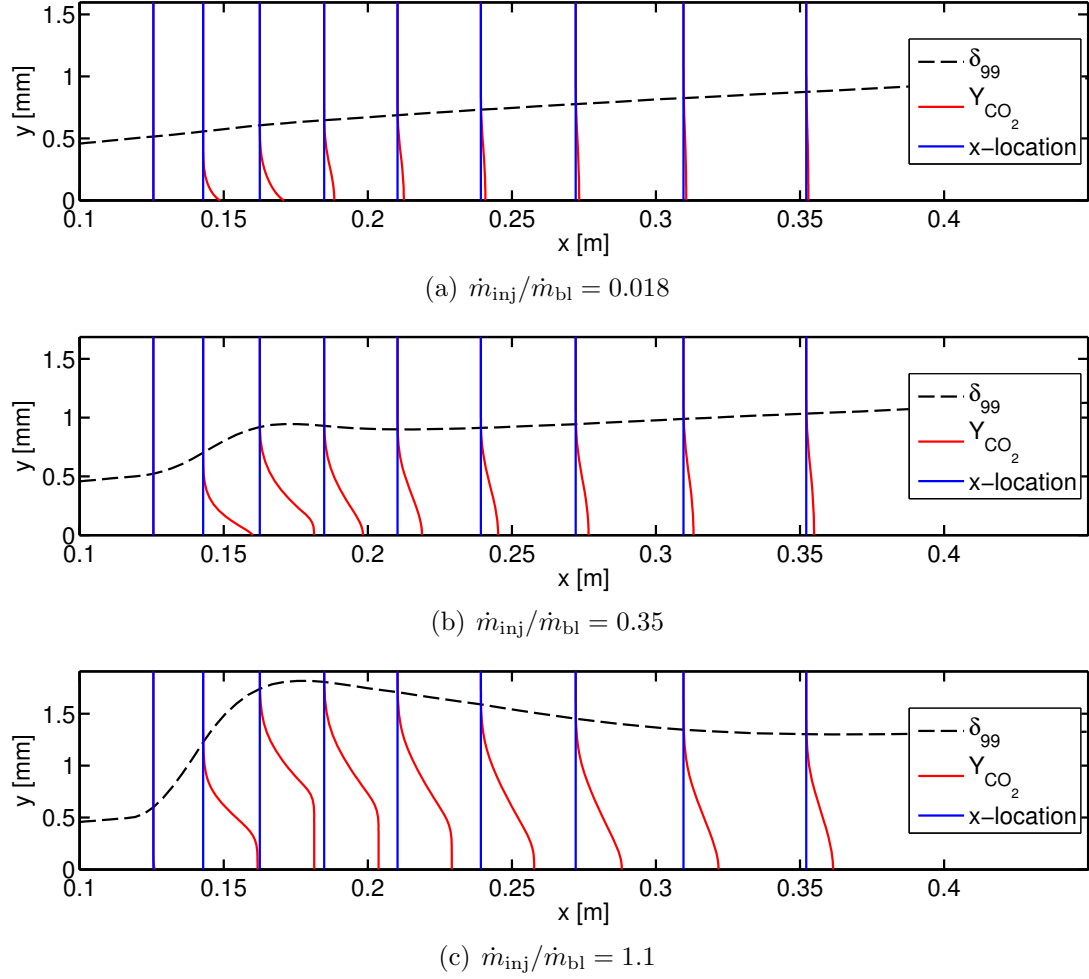
Figure 7.19: DPLR $Y_{\mathrm{CO_2}}$ results for shot 2789 freestream with (from top to bottom) $\dot{m}_{\mathrm{inj}}/\dot{m}_{\mathrm{bl}} = 0.018$, 0.35, and 1.1, presented in normalized form. Higher values of $\dot{m}_{\mathrm{inj}}/\dot{m}_{\mathrm{bl}}$ result in a bubble of near-100% CO_2 concentration near the wall around the injection section, but diffusion to the upper part of the boundary layer is not immediate. These profiles are similar to the schematic mass-concentration boundary layer in Figure 7.9. See also Figure 7.17.

(a) $x = 0.18$ m

(b) $x = 0.21$ m

(c) $x = 0.24$ m

(d) $x = 0.27$ m

(e) $x = 0.31$ m

(f) $x = 0.35$ m
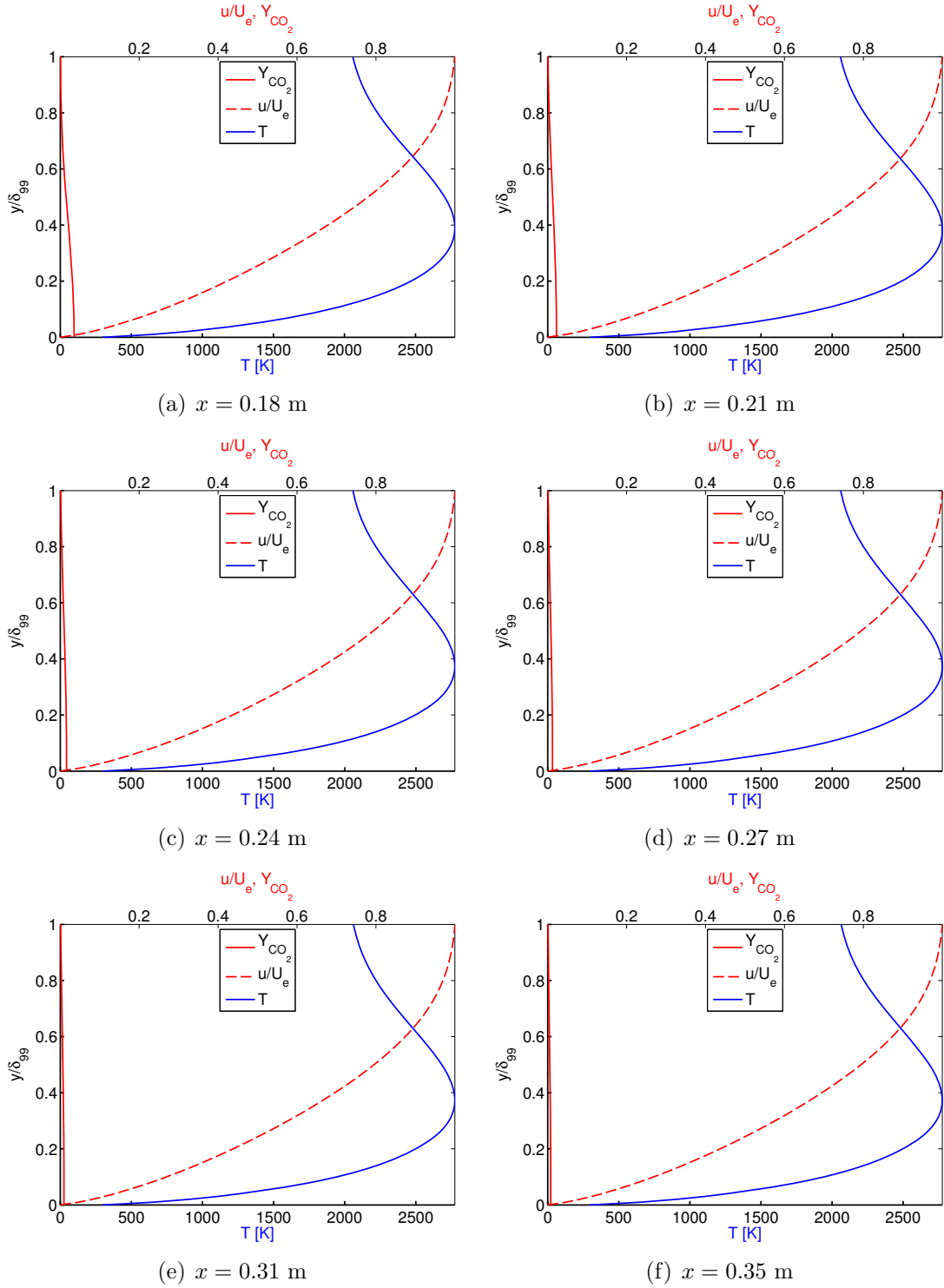
Figure 7.20: DPLR results for shot 2789 freestream with $\dot{m}_{\mathrm{inj}}/\dot{m}_{\mathrm{bl}} = 0.018$, including boundary layer CO_2 mass fraction, temperature profile, and velocity profile, at six different x-locations from the tip, all downstream of the porous injector.

(a) $x = 0.18$ m

(b) $x = 0.21$ m

(c) $x = 0.24$ m

(d) $x = 0.27$ m

(e) $x = 0.31$ m

(f) $x = 0.35$ m
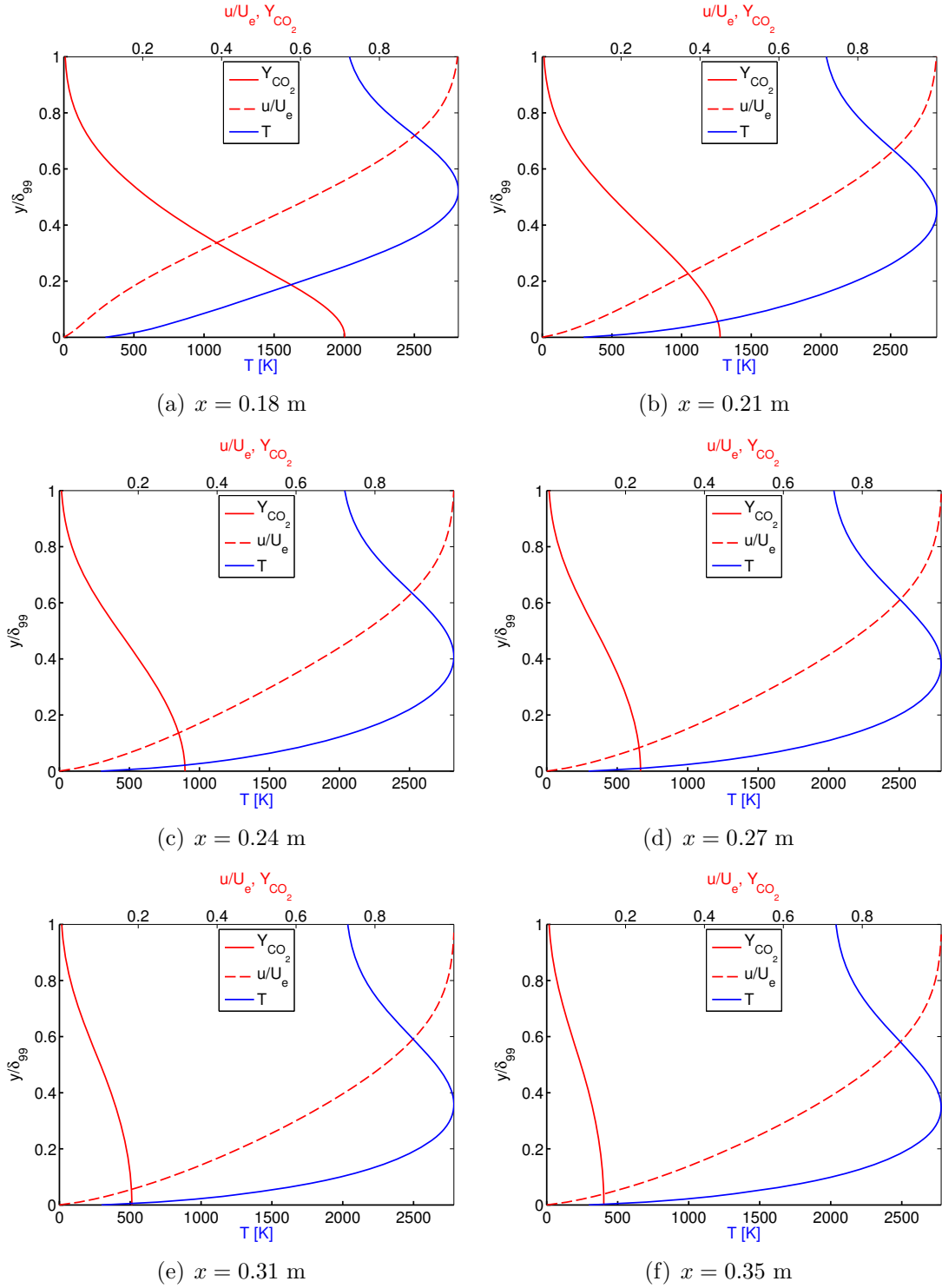
Figure 7.21: DPLR results for shot 2789 freestream with $\dot{m}_{\mathrm{inj}}/\dot{m}_{\mathrm{bl}} = 0.35$, including boundary layer CO_2 mass fraction, temperature profile, and velocity profile, at six different x-locations from the tip, all downstream of the porous injector.
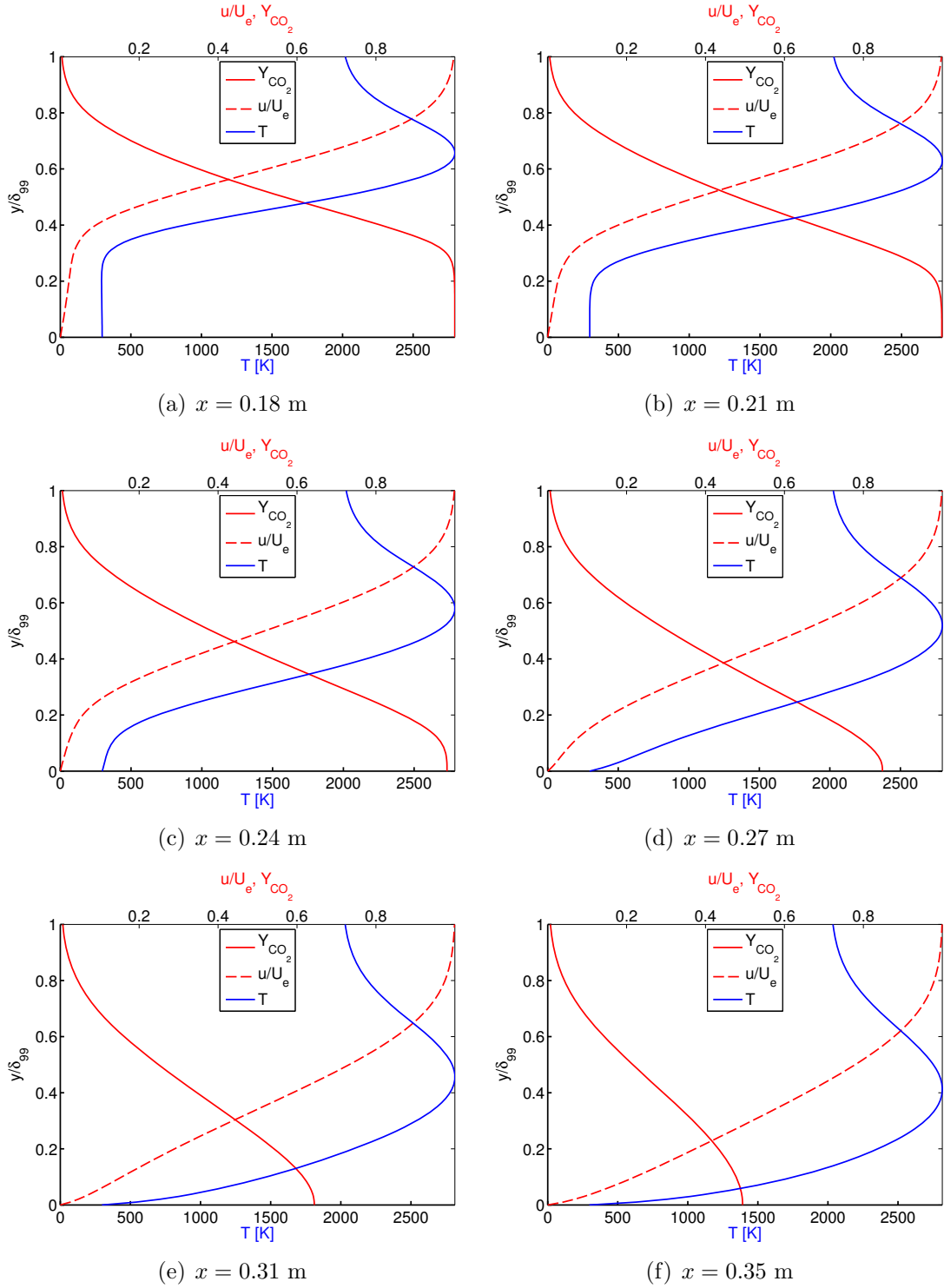
Figure 7.22: DPLR results for shot 2789 freestream with $\dot{m}_{\mathrm{inj}}/\dot{m}_{\mathrm{bl}} = 1.1$, including boundary layer CO_2 mass fraction, temperature profile, and velocity profile, at six different x-locations from the tip, all downstream of the porous injector.

7.3.5 PSE-Chem Stability Computations

Stability analysis was performed on each injection case up to an $\dot{m}_{\text{inj}}/\dot{m}_{\text{bl}}$ ratio of 1.10 with the PSE-Chem software implemented in the STABL package (see Section 4.3.1). The resulting N factor distributions over the surface of the cone are compared to each other, and to the baseline conditions of shot 2789 with no injection, in Figure 7.23. This experiment, which used a solid cone without injection, had transition onset at $x = 0.725$ m, or N ≈ 10. Based upon the present stability calculations, $\dot{m}_{\text{inj}}/\dot{m}_{\text{bl}}$ injection ratios up to 0.032 can be safely injected into the boundary layer without causing an immediate jump in the N factor past 10, but greater injection ratios risk promoting transition.
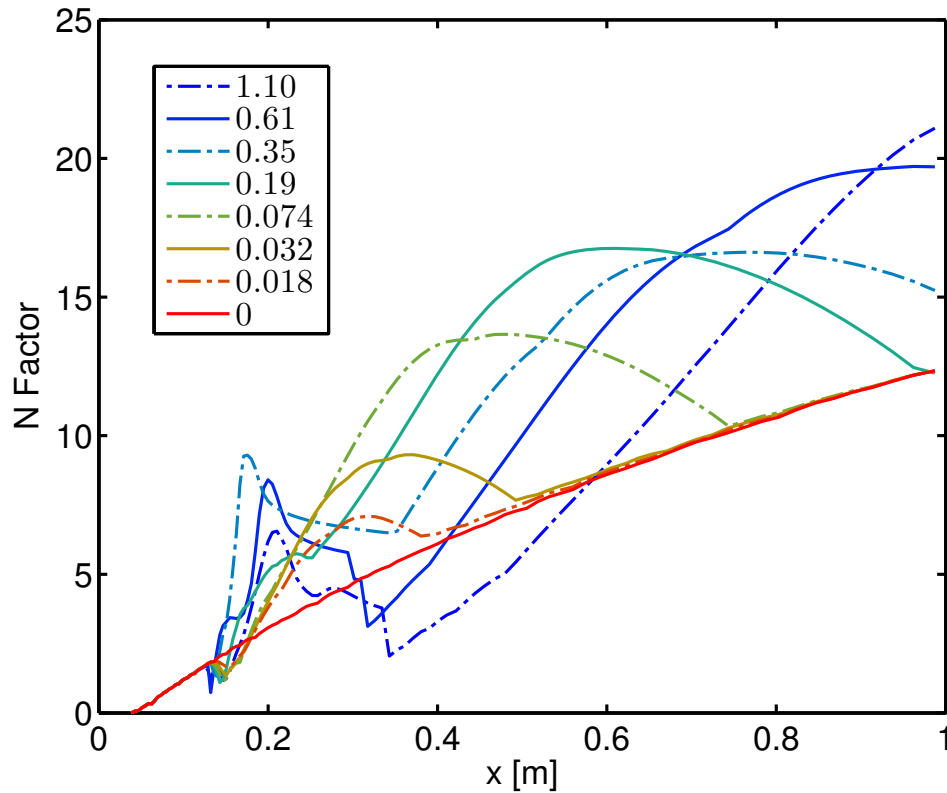
Figure 7.23: N factors for the freestream conditions of shot 2789, computed with various CO_2 injection ratios $\dot{m}_{\text{inj}}/\dot{m}_{\text{bl}}$

7.4 Gas Injection Experiments[2]

7.4.1 Scope of Study

A total of 16 experiments in T5 make up the data set for the present study. All have the same nominal reservoir conditions: air at $h_{\mathrm{res}} \approx 9.7$ MJ/kg and $P_{\mathrm{res}} \approx 55$ MPa. These tunnel parameters result in conditions at the boundary layer edge of $P_{\mathrm{e}} \approx 43$ kPa, $U_{\mathrm{e}} \approx 4000$ m/s, $\rho_{\mathrm{e}} \approx 0.09$ kg/m^3, and $T_{\mathrm{e}} \approx 1600$ K. CO_2 injection ratios $\dot{m}_{\mathrm{inj}}/\dot{m}_{\mathrm{bl}}$ were varied from 0 (*i.e.*, no injection) to 0.052. Argon was chosen as a chemically inert control injectant for its similar density to CO_2, and Ar injection ratios were varied from 0 (*i.e.*, no injection) to 0.017. These cases were also compared to cases at the same freestream conditions with a smooth, solid injector piece mounted in place of the porous injector.

7.4.2 Results

The results from gas injection experiments performed at similar tunnel conditions are tabulated in Table 7.4. Average heat fluxes for several exemplar conditions are presented in Figure 7.24. Apparent transition onset delays were documented in shots with CO_2 injection, compared both to shots with a porous injector but no injection, and control shots with a smooth injector section, as presented graphically in Figures 7.25 and 7.26. The data show a general trend of increasing delay with injection rate, before a sharp dropoff at the highest injection rate. All three Argon injection conditions transitioned earlier than any CO_2 injection or no-injection conditions. The error bars in Figures 7.25 and 7.26 represent the uncertainty in measurement of the transition location from each experiment, but no attempt has been made to account for potential systematic uncertainty, which may be larger in magnitude.

---

[2]Portions of this section are adapted from, and correct, Jewell et al. (2011). In particular, the injection mass flow rates listed here in Table 7.4 are the correct values.
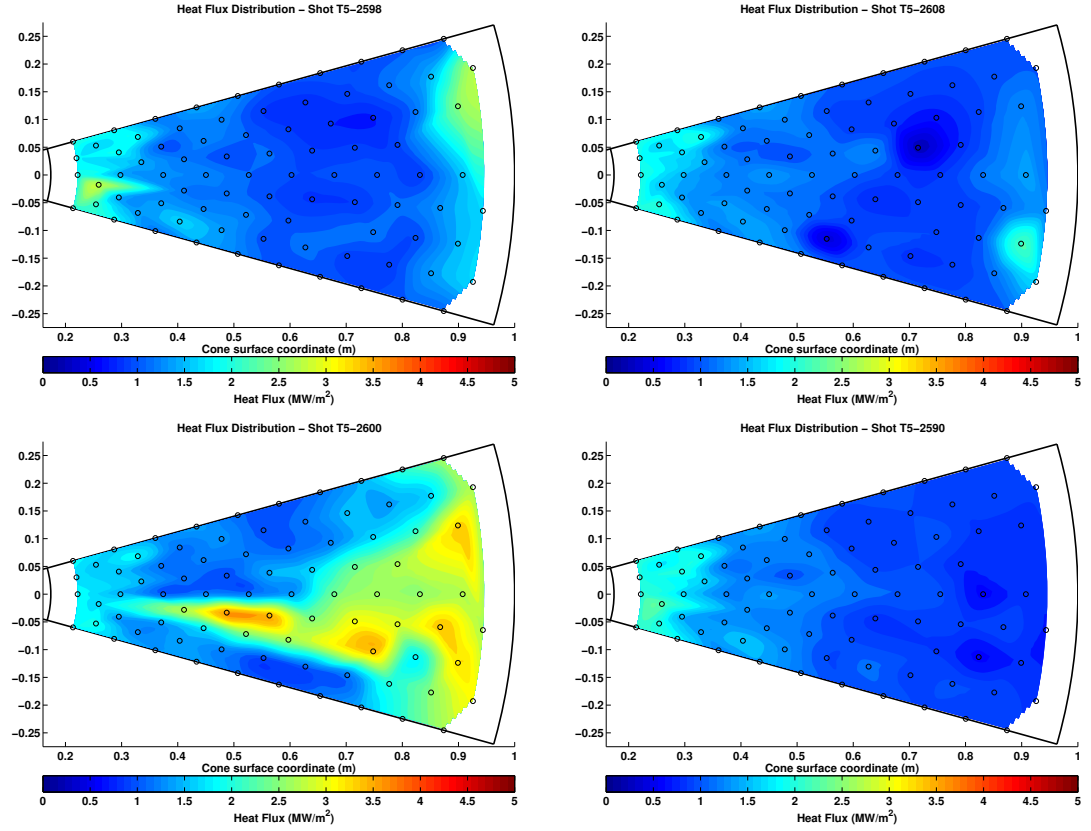
Figure 7.24: Heat flux contour plots on the developed cone surface for four selected cases. Top left: porous injector with no injection. Top right: solid injector section, no injection. Bottom left: Ar injection at 0.017 mass flow ratio. Bottom right: CO_2 injection at 0.017 mass flow ratio.

The six CO_2 injection cases were simulated with DPLR and PSE-Chem following the procedure described in Sections 7.3.4 and 7.3.5, along with equivalent simulations for the same freestream conditions with no injection. The resulting N factor distributions over the surface of the cone are compared to each other, and to the baseline conditions of each shot with no injection, in Figure 7.27. The highest injection ratio, 0.052 for shot 2594, reaches a local peak N factor of 14.6, sufficient for early transition, which matches observations. For shots with very low injection ratios $\dot{m}_{inj}/\dot{m}_{bl}$, the injection computations closely match their zero injection counterparts. For these conditions the PSE-Chem computations do not predict any decrease in N factor, except in the region of the injector and immediately downstream, which does

Shot	h_{res} MJ/kg	P_{res} MPa	$\dot{m}_{inj}$ g/s	$\dot{m}_{inj}/\dot{m}_{bl}$	Re_{Tr}	Re_{Tr}^*	x_{Tr}/δ_{99Tr}
2587	9.65	51.9	0.029 (Ar)	0.004	3.17×10^6	2.85×10^6	545
2589	10.07	56.3	0.053 (CO_2)	0.007	4.82×10^6	4.29×10^6	654
2590	9.63	55.9	0.130 (CO_2)	0.017	5.44×10^6	4.84×10^6	692
2591	9.19	53.2	0.028 (CO_2)	0.004	5.19×10^6	4.51×10^6	670
2592	9.59	52.5	0.017 (CO_2)	0.002	4.87×10^6	4.33×10^6	662
2593	9.69	55.2	0.241 (CO_2)	0.032	4.94×10^6	4.41×10^6	667
2594	9.55	56.1	0.380 (CO_2)	0.052	4.15×10^6	3.70×10^6	613
2596	9.73	54.1	0	0	4.23×10^6	3.82×10^6	627
2597	9.80	55.6	0.122 (Ar)	0.017	3.60×10^6	3.24×10^6	576
2598	9.97	55.3	0	0	4.32×10^6	3.83×10^6	619
2600	9.59	54.7	0.093 (Ar)	0.013	3.37×10^6	3.01×10^6	557
2607	9.50	54.5	a		4.38×10^6	3.92×10^6	636
2608	9.46	55.2	a		4.70×10^6	4.16×10^6	650
2609	9.62	55.7	a		4.65×10^6	4.11×10^6	642
2610	10.07	54.9	a		4.13×10^6	3.74×10^6	621
2611	10.15	54.6	a		4.51×10^6	4.11×10^6	646
			a Solid plastic injector section, no flow.				

Table 7.4: Similar tunnel conditions ($h_{res} \approx 9.7$ MJ/kg, $P_{res} \approx 55$ MPa), and varying gas injection conditions, with resulting transition Reynolds numbers, determined with the intermittency method described in Section 3.1.2.3. $\dot{m}_{inj}/\dot{m}_{bl}$ is the mass flow fraction of the injectant gas in terms of the boundary layer mass flow rate at the beginning of the injector section for the baseline case.
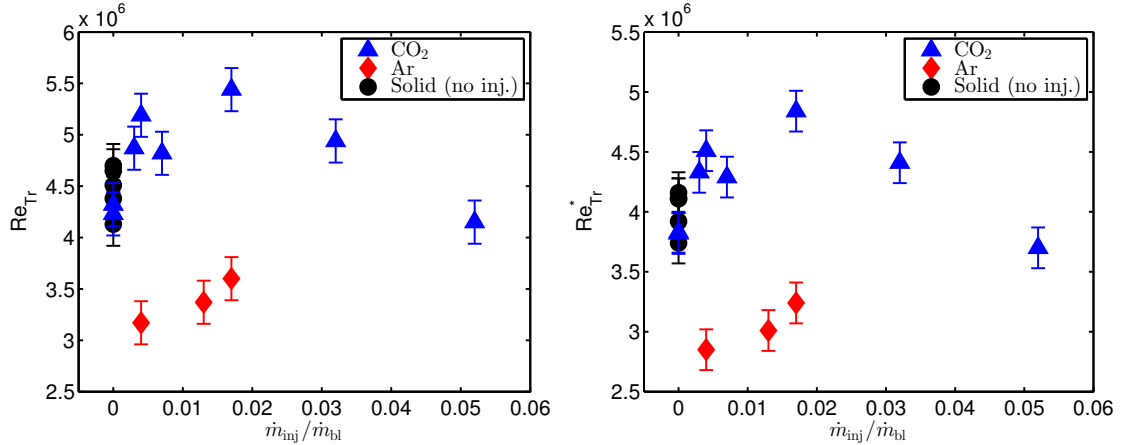
Figure 7.25: Re_{Tr} (left) and Re_{Tr}^* (right) for gas injection and control (solid) experiments at similar tunnel conditions ($h_{res} \approx 9.7$ MJ/kg, $P_{res} \approx 55$ MPa). Transition location is determined using the intermittency method described in Section 3.1.2.3.
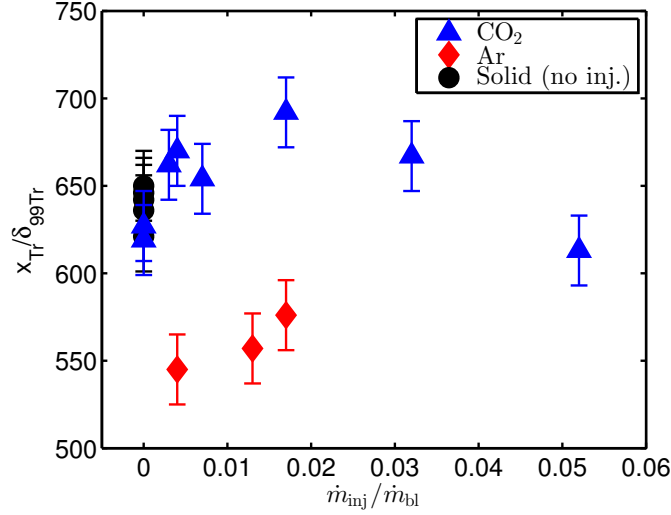
Figure 7.26: x_{Tr}/δ_{99Tr} for gas injection and control (solid) experiments at similar tunnel conditions ($h_{res} \approx 9.7$ MJ/kg, $P_{res} \approx 55$ MPa).

not match the experimental observations. However, the PSE-Chem computations do not take into account the noise environment of the tunnel or boundary layer receptivity. Experiments by Henderson et al. (1969), as well as computations by Bertolotti (1998), indicate that vibrational-vibrational energy transfer between CO_2 and N_2, which is not presently modeled in PSE-Chem, can contribute to larger reductions in the net relaxation time of a gas mixture than those attributable to CO_2 vibrational-translational energy transfer, which is presently modeled in PSE-Chem. The effect was found by Bertolotti and Henderson et al. to be present even for low (4% or less) CO_2 concentrations, and especially prominent in the temperature range of about 300–1200 K, which is easily achieved in a typical T5 boundary layer. For example, for a temperature of 1000 K, Bertolotti (1998) calculates that even 300 ppm (comparable to atmospheric levels) admixture of CO_2 in air reduces τ for both O_2 and N_2 by about 50%. Bertolotti also found that 1% CO_2 and H_2O admixture in air reduces the vibrational relaxation time for the O_2 molecule by about two orders of magnitude, and for the N_2 molecule by more than one order of magnitude. In addition to contributing to greater absorption of acoustic energy at the relevant (higher) frequencies through
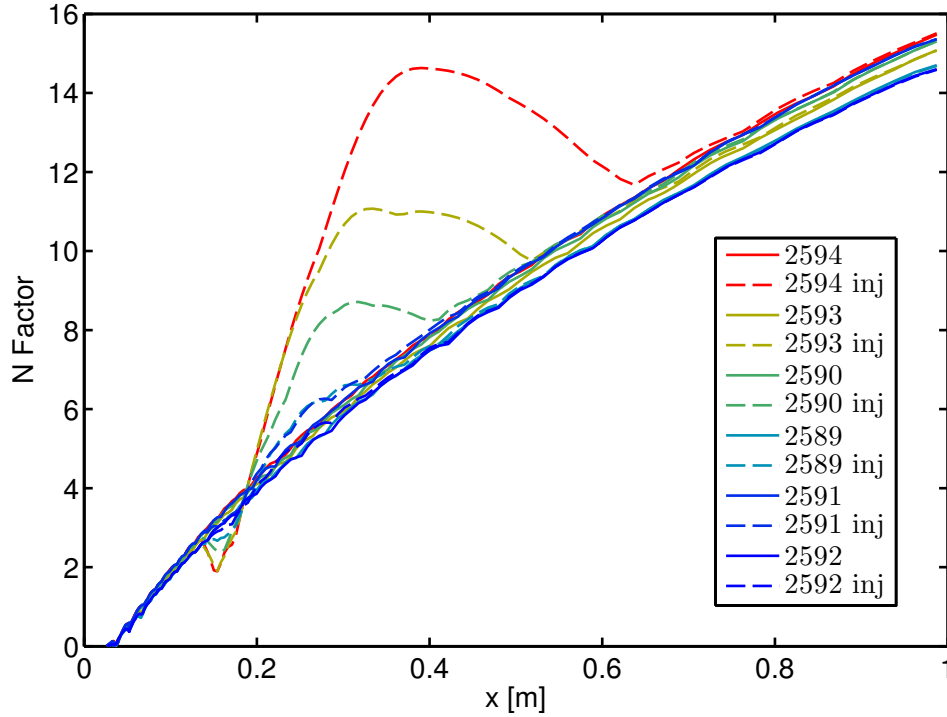
Figure 7.27: N factors for the six CO_2 injection experiments in Table 7.4, computed with the listed injection ratios $\dot{m}_{inj}/\dot{m}_{bl}$ and, for comparison, the same freestream conditions with zero injection. The highest injection ratio, for shot 2594, reaches a local peak N factor of 14.6, sufficient for early transition, which matches observations.

reducing the relaxation time, which would tend to increase transition delay, the frequency shift itself may change the receptivity of the boundary layer to the particular noise spectrum in T5, which could either promote or suppress transition. Parziale et al. (2014) found that the power spectral density of acoustic disturbances in the T5 freestream decreased with increasing frequency for one set of conditions, but to date the T5 noise spectrum has not been exhaustively characterized.

7.4.3 Conclusions and Future Work

The present injection results are not conclusive. In particular, no injection experiments have been performed under the clean tunnel conditions described in Section 2.1.3, and the mass flow rates for the experiments that were performed have been calculated indirectly from the recorded run tank pressure. As a consequence,

there is potentially large systematic uncertainty in the measured transition location. While injection computations for low mass flow rate CO_2 injection conditions, equivalent to the calculated experimental mass flow rates, did not predict boundary layer disturbance growth beyond the N factor presumed to cause transition, they also did not predict a reduction in N factor below the equivalent cases without injection. Prior to undertaking further experimental study of injection, numerical simulations which include the τ reducing effects of small quantities of CO_2 on the O_2 and N_2 molecules described in Bertolotti (1998) should be performed to investigate the potential of this mechanism for increased acoustic damping. A computational study to optimize injector size and positioning would also be useful.

The sintered porous metal appears to work well for gas injection, but it would be worthwhile to examine the mass flow characteristics of injectors with different porosities. Future injection experiments should use the state-of-the-art cleaning method to be fully comparable with the transition onset results described in the rest of this thesis. Furthermore, the design of any future injection mechanism should include a mass flow meter in the flow path, as well as high-speed pressure and temperature measurements in the injector plenum to temporally resolve the mass flow rate of the injectant.

Chapter 8

Conclusions

8.1 Introduction

When a vehicle's boundary layer transitions from laminar to turbulent flow, skin friction and the heat flux through the surface increase in magnitude. In the flow regime associated with sustained atmospheric hypervelocity flight, heat transfer and thermal management are dominant design considerations, and the more massive thermal protection system required to safely dissipate the heat from turbulent flow imposes significant mass and efficiency penalties. In hypervelocity flow over cold, slender bodies, the most significant instability mechanism is the so-called second or Mack mode, which is two-dimensional and acoustic in nature. These flows are characteristic of high-enthalpy facilities like the T5 shock tunnel at Caltech. When the acoustic characteristic time and relaxation time of the gas are similar, some finite time is required for molecular collisions to achieve a new density under an acoustic pressure disturbance. This results in a work cycle, as the density changes lag the pressure changes. In a flow of gas that absorbs energy most efficiently at frequencies similar to the most strongly amplified frequencies implied by the geometry of the boundary layer, laminar to turbulent transition is expected to be delayed. The flow of carbon dioxide and carbon dioxide/air mixtures over a slender cone at T5 conditions allows for such a match in frequencies and a significant effect on the predicted stability properties of

the boundary layer, as shown in Figure 8.1. Previous studies have observed marked differences in transition Re and Re* between flows in CO_2 and air.
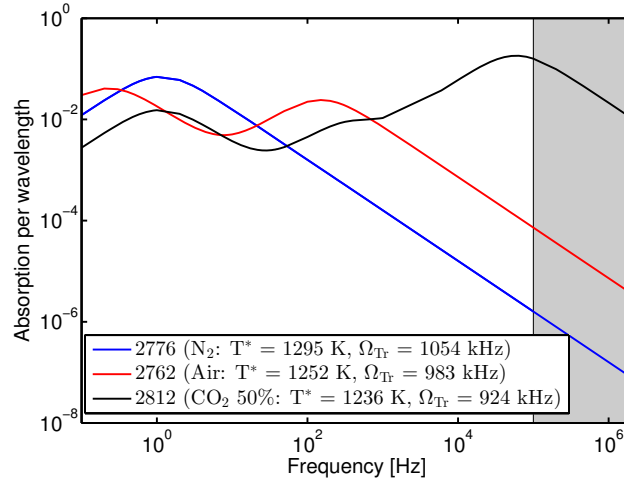
Figure 8.1: Fujii acoustic absorption per wavelength for air, N_2, and 50% CO_2 calculated at similar conditions. The area of the graph highlighted in gray, which extends from 100 kHz to 2 MHz, is the most relevant frequency range for the present study and encompasses the predicted most amplified frequencies at transition for all of the included cases. In this range, the computed acoustic absorption per wavelength for 50% CO_2 is more than 3 orders of magnitude larger than the air case.

8.2 Facility and Experiments

The facility used for all experiments in the present study was the T5 Hypervelocity Reflected Shock Tunnel at Caltech. To address concerns about the extent of gaseous diffusion in the shock tube for air and CO_2 mixture experiments, a mixing tank of approximately 400 L volume was constructed (Section 2.1.2). As particulates in the freestream can destabilize the boundary layer and can lead to early instability and transition, a new and more extensive shock tube cleaning procedure was developed for use in between experiments (Section 2.1.3). The shock tube fill gas was taken only from research-quality gas bottles with lower tolerances for contamination and mixture uncertainty than previously used industrial air. These measures were successful in mitigating the effects of particulate contamination and resulted in more consistent,

clean, and repeatable transition measurements. It is recommended that these cleaning and contaminant minimization measures be maintained for all future T5 experiments where flow purity, optical measurements, and avoiding particulate contamination are important.

Nozzle flows were computed both with a simple one-dimensional calculation and an axisymmetric nozzle code, which serves to provide the input condition for the STABL-DPLR boundary layer solver. Estimates were made of the uncertainty in inflow conditions based upon the uncertainty in measured tunnel quantities. The properties were found to be relatively insensitive to cone-nozzle position uncertainty within 5 cm (Section 2.6).
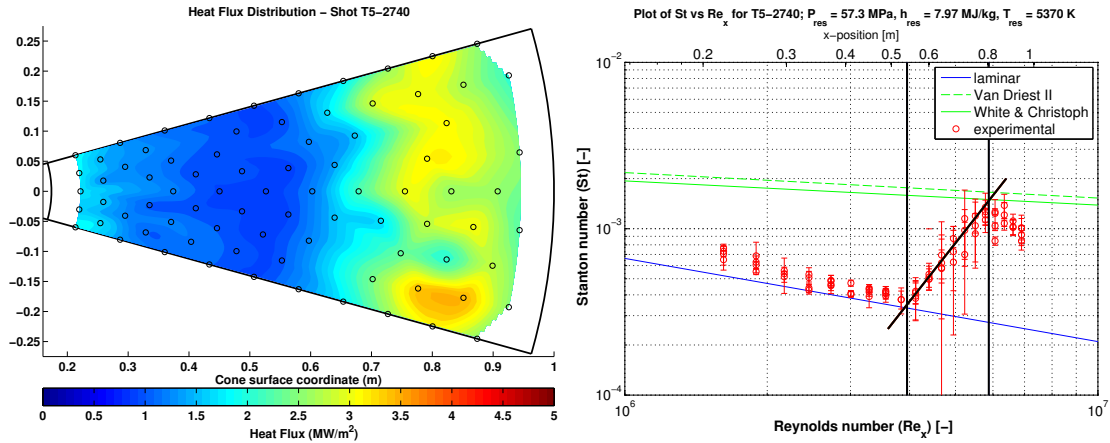
Figure 8.2: Experimentally measured distance between transition onset and transition completion for shot 2740. The contour plot at left presents the average heat flux during the test time over the surface of the cone. On the Re *vs.* St plot at right, a line is fit through the transitional region, and the transition onset location x_{Tr} is taken as the intersection of the fit with the laminar correlation. The transition completion location x_{TrComp} is taken as the intersection of the fit with the White and Christoph (1972) turbulent correlation. The distance between the two points is Δx_{Tr}.

The model was a smooth, 1 m long 5-degree half-angle aluminum cone, similar to that used in a number of previous experimental studies in T5, instrumented with 80 flush-mounted fast-response annular thermocouples sampled at 200 kHz. A spectral deconvolution method was used to compute time-resolved heat flux. Estimates of the

swallowing distance were made based on the observed nose tip bluntness, and found in all cases to be shorter than the distance from the tip to the first sensor, indicating that the cone is effectively sharp over the study's entire range of Reynolds numbers from the standpoint of the heat transfer measurements (Section 3.1).

Heat flux results were analyzed with Stanton number *versus* Reynolds number correlations for both laminar and turbulent boundary layers. In all, transition sufficiently clear to establish an onset location was observed in 55 cases after the initiation of the more intensive cleaning procedures described above. Of these 55 cases, transition completion was observed in 17. The transition onset and completion determination method used is presented graphically in Figure 8.2.

8.3   Analysis

The hypersonic boundary layer mean flow was computed as a similarity solution with frozen boundary layer composition to derive simplified boundary layer relationships and arrive at an approximate solution, and also with a more sophisticated axisymmetric reacting-flow CFD solver as implemented in STABL/DPLR (Section 4.1). The semi-empirical e^N method was reviewed and described. Stability analyses were performed using the STABL/PSE-Chem solver, which solves the reacting, two-dimensional, axisymmetric, linear parabolized stability equations to predict the amplification of disturbances within the boundary layer. In addition to fully reacting, vibrationally active flows, the effect of vibrational rate processes on the damping of second mode disturbances was investigated by altering the relevant parameters in the physical model to simulate vibrationally frozen and equilibrium cases. Analysis of the behavior of the pressure disturbance eigenfunction for simulated T5 cases indicated that Mack's so-called second mode is the dominant instability in these boundary layers (Section 4.3.1).

8.4 Results

8.4.1 Transition Onset

An alternative nondimensionalization of the transition onset location by the local laminar boundary layer thickness $(x/\delta_{99})_{\text{Tr}}$ was compared with Re_{Tr} and Re^*_{Tr}, and used to correlate the N factor results of boundary layer stability analyses with and without vibrational effects. At the conditions examined in the present study, vibrational effects were shown to be quite large for conditions with both pure and 50% CO_2 free streams, much less significant for air, and of essentially no consequence for N_2. The maximum observed $(x/\delta_{99})_{\text{Tr}}$ was 858 for CO_2, which is 25% higher than the maximum air $(x/\delta_{99})_{\text{Tr}}$ of 688, and 789 for 50% CO_2, which is 15% higher than the maximum for air. The results for $(x/\delta_{99})_{\text{Tr}}$ correlate with both Re^*_{Tr} and Re_{Tr}, which are nondimensional parameters that have been examined previously in hypersonic transition studies. The presence of vibrationally active CO_2 in the flow was found to have a large effect on the computed stability properties of the boundary layer.

The data for all gas types collapse onto one curve for the no vibration case due to the inviscid nature of the instability and the relative unimportance of chemical reactions for stability in this regime (see Section 5.2.1 for the details on the "no vibration" and "vibrational" models and their application in the present analysis). The results of Figure 8.3(a), computed without vibrational damping, predict values of $N_{\text{Tr}} > 12$ at the observed transition onset location when $(x/\delta_{99})_{\text{Tr}}$ exceeds 600, with values up to 25 at the extreme. These values are quite extraordinary and unprecedented; according to the results of Fedorov and Averkin (2010), calculated for cold-flow shock tunnel conditions at Mach 6.8, transition N factor values over 15 are inconsistent with physical reality as unavoidable kinetic fluctuations provide a noise floor even for an "absolutely quiet" free stream. With the inclusion of vibrational damping in Figure 8.3(b), the maximum values of N_{Tr} are now limited to much more

realistic, although still large, values of 10–13. These results provide strong evidence of
the essential role of vibrational relaxation in damping instabilities not only in carbon
dioxide but also air.

(a) $N_{TrNovib}$ vs. $(x/\delta_{99})_{Tr}$ (b) N_{Tr} vs. $(x/\delta_{99})_{Tr}$
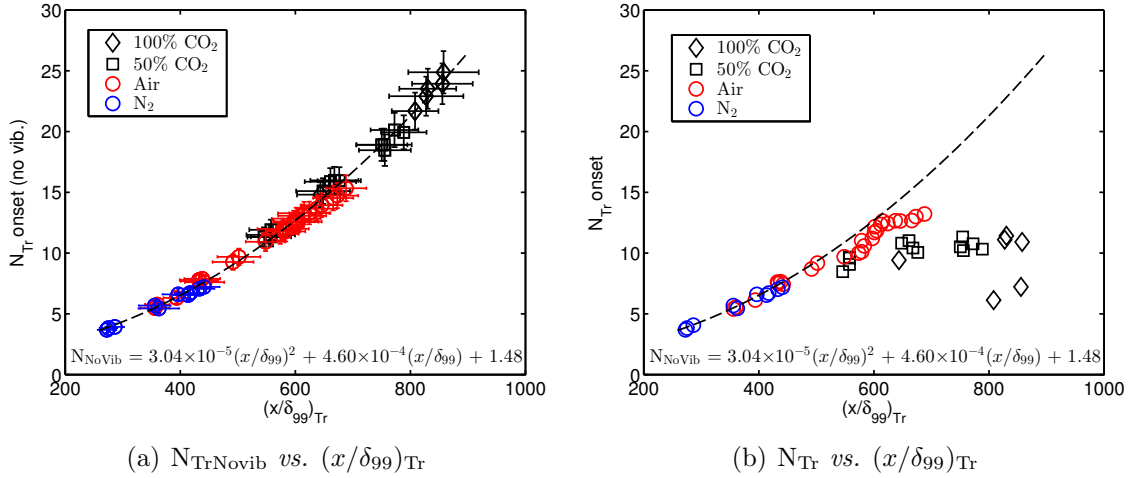
Figure 8.3: (a) N factor at transition computed with the no vibration model, with a
fit of the data; (b) N factor at transition computed with the vibration model, with the
no vibration fit repeated to highlight the difference and therefore the relative effect
of vibrational relaxation on the stability and nondimensional transition length. The
difference in N_{Tr} is large for CO_2, smaller for air, and insignificant for N_2.

The stability results were shown to depend upon the reference temperature in the
boundary layer as well as the gas type, as presented in Figure 8.4, and compare well
with computations for acoustic absorption due to vibrational relaxation performed
using the Fujii and Hornung (2001) code.

The N factor range for air in the present study was N_{Tr} = 5.4–13.2, the upper
part of which exceeds any previously computed shock tunnel transition results. One
possible explanation for the very high transition N factor results, which are more
typical of "quiet" tunnels, is the mismatch between the strongest noise frequencies
in the T5 freestream and the second mode frequencies preferentially amplified by
the boundary layer. Laser differential interferometry performed by Parziale et al.
(2014) indicated that most of the noise in the T5 freestream is at frequencies that are
relatively lower (< 500 kHz) than the relevant Mack second mode frequencies in the

present study.

(a) ΔN_{Tr} *vs.* T^* (b) Fujii absorption *vs.* T^*
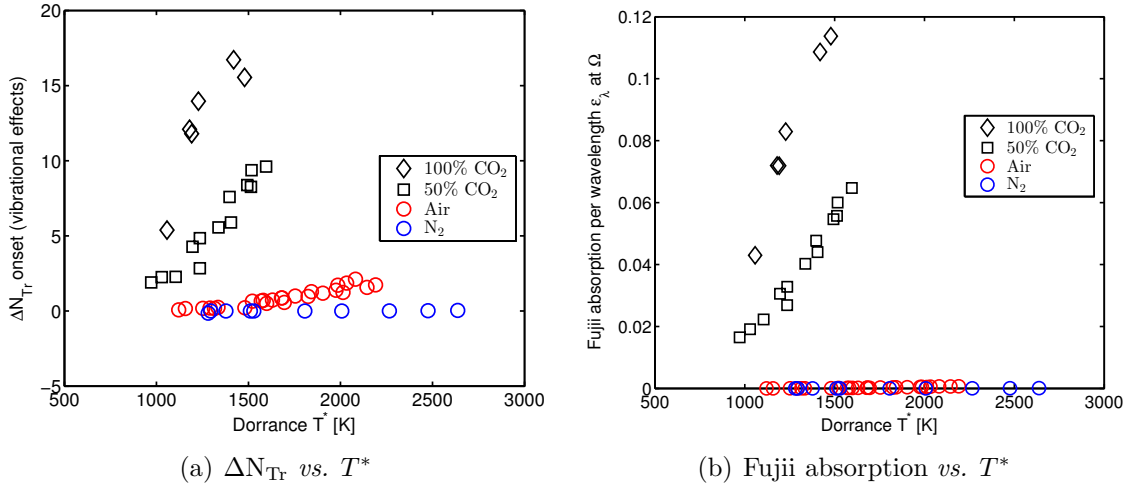
Figure 8.4: (a) The difference in N factor at transition between PSE-Chem computations made with the vibration and no vibration models, plotted against the Dorrance reference temperature; (b) Acoustic absorption rate (per wavelength) due to vibrational relaxation of Fujii and Hornung (2001), computed at reference conditions for the PSE-Chem-predicted most-amplified frequency Ω at transition for each case, plotted against the Dorrance reference temperature.

A strong unit Reynolds number effect on the transition Reynolds number and other relevant transition parameters has been found, consistent with a variable noise spectrum radiating from the boundary layer which forms on the nozzle wall. A slight plateau of the CO_2 and 50% CO_2 unit Re results is observed, and may be due to a difference in the radiated noise spectrum from the T5 nozzle for CO_2 flows (Section 5.2.2).

Transition onset data have been correlated by performing multivariable linear regression analysis, taking P_{res} and h_{res} (normalized by each data set's maximum pressure and enthalpy) as the possible predictor variables and the measured, normalized values of x_{Tr}, Re^*_{Tr} and Re_{Tr} as the modeled variables. Transition onset data reported in Germain and Hornung (1997) and Adam and Hornung (1997) have been re-analyzed in the same way to compare (Section 5.3.2). Controlling for variations in P_{res}, no statistically significant dependence of Re^*_{Tr} on h_{res} was found for either the

present air or N_2 data or the historical air and N_2 data. While a small but statistically significant relationship was found for the dependence of Re^*_{Tr} on h_{res} for historical CO_2 and the present 50% CO_2 results, it is negative for the former case and positive for the latter (in historical data the relationship has always been stated as positive).

8.4.2 Turbulent Spot Observations

Time- and spatially-resolved heat transfer in a high-enthalpy hypervelocity flow on a 5-degree half-angle cone were measured with thermocouples. Turbulent spots were observed propagating in both heat transfer traces and heat flux "movies" of the developed cone surface (Section 6.2). These observations were used to calculate turbulent spot convection rates, which were compared with previous experimental and computational results. Although the present results were obtained at different conditions from past experiments, the normalized spot propagation results for the present Mach ~ 5 conditions appeared to be generally consistent with past supersonic and hypersonic experiments, as well as with the computational results (Section 6.4).

However, the flow conditions in all of the reviewed simulations were essentially nonreactive (cold flow with frozen composition), and the ratios of freestream to wall temperature, as well as adiabatic to nonadiabatic wall temperature, in the simulations were far from the present experimental conditions. The flow conditions in these T5 tests were designed to simulate hypervelocity atmospheric flight and the flow over the model is hot, partially dissociated gas with some amount of chemical and vibrational nonequilibrium due to the rapid expansion process in the nozzle. The available computational results of spot propagation in hypersonic flow in the present literature survey simulated much higher wall temperature ratios T_w/T_e and adiabatic wall temperature ratios T_w/T_{aw} than actually occur in reflected shock tunnel experiments and flight (see Table 6.3 and Figure 6.18).

Due to the sparse number and nature of the thermocouple data, there is substantial

uncertainty in defining the precise leading and trailing edges of the spot. Taking the results of all 29 isolated spot examples together, the putative leading edge propagates downstream at about $0.90U_e$ (95% confidence interval: 0.88 to 0.93), the peak or centroid at $0.76U_e$ (95% confidence interval: 0.72 to 0.80), and the trailing edge at $0.63U_e$ (95% confidence interval: 0.59 to 0.67).
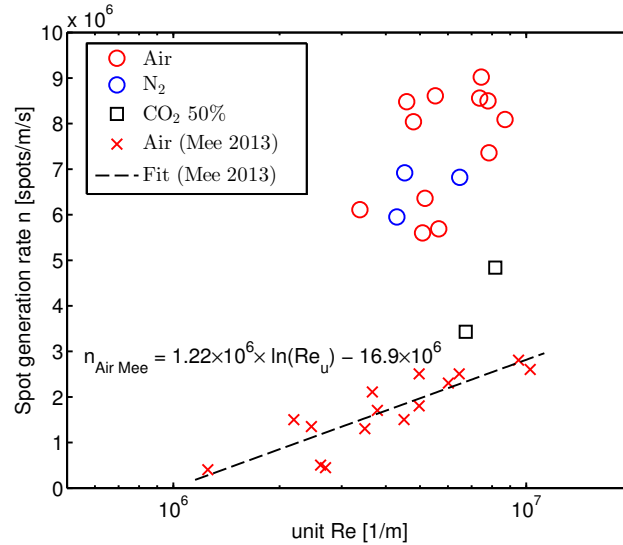
Figure 8.5: Spot generation rates for the present data compared with the results from Mee and Tanguy (2013).

With the measured parameters, a simple geometric model for the propagation of turbulent spots has been adapted from Jewell (2008) and used, following Mee and Tanguy (2013), to infer turbulent spot generation rates n from a set of 17 experimentally measured transition onset and completion distances in three different gas mixtures. Turbulent spot generation is the outcome of the boundary layer receptivity process (Fedorov, 2003) and is therefore important for understanding both receptivity and the region of intermittent turbulence which occurs between transition onset and completion. The results indicate that n is significantly higher in air and N_2 boundary layers than for experiments with 50% CO_2. The measured spot generation rates, which are presented graphically in Figure 8.5, ranged from 5.5×10^6 to 9×10^6 spots/m/s for air and N_2, and 3×10^6 to 5×10^6 spots/m/s for 50% CO_2 cases. While spot generation

rates were higher than those found by Mee and Tanguy (2013), most of the difference is accounted for by differing model inputs for C_{te}, and the Mee results were acquired on a flat plate in a different facility.

8.5   Gas Injection Study

Past transition experiments performed with blowing and ablation in various configurations were discussed. An injection system based upon a 10 μm sintered metal injector was developed and found to be superior to previous designs using macroscopic holes for injection, in that the porous injector did not immediately trip the boundary layer. This injection system was analyzed and calibrated (Section 7.1).

Estimates of the effects of injection on the boundary layer were made by adapting the compressible similarity solution and the diffusion properties of injectants into the boundary layer were calculated. The qualitative properties of these injection estimates were found to be similar to a more sophisticated parametric study performed with STABL/DPLR modeling the porous injector as an axisymmetric "top hat" injection profile at the cone's surface. Boundary layer contours for species mass concentration were presented and normalized by the concentration at the wall, and the stability properties of injection boundary layers computed with STABL/PSE-Chem. An example of a series of boundary layer contours, showing the evolution of the CO_2 concentration in the boundary layer downstream of the injection location, is presented in Figure 8.6. The stability characteristics of flows with injection ratios of a small magnitude are found to be comparable to the no-injection case, but flows with injection ratios on the order of the boundary layer mass flux were found to be highly unstable compared to the no-injection case (Section 7.3.4).

The results from gas injection experiments performed at similar tunnel conditions were presented (Section 7.4). Apparent transition onset delays were documented in
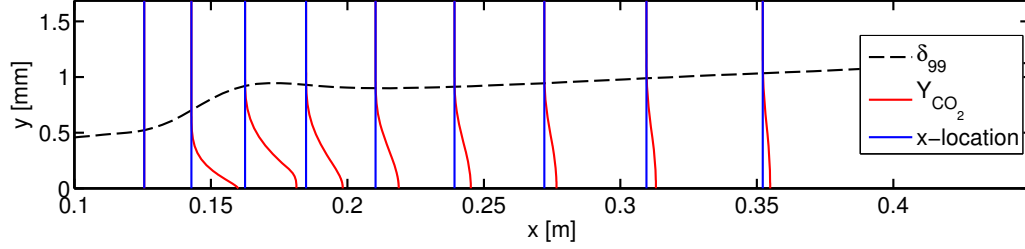
Figure 8.6: DPLR Y_{CO_2} results for shot 2789 freestream with $\dot{m}_{inj}/\dot{m}_{bl} = 0.35$, presented in normalized form. See also Figure 7.17.

shots with CO_2 injection up to a critical mass flow ratio, compared both to shots with a porous injector but no injection, control shots with a smooth injector section, and control shots using similar mass flow rates of argon. Computations indicated that injection magnitudes exceeding this critical mass flow ratio are destabilizing. However, the present experimental injection results, presented in Figure 8.7, are not conclusive. In particular, no injection experiments were performed under the clean tunnel conditions described in Section 2.1.3, and the mass flow rates for the experiments that were performed were calculated indirectly from the recorded run tank pressure. The sintered porous material appeared to work well for gas injection. However, future injection experiments should use the state-of-the-art cleaning method to be fully comparable with the transition onset results described in the rest of this thesis. Furthermore, the design of any future injection mechanism should include a mass flow meter in the flow path, as well as high-speed pressure and temperature measurements in the injector plenum to temporally resolve the mass flow rate of the injectant. Prior to undertaking further experimental study of injection, numerical simulations which include the τ reducing effects of small quantities of CO_2 on the O_2 and N_2 molecules described in Bertolotti (1998) should be performed to investigate the potential of this mechanism for increased acoustic damping.
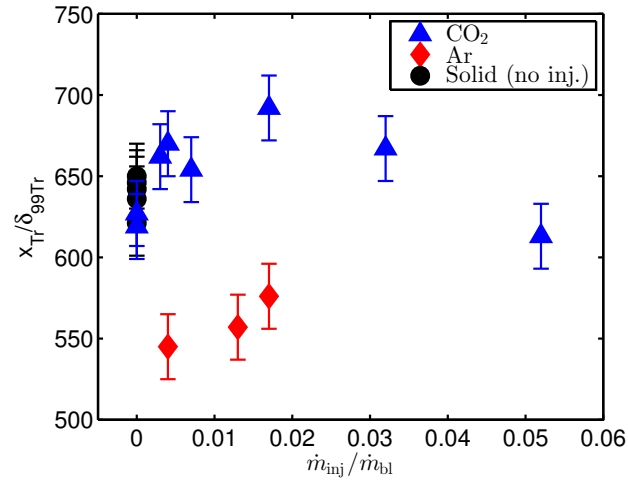
Figure 8.7: $x_{\mathrm{Tr}}/\delta_{99\mathrm{Tr}}$ for gas injection and control (solid) experiments at similar tunnel conditions ($h_{\mathrm{res}} \approx 9.7$ MJ/kg, $P_{\mathrm{res}} \approx 55$ MPa).

Bibliography

B. J. Abu-Ghannam and R. Shaw. Natural transition of boundary layers–the effects of turbulence, pressure gradient, and flow history. *Journal of Mechanical Engineering Science*, 22(5):213–228, 1980. doi: 10/ff9t6n.

(Referenced on page 128.)

P. H. Adam. *Enthalpy Effects on Hypervelocity Boundary Layers*. PhD thesis, California Institute of Technology, Pasadena, CA, 1997.

(Referenced on pages 47, 49, 52, 56, 75, 119, 123, and 124.)

P. H. Adam and H. G. Hornung. Enthalpy Effects on Hypervelocity Boundary-layer Transition: Ground Test and Flight Data. *Journal of Spacecrafts and Rockets*, 34 (5):614–619, 1997. doi: 10.2514/2.3278.

(Referenced on pages 8, 44, 53, 96, 98, 109, 111, 119, 120, 121, 122, 123, 124, 125, 127, and 201.)

I. E. Alber. *Aerospace Engineering on the Back of an Envelope*. Springer-Verlag, 2012.

(Referenced on pages 2 and 49.)

J. D. Anderson. *Modern Compressible Flow With Historical Perspective*. McGraw-Hill, second edition, 1990.

(Referenced on pages 50 and 161.)

J. D. Anderson. *Hypersonic and High-Temperature Gas Dynamics*. AIAA Education

Series, second edition, 2006.

(Referenced on pages 2, 168, and 169.)

J. D. Anderson. *Fundamentals of Aerodynamics*. McGraw-Hill, fourth edition, 2007.

(Referenced on page 49.)

R. J. Anthony, T. V. Jones, and J. E. LaGraff. High frequency surface heat flux imaging of bypass transition. *Journal of Turbomachinery*, 127(2):241–250, 2005. doi: 10.1115/1.1860379.

(Referenced on page 130.)

T. A. Barber, B. A. Maicke, and J. Majdalani. Current State of High Speed Propulsion: Gaps, Obstacles, and Technological Challenges in Hypersonic Applications. In *45th AIAA/ASME/SAE/ASEE Joint Propulsion Conference & Exhibit*, Denver, CO, 2009. AIAA-2009-5118. doi: 10.2514/6.2009-5118.

(Referenced on page 1.)

A. K.-W. Beierholm, I.A. Leyva, S. J. Laurence, J. S. Jewell, and H. G. Hornung. Transition Delay in a Hypervelocity Boundary Layer using Nonequilibrium CO_2 Injection. Technical report, GALCIT Report FM 2008.001, Pasadena, California, 2008.

(Referenced on pages 10, 22, 23, and 168.)

J. Belanger and H. G. Hornung. Numerical Predictions and Actual Behavior of the Free Piston Shock Tunnel T5. In *18th AIAA Aerospace Ground Testing Conference*, Colorado Springs, CO, 1994. AIAA-1994-2527. doi: 10.2514/6.1994-2527.

(Referenced on pages 62, 63, and 64.)

J. J. Bertin. *Hypersonic Aerothermodynamics*. AIAA, 1994.

(Referenced on page 2.)

F. P. Bertolotti. The influence of rotational and vibrational energy relaxation on boundary-layer stability. *Journal of Fluid Mechanics*, 372(1):93–118, 1998. doi: 10.1017/S0022112098002353.

(Referenced on pages 192, 194, and 205.)

D. Bose and G. V. Candler. Thermal Rate Constants of the $N_2 + O \rightarrow NO + N$ Reaction Using Ab Initio $3A''$ and $3A'$ Potential Energy Surfaces. *Journal of Chemical Physics*, 104(8):2825–2833, 1996. doi: 10.1063/1.471106.

(Referenced on page 82.)

D. Bose and G. V. Candler. Thermal Rate Constants of the $O+N \rightarrow NO+O$ Reaction Based on the $2A'$ and $4A'$ Potential Energy Surfaces. *Journal of Chemical Physics*, 107(16):6136–6145, 1997. doi: 10.1063/1.475132.

(Referenced on page 82.)

S. Browne, J. Ziegler, and J.E. Shepherd. Numerical solution methods for shock and detonation jump conditions. Technical report, California Institute of Technology, Pasadena, CA, July 2008. GALCIT Report FM2006.006.

(Referenced on pages 19, 21, and 60.)

M. Camac. CO_2 relaxation rocesses in shock waves. In J.G. Hall, editor, *Fundamental Phenomena in Hypersonic Flow*, pages 195–215. Cornell University Press, 1966.

(Referenced on pages 6, 82, 99, 105, and 107.)

G. V. Candler. Hypersonic Nozzle Analysis Using an Excluded Volume Equation of State. In *Proceedings of 38th AIAA Thermophysics Conference*, Toronto, Ontario Canada, 2005. AIAA-2005-5202. doi: 10.2514/6.2005-5202.

(Referenced on page 24.)

G. V. Candler and R. W. MacCormack. Computation of weakly ionized hypersonic flows in thermochemical nonequilibrium. *Journal of Thermophysics and Heat*

Transfer, 5(3):266–273, 1991. doi: 10.2514/3.260.

(Referenced on page 82.)

K. M. Casper, H. B. Johnson, and S. P. Schneider. Effect of freestream noise on roughness-induced transition for a slender cone. *Journal of Spacecraft and Rockets*, 48(3):406–413, 2011. doi: 10.2514/1.48300.

(Referenced on page 41.)

S. Catris and B. Aupoix. Density Corrections for Turbulence Models. *Aerospace Science and Technology*, 4(1):1–11, 2000. doi: 10.1016/S1270-9638(00)00112-7.

(Referenced on page 24.)

T. Cebeci and A. M. O. Smith. *Analysis of turbulent boundary layers*. Academic Press, London, 1974.

(Referenced on page 138.)

K. K. Chen and N. A. Thyson. Extension of Emmons' spot theory to flows on blunt bodies. *AIAA Journal*, 9(5):821–825, 1971. doi: 10.2514/3.6281.

(Referenced on page 128.)

T. P. Chong and S. Zhong. On the three-dimensional structure of turbulent spots. *Journal of Turbomachinery*, 127(3):545–551, 2005. doi: 10.1115/GT2003-38435.

(Referenced on page 150.)

J. P. Clark. *A Study of Turbulent-Spot Propagation in Turbine-Representative Flows*. PhD thesis, University of Oxford, Oxford, UK, 1993.

(Referenced on pages 136 and 149.)

J. P. Clark, T. V. Jones, and J. E. LaGraff. On the propagation of naturally-occurring turbulent spots. *Journal of Engineering Mathematics*, 28(1):1–19, 1994. doi: 10.1007/BF02383602.

(Referenced on pages 58, 128, 137, 138, 149, 152, and 153.)

J. F. Clarke and M. McChesney. *The Dynamics of Real Gases*, volume 175. Butterworths, 1964.

(Referenced on page 5.)

J.-P. Davis. *High-Enthalpy Shock/Boundary-Layer Interaction on a Double Wedge.* PhD thesis, California Institute of Technology, Pasadena, CA, 1999.

(Referenced on page 48.)

A. Demetriades. An Experiment on the Stability of Hypersonic Laminar Boundary Layers. *Journal of Fluid Mechanics*, 7(3):385–396, 1960. ISSN 0022-1120. doi: 10.1017/S0022112060000153.

(Referenced on page 3.)

S. Dhawan and R. Narasimha. Some properties of boundary layer flow during the transition from laminar to turbulent motion. *Journal of Fluid Mechanics*, 3(4): 418–436, 1958. doi: 10.1017/S0022112058000094.

(Referenced on page 128.)

D. J. Doorley and F. T. Smith. Initial-value problems for spot disturbances in incompressible or compressible boundary layers. *Journal of Engineering Mathematics*, 26 (1):87–106, 1992. doi: 10.1007/BF00043229.

(Referenced on pages 137 and 154.)

W. H. Dorrance. *Viscous hypersonic flow: theory of reacting and hypersonic boundary layers.* McGraw-Hill, 1962.

(Referenced on pages 53 and 121.)

L. Duan and M. P. Martin. Direct numerical simulation of hypersonic turbulent boundary layers. Part 4. Effect of high enthalpy. *Journal of Fluid Mechanics*, 684 (1):25–59, 2011. doi: 10.1017/jfm.2011.252.

(Referenced on page 54.)

L. Duan, I. Beekman, and M. P. Martin. Direct numerical simulation of hypersonic turbulent boundary layers. Part 2. Effect of wall temperature. *Journal of Fluid Mechanics*, 655:419–445, 2010. doi: 10.1017/S0022112010000959.

(Referenced on page 54.)

L. Duan, I. Beekman, and M. P. Martin. Direct numerical simulation of hypersonic turbulent boundary layers. Part 3. Effect of Mach number. *Journal of Fluid Mechanics*, 672:245–267, 2011. doi: 10.1017/S0022112010005902.

(Referenced on page 54.)

H. W. Emmons. The laminar-turbulent transition in a boundary layer: Part I. *Journal of the Aeronautical Sciences*, 18(7), 1951. doi: 10.2514/8.2010.

(Referenced on pages 128 and 138.)

A. Fedorov. Transition and Stability of High-Speed Boundary Layers. *Annual Review of Fluid Mechanics*, 43:79–95, 2011a. doi: 10.1146/annurev-fluid-122109-160750.

(Referenced on pages 2, 3, 4, and 81.)

A. V. Fedorov. Receptivity of a High-Speed Boundary Layer to Acoustic Disturbances. *Journal of Fluid Mechanics*, 491:101–129, 2003. doi: 10.1017/S0022112003005263.

(Referenced on pages 134, 155, and 203.)

A. V. Fedorov. Lectures on transition and control of high-speed boundary layers. Lecture series, 2011b. Graduate Aerospace Laboratories, California Institute of Technology, Pasadena, CA.

(Referenced on pages 80 and 103.)

A. V. Fedorov. Receptivity of a supersonic boundary layer to solid particulates. *Journal of Fluid Mechanics*, 737:105–131, 2013. doi: 10.1017/jfm.2013.564.

(Referenced on pages 16 and 134.)

A. V. Fedorov and S. N. Averkin. Receptivity of compressible boundary layer to kinetic fluctuations. In P. Schlatter and D. S. Henningson, editors, *Seventh IUTAM Symposium on Laminar-Turbulent Transition*, volume 18, pages 485–488. 2010. doi: 10.1007/978-90-481-3723-7.

(Referenced on pages 102, 103, and 199.)

A. V. Fedorov and M. V. Koslov. Receptivity of high-speed boundary layer to solid particulates. In *6th AIAA Theoretical Fluid Dynamics Conference*, Honolulu, HI, 2011. AIAA-2011-3925. doi: 10.2514/6.2011-3925.

(Referenced on page 16.)

A. V. Fedorov, N. D. Malmuth, and H. G. Hornung. Stabilization of hypersonic boundary layers by porous coatings. *AIAA Journal*, 39(4):605–610, 2001. doi: 10.2514/2.1382.

(Referenced on page 9.)

A. Fiala, R. Hillier, S. G. Mallinson, and H. S. Wijesinghe. Heat transfer measurement of turbulent spots in a hypersonic blunt-body boundary layer. *Journal of Fluid Mechanics*, 555:81–111, 2006. doi: 10.1017/S0022112006009396.

(Referenced on pages 128, 130, 134, 150, 151, 152, and 154.)

M. C. Fischer. Spreading of a turbulent disturbance. *AIAA Journal*, 10(7):957–959, 1972. doi: 10.2514/3.50265.

(Referenced on pages 128 and 137.)

K. Fujii and H. G. Hornung. A procedure to estimate absorption rate of sound propagating through high temperature gas. Technical report, California Institute of Technology, Pasadena, CA, August 2001. GALCIT Report FM2001.004.

(Referenced on pages 5, 6, 7, 9, 104, 105, 106, 107, 108, 200, and 201.)

P. Germain. *The Boundary Layer on Sharp Cone in High-Enthalpy Flow*. PhD thesis,

California Institute of Technology, Pasadena, CA, 1993.

(Referenced on pages 8, 47, 75, 109, 111, and 119.)

P. D. Germain and H. G. Hornung. Transition on a Slender Cone in Hypervelocity Flow. *Experiments in Fluids*, 22:183–190, 1997. doi: 10.1007/s003480050036.

(Referenced on pages 96, 119, 122, 123, 124, 125, 127, and 201.)

D. Goodwin. Cantera: An object-oriented software toolkit for chemical kinetics, thermodynamics, and transport processes. Available: http://code.google.com/p/cantera, 2009. Accessed: 12/12/2012.

(Referenced on pages 21 and 60.)

D. G. Goodwin. An Open-Source, Extensible Software Suite for CVD Process Simulation. Technical report, Pennington, NJ, 2003. Chemical Vapor Deposition XVI and EUROCVD.

(Referenced on pages 21 and 60.)

J. E. Gronvall. *Computational Study of Hypersonic Boundary Layer Stability on Cones.* PhD thesis, University of Minnesota, Minneapolis, MN, 2012.

(Referenced on pages 84 and 97.)

J. E. Gronvall, H. B. Johnson, and G. V. Candler. Boundary Layer Stability Analysis of the Free-Piston Shock Tunnel HIEST Transition Experiments. In *48th Aerospace Sciences Meeting*, Orlando, FL, 2010. AIAA. doi: 10.2514/6.2010-896. AIAA-2010-0896.

(Referenced on pages 97, 98, and 102.)

J. E. Gronvall, H. B. Johnson, and G. V. Candler. Boundary-Layer Stability Analysis of the High Enthalpy Shock Tunnel Transition Experiments. *Journal of Spacecraft and Rockets*, pages 1–13, 2014. doi: 10.2514/1.A32577.

(Referenced on pages 81, 84, 97, and 99.)

R. N. Gupta, J. M. Yos, R. A. Thompson, and K. P. Lee. A review of reaction rates and thermodynamic and transport properties for an 11-species air model for chemical and thermal nonequilibrium calculations to 30000 K. NASA-RP-1232, 1990.

(Referenced on page 23.)

M. C. Henderson, K. F. Herzfeld, J. Bry, R. Coakley, and G. Carriere. Thermal relaxation in nitrogen with wet carbon dioxide as impurity. *The Journal of the Acoustical Society of America*, 45(1):109–114, 1969. doi: 10.1121/1.1911343.

(Referenced on page 192.)

T. Herbert. Parabolized stability equations. *Annual Review of Fluid Mechanics*, 29 (1):245–283, 1997. doi: 10.1146/annurev.fluid.29.1.245.

(Referenced on pages 77 and 81.)

E. H. Hirschel. *Basics of Aerothermodynamics*. Springer-Verlag, 2005.

(Referenced on page 170.)

A. J. Hofeldt, Jr. *The Investigation of Naturally-Occurring Turbulent Spots Using Thin-Film Gauges*. PhD thesis, University of Oxford, Oxford, UK, 1996.

(Referenced on page 149.)

H. G. Hornung. T5 Data Plots: T5-1 to T5-67. Unpublished early T5 data, October 1991.

(Referenced on page 21.)

H. G. Hornung. Performance Data of the New Free-Piston Shock Tunnel at GALCIT. In *Proceedings of 17th AIAA Aerospace Ground Testing Conference*, Nashville, TN, 1992. AIAA. doi: 10.2514/6.1992-3943. AIAA-1992-3943.

(Referenced on page 12.)

H. G. Hornung and J. Belanger. Role and techniques of ground testing for simulation of flows up to orbital speed. In *16th Aerodynamic Ground Testing Conference*, Seattle, WA, 1990. AIAA. doi: 10.2514/6.1990-1377. AIAA-1990-1377.

(Referenced on pages 12, 19, 62, and 64.)

M. L. Hudson, N. Chokani, and G. V. Candler. Linear stability of hypersonic flow in thermochemical nonequilibrium. *AIAA Journal*, 35(6):958–964, 1997. doi: 10.2514/2.204.

(Referenced on page 84.)

C. R. Illingworth. Unsteady laminar flow of gas near an infinite flat plate. *Mathematical Proceedings of the Cambridge Philosophical Society*, 46(4):603–613, 1950. doi: 10.1017/S0305004100026165.

(Referenced on page 70.)

P. S. Iyer and K. Mahesh. High-speed boundary-layer transition induced by a discrete roughness element. *Journal of Fluid Mechanics*, 729:524–562, 2013. doi: 10.1017/jfm.2013.311.

(Referenced on page 40.)

C. S. James. Observations of turbulent-burst geometry and growth in supersonic flow. NACA-TN-4235, NACA, April 1958.

(Referenced on page 128.)

J. S. Jewell. Boundary Layer Transition in Hypersonic Flows. Master's thesis, University of Oxford, Oxford, UK, 2008.

(Referenced on pages 136, 154, and 203.)

J. S. Jewell and J. E. Shepherd. T5 conditions report: Shots 2526–2823. Technical report, California Institute of Technology, Pasadena, CA, June 2014. GALCIT

Report FM2014.002.

(Referenced on page 60.)

J. S. Jewell, I. A. Leyva, N. J. Parziale, and J. E. Shepherd. Effect of gas injection on transition in hypervelocity boundary layers. In *Proceedings of the 28th International Symposium on Shock Waves*, pages 735–740, Manchester, UK, July 2011. ISSW28-2767. doi: 10/bf78.

(Referenced on pages 11, 119, 120, 159, and 189.)

J. S. Jewell, N. J. Parziale, I. A. Leyva, J. E. Shepherd, and H. G. Hornung. Turbulent Spot Observations within a Hypervelocity Boundary Layer on a 5-degree Half-Angle Cone. In *42nd AIAA Fluid Dynamics Conference and Exhibit*, New Orleans, LA, 2012. AIAA-2012-3062. doi: 10.2514/6.2012-3062.

(Referenced on page 129.)

J. S. Jewell, J. S. Shepherd, and I. A. Leyva. Shock tunnel operation and correlation of boundary layer transition on a cone in hypervelocity flow. In *Proceedings of the 29th International Symposium on Shock Waves*, pages 723–728, Madison, WI, July 2013a. ISSW29-000300. doi: 10/bf8d.

(Referenced on page 117.)

J. S. Jewell, J. S. Shepherd, and I. A. Leyva. Supplemental data for "Shock tunnel operation and correlation of boundary layer transition on a cone in hypervelocity flow". Available at: http://www.joejewell.com, California Institute of Technology, July 2013b.

(Referenced on page 117.)

J. S. Jewell, R. M. Wagnild, I. A. Leyva, G. V. Candler, and J. E. Shepherd. Transition Within a Hypervelocity Boundary Layer on a 5-Degree Half-Angle Cone in Air/CO_2 Mixtures. In *51st AIAA Aerospace Sciences Meeting including the New Horizons*

Forum and Aerospace Exposition, Grapevine, TX, 2013c. AIAA-2013-0523. doi: 10.2514/6.2013-523.

(Referenced on pages 74, 81, 83, 99, and 100.)

A. Jocksch. *Direct numerical simulation of turbulent spots in high-speed boundary layers*. PhD thesis, Eidgenössische Technische Hochschule ETH Zürich, Nr. 18104, Zürich, Switzerland, 2009.

(Referenced on pages 151 and 152.)

A. Jocksch and L. Kleiser. Growth of turbulent spots in high-speed boundary layers on a flat plate. *International Journal of Heat and Fluid Flow*, 29(6):1543–1557, 2008. doi: 10.1016/j.ijheatfluidflow.2008.08.008.

(Referenced on pages 150, 151, and 152.)

H. B. Johnson. *Thermochemical Interactions in Hypersonic Boundary Layer Stability*. PhD thesis, University of Minnesota, Minneapolis, MN, 2000.

(Referenced on pages 75, 78, 80, 84, 97, and 102.)

H. B. Johnson and G. V. Candler. Hypersonic boundary layer stability analysis using PSE-Chem. In *35th Fluid Dynamics Conference and Exhibit*. AIAA, 2005. doi: 10.2514/6.2005-5023. AIAA-2005-5023.

(Referenced on page 81.)

H. B. Johnson, T. G. Seipp, and G. V. Candler. Numerical study of hypersonic reacting boundary layer transition on cones. *Physics of Fluids*, 10:2676–2685, 1998. doi: 10.1063/1.869781.

(Referenced on pages 8, 81, 98, and 102.)

T. J. Juliano and S. P. Schneider. Instability and Transition on the HIFiRE-5 in a Mach-6 Quiet Tunnel. In *Proceedings of the 40th AIAA Fluid Dynamics Conference*

and Exhibit, Chicago, IL, 2010. AIAA-2010-5004. doi: 10.2514/6.2010-5004.

(Referenced on page 103.)

S. Karl, K. Hannemann, and H. G. Hornung. Bluntness effects in hypersonic flow over slender cones and wedges. In *Proceedings of the 28th International Symposium on Shock Waves*, pages 691–696, Manchester, UK, July 2011. ISSW28-2710. doi: 10/bf77.

(Referenced on page 37.)

W. Kays, M. Crawford, and B. Weigand. *Convective Heat and Mass Transfer*. McGraw-Hill, fourth edition, 2005.

(Referenced on pages 170 and 171.)

R. L. Kimmel. The effect of pressure gradients on transition zone length in hypersonic boundary layers. WL-TR-94-3012, Wright Laboratory, December 1993.

(Referenced on page 136.)

R. L. Kimmel. Aspects of Hypersonic Boundary-Layer Transition Control. In *Proceedings of the 41st AlAA Aerospace Sciences Meeting and Exhibit*, Reno, NV, 2003. AIAA-2003-0772. doi: 10.2514/6.2003-772.

(Referenced on page 9.)

R. L. Kimmel, D. Adamczak, D. Gaitonde, A. Rougeux, and J. R. Hayes. HIFiRE-1 boundary layer transition experiment design. In *Proceedings of the 45th AlAA Aerospace Sciences Meeting and Exhibit*, Reno, NV, 2007. AIAA-2007-0534. doi: 10.2514/6.2007-534.

(Referenced on page 98.)

L. E. Kinsler, A. R. Frey, A. B. Coppens, and J. V. Sanders. *Fundamentals of Acoustics (Third Edition)*. John Wiley & Sons, Inc., New York, 1982.

(Referenced on page 5.)

L. Krishnan and N. D. Sandham. Effect of Mach number on the structure of turbulent spots. *Journal of Fluid Mechanics*, 566:225–234, 2006. doi: 10.1017/S0022112006002412.

(Referenced on pages 150, 151, and 152.)

S. J. Laurence, A. Wagner, K. Hannemann, V. Wartemann, H. Lüdeke, H. Tanno, and K. Itoh. Time-Resolved Visualization of Instability Waves in a Hypersonic Boundary Layer. *AIAA Journal*, 50(1):243–246, 2012. doi: 10.2514/1.J05112.

(Referenced on page 150.)

L. Lees. The Stability of the Laminar Boundary Layer. NACA Report 876, NACA TN 1360, NACA, 1947.

(Referenced on page 3.)

L. Lees. Laminar heat transfer over blunt-nosed bodies at hypersonic flight speeds. *Jet Propulsion*, 26:259–269, 1956. doi: 10.2514/8.6977.

(Referenced on pages 53 and 70.)

I. A. Leyva, J. S. Jewell, S. Laurence, H. G. Hornung, and J. E. Shepherd. On the Impact of Injection Schemes on Transition in Hypersonic Boundary Layers. In *16th AIAA/DLR/DGLR International Space Planes and Hypersonic Systems and Technologies Conference*, Bremen, Germany, 2009a. AIAA-2009-7204. doi: 10.2514/6.2009-7204.

(Referenced on pages 156, 157, and 158.)

I. A. Leyva, S. Laurence, A. K.-W. Beierholm, H. G. Hornung, R. W. Wagnild, and G. C. Candler. Transition Delay in Hypervelocity Boundary Layers by Means of CO_2/Acoustic Instability Interactions. In *47th AIAA Aerospace Sciences Meeting Including the New Horizons Forum and Aerospace Exposition*, Orlando, Florida,

2009b. AIAA-2009-1287. doi: 10.2514/6.2009-1287.

(Referenced on page 5.)

F. Li, M. Choudhari, C.-L. Chang, R. Kimmel, D. Adamczak, and M. Smith. Transition Analysis for the HIFiRE-1 Flight Experiment. In *Proceedings of the 41st AlAA Fluid Dynamics Conference and Exhibit*, Honolulu, HI, 2011. AIAA-2011-3414. doi: 10.2514/6.2011-3414.

(Referenced on page 98.)

J. A. Lordi, R. E. Mates, and J. R. Moselle. Computer program for the numerical solution of nonequilibrium expansions of reacting gas mixtures. NASA CR-472, 1966.

(Referenced on pages 23, 24, 105, and 106.)

L. M. Mack. Boundary-Layer Stability Theory. JPL 900-277 Rev. A, also also NASA CR131501, 1969.

(Referenced on page 84.)

L. M. Mack. Boundary-layer linear stability theory. special course on stability and transition of laminar flow advisory group for aerospace research and development. Technical report, 1984. AGARD Report No. 709.

(Referenced on pages 4, 83, and 84.)

M. MacLean, T. Wadhams, M. Holden, and H. Johnson. Ground test studies of the HIFiRE-1 transition experiment, Part 2: Computational analysis. *Journal of Spacecraft and Rockets*, 45(6):1149–1164, 2008. doi: 10.2514/1.37693.

(Referenced on page 98.)

M. R. Malik. Hypersonic Flight Transition Data Analysis Using Parabolized Stability Equations with Chemistry Effects. *Journal of Spacecraft and Rockets*, 40(3):332–

344, 2003. doi: 10.2514/2.3968.

(Referenced on pages 2, 4, 81, and 98.)

M. R. Malik and E. C. Anderson. Real gas effects on hypersonic boundary-layer stability. *Physics of Fluids A: Fluid Dynamics*, 3(5):803–821, 1991. doi: 10.1063/1.858012.

(Referenced on pages 81 and 84.)

E. C. Marineau and H. G. Hornung. Modeling and calibration of fast-response coaxial heat flux gages. In *47th Aerospace Sciences Meeting*, Orlando, FL, 2009. AIAA. doi: 10.2514/6.2009-737. AIAA-2009-0737.

(Referenced on pages 44 and 48.)

A. Martellucci and H. Rie. Effects of mass additions on viscous flow parameters. Technical report, DTIC Document, January 1971. Space and Missile Systems Organization TR-71-60.

(Referenced on page 159.)

M. P. Martin. Direct numerical simulation of hypersonic turbulent boundary layers. Part 1. Initialization and comparison with experiments. *Journal of Fluid Mechanics*, 570:347–364, 2007. doi: 10.1017/S0022112006003107.

(Referenced on page 54.)

B. J. McBride, M. J. Zehe, and S. Gordon. NASA Glenn coefficients for calculating thermodynamic properties of individual species. Technical report, 2002. Report TP-2002-21155.

(Referenced on page 82.)

D. J. Mee. Boundary-layer transition measurements in hypervelocity flows in a shock tunnel. *AIAA Journal*, 40(8):1542–1548, 2002. doi: 10.2514/2.1851.

(Referenced on pages 128, 137, 145, 149, 151, 152, and 154.)

D. J. Mee and C. P. Goyne. Turbulent spots in boundary layers in a free-piston shock-tunnel flow. *Shock Waves*, 6(6):337–343, 1996. doi: 10.1007/BF02511324. (Referenced on pages 58, 59, and 149.)

D. J. Mee and G. Tanguy. Turbulent spot initiation rates in boundary layers in a shock tunnel. In *Proceedings of the 29th International Symposium on Shock Waves*, pages 623–628, Madison, WI, July 2013. ISSW29-000194. doi: 10/bf8b. (Referenced on pages 136, 137, 138, 143, 144, 145, 147, 148, 149, 154, 203, and 204.)

R. C. Millikan and D. R. White. Systematics of Vibrational Relaxation. *The Journal of Chemical Physics*, 39(12):3209–3213, 1963. doi: 10.1063/1.1734182. (Referenced on pages 99, 105, and 107.)

M. J. Moran, H. N. Shapiro, B. R. Munson, and D. P. DeWitt. *Introduction to Thermal Systems Engineering: Thermodynamics, Fluid Mechanics, and Heat Transfer*. Wiley, 2003. (Referenced on pages 162 and 163.)

R. Morgan. Free piston-driven reflected shock tunnels. In G. Ben-Dor, O. Igra, and T. Elperin, editors, *Handbook of Shock Waves, Volume I: Theoretical, Experimental, and Numerical Techniques*, pages 587–601. Academic Press, San Diego, CA, 2001. (Referenced on pages 63 and 64.)

M. V. Morkovin. Effects of compressibility on turbulent flows. *Mecanique de la Turbulence*, pages 367–380, 1962. (Referenced on page 54.)

M. V. Morkovin. Recent Insights Into Instability and Transition to Turbulence in Open-Flow Systems. NASA CR-181693, 1988. (Referenced on page 113.)

Mott Corporation. Mott Porous Metal Data Sheet (MG10. Available: http://www.mottcorp.com/resource/pdf/RS_Perm_mg10.pdf, 2010. Accessed: 12/23/2013.

(Referenced on page 157.)

R. Narasimha. On the distribution of intermittency in the transition region of a boundary layer. *Journal of the Aeronautical Sciences*, 24(9):711–712, 1957. doi: doi: 10.2514/8.3944.

(Referenced on pages 128, 137, 140, and 142.)

R. Narasimha. The laminar-turbulent transition zone in the boundary layer. *Progress in Aerospace Sciences*, 22:29–80, 1985. doi: 10.1016/0376-0421(85)90004-1.

(Referenced on pages 58, 59, 128, 136, and 138.)

N. W. Page and R. J. Stalker. Pressure losses in free piston driven shock tubes. In *Proceedings of the 14th International Symposium on Shock Tubes and Shock Waves*, pages 118–125, Sydney, Australia, August 1983. New South Wales University Press.

(Referenced on page 63.)

C. Park. *Nonequilibrium Hypersonic Aerothermodynamics*. Wiley, New York, 1990.

(Referenced on page 82.)

C. Park, J. T. Howe, R. L. Jaffe, and G. V. Candler. Review of Chemical-Kinetic Problems of Future NASA Missions, II: Mars Entries. *Journal of Thermophysics and Heat transfer*, 8(1):9–23, 1994. doi: 10.2514/3.496.

(Referenced on pages 82 and 99.)

N. J. Parziale. *Slender-Body Hypervelocity Boundary-Layer Instability*. PhD thesis, California Institute of Technology, Pasadena, CA, 2013.

(Referenced on pages 9, 16, and 59.)

N. J. Parziale, J. S. Jewell, J. E. Shepherd, and H. G. Hornung. Shock Tunnel Noise Measurement with Resonantly Enhanced Focused Schlieren Deflectometry. In *Proceedings of the 28th International Symposium on Shock Waves*, pages 747–752, Manchester, UK, July 2011. ISSW. doi: 10/bf8c.

(Referenced on page 134.)

N. J. Parziale, J. E. Shepherd, and H. G. Hornung. Reflected Shock Tunnel Noise Measurement by Focused Differential Interferometry. In *Proceedings of the 42nd AIAA Fluid Dynamics Conference and Exhibit*, New Orleans, Louisiana, 2012. AIAA-2012-3261. doi: 10.2514/6.2012-3261.

(Referenced on page 134.)

N. J. Parziale, J. E. Shepherd, and H. G. Hornung. Free-stream density perturbations in a reflected-shock tunnel. *Experiments in Fluids*, 55(2):1–10, 2014. doi: 10.1007/s00348-014-1665-0.

(Referenced on pages 103, 114, 115, 193, and 200.)

S. R. Pate. Measurements and Correlations of Transition Reynolds Numbers on Sharp Slender Cones at High Speeds. *AIAA Journal*, 9(6):1082–1090, 1971. doi: 10.2514/3.49919.

(Referenced on page 113.)

S. R. Pate and C. J. Schueler. Radiated Aerodynamic Noise Effects on Boundary-layer Transition in Supersonic and Hypersonic Wind Tunnels. *AIAA Journal*, 7(3): 450–457, 1969. doi: 10.2514/3.5128.

(Referenced on page 114.)

A. Rasheed. *Passive Hypervelocity Boundary Layer Control Using an Acoustically Absorptive Surface.* PhD thesis, California Institute of Technology, Pasadena, CA,

2001.

(Referenced on pages 48 and 52.)

A. Rasheed, H. G. Hornung, A. V. Fedorov, and N. D. Malmuth. Experiments on passive hypervelocity boundary-layer control using an ultrasonically absorptive surface. *AIAA Journal*, 40(3):481–489, 2002. doi: 10.2514/2.1671.

(Referenced on pages 9 and 44.)

Lord (J. W. Strutt) Rayleigh. On the instability of jets. *Proceedings of the Royal Society of London*, 10:4–13, 1879. doi: 10.1112/plms/s1-10.1.4.

(Referenced on page 2.)

R. W. Reagan. Address Before a Joint Session of Congress on the State of the Union. *Congressional Record*, 132(9):H321, February 1986.

(Referenced on page 1.)

D. C. Reda. Review and Synthesis of Roughness-Dominated Transition Correlations for Reentry Applications. *Journal of Spacecraft and Rockets*, 39(2):161–167, 2002. doi: 10.2514/2.3803.

(Referenced on pages 39 and 40.)

D. C. Reda, M. C. Wilder, and D. K. Prabhu. Transition Experiments on Blunt Bodies with Isolated Roughness Elements in Hypersonic Flight. *Journal of Spacecraft and Rockets*, 47(5):828–835, 2010. doi: 10.2514/1.49112.

(Referenced on page 40.)

D. C. Reda, M. C. Wilder, and D. K. Prabhu. Transition Experiments on Slightly Blunted Cones with Distributed Roughness in Hypersonic Flight. *AIAA Journal*, 50(10):2248–2254, 2012. doi: 10.2514/1.J051616.

(Referenced on page 40.)

N. M. Reddy. An Analytical Method for Real Gas Tailoring in a Shock Tube. *AIAA Journal*, 9(12):2458–2460, 1971. doi: 10.2514/3.6532.

(Referenced on pages 60 and 62.)

H. L. Reed, W. S. Saric, and D. Arnal. Linear Stability Theory Applied to Boundary Layers. *Annual Review of Fluid Mechanics*, 28(1):389–428, 1996. doi: 10.1146/annurev.fl.28.010196.002133.

(Referenced on page 81.)

E. Reshotko. Boundary-Layer Stability and Transition. *Annual Review of Fluid Mechanics*, 8:311–349, 1976. doi: 10.1146/annurev.fl.08.010176.001523.

(Referenced on page 3.)

O. Reynolds. An experimental investigation of the circumstances which determine whether the motion of water shall be direct or sinuous, and of the law of resistance in parallel channels. *Proceedings of the Royal Society of London*, 35(224–226):84–99, 1883. doi: 10.1098/rspl.1883.0018.

(Referenced on page 2.)

N. R. Rotta. Effects of nose bluntness on the boundary layer characteristics of conical bodies at hypersonic speeds. New York University Report NYUAA-66-66, 1966.

(Referenced on page 37.)

S. R. Sanderson. *Shock Wave Interaction in Hypervelocity Flow*. PhD thesis, California Institute of Technology, Pasadena, CA, 1995.

(Referenced on page 48.)

S. R. Sanderson and B. Sturtevant. Transient heat flux measurement using a surface junction thermocouple. *Review of Scientific Instruments*, 73(7):2781–2787, 2002. doi: 10.1063/1.1484255.

(Referenced on page 44.)

W. S. Saric, H. L. Reed, and E. J. Kerschen. Boundary Layer Receptivity to Freestream Disturbances. *Annual Review of Fluid Mechanics*, 34:291–319, 2002. doi: 10.1146/annurev.fluid.34.082701.161921.

(Referenced on page 79.)

H. Schlichting and K. Gersten. *Boundary Layer Theory*. Springer-Verlag, eighth edition, 2001.

(Referenced on pages 3, 77, and 97.)

S. P. Schneider. Flight Data for Boundary-Layer Transition at Hypersonic and Supersonic Speeds. *Journal of Spacecraft and Rockets*, 36(1):8–20, 1999. doi: 10.2514/2.3428.

(Referenced on pages 96 and 98.)

S. P. Schneider. Effects of High-Speed Tunnel Noise on Laminar-Turbulent Transition. *Journal of Spacecraft and Rockets*, 38(3):323–333, 2001. doi: 10.2514/2.3705.

(Referenced on pages 80, 96, 97, 113, and 114.)

S. P. Schneider. Hypersonic Laminar-Turbulent Transition on Circular Cones and Scramjet Forebodies. *Progress in Aerospace Sciences*, 40(1-2):1–50, 2004. doi: 10.1016/j.paerosci.2003.11.001.

(Referenced on pages 96 and 97.)

S. P. Schneider. Development of Hypersonic Quiet Tunnels. *Journal of Spacecraft and Rockets*, 45(4):641–664, 2008a. doi: 10.2514/1.34489.

(Referenced on pages 80, 97, 103, and 113.)

S. P. Schneider. Effects of Roughness on Hypersonic Boundary-Layer Transition. *Journal of Spacecraft and Rockets*, 45(2):193–209, 2008b. doi: 10.2514/1.29713.

(Referenced on page 40.)

S. P. Schneider. Hypersonic boundary-layer transition with ablation and blowing. *Journal of Spacecraft and Rockets*, 47(2):225–237, 2010. doi: 10.2514/1.43926.

(Referenced on pages 10, 158, and 159.)

G. B. Schubauer and P. S. Klebanoff. Contributions on the Mechanics of Boundary-Layer Transition. NACA-TR-1289, 1955.

(Referenced on page 129.)

G. B. Schubauer and H. K. Skramstad. Laminar-Boundary-Layer Oscillations and Transition on a Flat Plate. NACA-TR-909, 1948.

(Referenced on pages 3 and 96.)

D. L. Schulz and T. V. Jones. Heat transfer measurements in short duration hypersonic facilities. Technical report, 1973. AGARD Technical Report AG-165.

(Referenced on page 47.)

J. Sivasubramanian and H. F. Fasel. Direct numerical simulation of a turbulent spot in a cone boundary-layer at Mach 6. In *Proceedings of 40th AIAA Fluid Dynamics Conference and Exhibit*, Chicago, IL, 2010. AIAA-2010-4599. doi: 10.2514/6.2010-4599.

(Referenced on pages 150, 151, and 152.)

A. M. O. Smith and N. Gamberoni. Transition, pressure gradient and stability theory. Technical report, 1956. Douglas Aircraft Company, ES-26388.

(Referenced on page 76.)

G. P. Smith, D. M. Golden, M. Frenklach, N. W. Moriarty, B. Eiteneer, M. Goldenberg, C. T. Bowman, R. K. Hanson, S. Song, W. C. Gardiner, V. V. Lissianski, and Z. Qin. GRI-Mech 3.0. Available: http://www.me.berkeley.edu/gri_mech/, 1999. Accessed: 12/12/2012.

(Referenced on pages 21 and 23.)

P. R. Spalart and S. R. Allmaras. A one-equation turbulence model for aerodynamic flows. In *30th Aerospace Sciences Meeting and Exhibit*, Reno, NV, 1992. AIAA. doi: 10.2514/6.1992-439. AIAA-1992-0439.

(Referenced on page 24.)

R. J. Stalker. Hypervelocity aerodynamics with chemical nonequilibrium. *Annual Review of Fluid Mechanics*, 21:37–60, 1989. doi: 10.1146/annurev.fluid.21.1.37.

(Referenced on page 24.)

J. L. Steger and R. F. Warming. Flux vector splitting of the inviscid gasdynamic equations with application to finite-difference methods. *Journal of Computational Physics*, 40(2):263–293, 1981. doi: 10.1016/0021-9991(81)90210-2.

(Referenced on page 24.)

K. F. Stetson. Nosetip Bluntness Effects on Cone Frustum Boundary Layer Transition in Hypersonic Flow. In *Proceedings of the AlAA 16th Fluid and Plasma Dynamics Conference*, Danvers, Massachusetts, 1983. AIAA-1983-1763. doi: 10.2514/6.1983-1763.

(Referenced on pages 37, 38, and 97.)

K. F. Stetson. Hypersonic boundary-layer transition. In J.J. Bertin, J. Periauz, and J. Ballman, editors, *Advances in Hypersonics*, pages 324–417. Birkhauser, Boston, MA, 1992.

(Referenced on page 4.)

K. F. Stetson and R. L. Kimmel. On Hypersonic Boundary-Layer Stability. In *Proceedings of the 13th AIAA Aerospace Sciences Meeting and Exhibit*, Reno, NV, 1992. AIAA-1992-0737. doi: 10.2514/6.1992-737.

(Referenced on page 3.)

N. Sudani and H. G. Hornung. Gasdynamical Detectors of Driver Gas Contamination in a High-Enthalpy Shock Tunnel. *AIAA Journal*, 36(3):313–319, 1998. doi: 10.2514/2.383.

(Referenced on page 21.)

N. Sudani, B. Valiferdowsi, and H. G. Hornung. Test Time Increase by Delaying Driver Gas Contamination for Reflected Shock Tunnels. *AIAA Journal*, 38(9): 1497–1503, 2000. doi: 10.2514/2.1138.

(Referenced on page 21.)

P. A. Thompson. *Compressible-Fluid Dynamics*. McGraw-Hill, 1972.

(Referenced on pages 19 and 50.)

C. Tropea, A. L. Yarin, and J. F. Foss. *Springer Handbook of Experimental Fluid Mechanics*. Springer-Verlag, 2007.

(Referenced on pages 12 and 22.)

E. R. van Driest. Turbulent boundary layer on a cone in a supersonic flow at zero angle of attack. *Journal of the Aeronautical Sciences*, 19(1), 1952. doi: 10.2514/8.2149.

(Referenced on pages 2, 55, and 56.)

J. L. van Ingen. A suggested semi-empirical method for the calculation of the boundary layer transition region. Technical report, 1956. Report UTHL-74.

(Referenced on page 76.)

J. L. van Ingen. The e^N method for transition prediction: Historical review of work at TU Delft. In *38th AIAA Fluid Dynamics Conference and Exhibit*, Seattle, WA, 2008. AIAA-2008-3830. doi: 10.2514/6.2008-3830.

(Referenced on page 77.)

B. van Leer. Towards the ultimate conservative difference scheme. V. A second-order sequel to Godunov's method. *Journal of Computational Physics*, 32(1):101–136,

1979. doi: 10.1016/0021-9991(79)90145-1.

(Referenced on page 24.)

W. G. Vincenti and C. H. Kruger. *Introduction to Physical Gas Dynamics.* Wiley, New York, 1965.

(Referenced on pages 5 and 87.)

N. Vinod and G. Rama. Pattern of breakdown of laminar flow into turbulent spots. *Physical Review Letters*, 93(11):114501–1–4, 2004. doi: 10.1103/PhysRevLett.93.114501.

(Referenced on page 138.)

A. Wagner, S. Laurence, J. Martinez Schramm, K. Hannemann, V. Wartemann, H. Lüdeke, H. Tanno, and K. Ito. Experimental investigation of hypersonic boundary-layer transition on a cone model in the High Enthalpy Shock Tunnel (HEG) at Mach 7.5. In *Proceedings of the 17th AIAA International Space Planes and Hypersonic Systems and Technologies Conference*, San Francisco, CA, 2011. AIAA-2011-2374. doi: 10.2514/6.2011-2374.

(Referenced on page 113.)

A. Wagner, M. Kuhn, V. Wartemann, J. M. Schramm, and K. Hannemann. Experimental investigation of hypersonic boundary layer transition delay by means of ultrasonically absorptive carbon-carbon material in the High Enthalpy Shock Tunnel Göttingen (HEG). DLR eLibrary, 2013.

(Referenced on page 113.)

R. M. Wagnild. *High Enthalpy Effects on Two Boundary Layer Disturbances in Supersonic and Hypersonic Flow.* PhD thesis, University of Minnesota, Minneapolis, MN, 2012.

(Referenced on pages 10, 24, 25, 75, 79, 83, 99, 104, 105, and 183.)

R. M. Wagnild, G. V. Candler, I. A. Leyva, J. S. Jewell, and H. G. Hornung. Carbon dioxide injection for hypervelocity boundary layer stability. In *48th Aerospace Sciences Meeting*, Orlando, FL, 2010. AIAA. doi: 10.2514/6.2010-1244. AIAA-2010-1244.

(Referenced on pages 10 and 81.)

R. M. Wagnild, G. V. Candler, P. Subbareddy, and H. Johnson. Vibrational Relaxation Effects on Acoustic Disturbances in a Hypersonic Boundary Layer over a Cone. In *50th Aerospace Sciences Meeting*, Nashville, TN, 2012. AIAA. doi: 10.2514/6.2012-922. AIAA-2012-0922.

(Referenced on pages 81, 99, and 101.)

C. A. C. Ward, R. R. Greenwood, A. D. Abney, and S. P. Schneider. Boundary-layer transition experiments in a hypersonic quiet wind tunnel. In *38th AIAA Fluid Dynamics Conference and Exhibit*, Seattle, WA, 2013. AIAA-2013-2738. doi: 10.2514/6.2013-2738.

(Referenced on page 156.)

F. White. *Viscous Fluid Flow*. McGraw-Hill, second edition, 1991.

(Referenced on pages 52, 53, 54, 55, 69, 70, 71, 73, 109, and 110.)

F. M. White and G. H. Christoph. A simple theory for the two-dimensional compressible turbulent boundary layer. *Journal of Basic Engineering*, 94(3):636–642, 1972. doi: 10.1115/1.3425519.

(Referenced on pages 55, 144, and 197.)

C. E. Wittliff, M. R. Wilson, and A. Hertzberg. The Tailored-Interface Hypersonic Shock Tunnel. *Journal of the Aerospace Sciences*, 26(4):219–228, 1959. doi: 10.2514/8.8016.

(Referenced on page 60.)

M. J. Wright, G. V. Candler, and D. Bose. Data-parallel line relaxation method for the Navier-Stokes equations. *AIAA Journal*, 36(9):1603–1609, 1998. doi: 10.2514/2.586.

(Referenced on page 24.)

M. Zanchetta and R. Hillier. Boundary Layer Transition on Slender Blunt Cones at Hypersonic Speeds. In *Proceedings of the 20th International Symposium on Shock Waves*, pages 699–704, Pasadena, CA, July 1996. ISSW.

(Referenced on page 152.)

Y. B. Zeldovich and Y. P. Raizer. *Physics of shock waves and high-temperature hydrodynamic phenomena.* Academic Press, New York, NY, 1967.

(Referenced on page 5.)

E. Zoby and R. Wright. Flight boundary layer transition measurements on a slender cone at Mach 20. In *Proceedings of 10th Fluid and Plasmadynamics Conference*, Albuquerque, NM, 1977. AIAA-1977-719. doi: 10.2514/6.1977-719.

(Referenced on pages 81 and 98.)

Appendix A

T5 Run Conditions

A.1 Measured and Reservoir Conditions

Measured quantities and computed shock and reservoir conditions for all T5 experiments performed on the 5° half angle cone during the present study. The computed values for P_4 and P_5 are based upon the measured U_s, P_1, and gas composition, and the computed values for T_{res} and ρ_{res} are obtained by isentropically expanding the gas after the reflected shock from the computed P_5 to the measured reservoir pressure P_{res}.

		Measured			Computed				
Shot	Gas	U_s	P_1	P_{res}	T_{res}	ρ_{res}	P_4	P_5	P_{res}/P_5
		m/s	kPa	MPa	K	kg/m^3	MPa	MPa	
2526	Air	3092	90.50	50.4	5818	27.5	8.9	83.6	0.60
2527	Air	3209	86.00	48.5	6042	25.1	9.1	87.9	0.55
2528	Air	3226	85.00	48.7	6089	25.0	9.1	88.2	0.55
2529	Air	3243	85.00	48.9	6126	24.9	9.2	89.4	0.55
2535	Air	3115	85.00	51.5	5931	27.4	8.5	80.1	0.64
2536	Air	3158	85.00	51.2	6008	26.8	8.7	83.2	0.62
2537	Air	2703	150.00	44.7	4688	31.9	11.2	96.4	0.46
2538	Air	2542	151.70	42.6	4378	32.9	9.9	83.2	0.51

	Measured				Computed				
Shot	Gas	U_s	P_1	P_res	T_res	ρ_res	P_4	P_5	P_res/P_5
		m/s	kPa	MPa	K	kg/m^3	MPa	MPa	
2539	Air	3226	85.40	48.8	6087	25.1	9.2	88.6	0.55
2540	Air	3061	85.25	51.6	5828	28.1	8.2	76.7	0.67
2541	Air	3125	85.15	50.9	5938	27.0	8.6	81.0	0.63
2568	Air	3141	85.00	55.1	6052	28.6	8.6	82.0	0.67
2569	Air	3158	85.00	54.0	6064	28.0	8.7	83.2	0.65
2570	Air	3297	85.00	53.0	6316	26.0	9.6	93.5	0.57
2571	Air	3209	85.30	53.8	6155	27.3	9.1	87.2	0.62
2572	Air	3175	85.00	54.3	6101	27.9	8.8	84.4	0.64
2573	Air	3191	85.10	53.0	6108	27.1	8.9	85.7	0.62
2574	Air	3175	85.00	53.5	6087	27.6	8.8	84.4	0.63
2575	Air	3025	85.00	53.7	5799	29.5	8.0	74.0	0.73
2576	Air	3123	85.00	53.2	5979	28.0	8.5	80.7	0.66
2577	Air	3046	85.00	51.7	5803	28.3	8.1	75.4	0.69
2578	Air	3175	85.50	52.3	6058	27.1	8.9	84.9	0.62
2579	Air	2765	150.00	46.4	4821	32.0	11.7	102.3	0.45
2580	Air	2390	252.50	50.3	3925	43.9	14.6	118.4	0.42
2581	Air	2542	90.00	29.9	4441	22.6	5.9	49.3	0.61
2582	Air	2344	90.30	29.6	4110	24.5	5.0	40.2	0.74
2583	Air	2238	91.00	31.1	3964	26.8	4.6	36.1	0.86
2584	Air	2344	90.70	29.9	4115	24.7	5.0	40.4	0.74
2585	Air	2400	90.00	30.4	4223	24.4	5.2	42.6	0.72
2586	Air	2317	90.30	29.6	4067	24.8	4.9	39.0	0.76
2587	Air	3160	85.00	51.9	6026	27.0	8.7	83.3	0.62
2588	Air	3209	84.85	54.8	6180	27.7	9.0	86.7	0.63
2589	Air	3215	85.15	56.3	6218	28.3	9.1	87.5	0.64

		Measured				Computed			
Shot	Gas	U_{s}	P_1	P_{res}	T_{res}	ρ_{res}	P_4	P_5	P_{res}/P_5
		m/s	kPa	MPa	K	kg/m^3	MPa	MPa	
2590	Air	3125	85.10	55.9	6032	29.1	8.6	80.9	0.69
2591	Air	3051	84.90	53.2	5842	28.9	8.1	75.7	0.70
2592	Air	3143	85.05	52.5	6005	27.5	8.7	82.2	0.64
2593	Air	3143	85.00	55.2	6058	28.6	8.7	82.2	0.67
2594	Air	3107	85.00	56.1	6002	29.5	8.4	79.6	0.71
2595	Air	3152	85.10	55.3	6074	28.6	8.7	82.8	0.67
2596	Air	3160	85.00	54.1	6069	28.0	8.7	83.3	0.65
2597	Air	3164	85.20	55.6	6103	28.6	8.8	83.8	0.66
2598	Air	3200	84.90	55.3	6171	28.0	9.0	86.1	0.64
2599	Air	3209	67.35	47.7	6217	23.8	7.2	69.1	0.69
2600	Air	3125	85.05	54.7	6012	28.7	8.6	80.9	0.68
2601	Air	3191	102.90	74.9	6323	37.1	10.8	103.4	0.72
2602	Air	3226	103.15	72.4	6353	35.6	11.1	106.7	0.68
2603	Air	3093	103.00	78.8	6176	40.3	10.1	95.0	0.83
2604	Air	3209	103.15	78.6	6408	38.3	11.0	105.1	0.75
2605	Air	3175	103.15	80.0	6358	39.4	10.7	102.1	0.78
2606	Air	3175	130.10	80.4	6171	41.2	13.5	128.4	0.63
2607	Air	3109	85.00	54.5	5977	28.8	8.5	79.7	0.68
2608	Air	3093	84.85	55.2	5961	29.3	8.4	78.5	0.70
2609	Air	3125	85.00	55.7	6031	29.1	8.5	80.9	0.69
2610	Air	3226	85.00	54.9	6214	27.5	9.1	88.2	0.62
2611	Air	3243	84.95	54.6	6243	27.2	9.2	89.4	0.61
2612	Air	3279	85.00	55.5	6329	27.2	9.4	92.1	0.60
2613	Air	3226	85.00	54.6	6208	27.4	9.1	88.2	0.62
2614	Air	3109	100.00	53.3	5830	29.0	9.9	93.6	0.57

Measured					Computed					
Shot	Gas	U_s	P_1	P_{res}	T_{res}	ρ_{res}	P_4	P_5	P_{res}/P_5	
		m/s	kPa	MPa	K	kg/m^3	MPa	MPa		
2615	Air	3030	115.00	53.2	5578	30.6	10.8	100.3	0.53	
2616	Air	2927	125.00	53.8	5343	32.7	11.0	99.2	0.54	
2617	Air	2956	115.00	52.3	5427	31.2	10.3	93.8	0.56	
2618	Air	2970	114.60	53.2	5472	31.4	10.4	94.7	0.56	
2619	Air	2885	115.10	53.2	5316	32.6	9.8	87.9	0.61	
2620	Air	3000	116.00	51.7	5490	30.4	10.7	98.4	0.52	
2621	Air	2956	115.45	52.4	5426	31.2	10.3	94.1	0.56	
2623	Air	2956	114.90	49.3	5376	29.7	10.3	93.7	0.53	
2624	Air	2941	114.95	49.7	5357	30.1	10.2	92.5	0.54	
2625	Air	3030	114.85	50.1	5523	29.2	10.8	100.2	0.50	
2626	Air	2830	115.00	51.9	5197	32.7	9.4	83.5	0.62	
2627	Air	2844	115.00	53.4	5245	33.3	9.5	84.5	0.63	
2628	Air	2844	115.00	49.1	5173	31.1	9.5	84.5	0.58	
2629	Air	2765	115.00	47.9	5017	31.5	9.0	78.5	0.61	
2630	Air	2857	115.00	48.8	5192	30.7	9.6	85.6	0.57	
2631	Air	3015	115.00	49.8	5490	29.2	10.7	98.9	0.50	
2632	Air	3030	115.45	52.0	5554	30.1	10.9	100.7	0.52	
2633	Air	2913	115.40	54.1	5377	32.7	10.0	90.5	0.60	
2634	Air	2927	115.00	52.8	5385	31.8	10.1	91.3	0.58	
2635	Air	2871	115.30	51.5	5261	32.0	9.7	86.9	0.59	
2636	Air	2941	115.00	53.3	5419	31.9	10.2	92.5	0.58	
2637	Air	2941	115.45	53.8	5424	32.1	10.2	92.9	0.58	
2638	Air	2817	115.00	54.3	5211	34.1	9.3	82.4	0.66	
2639	Air	3030	115.00	53.3	5580	30.7	10.8	100.3	0.53	
2640	Air	3000	115.00	53.3	5525	31.1	10.6	97.6	0.55	

		Measured				Computed			
Shot	Gas	U_s	P_1	P_{res}	T_{res}	ρ_{res}	P_4	P_5	P_{res}/P_5
		m/s	kPa	MPa	K	kg/m^3	MPa	MPa	
2641	Air	2985	115.00	53.6	5503	31.4	10.5	96.3	0.56
2642	Air	3191	85.00	54.3	6135	27.7	8.9	85.6	0.63
2643	Air	3046	85.10	55.5	5872	30.0	8.1	75.5	0.74
2644	Air	2955	85.10	55.1	5690	31.0	7.6	69.5	0.79
2645	Air	3209	85.35	54.3	6166	27.5	9.1	87.2	0.62
2646	Air	3261	85.00	53.7	6259	26.7	9.3	90.8	0.59
2647	Air	2419	90.00	30.6	4258	24.3	5.3	43.4	0.70
2648	Air	2174	90.00	14.0	3377	14.3	4.3	33.2	0.42
2649	Air	2256	90.00	22.2	3785	20.1	4.6	36.4	0.61
2650	Air	3175	90.00	51.5	6001	27.0	9.3	89.3	0.58
2651	Air	3206	85.05	51.9	6116	26.5	9.0	86.8	0.60
2652	Air	3226	103.20	72.5	6353	35.6	11.1	106.7	0.68
2653	Air	3175	103.20	73.1	6259	36.6	10.7	102.2	0.71
2654	Air	3243	103.20	74.1	6414	36.0	11.2	108.3	0.68
2655	Air	3243	103.15	73.7	6407	35.8	11.2	108.2	0.68
2656	Air	2727	168.50	78.4	5102	51.0	12.8	110.8	0.71
2657	Air	2899	140.50	78.3	5549	45.9	12.1	108.6	0.72
2658	Air	2830	140.10	64.8	5253	40.5	11.5	101.6	0.64
2659	Air	2844	140.90	68.2	5319	42.0	11.6	103.5	0.66
2660	Air	2817	139.90	71.7	5319	44.2	11.3	100.2	0.72
2661	Air	2857	140.50	69.9	5367	42.6	11.7	104.5	0.67
2662	Air	2830	140.20	61.4	5207	38.7	11.5	101.7	0.60
2663	Air	2857	140.10	67.1	5333	41.2	11.7	104.2	0.64
2664	Air	2913	140.05	72.0	5499	42.6	12.2	109.6	0.66
2665	N$_2$	2817	140.00	72.0	6314	38.1	10.9	90.8	0.79

	Measured				Computed				
Shot	Gas	U_s	P_1	P_{res}	T_{res}	ρ_{res}	P_4	P_5	P_{res}/P_5
		m/s	kPa	MPa	K	kg/m^3	MPa	MPa	
2666	N$_2$	2857	140.00	72.6	6416	37.8	11.2	93.8	0.77
2667	N$_2$	3175	85.00	52.2	7177	23.9	8.4	71.8	0.73
2668	N$_2$	3226	85.00	51.8	7259	23.3	8.7	74.4	0.70
2669	N$_2$	3131	85.00	50.7	7067	23.6	8.2	69.7	0.73
2670	N$_2$	3226	85.00	48.3	7187	22.0	8.7	74.4	0.65
2671	N$_2$	3141	85.00	46.7	7001	22.0	8.2	70.2	0.67
2672	N$_2$	3279	85.00	49.0	7295	21.9	9.0	77.1	0.64
2673	N$_2$	3261	85.00	51.0	7304	22.8	8.9	76.2	0.67
2674	N$_2$	3226	85.00	50.2	7227	22.7	8.7	74.4	0.67
2675	N$_2$	3061	85.00	50.2	6926	24.0	7.8	66.3	0.76
2676	Air	2970	84.85	51.0	5648	28.9	7.7	70.3	0.73
2677	Air	3093	85.10	53.3	5922	28.4	8.4	78.7	0.68
2678	Air	3030	84.90	52.0	5780	28.6	8.0	74.3	0.70
2679	Air	3000	85.00	50.5	5693	28.3	7.9	72.3	0.70
2680	Air	3015	104.00	71.2	5907	38.4	9.7	89.6	0.80
2681	Air	2667	141.00	70.7	5028	46.7	10.2	87.5	0.81
2682	Air	2667	140.00	67.7	4996	45.0	10.1	86.8	0.78
2683	Air	2817	85.00	44.8	5250	27.8	6.9	61.0	0.73
2695	Air	2655	115.10	48.4	4834	33.3	8.2	70.6	0.69
2696	Air	2703	114.65	46.0	4880	31.3	8.5	73.7	0.62
2697	Air	2899	85.05	49.3	5482	29.0	7.3	65.9	0.75
2698	Air	2899	85.25	50.1	5495	29.4	7.3	66.1	0.76
2699	Air	2913	85.10	50.3	5525	29.3	7.4	66.8	0.75
2700	Air	3681	50.00	49.4	7425	19.5	7.1	74.5	0.66
2701	Air	2955	85.00	48.5	5572	27.9	7.6	69.4	0.70

		Measured			Computed				
Shot	Gas	U_s	P_1	P_{res}	T_{res}	ρ_{res}	P_4	P_5	P_{res}/P_5
		m/s	kPa	MPa	K	kg/m^3	MPa	MPa	
2702	Air	2913	85.00	49.9	5518	29.1	7.4	66.8	0.75
2703	Air	2927	85.15	48.5	5517	28.3	7.5	67.8	0.72
2704	Air	2913	85.00	49.5	5511	28.9	7.4	66.8	0.74
2705	Air	2899	85.00	50.0	5494	29.3	7.3	65.9	0.76
2706	Air	3093	84.75	49.0	5842	26.6	8.3	78.4	0.63
2707	Air	3061	85.00	49.5	5789	27.1	8.2	76.4	0.65
2708	Air	2804	100.00	49.6	5205	31.1	8.0	70.8	0.70
2709	Air	2844	100.00	47.9	5246	29.8	8.3	73.6	0.65
2710	Air	2727	115.00	45.9	4917	30.9	8.7	75.7	0.61
2711	Air	2727	115.00	46.1	4921	31.0	8.7	75.7	0.61
2712	Air	2715	100.00	42.4	4923	28.5	7.5	65.1	0.65
2713	CO$_2$	3061	60.00	39.0	4191	38.9	9.4	143.9	0.27
2714	Air	3109	105.20	67.1	6023	35.3	10.5	98.4	0.68
2715	Air	3226	87.00	68.8	6439	33.2	9.3	90.2	0.76
2716	Air	3261	80.00	67.4	6557	31.7	8.8	85.5	0.79
2717	Air	3226	82.00	70.0	6507	33.3	8.8	85.1	0.82
2718	Air	3125	82.00	70.1	6301	34.8	8.2	78.0	0.90
2719	CO$_2$	2970	85.00	44.8	4075	47.5	12.4	186.2	0.24
2720	CO$_2$	3209	55.00	59.3	4563	51.8	9.4	150.5	0.39
2721	CO$_2$	3125	60.90	58.3	4433	53.7	9.9	154.6	0.38
2722	CO$_2$	3061	66.00	60.3	4356	57.5	10.3	158.0	0.38
2723	CO$_2$	2941	71.00	54.3	4160	55.9	10.2	151.8	0.36
2724	CO$_2$	2941	75.15	53.2	4140	55.3	10.8	160.5	0.33
2725	CO$_2$	2927	82.00	57.0	4132	59.6	11.7	172.5	0.33
2726	CO$_2$	2830	95.00	57.8	4000	64.1	12.6	181.4	0.32

		Measured				Computed			
Shot	Gas	$U_{\rm s}$	P_1	$P_{\rm res}$	$T_{\rm res}$	$\rho_{\rm res}$	P_4	P_5	$P_{\rm res}/P_5$
		m/s	kPa	MPa	K	kg/m^3	MPa	MPa	
2727	CO_2	2752	115.00	57.1	3870	67.0	14.4	202.7	0.28
2728	CO_2 75%	2857	92.60	56.6	4190	54.2	10.9	138.0	0.41
2729	CO_2 50%	3046	103.20	57.7	4661	44.5	12.3	144.5	0.40
2730	CO_2 50%	2941	120.00	58.1	4472	47.7	13.3	151.5	0.38
2731	CO_2 75%	3141	88.30	59.0	4557	49.1	12.7	173.1	0.34
2732	CO_2 50%	2956	120.25	57.0	4480	46.6	13.5	153.9	0.37
2733	CO_2	2857	135.00	56.6	3944	64.3	18.2	263.4	0.21
2734	CO_2	2632	134.85	54.4	3688	69.0	15.4	209.4	0.26
2735	CO_2 50%	2715	134.75	58.2	4152	53.3	12.6	134.9	0.43
2736	CO_2 75%	2956	117.00	57.0	4242	53.4	14.8	191.5	0.30
2737	CO_2 75%	2817	117.00	56.1	4080	56.0	13.4	166.8	0.34
2738	CO_2 75%	3046	97.00	56.6	4395	50.0	13.1	173.7	0.33
2739	Air	2927	130.00	57.5	5374	34.8	11.4	103.2	0.56
2740	Air	2913	130.00	57.3	5346	34.9	11.3	101.8	0.56
2741	Air	2970	120.00	56.9	5501	33.4	10.9	99.1	0.57
2742	Air	3015	110.50	55.7	5623	31.8	10.3	95.1	0.59
2743	Air	3077	101.00	56.3	5816	30.8	9.8	91.9	0.61
2744	Air	2844	137.80	60.7	5232	38.0	11.4	101.2	0.60
2745	CO_2	3261	67.90	58.5	4564	51.0	12.0	193.4	0.30
2746	Air	2819	159.85	61.9	5105	40.0	13.0	114.7	0.54
2747	CO_2	3194	68.00	60.3	4501	54.1	11.6	183.0	0.33
2748	CO_2 50%	2901	80.00	61.4	4595	48.5	8.6	97.7	0.63
2749	CO_2 50%	3161	70.00	60.4	5006	41.8	9.0	110.0	0.55
2750	CO_2 50%	3079	79.75	60.0	4831	43.9	9.7	115.9	0.52
2751	CO_2	3144	71.85	60.2	4429	55.6	11.8	184.9	0.33

		Measured			Computed				
Shot	Gas	U_s	P_1	P_{res}	T_{res}	ρ_{res}	P_4	P_5	P_{res}/P_5
		m/s	kPa	MPa	K	kg/m^3	MPa	MPa	
2752	Air	2988	101.00	61.5	5731	34.3	9.2	84.9	0.72
2753	Air	2988	94.90	52.1	5619	29.7	8.7	79.8	0.65
2754	CO_2	3211	62.00	53.4	4486	47.8	10.7	169.7	0.31
2755	Air	2988	92.00	56.7	5722	31.7	8.4	77.4	0.73
2756	CO_2	3079	68.00	57.5	4348	54.8	10.7	165.4	0.35
2757	Air	3203	92.40	60.7	6207	30.6	9.8	93.9	0.65
2758	Air	3298	82.00	72.0	6688	33.1	9.2	90.4	0.80
2759	Air	3125	92.20	60.4	6051	31.5	9.3	87.6	0.69
2760	Air	2630	90.00	27.2	4515	20.2	6.3	53.9	0.51
2761	Air	2390	90.10	28.2	4154	23.0	5.2	42.2	0.67
2762	Air	2492	75.00	27.8	4414	21.1	4.7	39.0	0.71
2763	Air	2555	60.00	27.2	4630	19.5	4.0	33.3	0.82
2764	Air	2374	60.10	16.5	4008	14.0	3.4	27.6	0.60
2765	Air	2693	60.00	17.5	4532	12.8	4.4	38.3	0.46
2766	Air	2873	45.10	17.0	4949	11.1	3.8	34.3	0.49
2767	Air	3128	35.00	16.6	5513	9.4	3.5	33.8	0.49
2768	Air	3128	45.00	25.2	5726	13.7	4.5	43.3	0.58
2769	Air	3211	75.00	60.8	6397	29.5	8.0	77.0	0.79
2770	Air	3336	72.95	59.5	6650	27.4	8.4	83.1	0.72
2771	Air	3264	83.00	60.6	6415	29.3	9.1	88.9	0.68
2772	N_2	2958	44.95	16.7	6163	9.0	3.9	32.4	0.52
2773	N_2	3144	40.00	16.7	6601	8.3	3.9	33.0	0.51
2774	N_2	3336	35.00	16.7	7009	7.8	3.8	32.9	0.51
2775	N_2	2819	52.00	17.4	5778	10.1	4.0	33.7	0.52
2776	N_2	2767	130.00	45.9	5768	26.7	9.7	81.0	0.57

	Measured					Computed			
Shot	Gas	U_s	P_1	P_{res}	T_{res}	ρ_{res}	P_4	P_5	P_{res}/P_5
		m/s	kPa	MPa	K	kg/m^3	MPa	MPa	
2777	N_2	3079	85.00	38.9	6691	19.3	7.9	67.1	0.58
2778	N_2	3374	72.00	41.4	7411	18.1	8.1	69.6	0.60
2779	N_2	3532	60.00	42.3	7800	17.3	7.4	64.3	0.66
2780	N_2	3730	50.05	44.5	8230	16.8	6.9	61.2	0.73
2781	N_2	3977	50.00	43.4	8506	15.5	7.9	72.0	0.60
2782	N_2	3849	50.00	53.9	8565	19.2	7.3	66.2	0.81
2783	N_2	4030	50.10	53.3	8767	18.2	8.1	74.8	0.71
2784	N_2	4003	50.00	60.4	8862	20.4	8.0	73.3	0.82
2785	N_2	4003	49.95	61.8	8886	20.8	8.0	73.2	0.84
2786	Air	3228	85.00	53.6	6193	27.0	9.1	88.4	0.61
2787	Air	3336	80.00	54.7	6479	26.0	9.2	91.0	0.60
2788	Air	3707	65.00	54.7	7375	21.9	9.3	98.0	0.56
2789	Air	3491	70.30	56.4	6932	24.6	8.9	90.5	0.62
2790	Air	3451	75.00	57.4	6818	25.6	9.3	93.5	0.61
2791	CO_2	3111	22.00	17.6	4135	17.2	3.6	56.3	0.31
2792	CO_2	2742	32.00	18.3	3717	21.9	4.0	56.9	0.32
2793	CO_2	2224	50.00	22.7	3179	35.3	4.0	49.5	0.46
2794	CO_2	2392	47.00	23.2	3375	32.9	4.4	56.7	0.41
2795	CO_2	2431	41.00	22.6	3433	31.3	4.0	51.7	0.44
2796	CO_2	2402	47.00	23.1	3383	32.7	4.5	57.3	0.40
2797	CO_2	2588	100.65	56.7	3718	71.0	11.1	149.8	0.38
2798	CO_2	2555	100.60	54.4	3668	69.7	10.8	144.5	0.38
2799	CO_2	2555	100.20	55.1	3672	70.3	10.8	143.9	0.38
2800	CO_2	2523	100.00	53.7	3629	69.9	10.5	138.7	0.39
2801	CO_2	2544	100.00	54.9	3660	70.5	10.7	141.9	0.39

	Measured				Computed				
Shot	Gas	U_{s}	P_1	P_{res}	T_{res}	ρ_{res}	P_4	P_5	P_{res}/P_5
		m/s	kPa	MPa	K	kg/m^3	MPa	MPa	
2802	CO_2	2464	115.05	54.7	3540	74.0	11.5	149.3	0.37
2803	CO_2	2392	130.00	54.5	3433	77.3	12.2	155.6	0.35
2804	CO_2	2319	150.00	52.7	3306	78.8	13.2	165.0	0.32
2805	CO_2	2425	86.35	41.4	3467	57.3	8.3	107.5	0.38
2806	CO_2	2451	131.00	53.0	3488	73.3	12.9	167.4	0.32
2807	CO_2	2451	100.30	54.3	3553	73.1	9.9	128.5	0.42
2808	CO_2	2461	99.55	54.5	3567	73.0	9.9	128.9	0.42
2809	CO_2 50%	2873	103.30	57.1	4429	47.6	10.9	122.1	0.47
2810	CO_2 50%	2705	120.75	58.2	4176	52.9	11.2	119.8	0.49
2811	CO_2 50%	2755	120.00	56.3	4223	50.3	11.6	125.4	0.45
2812	CO_2 50%	2597	50.00	22.3	3886	21.9	4.3	44.6	0.50
2813	CO_2 50%	2383	75.00	23.3	3557	25.9	5.4	52.7	0.44
2814	CO_2 50%	2313	91.85	22.5	3409	26.5	6.2	59.7	0.38
2816	CO_2 50%	2258	92.00	23.0	3355	27.8	5.9	56.2	0.41
2817	CO_2 50%	2184	120.00	23.3	3193	29.9	7.2	67.5	0.35
2818	CO_2 50%	2588	120.00	40.7	3879	40.8	10.2	105.2	0.39
2819	CO_2 50%	2566	146.00	39.8	3784	41.2	12.2	124.9	0.32
2820	CO_2 50%	2806	85.00	41.3	4246	36.2	8.5	94.1	0.44
2821	CO_2 50%	2717	100.00	42.5	4102	39.2	9.4	100.7	0.42
2822	Air	2958	96.50	42.9	5376	25.7	8.7	79.0	0.54
2823	Air	3048	85.00	42.6	5620	24.1	8.1	75.6	0.56

A.2 Boundary Layer Edge and Reference Conditions

Boundary layer edge and reference conditions for all T5 experiments performed on the 5° half angle cone during the present study.

Shot	Gas	h_{res}	P_{res}	U_e	P_e	ρ_e	M_e	T_e	unit Re	T^*	unit Re*
		MJ/kg	MPa	m/s	kPa	kg/m^3		K		K	
2526	Air	9.16	50.4	3807	38.6	0.085	4.77	1562	5.83×10^6	1760	5.17×10^6
2527	Air	9.73	48.5	3902	37.9	0.078	4.72	1668	5.23×10^6	1847	4.73×10^6
2528	Air	9.84	48.7	3920	38.2	0.078	4.71	1689	5.19×10^6	1865	4.70×10^6
2529	Air	9.93	48.9	3935	38.5	0.077	4.71	1706	5.16×10^6	1879	4.68×10^6
2535	Air	9.42	51.5	3853	39.9	0.085	4.75	1613	5.77×10^6	1803	5.16×10^6
2536	Air	9.61	51.2	3885	39.9	0.083	4.73	1649	5.60×10^6	1832	5.05×10^6
2537	Air	6.55	44.7	3291	29.0	0.097	5.08	1037	7.39×10^6	1335	5.74×10^6
2538	Air	5.89	42.6	3142	24.9	0.096	5.21	901	7.55×10^6	1224	5.55×10^6
2539	Air	9.83	48.8	3920	38.3	0.078	4.71	1688	5.21×10^6	1864	4.71×10^6
2540	Air	9.17	51.6	3810	39.5	0.087	4.77	1565	5.96×10^6	1762	5.29×10^6
2541	Air	9.45	50.9	3856	39.4	0.084	4.75	1617	5.69×10^6	1805	5.09×10^6
2568	Air	9.68	55.1	3899	43.2	0.089	4.73	1665	5.99×10^6	1844	5.40×10^6
2569	Air	9.72	54.0	3905	42.4	0.087	4.72	1672	5.84×10^6	1850	5.28×10^6
2570	Air	10.35	53.0	4007	42.4	0.081	4.68	1789	5.33×10^6	1946	4.90×10^6
2571	Air	9.94	53.8	3942	42.5	0.085	4.71	1715	5.66×10^6	1885	5.15×10^6
2572	Air	9.81	54.3	3920	42.7	0.087	4.72	1689	5.81×10^6	1863	5.26×10^6
2573	Air	9.84	53.0	3923	41.7	0.084	4.71	1694	5.64×10^6	1868	5.12×10^6
2574	Air	9.78	53.5	3915	42.1	0.086	4.72	1683	5.74×10^6	1859	5.20×10^6
2575	Air	9.08	53.7	3796	41.1	0.091	4.78	1548	6.28×10^6	1749	5.56×10^6
2576	Air	9.52	53.2	3871	41.4	0.087	4.74	1634	5.89×10^6	1818	5.29×10^6
2577	Air	9.11	51.7	3799	39.6	0.088	4.78	1553	6.02×10^6	1753	5.34×10^6

Shot	Gas	h_{res}	P_{res}	U_e	P_e	ρ_e	M_e	T_e	unit Re	T^*	unit Re*
		MJ/kg	MPa	m/s	kPa	kg/m^3		K		K	
2578	Air	9.72	52.3	3904	41.0	0.084	4.72	1672	5.65×10^6	1850	5.11×10^6
2579	Air	6.84	46.4	3354	30.9	0.098	5.04	1095	7.38×10^6	1382	5.85×10^6
2580	Air	4.96	50.3	2930	22.4	0.111	5.51	700	9.49×10^6	1066	6.24×10^6
2581	Air	6.10	29.9	3180	18.6	0.068	5.13	952	5.23×10^6	1260	3.95×10^6
2582	Air	5.39	29.6	3017	15.9	0.069	5.29	804	5.53×10^6	1141	3.90×10^6
2583	Air	5.09	31.1	2946	15.2	0.071	5.39	740	5.93×10^6	1089	4.03×10^6
2584	Air	5.40	29.9	3019	16.1	0.069	5.29	807	5.59×10^6	1143	3.94×10^6
2585	Air	5.62	30.4	3071	17.3	0.070	5.23	853	5.59×10^6	1180	4.04×10^6
2586	Air	5.30	29.6	2996	15.6	0.069	5.32	786	5.58×10^6	1126	3.90×10^6
2587	Air	9.65	51.9	3891	40.5	0.084	4.73	1657	5.65×10^6	1838	5.10×10^6
2588	Air	9.99	54.8	3951	43.5	0.086	4.70	1725	5.74×10^6	1893	5.23×10^6
2589	Air	10.07	56.3	3965	44.8	0.088	4.70	1741	5.84×10^6	1906	5.34×10^6
2590	Air	9.62	55.9	3890	43.7	0.091	4.73	1655	6.11×10^6	1836	5.51×10^6
2591	Air	9.19	53.2	3814	40.8	0.090	4.77	1569	6.13×10^6	1766	5.45×10^6
2592	Air	9.59	52.5	3882	40.9	0.085	4.73	1647	5.76×10^6	1829	5.18×10^6
2593	Air	9.69	55.2	3901	43.3	0.089	4.73	1668	5.99×10^6	1847	5.41×10^6
2594	Air	9.55	56.1	3878	43.8	0.092	4.74	1641	6.19×10^6	1824	5.57×10^6
2595	Air	9.73	55.3	3908	43.4	0.089	4.72	1675	5.96×10^6	1853	5.39×10^6
2596	Air	9.73	54.1	3907	42.5	0.087	4.72	1675	5.84×10^6	1852	5.28×10^6
2597	Air	9.80	55.6	3919	43.7	0.089	4.72	1689	5.95×10^6	1864	5.39×10^6
2598	Air	9.97	55.3	3947	43.8	0.087	4.70	1720	5.80×10^6	1889	5.29×10^6
2599	Air	10.17	47.7	3973	37.8	0.074	4.69	1748	4.89×10^6	1914	4.47×10^6
2600	Air	9.59	54.7	3883	42.7	0.089	4.74	1647	6.01×10^6	1830	5.41×10^6
2601	Air	10.15	74.9	3992	60.3	0.117	4.70	1771	7.72×10^6	1930	7.09×10^6
2602	Air	10.25	72.4	4006	58.4	0.112	4.69	1787	7.38×10^6	1943	6.79×10^6
2603	Air	9.77	78.8	3931	62.7	0.127	4.73	1696	8.52×10^6	1869	7.73×10^6

Shot	Gas	h_{res}	P_{res}	U_{e}	P_{e}	ρ_{e}	M_{e}	T_{e}	unit Re	T^*	unit Re*
		MJ/kg	MPa	m/s	kPa	kg/m^3		K		K	
2604	Air	10.33	78.6	4023	63.8	0.121	4.69	1807	7.94×10^6	1959	7.33×10^6
2605	Air	10.20	80.0	4003	64.7	0.125	4.70	1782	8.22×10^6	1939	7.55×10^6
2606	Air	9.75	80.4	3929	63.9	0.130	4.74	1692	8.71×10^6	1867	7.90×10^6
2607	Air	9.50	54.5	3869	42.4	0.089	4.74	1631	6.05×10^6	1816	5.43×10^6
2608	Air	9.46	55.2	3861	42.9	0.091	4.75	1623	6.16×10^6	1809	5.53×10^6
2609	Air	9.62	55.7	3890	43.6	0.091	4.73	1655	6.10×10^6	1836	5.50×10^6
2610	Air	10.07	54.9	3964	43.6	0.086	4.70	1741	5.69×10^6	1906	5.20×10^6
2611	Air	10.15	54.6	3976	43.5	0.085	4.69	1754	5.61×10^6	1918	5.14×10^6
2612	Air	10.35	55.5	4009	44.5	0.085	4.68	1793	5.57×10^6	1949	5.13×10^6
2613	Air	10.06	54.6	3962	43.4	0.086	4.70	1738	5.67×10^6	1903	5.18×10^6
2614	Air	9.16	53.3	3809	40.9	0.090	4.77	1563	6.17×10^6	1761	5.48×10^6
2615	Air	8.56	53.2	3701	39.6	0.095	4.83	1443	6.67×10^6	1664	5.79×10^6
2616	Air	7.99	53.8	3594	38.9	0.101	4.90	1329	7.30×10^6	1572	6.17×10^6
2617	Air	8.21	52.3	3634	38.2	0.096	4.87	1372	6.89×10^6	1606	5.88×10^6
2618	Air	8.31	53.2	3654	39.2	0.097	4.86	1392	6.92×10^6	1623	5.93×10^6
2619	Air	7.93	53.2	3583	38.4	0.101	4.91	1316	7.29×10^6	1562	6.14×10^6
2620	Air	8.36	51.7	3663	38.1	0.094	4.85	1403	6.66×10^6	1631	5.73×10^6
2621	Air	8.20	52.4	3634	38.3	0.097	4.87	1371	6.90×10^6	1606	5.89×10^6
2623	Air	8.11	49.3	3614	35.8	0.092	4.88	1351	6.58×10^6	1590	5.59×10^6
2624	Air	8.06	49.7	3605	36.0	0.093	4.89	1342	6.67×10^6	1582	5.66×10^6
2625	Air	8.46	50.1	3680	37.1	0.090	4.84	1421	6.36×10^6	1646	5.50×10^6
2626	Air	7.67	51.9	3529	36.8	0.101	4.94	1262	7.37×10^6	1518	6.13×10^6
2627	Air	7.77	53.4	3550	38.1	0.103	4.93	1282	7.48×10^6	1535	6.25×10^6
2628	Air	7.63	49.1	3521	34.7	0.096	4.94	1255	7.00×10^6	1512	5.81×10^6
2629	Air	7.28	47.9	3447	33.1	0.097	4.98	1183	7.18×10^6	1454	5.84×10^6
2630	Air	7.68	48.8	3529	34.6	0.095	4.93	1265	6.91×10^6	1519	5.75×10^6

Shot	Gas	h_{res}	P_{res}	U_e	P_e	ρ_e	M_e	T_e	unit Re	T^*	unit Re*
		MJ/kg	MPa	m/s	kPa	kg/m^3		K		K	
2631	Air	8.38	49.8	3665	36.7	0.090	4.85	1406	6.40×10^6	1634	5.50×10^6
2632	Air	8.51	52.0	3692	38.6	0.093	4.84	1433	6.56×10^6	1657	5.68×10^6
2633	Air	8.07	54.1	3610	39.3	0.101	4.89	1345	7.26×10^6	1585	6.16×10^6
2634	Air	8.10	52.8	3615	38.4	0.098	4.89	1350	7.07×10^6	1589	6.01×10^6
2635	Air	7.82	51.5	3559	36.9	0.099	4.92	1293	7.17×10^6	1543	6.01×10^6
2636	Air	8.18	53.3	3630	39.0	0.099	4.88	1366	7.06×10^6	1602	6.02×10^6
2637	Air	8.19	53.8	3632	39.3	0.099	4.88	1368	7.11×10^6	1603	6.07×10^6
2638	Air	7.68	54.3	3533	38.5	0.105	4.94	1265	7.70×10^6	1521	6.40×10^6
2639	Air	8.56	53.3	3702	39.7	0.095	4.83	1444	6.69×10^6	1665	5.80×10^6
2640	Air	8.43	53.3	3677	39.4	0.096	4.85	1417	6.80×10^6	1643	5.87×10^6
2641	Air	8.38	53.6	3667	39.6	0.097	4.85	1407	6.90×10^6	1635	5.93×10^6
2642	Air	9.89	54.3	3933	42.8	0.086	4.71	1705	5.75×10^6	1876	5.23×10^6
2643	Air	9.24	55.5	3825	42.8	0.093	4.77	1580	6.37×10^6	1775	5.67×10^6
2644	Air	8.81	55.1	3748	41.6	0.096	4.81	1494	6.68×10^6	1705	5.85×10^6
2645	Air	9.96	54.3	3946	43.0	0.086	4.71	1719	5.71×10^6	1888	5.20×10^6
2646	Air	10.20	53.7	3983	42.8	0.083	4.69	1763	5.49×10^6	1924	5.03×10^6
2647	Air	5.70	30.6	3089	17.7	0.071	5.22	868	5.59×10^6	1193	4.07×10^6
2648	Air	4.06	14.0	2662	5.7	0.035	5.61	558	3.20×10^6	914	1.95×10^6
2649	Air	4.78	22.2	2862	10.3	0.052	5.44	684	4.45×10^6	1037	2.93×10^6
2650	Air	9.59	51.5	3882	40.1	0.084	4.73	1646	5.64×10^6	1829	5.08×10^6
2651	Air	9.87	51.9	3928	40.9	0.083	4.71	1698	5.51×10^6	1871	5.00×10^6
2652	Air	10.25	72.5	4006	58.4	0.112	4.69	1788	7.39×10^6	1943	6.79×10^6
2653	Air	10.01	73.1	3968	58.5	0.115	4.71	1742	7.65×10^6	1906	6.99×10^6
2654	Air	10.38	74.1	4028	60.1	0.114	4.68	1815	7.44×10^6	1965	6.87×10^6
2655	Air	10.37	73.7	4026	59.7	0.113	4.68	1812	7.41×10^6	1963	6.84×10^6
2656	Air	7.30	78.4	3469	54.0	0.159	5.02	1181	11.85×10^6	1459	9.59×10^6

Shot	Gas	h_{res} MJ/kg	P_{res} MPa	U_e m/s	P_e kPa	ρ_e kg/m^3	M_e	T_e K	unit Re	T^* K	unit Re*
2657	Air	8.31	78.3	3669	58.1	0.144	4.88	1394	10.30×10^6	1629	8.81×10^6
2658	Air	7.71	64.8	3545	46.1	0.126	4.95	1269	9.21×10^6	1526	7.66×10^6
2659	Air	7.84	68.2	3573	49.1	0.131	4.93	1296	9.54×10^6	1549	7.99×10^6
2660	Air	7.82	71.7	3570	51.5	0.138	4.94	1291	10.07×10^6	1545	8.41×10^6
2661	Air	7.94	69.9	3594	50.5	0.133	4.92	1317	9.64×10^6	1566	8.10×10^6
2662	Air	7.62	61.4	3525	43.5	0.120	4.95	1252	8.82×10^6	1512	7.30×10^6
2663	Air	7.88	67.1	3580	48.3	0.128	4.93	1304	9.32×10^6	1555	7.82×10^6
2664	Air	8.23	72.0	3651	53.0	0.133	4.89	1378	9.54×10^6	1615	8.14×10^6
2665	N$_2$	8.04	72.0	3727	24.3	0.089	6.03	920	8.79×10^6	1424	5.68×10^6
2666	N$_2$	8.22	72.6	3765	25.0	0.089	6.00	947	8.72×10^6	1451	5.69×10^6
2667	N$_2$	9.95	52.2	4076	22.5	0.062	5.71	1224	5.60×10^6	1691	4.05×10^6
2668	N$_2$	10.17	51.8	4112	23.2	0.061	5.66	1268	5.50×10^6	1726	4.04×10^6
2669	N$_2$	9.69	50.7	4028	20.9	0.060	5.76	1177	5.50×10^6	1651	3.92×10^6
2670	N$_2$	10.01	48.3	4083	21.0	0.057	5.69	1236	5.17×10^6	1699	3.76×10^6
2671	N$_2$	9.56	46.7	4004	18.9	0.055	5.79	1150	5.13×10^6	1628	3.62×10^6
2672	N$_2$	10.29	49.0	4130	22.5	0.058	5.63	1293	5.18×10^6	1744	3.84×10^6
2673	N$_2$	10.30	51.0	4133	23.4	0.061	5.63	1293	5.39×10^6	1745	3.99×10^6
2674	N$_2$	10.10	50.2	4099	22.2	0.059	5.67	1254	5.34×10^6	1714	3.91×10^6
2675	N$_2$	9.35	50.2	3969	19.7	0.059	5.82	1117	5.56×10^6	1601	3.88×10^6
2676	Air	8.75	51.0	3734	38.4	0.089	4.81	1480	6.24×10^6	1694	5.45×10^6
2677	Air	9.38	53.3	3848	41.3	0.088	4.75	1607	6.00×10^6	1797	5.37×10^6
2678	Air	9.05	52.0	3789	39.7	0.089	4.78	1542	6.11×10^6	1744	5.40×10^6
2679	Air	8.86	50.5	3753	38.2	0.087	4.80	1503	6.08×10^6	1712	5.33×10^6
2680	Air	9.19	71.2	3827	55.1	0.121	4.78	1577	8.26×10^6	1773	7.34×10^6
2681	Air	7.17	70.7	3437	48.3	0.145	5.03	1156	10.85×10^6	1437	8.73×10^6
2682	Air	7.11	67.7	3425	46.0	0.139	5.03	1145	10.46×10^6	1428	8.38×10^6

Shot	Gas	h_{res}	P_{res}	U_{e}	P_{e}	ρ_{e}	M_{e}	T_{e}	unit Re	T^*	unit Re*
		MJ/kg	MPa	m/s	kPa	kg/m^3		K		K	
2683	Air	7.85	44.8	3561	32.0	0.085	4.91	1299	6.18×10^6	1547	5.19×10^6
2695	Air	6.85	48.4	3359	32.3	0.102	5.04	1098	7.68×10^6	1385	6.09×10^6
2696	Air	6.97	46.0	3383	31.0	0.096	5.02	1123	7.19×10^6	1405	5.74×10^6
2697	Air	8.36	49.3	3662	36.3	0.089	4.85	1402	6.35×10^6	1631	5.46×10^6
2698	Air	8.39	50.1	3667	37.0	0.091	4.85	1408	6.43×10^6	1635	5.54×10^6
2699	Air	8.46	50.3	3680	37.3	0.090	4.84	1422	6.39×10^6	1647	5.52×10^6
2700	Air	13.39	49.4	4452	41.8	0.061	4.53	2290	3.74×10^6	2379	3.60×10^6
2701	Air	8.59	48.5	3703	36.2	0.086	4.83	1447	6.06×10^6	1667	5.26×10^6
2702	Air	8.45	49.9	3678	36.9	0.090	4.84	1419	6.35×10^6	1644	5.48×10^6
2703	Air	8.46	48.5	3678	35.9	0.087	4.84	1421	6.16×10^6	1646	5.31×10^6
2704	Air	8.43	49.5	3675	36.6	0.089	4.84	1417	6.31×10^6	1642	5.44×10^6
2705	Air	8.39	50.0	3667	36.9	0.090	4.85	1408	6.41×10^6	1635	5.52×10^6
2706	Air	9.24	49.0	3819	37.6	0.082	4.76	1575	5.62×10^6	1771	5.00×10^6
2707	Air	9.10	49.5	3796	37.8	0.084	4.78	1549	5.77×10^6	1750	5.11×10^6
2708	Air	7.70	49.6	3535	35.2	0.096	4.93	1269	7.00×10^6	1524	5.83×10^6
2709	Air	7.82	47.9	3556	34.2	0.092	4.91	1292	6.65×10^6	1542	5.57×10^6
2710	Air	7.06	45.9	3401	31.2	0.095	5.01	1141	7.08×10^6	1419	5.69×10^6
2711	Air	7.07	46.1	3403	31.3	0.095	5.01	1142	7.11×10^6	1420	5.71×10^6
2712	Air	7.10	42.4	3407	28.9	0.087	5.00	1149	6.50×10^6	1425	5.24×10^6
2713	CO$_2$	8.37	39.0	3032	42.9	0.107	4.04	1863	5.86×10^6	1529	7.13×10^6
2714	Air	9.50	67.1	3877	52.5	0.111	4.75	1637	7.47×10^6	1822	6.23×10^6
2715	Air	10.49	68.8	4042	55.9	0.105	4.67	1832	6.82×10^6	1980	5.98×10^6
2716	Air	10.79	67.4	4089	55.1	0.100	4.65	1890	6.45×10^6	2026	5.72×10^6
2717	Air	10.64	70.0	4068	57.1	0.105	4.66	1863	6.81×10^6	2005	6.33×10^6
2718	Air	10.14	70.1	3987	56.3	0.110	4.70	1765	7.23×10^6	1925	6.63×10^6
2719	CO$_2$	7.74	44.8	2952	49.7	0.130	4.04	1807	7.15×10^6	1479	10.14×10^6

Shot	Gas	h_{res} MJ/kg	P_{res} MPa	U_e m/s	P_e kPa	ρ_e kg/m^3	M_e	T_e K	unit Re	T^* K	unit Re*
2720	CO_2	9.65	59.3	3231	68.3	0.145	3.98	2133	7.65×10^6	1717	9.51×10^6
2721	CO_2	9.09	58.3	3155	66.8	0.150	3.99	2050	7.97×10^6	1654	9.88×10^6
2722	CO_2	8.72	60.3	3107	69.1	0.160	4.00	2006	8.55×10^6	1618	10.60×10^6
2723	CO_2	7.97	54.3	2995	61.2	0.154	4.02	1876	8.38×10^6	1523	10.32×10^6
2724	CO_2	7.89	53.2	2983	59.9	0.152	4.02	1861	8.29×10^6	1513	10.19×10^6
2725	CO_2	7.81	57.0	2975	64.4	0.165	4.02	1862	8.94×10^6	1511	11.02×10^6
2726	CO_2	7.24	57.8	2894	65.0	0.176	4.03	1778	9.69×10^6	1447	11.90×10^6
2727	CO_2	6.73	57.1	2814	63.7	0.184	4.04	1688	10.26×10^6	1382	12.53×10^6
2728	CO_2 75%	7.52	56.6	3080	57.7	0.150	4.19	1684	8.81×10^6	1472	10.08×10^6
2729	CO_2 50%	8.45	57.7	3371	53.8	0.125	4.34	1705	7.67×10^6	1596	8.59×10^6
2730	CO_2 50%	7.80	58.1	3270	53.3	0.133	4.37	1600	8.35×10^6	1513	9.19×10^6
2731	CO_2 75%	8.95	59.0	3288	61.9	0.138	4.15	1907	7.82×10^6	1644	9.08×10^6
2732	CO_2 50%	7.84	57.0	3275	52.2	0.130	4.37	1602	8.16×10^6	1517	8.97×10^6
2733	CO_2	7.03	56.6	2860	63.4	0.177	4.04	1739	9.76×10^6	1419	13.91×10^6
2734	CO_2	6.06	54.4	2700	59.9	0.190	4.07	1555	10.87×10^6	1287	13.13×10^6
2735	CO_2 50%	6.71	58.2	3087	52.0	0.150	4.44	1404	9.83×10^6	1363	10.12×10^6
2736	CO_2 75%	7.73	57.0	3111	58.3	0.148	4.19	1716	8.65×10^6	1497	10.97×10^6
2737	CO_2 75%	7.10	56.1	3015	56.6	0.155	4.21	1612	9.23×10^6	1419	10.49×10^6
2738	CO_2 75%	8.34	56.6	3199	58.6	0.139	4.17	1808	8.03×10^6	1568	10.27×10^6
2739	Air	8.04	57.5	3606	41.7	0.108	4.90	1337	7.77×10^6	1580	5.88×10^6
2740	Air	7.97	57.3	3593	41.4	0.108	4.91	1324	7.82×10^6	1569	5.89×10^6
2741	Air	8.34	56.9	3663	42.0	0.104	4.86	1400	7.38×10^6	1630	5.70×10^6
2742	Air	8.64	55.7	3718	41.7	0.099	4.83	1461	6.92×10^6	1678	5.47×10^6
2743	Air	9.10	56.3	3801	43.1	0.096	4.78	1552	6.58×10^6	1753	5.36×10^6
2744	Air	7.69	60.7	3538	43.1	0.118	4.95	1265	8.64×10^6	1522	6.36×10^6
2745	CO_2	9.67	58.5	3232	67.3	0.143	3.98	2132	7.55×10^6	1718	9.37×10^6

Shot	Gas	h_{res} MJ/kg	P_{res} MPa	U_e m/s	P_e kPa	ρ_e kg/m^3	M_e	T_e K	unit Re	T^* K	unit Re*
2746	Air	7.39	61.9	3478	43.1	0.124	4.99	1203	9.19×10^6	1474	7.50×10^6
2747	CO$_2$	9.36	60.3	3193	69.5	0.152	3.99	2097	8.02×10^6	1688	9.96×10^6
2748	CO$_2$ 50%	8.19	61.4	3334	57.1	0.136	4.35	1672	8.40×10^6	1568	8.96×10^6
2749	CO$_2$ 50%	9.60	60.4	3541	57.9	0.119	4.29	1895	7.07×10^6	1744	7.68×10^6
2750	CO$_2$ 50%	9.01	60.0	3455	56.8	0.124	4.31	1801	7.48×10^6	1669	8.07×10^6
2751	CO$_2$	9.04	60.2	3150	69.2	0.156	3.99	2052	8.26×10^6	1654	10.25×10^6
2752	Air	8.85	61.5	3760	46.6	0.107	4.81	1505	7.43×10^6	1714	6.52×10^6
2753	Air	8.67	52.1	3720	39.0	0.092	4.82	1465	6.43×10^6	1681	5.10×10^6
2754	CO$_2$	9.41	53.4	3192	60.8	0.134	4.00	2072	7.10×10^6	1676	8.78×10^6
2755	Air	8.87	56.7	3760	43.0	0.098	4.80	1507	6.82×10^6	1716	5.99×10^6
2756	CO$_2$	8.73	57.5	3105	65.6	0.153	4.00	1997	8.16×10^6	1613	10.10×10^6
2757	Air	10.00	60.7	3956	48.3	0.096	4.70	1731	6.35×10^6	1898	5.80×10^6
2758	Air	11.07	72.0	4136	59.6	0.105	4.63	1947	6.69×10^6	2074	6.01×10^6
2759	Air	9.62	60.4	3894	47.4	0.098	4.73	1659	6.61×10^6	1839	5.55×10^6
2760	Air	6.30	27.2	3221	17.4	0.061	5.09	991	4.64×10^6	1292	3.06×10^6
2761	Air	5.49	28.2	3039	15.6	0.066	5.26	827	5.24×10^6	1158	3.10×10^6
2762	Air	6.06	27.8	3169	17.2	0.063	5.13	944	4.89×10^6	1253	3.13×10^6
2763	Air	6.57	27.2	3281	17.8	0.059	5.05	1044	4.47×10^6	1336	3.02×10^6
2764	Air	5.28	16.5	2974	9.1	0.040	5.26	791	3.20×10^6	1122	1.85×10^6
2765	Air	6.48	17.5	3248	11.4	0.038	5.04	1023	2.92×10^6	1317	1.95×10^6
2766	Air	7.55	17.0	3467	11.7	0.033	4.92	1216	2.43×10^6	1481	1.76×10^6
2767	Air	9.02	16.6	3732	12.1	0.028	4.80	1458	1.99×10^6	1692	1.71×10^6
2768	Air	9.32	25.2	3804	18.9	0.042	4.76	1547	2.88×10^6	1756	2.54×10^6
2769	Air	10.46	60.8	4032	49.1	0.092	4.67	1820	6.04×10^6	1970	5.28×10^6
2770	Air	11.10	59.5	4131	48.9	0.086	4.63	1938	5.51×10^6	2068	5.17×10^6
2771	Air	10.51	60.6	4039	49.0	0.092	4.66	1829	5.98×10^6	1977	5.53×10^6

Shot	Gas	h_res	P_res	U_e	P_e	ρ_e	M_e	T_e	unit Re	T^*	unit Re*
		MJ/kg	MPa	m/s	kPa	kg/m^3		K		K	
2772	N_2	8.00	16.7	3668	5.4	0.021	6.09	872	2.08×10^6	1377	0.99×10^6
2773	N_2	8.99	16.7	3859	6.0	0.020	5.93	1014	1.92×10^6	1510	0.99×10^6
2774	N_2	10.14	16.7	4052	7.2	0.020	5.73	1195	1.84×10^6	1666	1.32×10^6
2775	N_2	7.26	17.4	3511	5.2	0.023	6.17	779	2.30×10^6	1281	1.04×10^6
2776	N_2	7.17	45.9	3524	14.2	0.060	6.14	792	6.13×10^6	1295	2.79×10^6
2777	N_2	8.91	38.9	3876	14.3	0.046	5.90	1038	4.44×10^6	1529	2.32×10^6
2778	N_2	10.73	41.4	4193	20.5	0.050	5.54	1374	4.30×10^6	1806	2.68×10^6
2779	N_2	12.00	42.3	4389	24.3	0.050	5.32	1628	3.96×10^6	2007	2.75×10^6
2780	N_2	13.64	44.5	4625	28.5	0.048	5.11	1954	3.55×10^6	2266	2.74×10^6
2781	N_2	14.98	43.4	4794	29.5	0.044	4.96	2212	3.04×10^6	2469	2.72×10^6
2782	N_2	14.84	53.9	4791	37.0	0.055	4.95	2230	3.78×10^6	2476	3.15×10^6
2783	N_2	15.88	53.3	4915	38.0	0.051	4.84	2441	3.37×10^6	2637	2.95×10^6
2784	N_2	16.09	60.4	4948	43.8	0.057	4.80	2516	3.72×10^6	2689	3.48×10^6
2785	N_2	16.16	61.8	4959	45.0	0.058	4.80	2534	3.78×10^6	2703	3.55×10^6
2786	Air	10.04	53.6	3957	42.5	0.084	4.70	1733	5.58×10^6	1899	4.77×10^6
2787	Air	10.73	54.7	4069	44.3	0.081	4.65	1862	5.27×10^6	2007	4.64×10^6
2788	Air	13.15	54.7	4423	46.4	0.069	4.53	2272	4.20×10^6	2356	4.05×10^6
2789	Air	11.87	56.4	4244	47.0	0.077	4.58	2068	4.85×10^6	2178	4.43×10^6
2790	Air	11.56	57.4	4198	47.6	0.080	4.60	2016	5.08×10^6	2134	4.61×10^6
2791	CO_2	8.83	17.6	3042	18.1	0.047	4.13	1721	2.70×10^6	1468	3.16×10^6
2792	CO_2	6.80	18.3	2752	18.9	0.059	4.13	1498	3.50×10^6	1277	4.10×10^6
2793	CO_2	4.61	22.7	2401	23.6	0.097	4.12	1224	5.70×10^6	1058	7.04×10^6
2794	CO_2	5.27	23.2	2519	24.1	0.090	4.12	1325	5.32×10^6	1134	6.22×10^6
2795	CO_2	5.50	22.6	2558	23.5	0.085	4.12	1355	5.07×10^6	1158	5.93×10^6
2796	CO_2	5.31	23.1	2526	24.0	0.089	4.12	1329	5.29×10^6	1138	6.17×10^6
2797[1]	CO_2	6.15	56.7	2892	7.8	0.034	5.12	1115	2.51×10^6	1146	2.44×10^6

[1]This shot was performed with a nozzle throat yielding 400:1 area ratio.

Shot	Gas	h_{res} MJ/kg	P_{res} MPa	U_e m/s	P_e kPa	ρ_e kg/m³	M_e	T_e K	unit Re	T^* K	unit Re*
2798[1]	CO_2	5.98	54.4	2859	7.5	0.034	5.13	1089	2.46×10^6	1125	2.39×10^6
2799[1]	CO_2	5.99	55.1	2861	7.6	0.034	5.13	1092	2.49×10^6	1127	2.41×10^6
2800[1]	CO_2	5.85	53.7	2832	7.4	0.034	5.13	1071	2.47×10^6	1109	2.38×10^6
2801[1]	CO_2	5.95	54.9	2853	7.6	0.034	5.13	1086	2.49×10^6	1122	2.41×10^6
2802[1]	CO_2	5.52	54.7	2771	7.5	0.036	5.14	1032	2.61×10^6	1075	2.51×10^6
2803[1]	CO_2	5.16	54.5	2702	7.4	0.038	5.14	987	2.73×10^6	1037	2.60×10^6
2804[1]	CO_2	4.77	52.7	2625	7.1	0.038	5.15	937	2.78×10^6	992	2.62×10^6
2805	CO_2	5.38	41.4	2568	44.4	0.158	4.10	1400	9.32×10^6	1180	12.58×10^6
2806	CO_2	5.36	53.0	2577	57.7	0.204	4.09	1420	11.92×10^6	1191	16.24×10^6
2807	CO_2	5.57	54.3	2616	59.4	0.203	4.09	1463	10.42×10^6	1221	14.22×10^6
2808	CO_2	5.62	54.5	2625	59.7	0.202	4.08	1472	11.74×10^6	1228	16.14×10^6
2809	CO_2 50%	7.66	57.1	3247	52.2	0.133	4.38	1574	8.37×10^6	1493	9.15×10^6
2810	CO_2 50%	6.79	58.2	3101	52.1	0.149	4.43	1419	9.27×10^6	1375	9.79×10^6
2811	CO_2 50%	6.96	56.3	3129	50.5	0.141	4.42	1447	9.13×10^6	1397	9.70×10^6
2812	CO_2 50%	6.26	22.3	2943	18.7	0.062	4.52	1214	4.24×10^6	1236	4.12×10^6
2813	CO_2 50%	5.12	23.3	2737	19.3	0.075	4.56	1055	5.36×10^6	1105	4.95×10^6
2814	CO_2 50%	4.68	22.5	2646	18.6	0.078	4.57	986	5.37×10^6	1049	4.83×10^6
2816	CO_2 50%	4.52	23.0	2614	19.1	0.082	4.58	962	6.01×10^6	1029	5.35×10^6
2817	CO_2 50%	4.08	23.3	2519	19.3	0.090	4.59	892	6.73×10^6	971	5.81×10^6
2818	CO_2 50%	5.96	40.7	2927	35.1	0.116	4.50	1230	7.93×10^6	1236	7.86×10^6
2819	CO_2 50%	5.66	39.8	2869	34.1	0.118	4.52	1179	8.17×10^6	1196	7.97×10^6
2820	CO_2 50%	7.22	41.3	3151	36.4	0.101	4.43	1447	6.54×10^6	1405	6.88×10^6
2821	CO_2 50%	6.70	42.5	3063	37.2	0.110	4.46	1362	6.94×10^6	1337	7.17×10^6
2822	Air	8.18	42.9	3622	31.1	0.079	4.87	1363	5.65×10^6	1599	4.31×10^6
2823	Air	8.77	42.6	3732	31.8	0.074	4.81	1481	5.16×10^6	1695	4.11×10^6

A.3 Boundary Layer Stability Parameters

Boundary layer stability parameters for all T5 experiments referenced in Chapter 5.

Shot	Gas	x_{Tr}	N_{Tr}	N_{TrNovib}	α_{Fujii}	Re_{Tr}	Re_{Tr}^*	Ω_{Tr}	$\delta_{99\text{Tr}}$	$(x/\delta_{99})_{\text{Tr}}$
		m						kHz	mm	
2772	N_2	0.660	3.68	3.68	0.0000	1.39×10^6	0.65×10^6	491	2.42	272
2773	N_2	0.691	3.83	3.83	0.0000	1.36×10^6	0.68×10^6	492	2.51	275
2775	N_2	0.673	4.07	3.92	0.0000	1.59×10^6	0.70×10^6	461	2.35	286
2776	N_2	0.389	5.44	5.44	0.0000	2.39×10^6	1.09×10^6	1054	1.07	363
2777	N_2	0.486	5.68	5.68	0.0000	2.19×10^6	1.13×10^6	947	1.37	356
2778	N_2	0.550	6.60	6.60	0.0000	2.41×10^6	1.47×10^6	1050	1.39	397
2779	N_2	0.602	6.71	6.71	0.0000	2.40×10^6	1.66×10^6	1095	1.44	417
2780	N_2	0.621	6.54	6.55	0.0000	2.26×10^6	1.70×10^6	1136	1.50	414
2782	N_2	0.612	7.19	7.21	0.0001	2.35×10^6	1.93×10^6	1326	1.39	441
2783	N_2	0.628	7.02	7.06	0.0001	2.15×10^6	1.85×10^6	1361	1.45	433
2714	Air	0.493	11.02	11.99	0.0003	3.78×10^6	3.07×10^6	1817	0.85	579
2715	Air	0.704	13.00	14.72	0.0005	4.82×10^6	4.21×10^6	1631	1.05	673
2716	Air	0.722	12.67	14.53	0.0006	4.67×10^6	4.13×10^6	1595	1.08	666
2739	Air	0.556	12.36	13.07	0.0002	4.35×10^6	3.27×10^6	1514	0.91	612
2740	Air	0.537	12.17	12.84	0.0002	4.27×10^6	3.16×10^6	1514	0.89	602
2741	Air	0.559	11.84	12.57	0.0002	4.13×10^6	3.19×10^6	1514	0.92	605
2742	Air	0.584	11.69	12.56	0.0002	4.08×10^6	3.19×10^6	1514	0.97	601
2743	Air	0.686	12.66	13.65	0.0003	4.53×10^6	3.68×10^6	1405	1.08	637
2744	Air	0.514	12.62	13.28	0.0001	4.48×10^6	3.27×10^6	1590	0.84	615
2753	Air	0.680	12.43	13.30	0.0002	4.43×10^6	3.46×10^6	1326	1.09	624
2758	Air	0.740	13.21	15.33	0.0007	4.97×10^6	4.45×10^6	1633	1.08	688
2759	Air	0.681	12.65	13.94	0.0004	4.55×10^6	3.78×10^6	1464	1.05	646
2760	Air	0.510	7.49	7.69	0.0000	2.41×10^6	1.56×10^6	983	1.18	433
2761	Air	0.492	7.43	7.60	0.0000	2.58×10^6	1.53×10^6	984	1.11	442

Shot	Gas	x_{Tr}	N_{Tr}	N_{TrNovib}	α_{Fujii}	Re_{Tr}	Re^*_{Tr}	Ω_{Tr}	$\delta_{99\mathrm{Tr}}$	$(x/\delta_{99})_{\mathrm{Tr}}$
		m						kHz	mm	
2762	Air	0.493	7.61	7.79	0.0000	2.47×10^6	1.54×10^6	983	1.14	433
2763	Air	0.534	7.64	7.88	0.0001	2.44×10^6	1.61×10^6	983	1.22	438
2764	Air	0.531	5.40	5.47	0.0000	1.70×10^6	0.98×10^6	697	1.49	356
2765	Air	0.653	6.13	6.31	0.0000	1.91×10^6	1.28×10^6	701	1.66	394
2766	Air	0.639	5.54	5.76	0.0001	1.59×10^6	1.13×10^6	721	1.77	360
2769	Air	0.638	11.21	12.59	0.0005	3.95×10^6	3.37×10^6	1528	1.07	597
2786	Air	0.651	10.59	11.78	0.0004	3.65×10^6	3.11×10^6	1447	1.12	583
2787	Air	0.607	9.69	10.93	0.0005	3.27×10^6	2.82×10^6	1514	1.11	548
2789	Air	0.725	10.11	11.85	0.0007	3.60×10^6	3.22×10^6	1415	1.25	579
2790	Air	0.675	9.99	11.57	0.0006	3.50×10^6	3.11×10^6	1460	1.18	574
2822	Air	0.512	9.18	9.69	0.0002	2.93×10^6	2.21×10^6	1362	1.02	502
2823	Air	0.525	8.69	9.26	0.0002	2.75×10^6	2.16×10^6	1362	1.07	492
2729	CO_2 50%	0.758	10.32	19.94	0.0647	5.85×10^6	6.51×10^6	1500	0.96	789
2730	CO_2 50%	0.637	10.20	18.46	0.0557	5.32×10^6	5.85×10^6	1654	0.84	756
2732	CO_2 50%	0.707	10.76	20.13	0.0600	5.91×10^6	6.34×10^6	1500	0.92	772
2809	CO_2 50%	0.641	10.52	18.90	0.0546	5.47×10^6	5.87×10^6	1628	0.85	750
2811	CO_2 50%	0.599	11.32	18.91	0.0477	5.52×10^6	5.81×10^6	1683	0.79	754
2812	CO_2 50%	0.716	8.47	11.32	0.0269	2.99×10^6	2.88×10^6	924	1.31	546
2813	CO_2 50%	0.605	9.06	11.34	0.0223	3.05×10^6	2.85×10^6	1008	1.08	558
2816	CO_2 50%	0.563	9.66	11.91	0.0191	3.18×10^6	2.82×10^6	1051	1.01	558
2817	CO_2 50%	0.502	9.59	11.49	0.0165	3.08×10^6	2.69×10^6	1132	0.90	557
2818	CO_2 50%	0.562	11.02	15.87	0.0328	4.44×10^6	4.31×10^6	1458	0.85	661
2819	CO_2 50%	0.526	10.82	15.10	0.0306	4.19×10^6	4.06×10^6	1458	0.81	648
2820	CO_2 50%	0.684	10.05	15.95	0.0440	4.50×10^6	4.71×10^6	1308	1.01	676
2821	CO_2 50%	0.607	10.41	15.98	0.0403	4.49×10^6	4.52×10^6	1383	0.91	668
2719	CO_2	0.758	6.13	21.68	0.1137	5.46×10^6	7.68×10^6	1446	0.94	808

Shot	Gas	x_{Tr}	N_{Tr}	N_{TrNovib}	α_{Fujii}	Re_{Tr}	Re^*_{Tr}	Ω_{Tr}	$\delta_{99\text{Tr}}$	$(x/\delta_{99})_{\text{Tr}}$
		m						kHz	mm	
2733	CO_2	0.616	7.21	23.93	0.1086	$6.06{\times}10^6$	$8.57{\times}10^6$	1883	0.72	856
2793	CO_2	0.601	9.42	14.81	0.0430	$3.45{\times}10^6$	$4.23{\times}10^6$	1233	0.93	644
2805	CO_2	0.638	11.42	23.52	0.0720	$6.09{\times}10^6$	$7.61{\times}10^6$	1608	0.77	830
2806	CO_2	0.487	11.10	22.90	0.0719	$5.87{\times}10^6$	$7.52{\times}10^6$	2134	0.59	827
2808	CO_2	0.532	10.91	24.88	0.0829	$6.41{\times}10^6$	$8.24{\times}10^6$	1984	0.62	858

Appendix B

T5 Contour Nozzle Conditions Study

B.1   Shot 2764

Experiment 2764 was performed in T5 on 18 October 2012.

B.1.1   Geometry

The test article was a 1 m 5-degree half-angle cone with a sharp tip. The initial shock tube composition was 100% air by mass. Reservoir temperature, density, and composition are computed from the measured shock speed and shock tube initial conditions using a Cantera-based reflected-shock model adjusted for measured reservoir pressure.

B.1.2   Measured Quantities

Measurement	Symbol	Value	Units
Shock Speed	U_s	2370	m/s
Shock Tube Fill Pressure	P_1	60.10	kPa
Reservoir Pressure	P_res	16.5	MPa

Table B.1: Measured quantities, shot 2764

B.1.3 Computed Reservoir Conditions

Computed Quantity	Symbol	Value	Units
Reservoir Temperature	T_{res}	4008	K
Reservoir Density	ρ_{res}	13.97	kg/m^3
Reservoir Enthalpy	h_{res}	5.28	MJ/kg

Table B.2: Computed reservoir conditions, shot 2764

Y_{N_2}	Y_{O_2}	Y_{CO_2}	Y_{NO}	Y_{CO}	Y_{N}	Y_{O}
7.21×10^{-1}	1.56×10^{-1}	0	9.80×10^{-2}	0	6.05×10^{-5}	2.49×10^{-2}

Table B.3: Computed reservoir species mass fractions, shot 2764

B.1.4 Nozzle Position, Transition, and Chemistry Assumptions

These quantities are computed using the UMNAEM nozzle code with turbulent (unless otherwise stated) and laminar nozzle boundary layer assumptions, and the DPLR/STABL suite taking input freestream conditions at five different positions in the nozzle, and with and without the inclusion of chemical and vibrational rate processes. The results are compared to the results of a 1-D Cantera-based nozzle code with a Taylor-Maccoll shock and boundary layer similarity solution with conditions calculated from the nozzle exit, 100 cm downstream of the throat. The position 72 cm from the nozzle throat matches the best measurement of the experimental geometry, and the laminar-nozzle, frozen, and equilibrium cases are computed at this position.

	U_∞	T_∞	Tv_∞	M_∞	P_∞	ρ_∞	Unit Re_∞
	m/s	K	K	-	kPa	kg/m^3	1/m
1D 100 cm	3051	678.0	678.0	5.89	6.0	0.030	2.77×10^6
100 cm	3034	644.2	682.0	5.94	5.4	0.029	2.85×10^6
Lam 72 cm	3037	630.9	715.7	6.02	5.1	0.028	2.79×10^6
82 cm	3034	638.8	748.0	5.97	5.4	0.029	2.90×10^6
77 cm	3035	636.5	731.1	5.99	5.3	0.029	2.86×10^6
72 cm	3028	658.1	717.0	5.87	5.9	0.031	2.86×10^6
67 cm	3025	667.5	708.0	5.83	6.2	0.032	3.08×10^6
62 cm	3028	659.3	699.5	5.87	5.9	0.031	3.00×10^6

Table B.4: Computed freestream conditions, shot 2764

	Y_{N_2}	Y_{O_2}	Y_{CO_2}	Y_{NO}	Y_{CO}	Y_N	Y_O
1D 100 cm	7.37×10^{-1}	1.94×10^{-1}	0	6.44×10^{-2}	0	1.83×10^{-10}	4.66×10^{-3}
100 cm	7.33×10^{-1}	1.91×10^{-1}	0	7.36×10^{-2}	0	0	2.34×10^{-3}
Lam 72 cm	7.33×10^{-1}	1.91×10^{-1}	0	7.36×10^{-2}	0	0	2.34×10^{-3}
82 cm	7.33×10^{-1}	1.91×10^{-1}	0	7.36×10^{-2}	0	0	2.34×10^{-3}
77 cm	7.33×10^{-1}	1.91×10^{-1}	0	7.36×10^{-2}	0	0	2.34×10^{-3}
72 cm	7.33×10^{-1}	1.91×10^{-1}	0	7.36×10^{-2}	0	0	2.34×10^{-3}
67 cm	7.33×10^{-1}	1.91×10^{-1}	0	7.36×10^{-2}	0	0	2.34×10^{-3}
62 cm	7.33×10^{-1}	1.91×10^{-1}	0	7.36×10^{-2}	0	0	2.34×10^{-3}

Table B.5: Computed freestream species mass fractions, shot 2764

	U_e	T_e	Tv_e	M_e	P_e	ρ_e	Unit Re_e
	m/s	K	K	-	kPa	kg/m^3	1/m
1D 100 cm	3022	758.5	758.5	5.52	9.0	0.041	3.46×10^6
100 cm	2981	773.4	773.1	5.33	8.3	0.037	3.02×10^6
Lam 72 cm	2984	763.9	763.7	5.37	7.9	0.036	2.93×10^6
82 cm	2981	772.4	772.1	5.33	8.4	0.038	3.05×10^6
77 cm	2982	769.3	769.1	5.35	8.2	0.037	3.01×10^6
72 cm	2974	790.9	776.2	5.27	9.1	0.040	3.20×10^6
67 cm	2974	793.8	793.3	5.25	9.4	0.041	3.28×10^6
62 cm	2976	787.4	786.9	5.27	9.0	0.040	3.18×10^6

Table B.6: Computed boundary layer edge conditions, shot 2764

	Y_{N_2}	Y_{O_2}	Y_{CO_2}	Y_{NO}	Y_{CO}	Y_N	Y_O
1D 100 cm	7.37×10^{-1}	1.94×10^{-1}	0	6.44×10^{-2}	0	1.83×10^{-10}	4.66×10^{-3}
100 cm	7.33×10^{-1}	1.91×10^{-1}	0	7.36×10^{-2}	0	9.30×10^{-12}	2.34×10^{-3}
Lam 72 cm	7.33×10^{-1}	1.91×10^{-1}	0	7.36×10^{-2}	0	9.69×10^{-12}	2.34×10^{-3}
82 cm	7.33×10^{-1}	1.91×10^{-1}	0	7.36×10^{-2}	0	9.04×10^{-12}	2.33×10^{-3}
77 cm	7.33×10^{-1}	1.91×10^{-1}	0	7.36×10^{-2}	0	9.24×10^{-12}	2.33×10^{-3}
72 cm	7.33×10^{-1}	1.91×10^{-1}	0	7.36×10^{-2}	0	8.34×10^{-12}	2.33×10^{-3}
67 cm	7.33×10^{-1}	1.91×10^{-1}	0	7.36×10^{-2}	0	7.79×10^{-12}	2.33×10^{-3}
62 cm	7.33×10^{-1}	1.91×10^{-1}	0	7.36×10^{-2}	0	8.43×10^{-12}	2.33×10^{-3}

Table B.7: Computed boundary layer edge species mass fractions, shot 2764

	x_{Tr}	Re_{Tr}	N_{Tr}	Ω_{Tr}	Ω_{NTr}	δ_{99Tr}	$(x/\delta_{99})_{Tr}$	$Re_{\delta_{99}Tr}$
	m	-	-	kHz	kHz	mm	-	-
100 cm	0.531	1.60×10^6	5.05	653	655	1.547	343	4667
Lam 72 cm	0.531	1.56×10^6	4.90	631	646	1.573	337	4618
82 cm	0.531	1.62×10^6	5.09	653	655	1.543	344	4700
77 cm	0.531	1.60×10^6	5.00	642	655	1.552	342	4669
72 cm	0.531	1.70×10^6	5.40	697	694	1.492	356	4770
67 cm	0.531	1.74×10^6	5.55	714	714	1.467	362	4805
62 cm	0.531	1.69×10^6	5.39	679	694	1.492	356	4739
Frozen 72 cm	0.531	1.70×10^6	5.47	679	704	1.492	356	4770
Equil. 72 cm	0.531	1.70×10^6	5.50	679	685	1.492	356	4770

Table B.8: Boundary layer stability characteristics at experimentally observed transition location, shot 2764
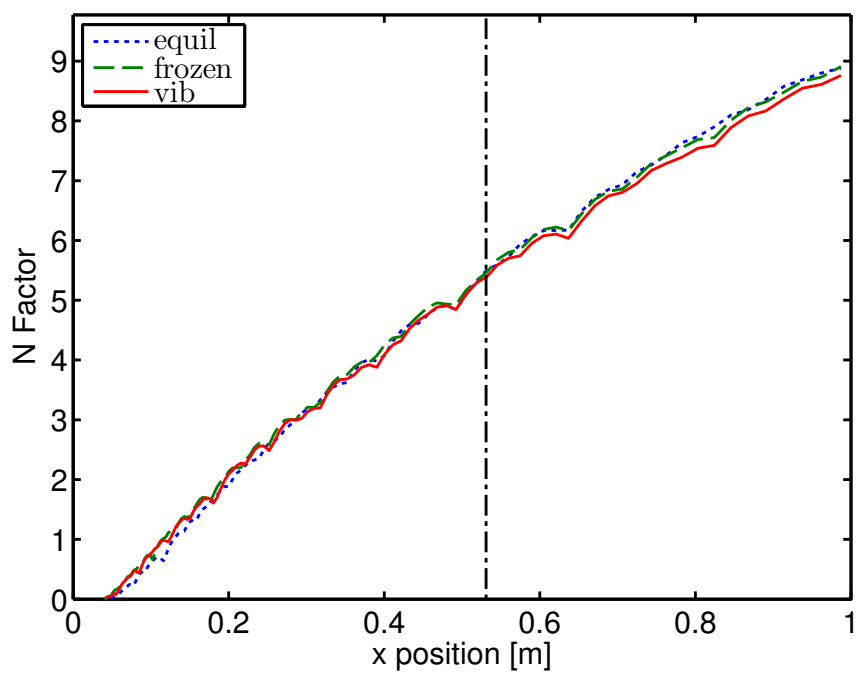
Figure B.1: N factor curves as a function of distance for realistic, frozen, and equilibrium vibrational energy transfer, shot 2764. The dot-dashed line indicates the experimentally measured transition onset location.
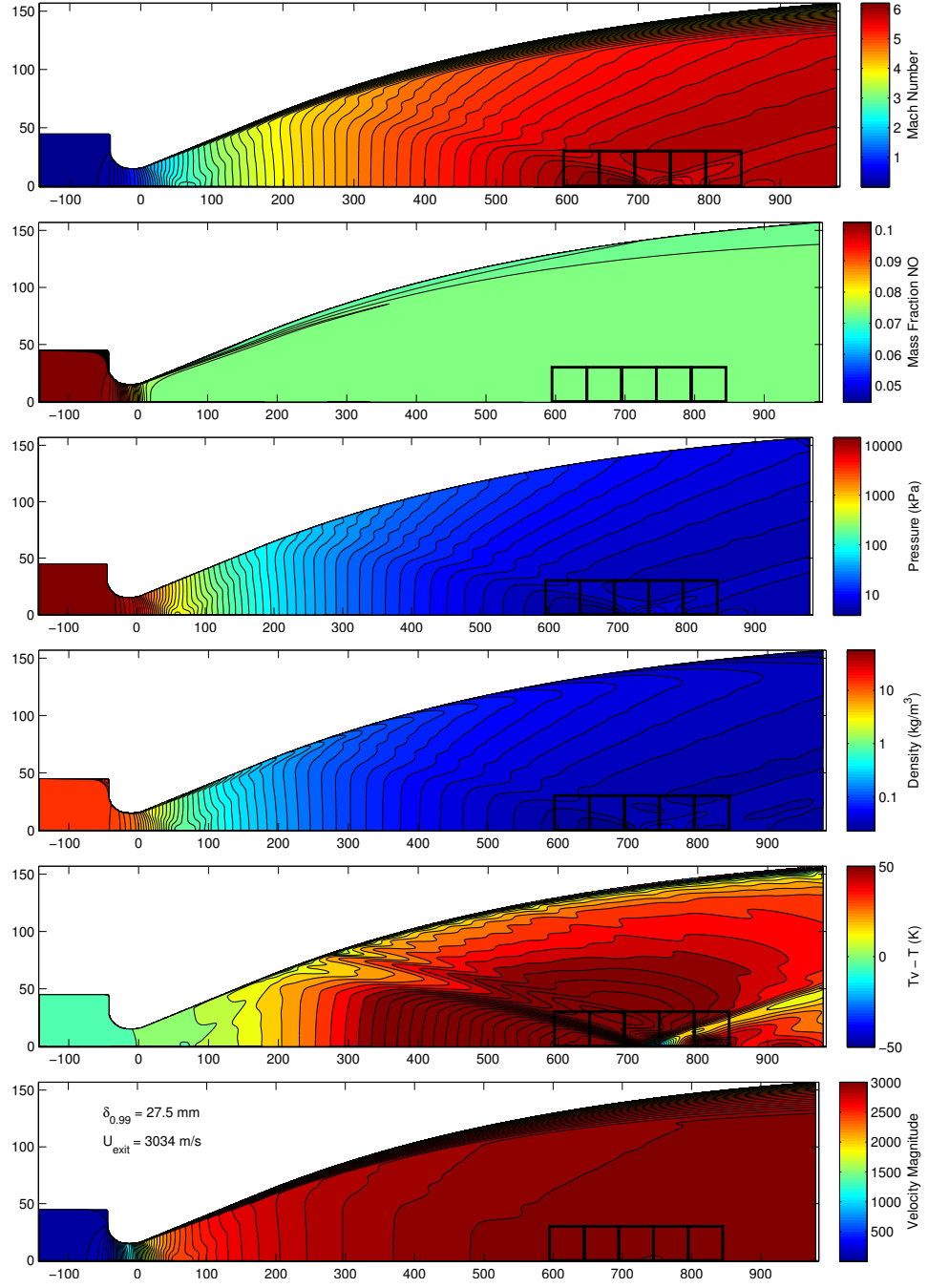
Figure B.2: Nozzle flow computed with the Spalart-Allmaras turbulence model for the wall, shot 2764. The black boxes highlight the averaged regions used to create STABL/DPLR inputs.
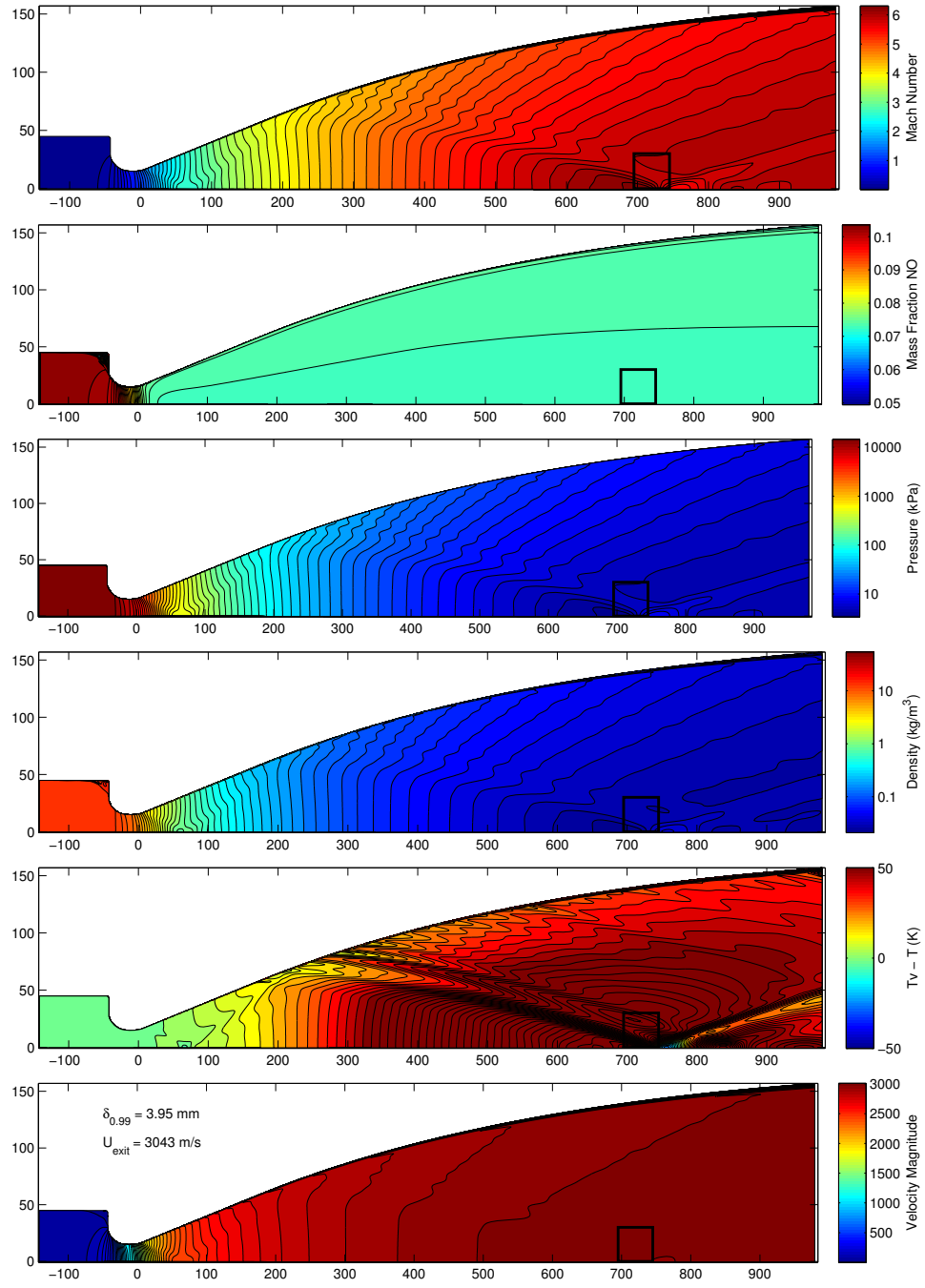
Figure B.3: Nozzle flow computed with laminar boundary layer growth for the wall, shot 2764. The black box highlights the averaged region used to create STABL/DPLR inputs.
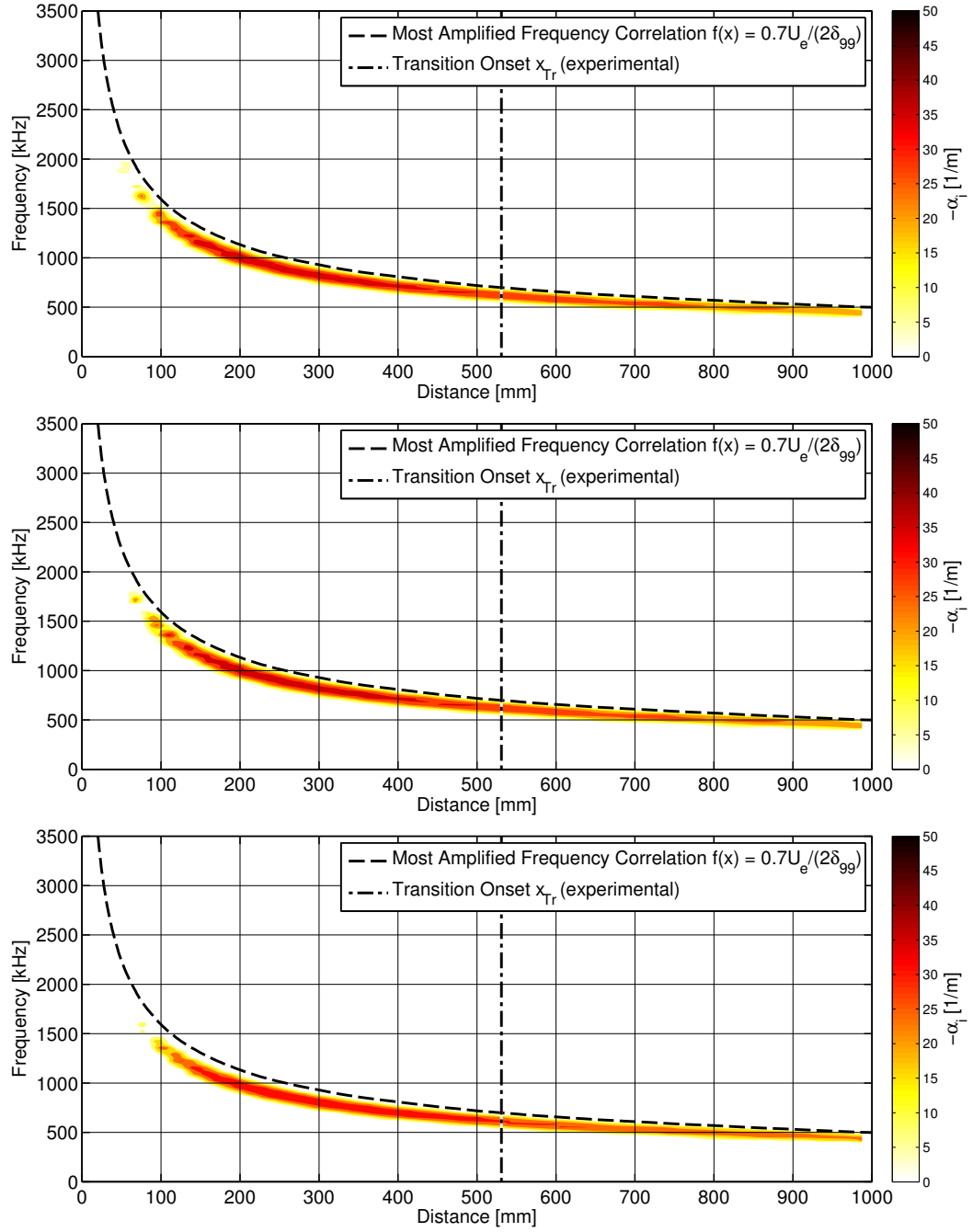
Figure B.4: Stability diagram with physical (top), frozen (middle), and equilibrium (bottom) vibrational energy transfer, shot 2764. Dashed line indicates $0.7U_{\mathrm{e}}/(2\delta_{99})$; dot-dashed line is the transition location.
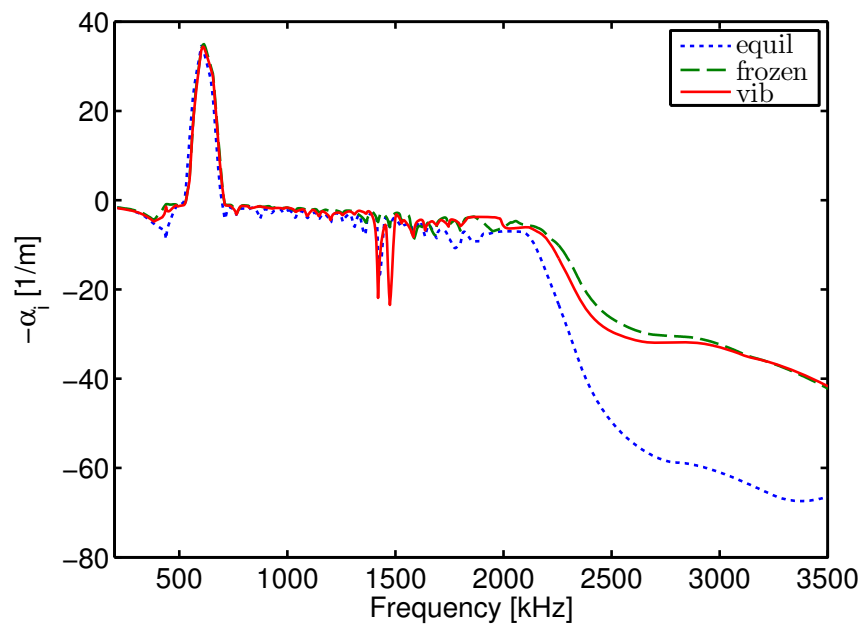
Figure B.5: Spatial amplification rate $-\alpha_i$ across frequencies calculated at x_{Tr}, with physical, frozen, and equilibrium vibrational energy transfer, shot 2764.
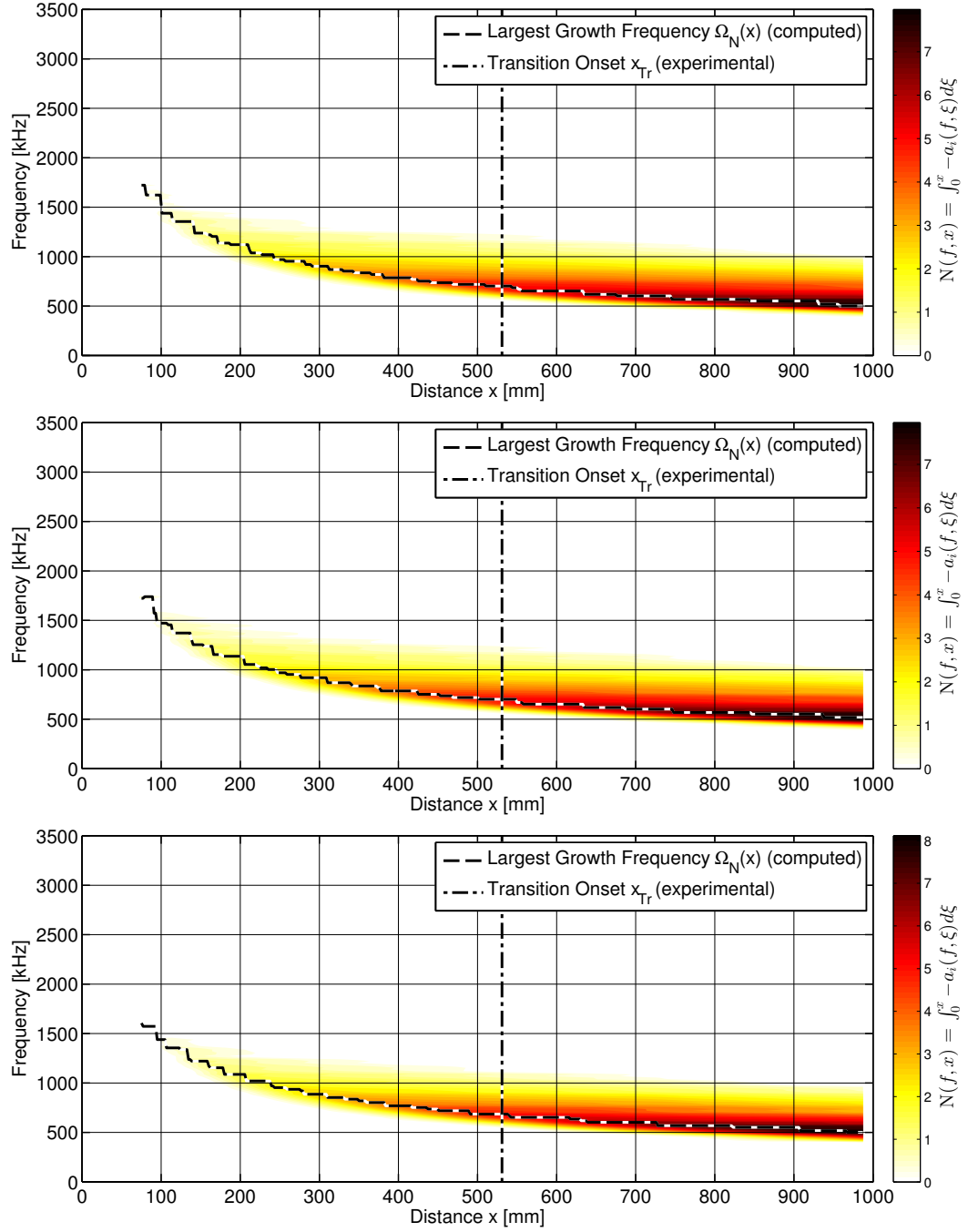
Figure B.6: Largest (integrated) growth frequency diagram with physical (top), frozen (middle), and equilibrium (bottom) vibrational energy transfer, shot 2764. Dashed line indicates the computed frequency of largest growth at each x-location; dot-dashed line is the transition x-location.
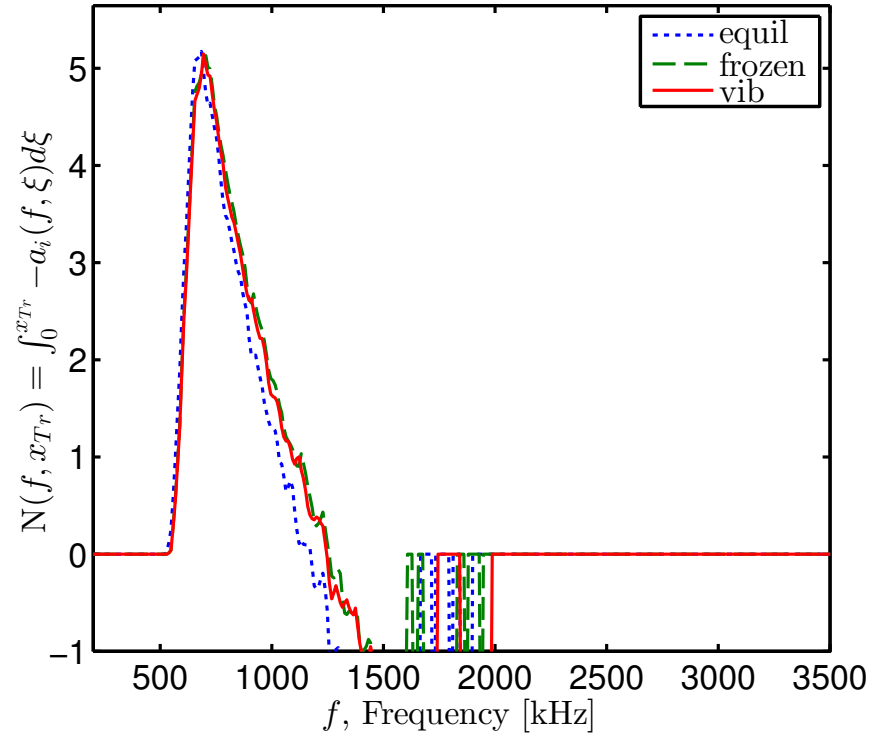
Figure B.7: $N(f, x) = \int_0^x -a_i(f, \xi)d\xi$ calculated at x_{Tr}, with physical, frozen, and equilibrium vibrational energy transfer, shot 2764.

B.2   Shot 2823

Experiment 2823 was performed in T5 on 31 July 2013.

B.2.1   Geometry

The test article was a 1 m 5-degree half-angle cone with a sharp tip. The initial
shock tube composition was 100% air by mass. Reservoir temperature, density, and
composition are computed from the measured shock speed and shock tube initial con-
ditions using a Cantera-based reflected-shock model adjusted for measured reservoir
pressure.

B.2.2   Measured Quantities

Measurement	Symbol	Value	Units
Shock Speed	U_s	3050	m/s
Shock Tube Fill Pressure	P_1	85.00	kPa
Reservoir Pressure	P_res	42.6	MPa

Table B.9: Measured quantities, shot 2823

B.2.3   Computed Reservoir Conditions

Computed Quantity	Symbol	Value	Units
Reservoir Temperature	T_res	5620	K
Reservoir Density	ρ_res	24.14	kg/m^3
Reservoir Enthalpy	h_res	8.77	MJ/kg

Table B.10: Computed reservoir conditions, shot 2823

Y_{N_2}	Y_{O_2}	Y_{CO_2}	Y_{NO}	Y_{CO}	Y_{N}	Y_{O}
7.02×10^{-1}	6.58×10^{-2}	0	1.34×10^{-1}	0	2.56×10^{-3}	9.54×10^{-2}

Table B.11: Computed reservoir species mass fractions, shot 2823

B.2.4 Nozzle Position, Transition, and Chemistry Assumptions

These quantities are computed using the UMNAEM nozzle code with turbulent (unless otherwise stated) and laminar nozzle boundary layer assumptions, and the DPLR/STABL suite taking input freestream conditions at five different positions in the nozzle, and with and without the inclusion of chemical and vibrational rate processes. The results are compared to the results of a 1-D Cantera-based nozzle code with a Taylor-Maccoll shock and boundary layer similarity solution with conditions calculated from the nozzle exit, 100 cm downstream of the throat. The position 72 cm from the nozzle throat matches the best measurement of the experimental geometry, and the laminar-nozzle, frozen, and equilibrium cases are computed at this position.

	U_∞	T_∞	Tv_∞	M_∞	P_∞	ρ_∞	Unit Re_∞
	m/s	K	K	-	kPa	kg/m^3	1/m
1D 100 cm	3824	1279.0	1279.0	5.44	19.3	0.052	4.06×10^6
100 cm	3817	1238.4	1241.2	5.37	17.8	0.050	3.99×10^6
Lam 72 cm	3800	1288.8	1296.6	5.24	21.2	0.057	4.42×10^6
82 cm	3790	1320.9	1319.5	5.17	23.4	0.061	4.67×10^6
77 cm	3790	1321.7	1323.5	5.16	23.5	0.061	4.68×10^6
72 cm	3795	1303.8	1313.0	5.21	22.3	0.059	4.53×10^6
67 cm	3804	1275.2	1289.0	5.28	20.4	0.055	4.32×10^6
62 cm	3808	1263.5	1270.6	5.31	19.5	0.053	4.21×10^6

Table B.12: Computed freestream conditions, shot 2823

	Y_{N_2}	Y_{O_2}	Y_{CO_2}	Y_{NO}	Y_{CO}	Y_N	Y_O
1D 100 cm	7.39×10^{-1}	1.84×10^{-1}	0	6.12×10^{-2}	0	6.72×10^{-10}	1.63×10^{-2}
100 cm	7.33×10^{-1}	1.84×10^{-1}	0	7.40×10^{-2}	0	7.90×10^{-10}	9.33×10^{-3}
Lam 72 cm	7.33×10^{-1}	1.84×10^{-1}	0	7.39×10^{-2}	0	1.52×10^{-9}	9.41×10^{-3}
82 cm	7.33×10^{-1}	1.84×10^{-1}	0	7.39×10^{-2}	0	1.95×10^{-9}	9.45×10^{-3}
77 cm	7.33×10^{-1}	1.84×10^{-1}	0	7.39×10^{-2}	0	2.06×10^{-9}	9.42×10^{-3}
72 cm	7.33×10^{-1}	1.84×10^{-1}	0	7.39×10^{-2}	0	1.78×10^{-9}	9.39×10^{-3}
67 cm	7.33×10^{-1}	1.84×10^{-1}	0	7.39×10^{-2}	0	1.35×10^{-9}	9.37×10^{-3}
62 cm	7.33×10^{-1}	1.84×10^{-1}	0	7.39×10^{-2}	0	1.10×10^{-9}	9.35×10^{-3}

Table B.13: Computed freestream species mass fractions, shot 2823

	U_e	T_e	Tv_e	M_e	P_e	ρ_e	Unit Re_e
	m/s	K	K	-	kPa	kg/m^3	1/m
1D 100 cm	3786	1397.0	1397.0	5.15	27.7	0.068	5.00×10^6
100 cm	3753	1416.7	1416.0	4.94	25.9	0.063	4.48×10^6
Lam 72 cm	3736	1466.7	1466.1	4.83	30.5	0.072	4.99×10^6
82 cm	3728	1495.7	1495.1	4.78	33.4	0.077	5.30×10^6
77 cm	3728	1496.4	1495.9	4.77	33.5	0.077	5.32×10^6
72 cm	3731	1479.5	1476.6	4.81	31.9	0.074	5.17×10^6
67 cm	3740	1455.1	1454.4	4.86	29.3	0.069	4.86×10^6
62 cm	3745	1441.1	1440.4	4.89	28.2	0.067	4.74×10^6

Table B.14: Computed boundary layer edge conditions, shot 2823

	Y_{N_2}	Y_{O_2}	Y_{CO_2}	Y_{NO}	Y_{CO}	Y_N	Y_O
1D 100 cm	7.39×10^{-1}	1.84×10^{-1}	0	6.12×10^{-2}	0	6.72×10^{-10}	1.63×10^{-2}
100 cm	7.33×10^{-1}	1.85×10^{-1}	0	7.40×10^{-2}	0	4.86×10^{-9}	8.92×10^{-3}
Lam 72 cm	7.33×10^{-1}	1.85×10^{-1}	0	7.39×10^{-2}	0	7.26×10^{-9}	8.89×10^{-3}
82 cm	7.33×10^{-1}	1.85×10^{-1}	0	7.39×10^{-2}	0	9.03×10^{-9}	8.85×10^{-3}
77 cm	7.33×10^{-1}	1.85×10^{-1}	0	7.39×10^{-2}	0	9.05×10^{-9}	8.83×10^{-3}
72 cm	7.33×10^{-1}	1.85×10^{-1}	0	7.39×10^{-2}	0	8.04×10^{-9}	8.84×10^{-3}
67 cm	7.33×10^{-1}	1.85×10^{-1}	0	7.39×10^{-2}	0	6.61×10^{-9}	8.88×10^{-3}
62 cm	7.33×10^{-1}	1.85×10^{-1}	0	7.39×10^{-2}	0	5.91×10^{-9}	8.89×10^{-3}

Table B.15: Computed boundary layer edge species mass fractions, shot 2823

	x_{Tr}	Re_{Tr}	N_{Tr}	Ω_{Tr}	Ω_{NTr}	δ_{99Tr}	$(x/\delta_{99})_{Tr}$	$Re_{\delta_{99}Tr}$
	m	-	-	kHz	kHz	mm	-	-
100 cm	0.525	2.35×10^6	7.87	1215	1200	1.155	455	5173
Lam 72 cm	0.525	2.62×10^6	8.30	1290	1326	1.083	485	5399
82 cm	0.525	2.78×10^6	8.79	1362	1394	1.047	502	5547
77 cm	0.525	2.79×10^6	8.78	1362	1394	1.047	502	5564
72 cm	0.525	2.75×10^6	8.69	1362	1336	1.067	492	5522
67 cm	0.525	2.55×10^6	8.36	1286	1258	1.101	477	5345
62 cm	0.525	2.49×10^6	8.21	1276	1258	1.117	470	5289
Frozen 72 cm	0.525	2.75×10^6	9.26	1362	1336	1.067	492	5522
Equil. 72 cm	0.525	2.75×10^6	9.34	1329	1326	1.067	492	5522

Table B.16: Boundary layer stability characteristics at experimentally observed transition location, shot 2823
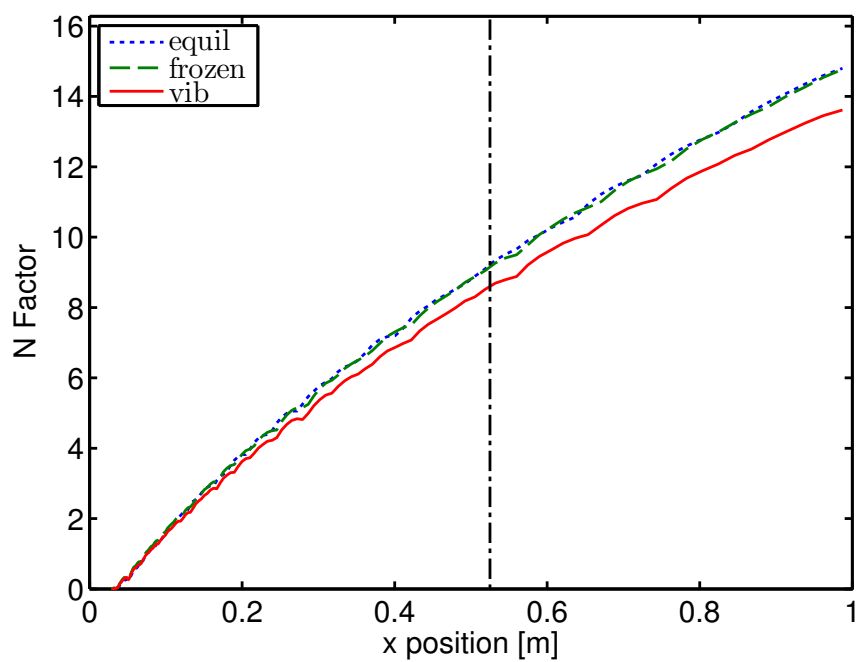
Figure B.8: N factor curves as a function of distance for realistic, frozen, and equilibrium vibrational energy transfer, shot 2823. The dot-dashed line indicates the experimentally measured transition onset location.
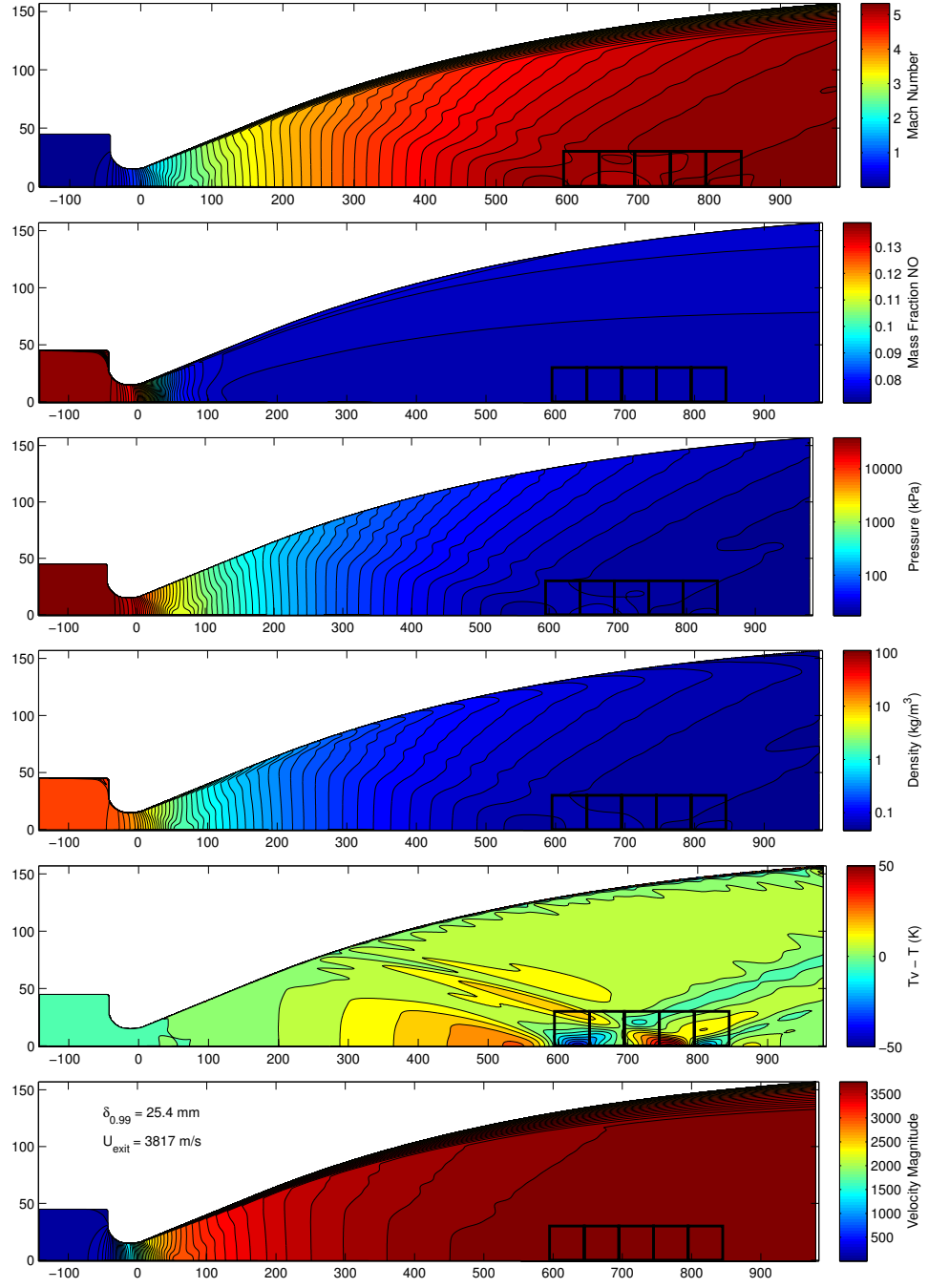
Figure B.9: Nozzle flow computed with the Spalart-Allmaras turbulence model for the wall, shot 2823. The black boxes highlight the averaged regions used to create STABL/DPLR inputs.
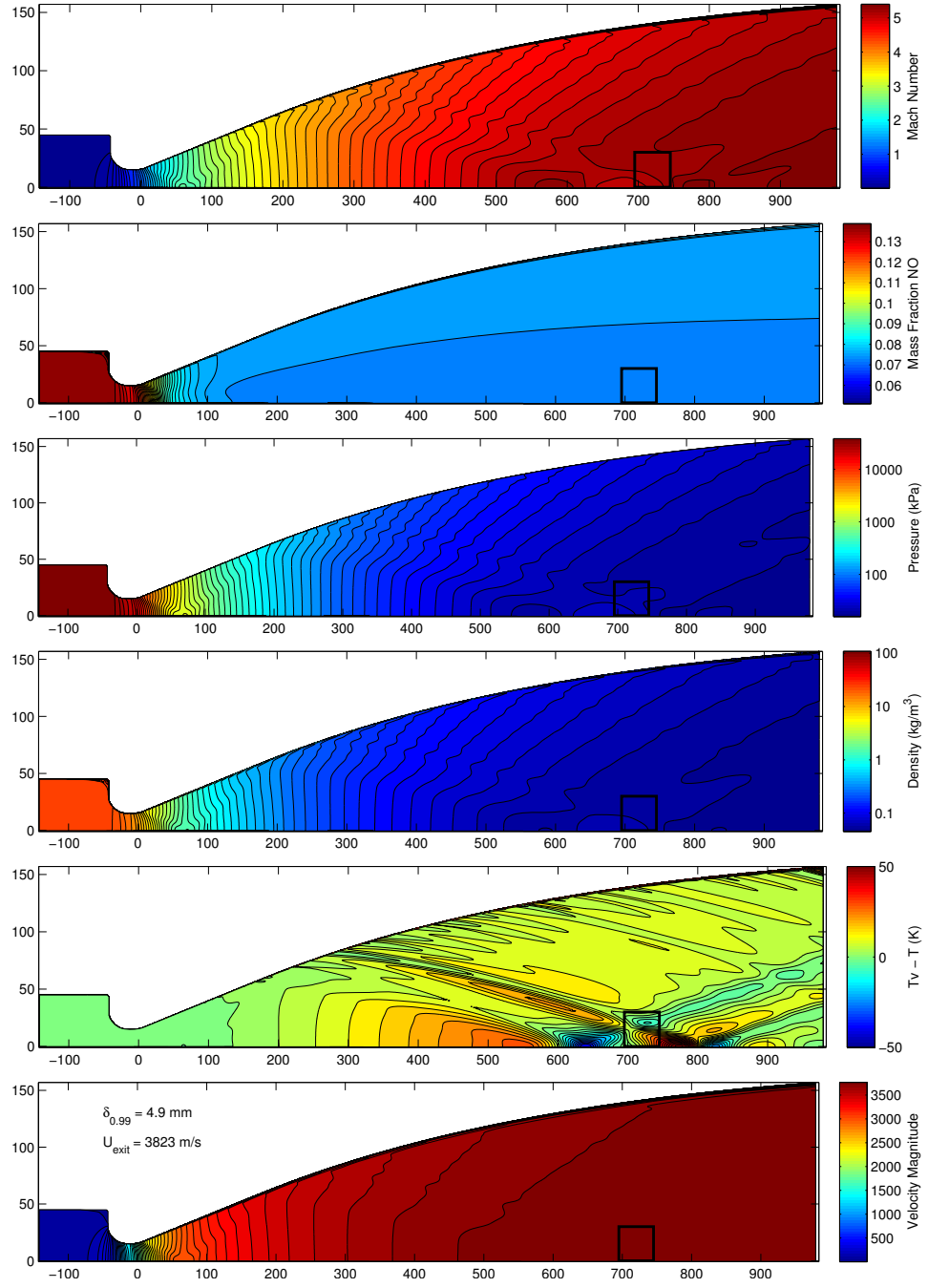
Figure B.10: Nozzle flow computed with laminar boundary layer growth for the wall, shot 2823. The black box highlights the averaged region used to create STABL/DPLR inputs.
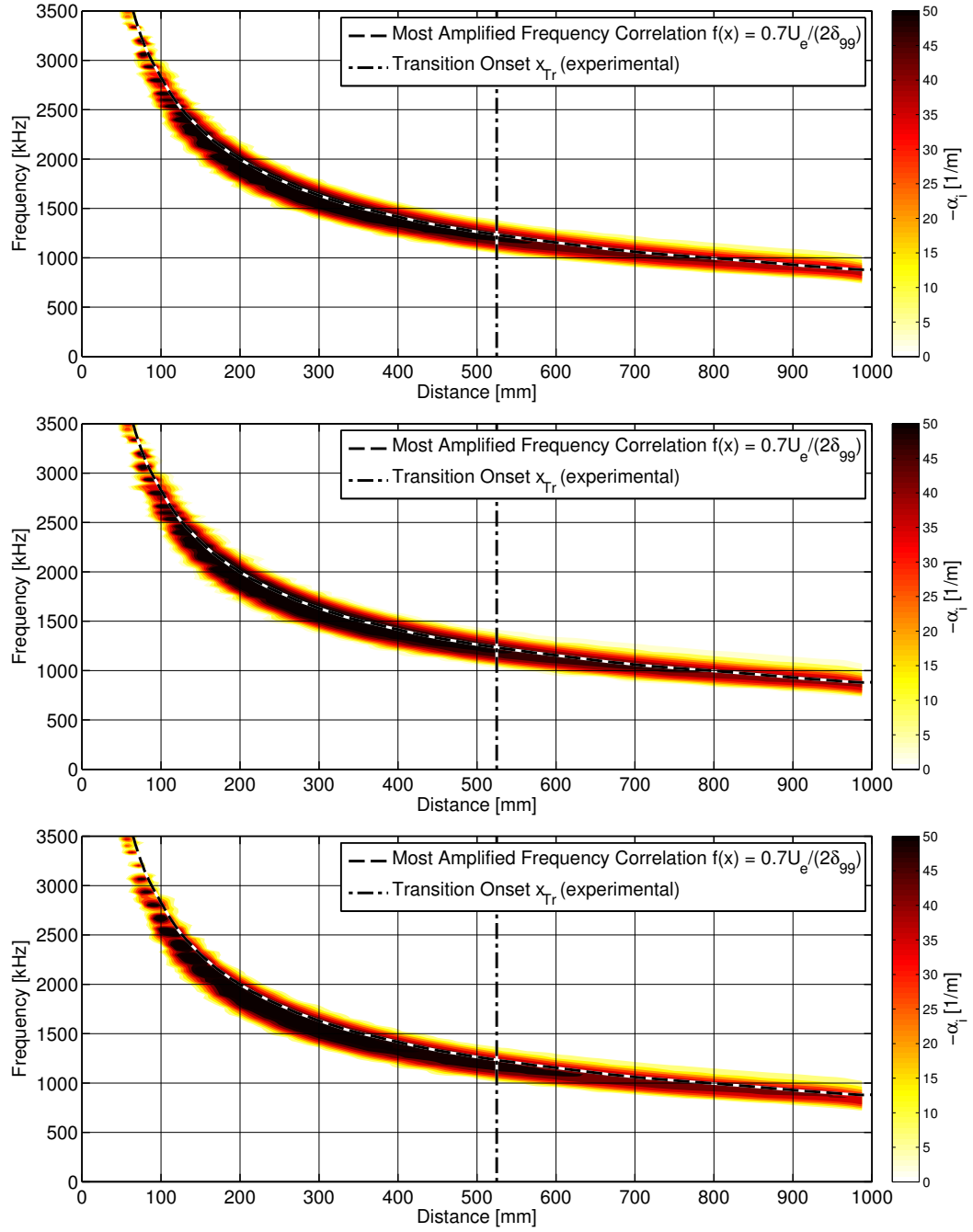
Figure B.11: Stability diagram with physical (top), frozen (middle), and equilibrium (bottom) vibrational energy transfer, shot 2823. Dashed line indicates $0.7U_\mathrm{e}/(2\delta_{99})$; dot-dashed line is the transition location.
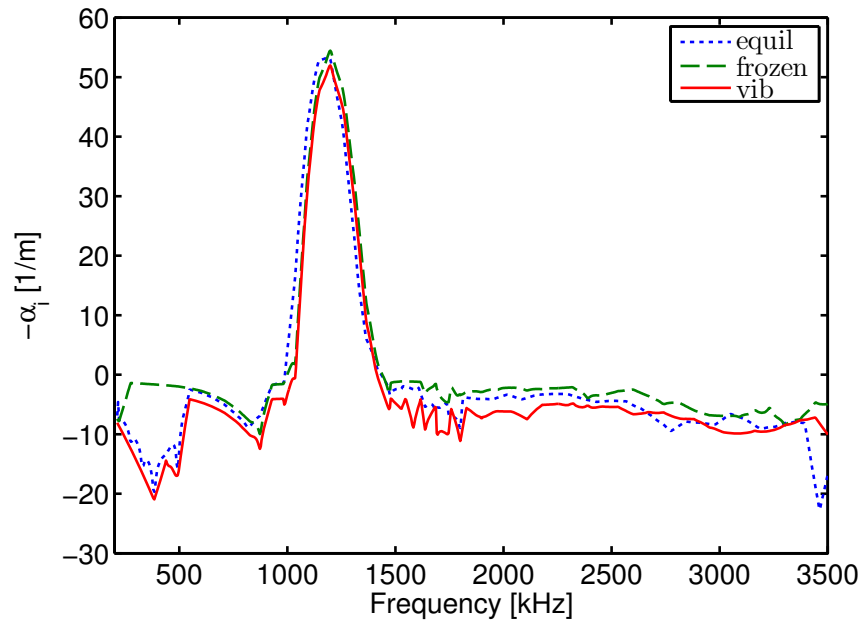
Figure B.12: Spatial amplification rate $-\alpha_i$ across frequencies calculated at x_{Tr}, with physical, frozen, and equilibrium vibrational energy transfer, shot 2823.
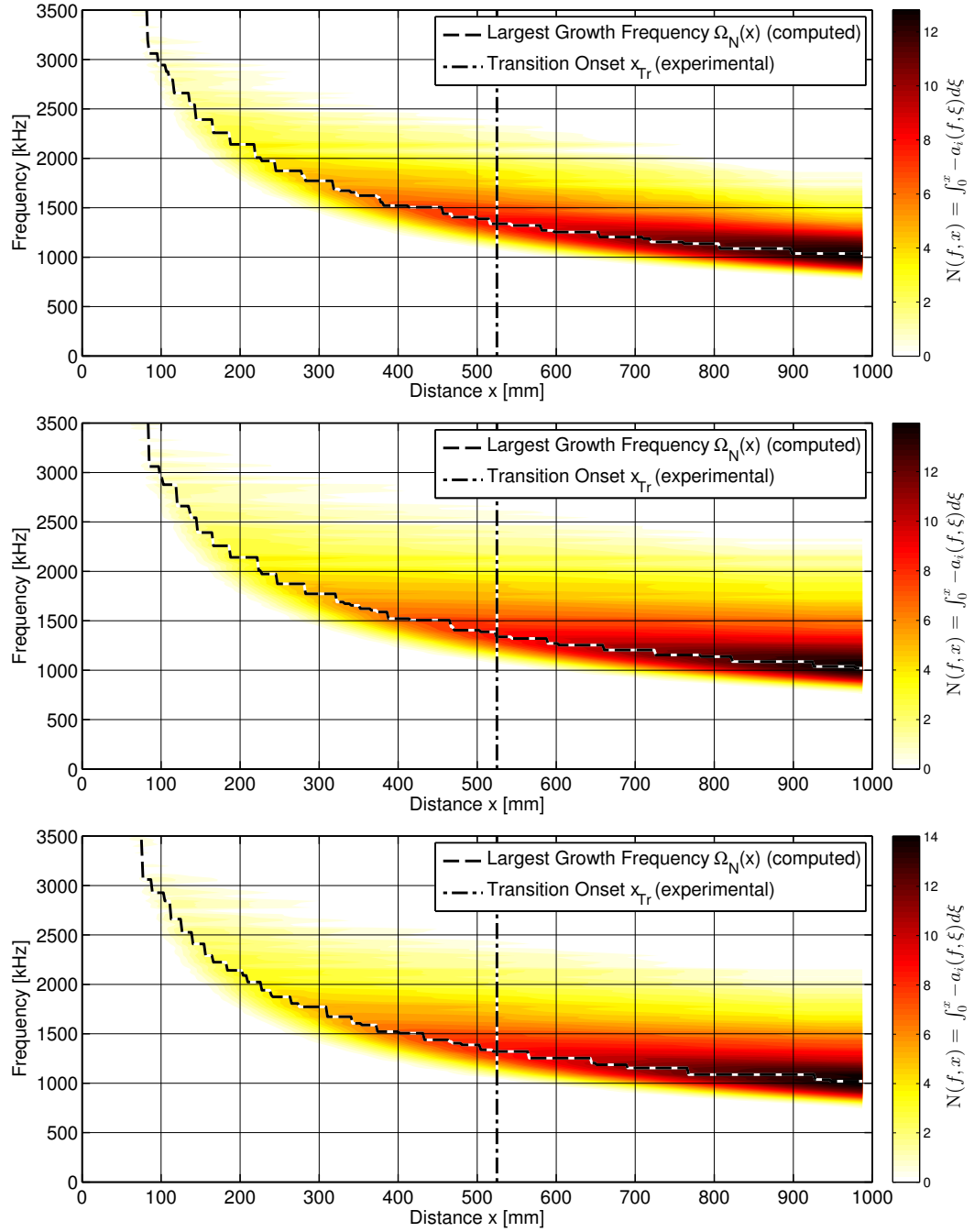
Figure B.13: Largest (integrated) growth frequency diagram with physical (top), frozen (middle), and equilibrium (bottom) vibrational energy transfer, shot 2823. Dashed line indicates the computed frequency of largest growth at each x-location; dot-dashed line is the transition x-location.
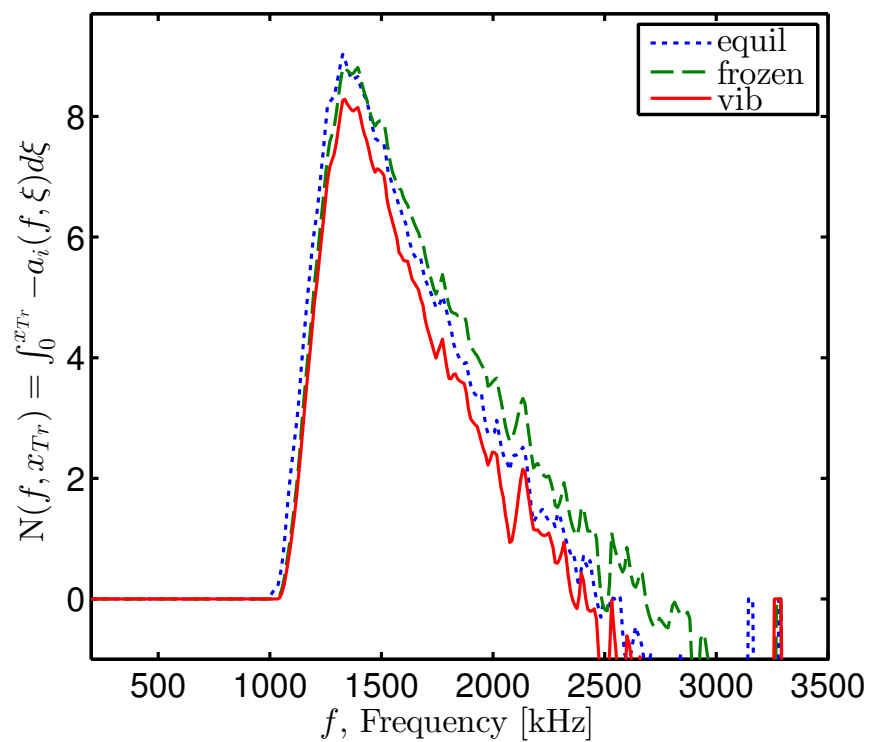
Figure B.14: $N(f,x) = \int_0^x -a_i(f,\xi)d\xi$ calculated at x_{Tr}, with physical, frozen, and equilibrium vibrational energy transfer, shot 2823.

B.3 Shot 2776

Experiment 2776 was performed in T5 on 14 November 2012.

B.3.1 Geometry

The test article was a 1 m 5-degree half-angle cone with a sharp tip. The initial shock tube composition was 100% N_2 by mass. Reservoir temperature, density, and composition are computed from the measured shock speed and shock tube initial conditions using a Cantera-based reflected-shock model adjusted for measured reservoir pressure.

B.3.2 Measured Quantities

Measurement	Symbol	Value	Units
Shock Speed	U_s	2770	m/s
Shock Tube Fill Pressure	P_1	130.00	kPa
Reservoir Pressure	P_{res}	45.9	MPa

Table B.17: Measured quantities, shot 2776

B.3.3 Computed Reservoir Conditions

Computed Quantity	Symbol	Value	Units
Reservoir Temperature	T_{res}	5769	K
Reservoir Density	ρ_{res}	26.69	kg/m^3
Reservoir Enthalpy	h_{res}	7.17	MJ/kg

Table B.18: Computed reservoir conditions, shot 2776

Y_{N_2}	Y_{O_2}	Y_{CO_2}	Y_{NO}	Y_{CO}	Y_N	Y_O
9.96×10^{-1}	0	0	0	0	3.75×10^{-3}	0

Table B.19: Computed reservoir species mass fractions, shot 2776

B.3.4 Nozzle Position, Transition, and Chemistry Assumptions

These quantities are computed using the UMNAEM nozzle code with turbulent (unless otherwise stated) and laminar nozzle boundary layer assumptions, and the DPLR/STABL suite taking input freestream conditions at five different positions in the nozzle, and with and without the inclusion of chemical and vibrational rate processes. The results are compared to the results of a 1-D Cantera-based nozzle code with a Taylor-Maccoll shock and boundary layer similarity solution with conditions calculated from the nozzle exit, 100 cm downstream of the throat. The position 72 cm from the nozzle throat matches the best measurement of the experimental geometry, and the laminar-nozzle, and no vibration/frozen cases are computed at this position.

	U_∞	T_∞	Tv_∞	M_∞	P_∞	ρ_∞	Unit Re_∞
	m/s	K	K	-	kPa	kg/m^3	1/m
1D 100 cm	3595	938.0	938.0	5.87	16.3	0.059	5.53×10^6
100 cm	3560	689.9	2586.5	6.65	11.7	0.057	6.80×10^6
Lam 72 cm	3587	598.1	2584.6	7.20	7.3	0.041	5.47×10^6
82 cm	3568	658.9	2582.8	6.82	10.2	0.052	6.45×10^6
77 cm	3577	631.3	2583.0	6.99	8.8	0.047	6.00×10^6
72 cm	3581	619.1	2583.1	7.07	8.3	0.045	5.41×10^6
67 cm	3581	618.5	2583.1	7.07	8.3	0.045	5.81×10^6
62 cm	3574	639.9	2582.9	6.94	9.3	0.049	6.13×10^6

Table B.20: Computed freestream conditions, shot 2776

	Y_{N_2}	Y_{O_2}	Y_{CO_2}	Y_{NO}	Y_{CO}	Y_N	Y_O
1D 100 cm	1.00	0	0	0	0	3.60×10^{-4}	0
100 cm	1.00	0	0	0	0	2.40×10^{-4}	0
Lam 72 cm	1.00	0	0	0	0	2.41×10^{-4}	0
82 cm	1.00	0	0	0	0	2.40×10^{-4}	0
77 cm	1.00	0	0	0	0	2.40×10^{-4}	0
72 cm	1.00	0	0	0	0	2.40×10^{-4}	0
67 cm	1.00	0	0	0	0	2.40×10^{-4}	0
62 cm	1.00	0	0	0	0	2.40×10^{-4}	0

Table B.21: Computed freestream species mass fractions, shot 2776

	U_e m/s	T_e K	Tv_e K	M_e -	P_e kPa	ρ_e kg/m^3	Unit Re$_e$ 1/m
1D 100 cm	3561	1042.2	1042.2	5.52	24.6	0.079	6.97×10^6
100 cm	3503	862.7	2566.9	5.85	19.3	0.075	6.89×10^6
Lam 72 cm	3529	772.7	2564.7	6.23	12.8	0.056	5.49×10^6
82 cm	3510	833.0	2562.9	5.97	17.2	0.069	6.51×10^6
77 cm	3519	805.5	2563.2	6.08	15.1	0.063	6.04×10^6
72 cm	3524	792.4	2563.6	6.14	14.2	0.060	6.13×10^6
67 cm	3524	791.7	2563.7	6.14	14.2	0.060	5.86×10^6
62 cm	3517	813.2	2563.4	6.05	15.7	0.065	6.19×10^6

Table B.22: Computed boundary layer edge conditions, shot 2776

	Y_{N_2}	Y_{O_2}	Y_{CO_2}	Y_{NO}	Y_{CO}	Y_N	Y_O
1D 100 cm	1.00	0	0	0	0	3.60×10^{-4}	0
100 cm	1.00	0	0	0	0	0	0
Lam 72 cm	1.00	0	0	0	0	0	0
82 cm	1.00	0	0	0	0	0	0
77 cm	1.00	0	0	0	0	0	0
72 cm	1.00	0	0	0	0	0	0
67 cm	1.00	0	0	0	0	0	0
62 cm	1.00	0	0	0	0	0	0

Table B.23: Computed boundary layer edge species mass fractions, shot 2776

	x_{Tr}	$\mathrm{Re}_{\mathrm{Tr}}$	N_{Tr}	Ω_{Tr}	Ω_{NTr}	$\delta_{99\mathrm{Tr}}$	$(x/\delta_{99})_{\mathrm{Tr}}$	$\mathrm{Re}_{\delta_{99}\mathrm{Tr}}$
	m	-	-	kHz	kHz	mm	-	-
100 cm	0.389	2.68×10^6	6.77	1207	1209	0.957	406	6590
Lam 72 cm	0.389	2.14×10^6	5.25	960	986	1.136	343	6234
82 cm	0.389	2.53×10^6	6.08	1163	1132	0.994	391	6471
77 cm	0.389	2.35×10^6	5.87	1061	1054	1.053	370	6355
72 cm	0.389	2.39×10^6	5.44	1054	1054	1.073	363	6573
67 cm	0.389	2.28×10^6	5.41	1054	1054	1.073	363	6281
62 cm	0.389	2.41×10^6	5.69	1061	1054	1.033	377	6392
Frozen 72 cm	0.389	2.39×10^6	5.44	1054	1054	1.073	363	6573

Table B.24: Boundary layer stability characteristics at experimentally observed transition location, shot 2776
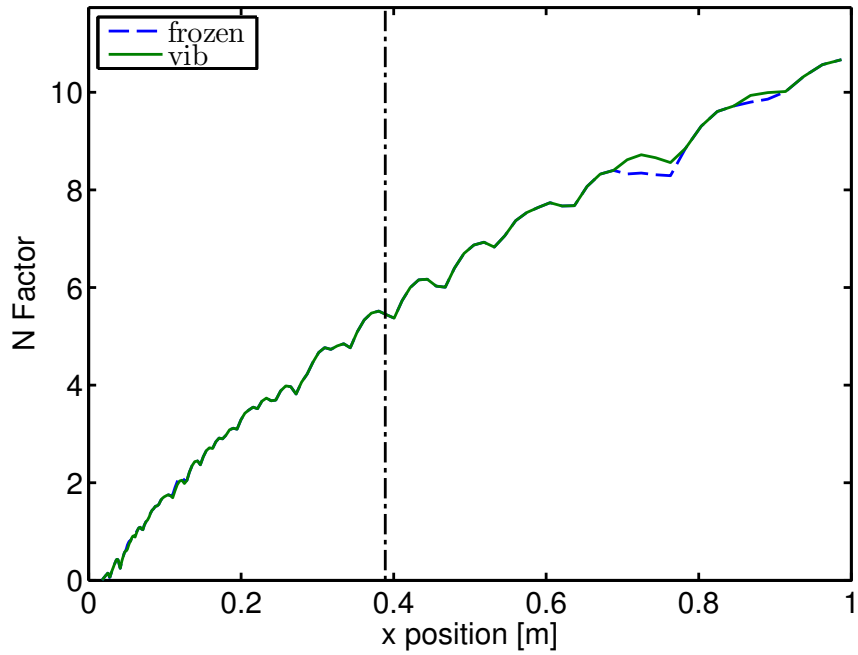
Figure B.15: N factor curves as a function of distance for realistic vibration and no vibration/frozen vibrational energy transfer, shot 2776. The dot-dashed line indicates the experimentally measured transition onset location. For the N_2 cases, the equilibrium case does not behave correctly due to the large amount of thermal nonequilibrium and is therefore omitted.
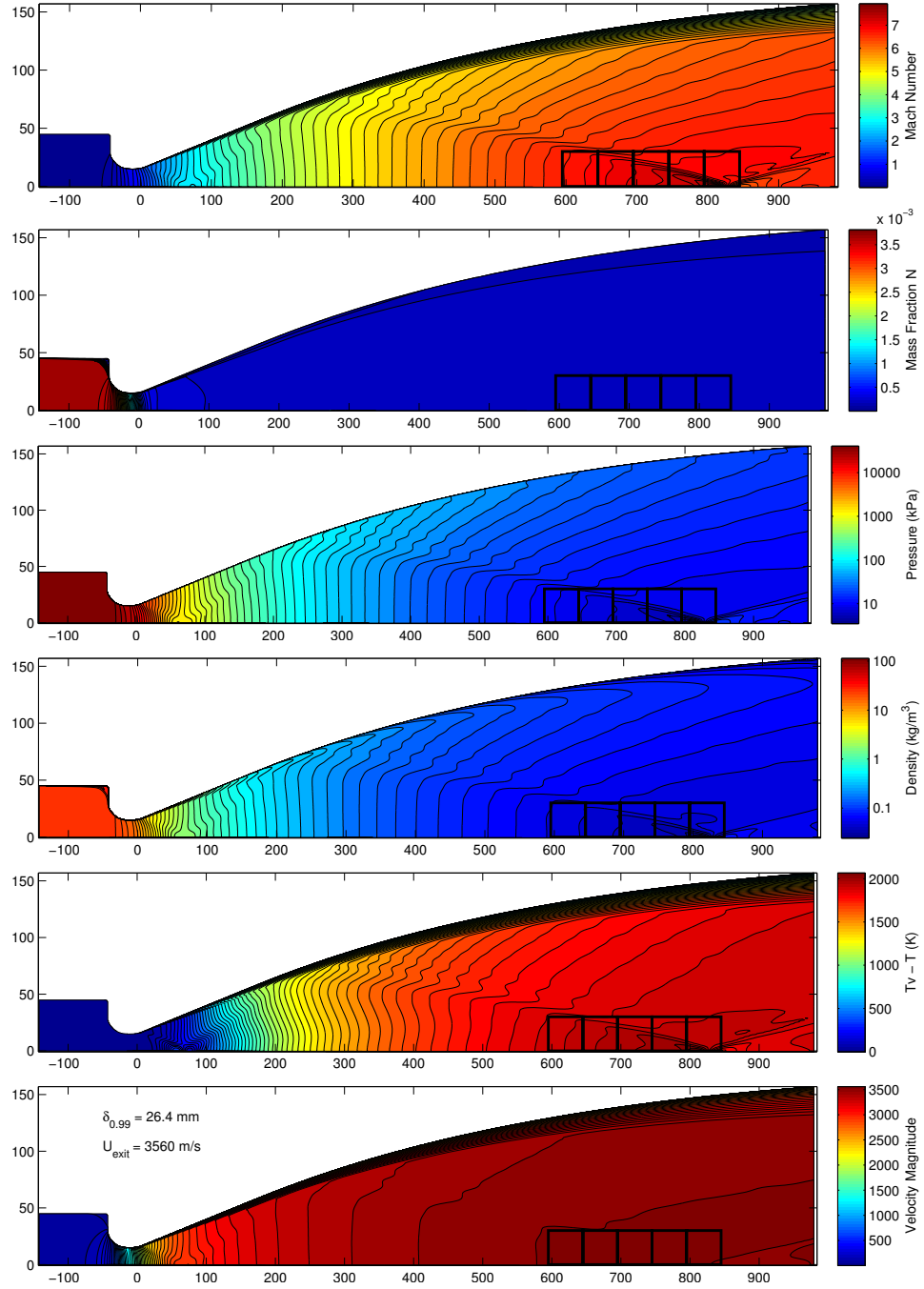
Figure B.16: Nozzle flow computed with the Spalart-Allmaras turbulence model for the wall, shot 2776. The black boxes highlight the averaged regions used to create STABL/DPLR inputs.
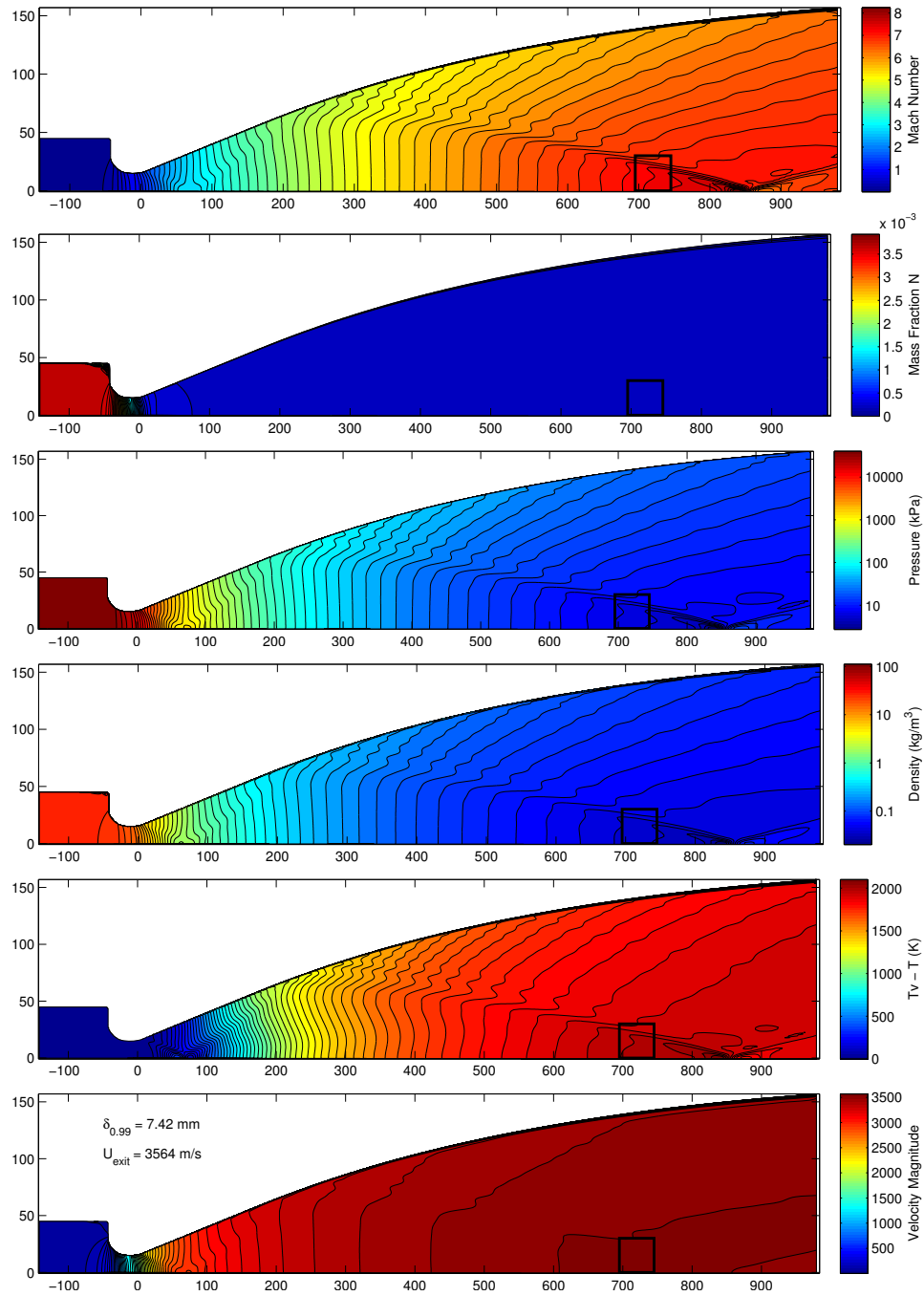
Figure B.17: Nozzle flow computed with laminar boundary layer growth for the wall, shot 2776. The black box highlights the averaged region used to create STABL/DPLR inputs.
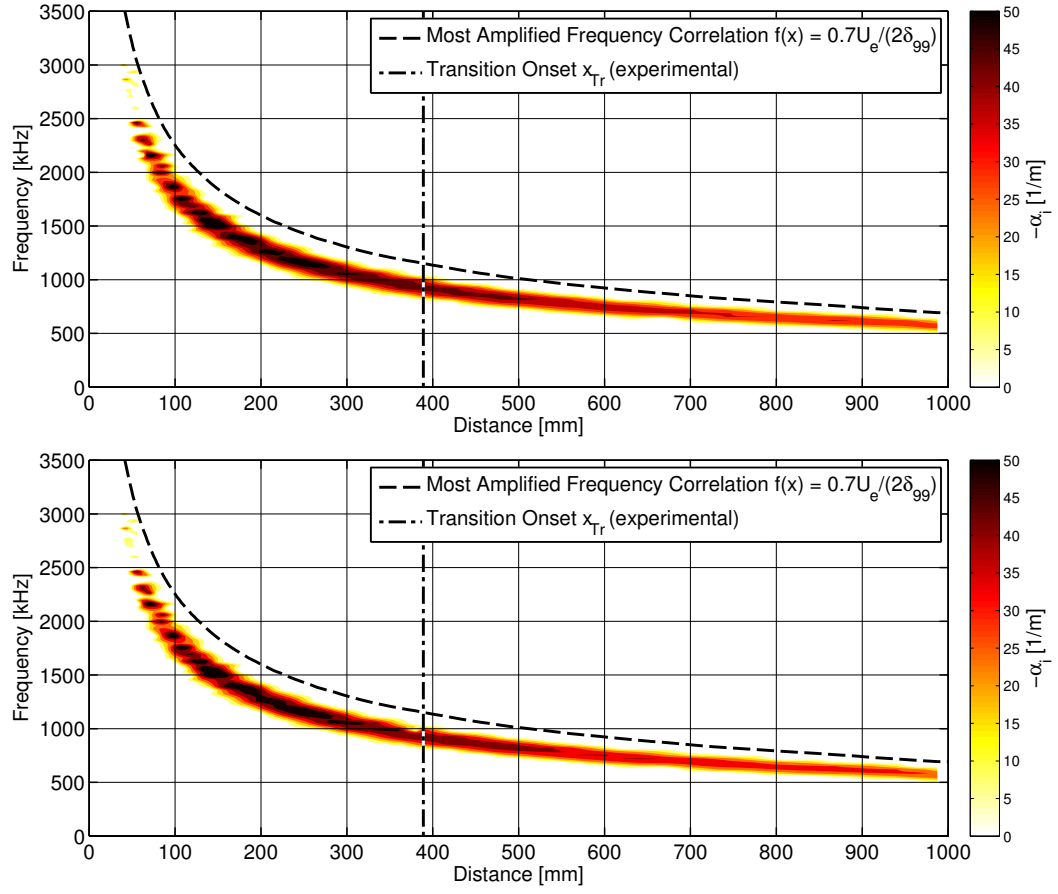
Figure B.18: Stability diagram with vibration (top) and no vibration/frozen (bottom) vibrational energy transfer, shot 2776. Dashed line indicates $0.7U_{\text{e}}/(2\delta_{99})$; dot-dashed line is the transition location.
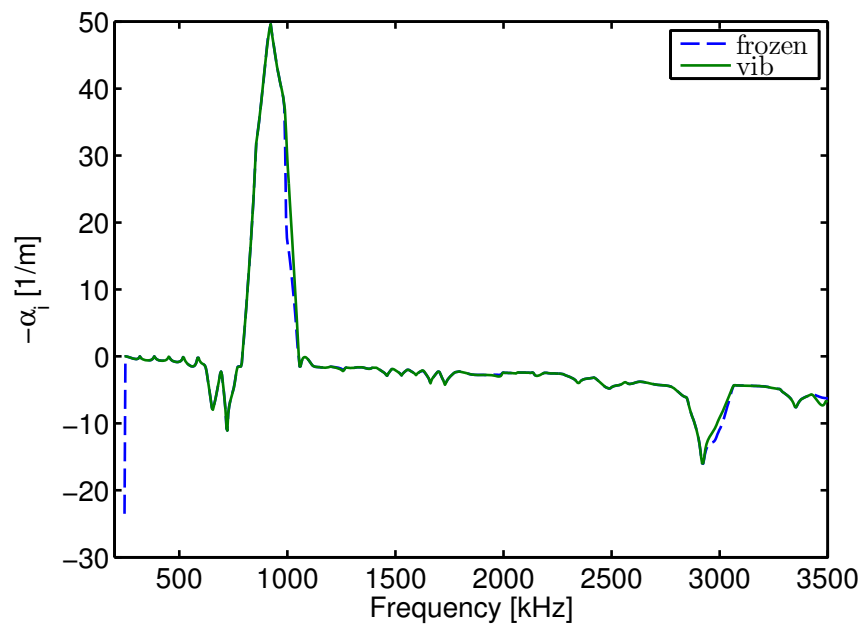
Figure B.19: Spatial amplification rate $-\alpha_i$ across frequencies calculated at x_{Tr}, with physical, frozen, and equilibrium vibrational energy transfer, shot 2776.
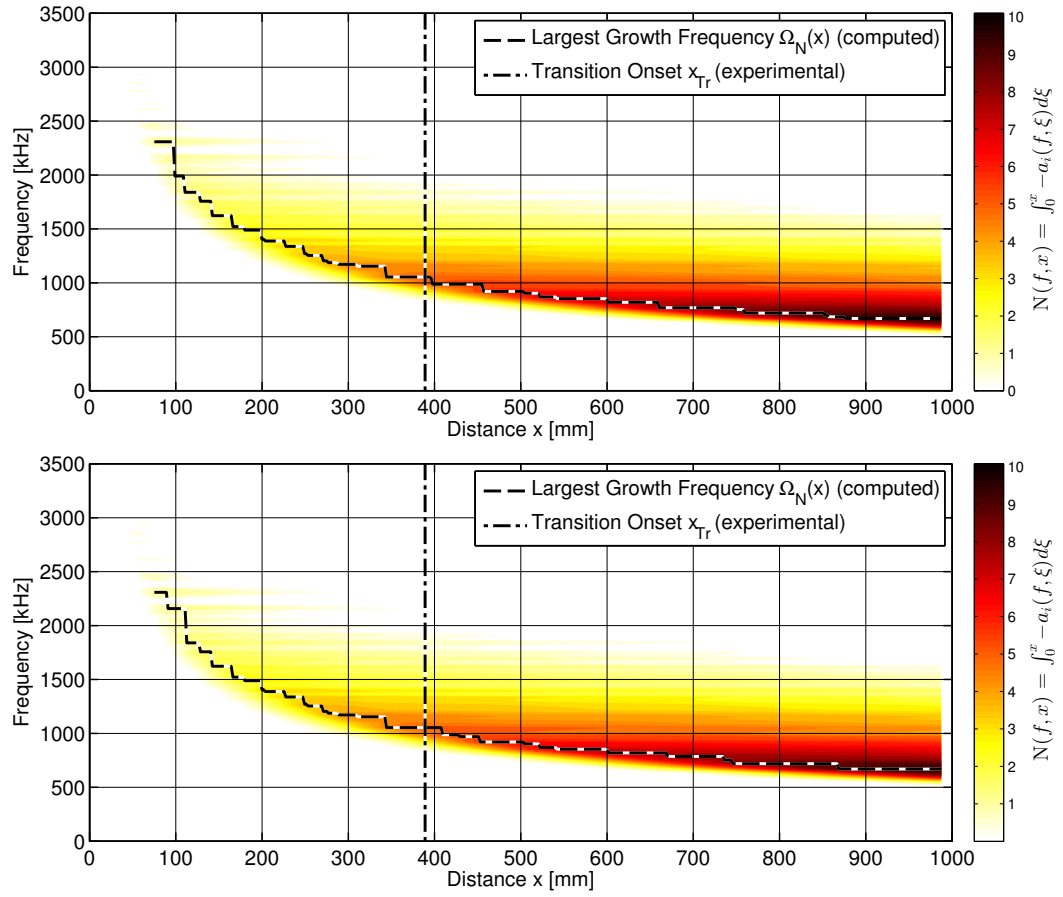
Figure B.20: Largest (integrated) growth frequency diagram with vibration (top) and no vibration/frozen (bottom) vibrational energy transfer, shot 2776. Dashed line indicates the computed frequency of largest growth at each x-location; dot-dashed line is the transition x-location.
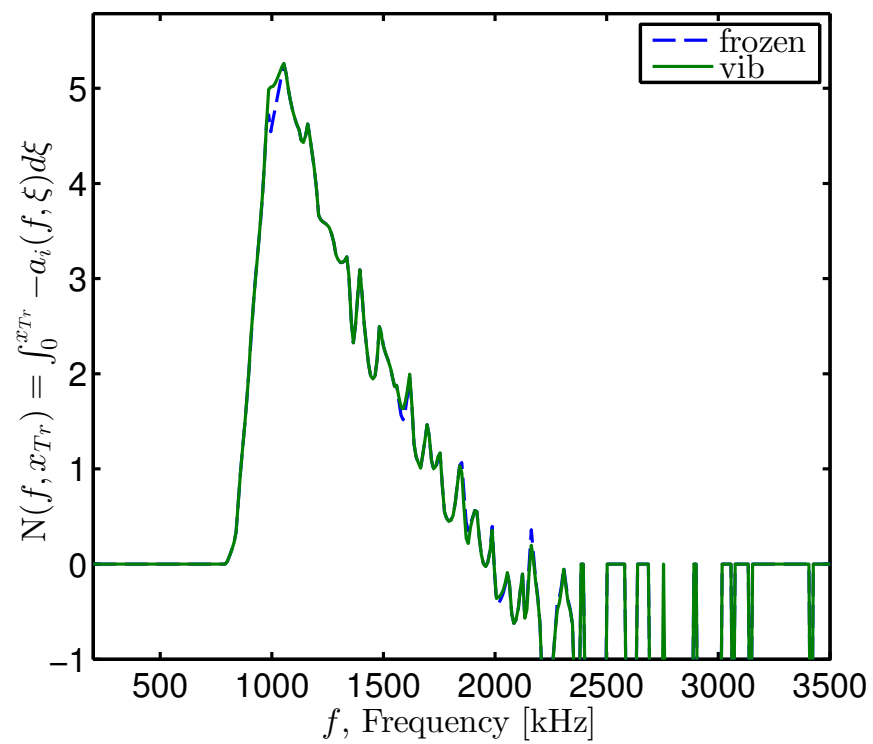
Figure B.21: $N(f, x) = \int_0^x -a_i(f, \xi)d\xi$ calculated at x_{Tr}, with physical, frozen, and equilibrium vibrational energy transfer, shot 2776.

B.4 Shot 2778

Experiment 2778 was performed in T5 on 16 November 2012.

B.4.1 Geometry

The test article was a 1 m 5-degree half-angle cone with a sharp tip. The initial shock tube composition was 100% N_2 by mass. Reservoir temperature, density, and composition are computed from the measured shock speed and shock tube initial conditions using a Cantera-based reflected-shock model adjusted for measured reservoir pressure.

B.4.2 Measured Quantities

| Measurement	Symbol	Value	Units
Shock Speed	U_s	3370	m/s
Shock Tube Fill Pressure	P_1	72.00	kPa
Reservoir Pressure	P_{res}	41.4	MPa

Table B.25: Measured quantities, shot 2778

B.4.3 Computed Reservoir Conditions

Computed Quantity	Symbol	Value	Units
Reservoir Temperature	T_{res}	7411	K
Reservoir Density	ρ_{res}	18.11	kg/m^3
Reservoir Enthalpy	h_{res}	10.7	MJ/kg

Table B.26: Computed reservoir conditions, shot 2778

Y_{N_2}	Y_{O_2}	Y_{CO_2}	Y_{NO}	Y_{CO}	Y_N	Y_O
9.61×10^{-1}	0	0	0	0	3.94×10^{-2}	0

Table B.27: Computed reservoir species mass fractions, shot 2778

B.4.4 Nozzle Position, Transition, and Chemistry Assumptions

These quantities are computed using the UMNAEM nozzle code with turbulent (unless otherwise stated) and laminar nozzle boundary layer assumptions, and the DPLR/STABL suite taking input freestream conditions at five different positions in the nozzle, and with and without the inclusion of chemical and vibrational rate processes. The results are compared to the results of a 1-D Cantera-based nozzle code with a Taylor-Maccoll shock and boundary layer similarity solution with conditions calculated from the nozzle exit, 100 cm downstream of the throat. The position 72 cm from the nozzle throat matches the best measurement of the experimental geometry, and the laminar-nozzle and no vibration/frozen cases are computed at this position.

	U_∞	T_∞	Tv_∞	M_∞	P_∞	ρ_∞	Unit Re_∞
	m/s	K	K	-	kPa	kg/m^3	1/m
1D 100 cm	4319	1493.0	1493.0	5.65	17.2	0.039	3.23×10^6
100 cm	4273	1083.2	3112.1	6.36	11.3	0.035	3.66×10^6
Lam 72 cm	4274	1080.6	3114.7	6.37	11.3	0.035	3.66×10^6
82 cm	4266	1113.3	3112.8	6.27	12.6	0.038	3.85×10^6
77 cm	4268	1104.3	3112.7	6.29	12.2	0.037	3.80×10^6
72 cm	4263	1123.6	3112.6	6.23	12.9	0.039	3.87×10^6
67 cm	4260	1139.5	3112.5	6.18	13.6	0.040	4.01×10^6
62 cm	4264	1121.7	3112.4	6.24	12.8	0.038	3.89×10^6

Table B.28: Computed freestream conditions, shot 2778

	Y_{N_2}	Y_{O_2}	Y_{CO_2}	Y_{NO}	Y_{CO}	Y_N	Y_O
1D 100 cm	9.96×10^{-1}	0	0	0	0	3.81×10^{-3}	0
100 cm	9.97×10^{-1}	0	0	0	0	2.91×10^{-3}	0
Lam 72 cm	9.97×10^{-1}	0	0	0	0	2.91×10^{-3}	0
82 cm	9.97×10^{-1}	0	0	0	0	2.91×10^{-3}	0
77 cm	9.97×10^{-1}	0	0	0	0	2.91×10^{-3}	0
72 cm	9.97×10^{-1}	0	0	0	0	2.91×10^{-3}	0
67 cm	9.97×10^{-1}	0	0	0	0	2.91×10^{-3}	0
62 cm	9.97×10^{-1}	0	0	0	0	2.91×10^{-3}	0

Table B.29: Computed freestream species mass fractions, shot 2778

	U_e	T_e	T_{v_e}	M_e	P_e	ρ_e	Unit Re_e
	m/s	K	K	-	kPa	kg/m^3	1/m
1D 100 cm	4278	1635.6	1635.6	5.34	25.2	0.052	3.99×10^6
100 cm	4203	1335.6	3081.7	5.63	18.2	0.046	3.89×10^6
Lam 72 cm	4203	1332.6	3084.5	5.64	18.1	0.046	3.89×10^6
82 cm	4196	1363.2	3082.1	5.57	19.9	0.049	4.12×10^6
77 cm	4198	1355.0	3082.1	5.59	19.4	0.048	4.05×10^6
72 cm	4193	1374.2	3081.3	5.54	20.5	0.050	4.30×10^6
67 cm	4191	1387.9	3081.2	5.51	21.4	0.052	4.30×10^6
62 cm	4194	1370.9	3081.6	5.55	20.4	0.050	4.16×10^6

Table B.30: Computed boundary layer edge conditions, shot 2778

	Y_{N_2}	Y_{O_2}	Y_{CO_2}	Y_{NO}	Y_{CO}	Y_N	Y_O
1D 100 cm	9.96×10^{-1}	0	0	0	0	3.81×10^{-3}	0
100 cm	1.00	0	0	0	0	0	0
Lam 72 cm	1.00	0	0	0	0	0	0
82 cm	1.00	0	0	0	0	0	0
77 cm	1.00	0	0	0	0	0	0
72 cm	1.00	0	0	0	0	0	0
67 cm	1.00	0	0	0	0	0	0
62 cm	1.00	0	0	0	0	0	0

Table B.31: Computed boundary layer edge species mass fractions, shot 2778

	x_{Tr}	Re_{Tr}	N_{Tr}	Ω_{Tr}	Ω_{NTr}	δ_{99Tr}	$(x/\delta_{99})_{Tr}$	$Re_{\delta_{99}Tr}$
	m	-	-	kHz	kHz	mm	-	-
100 cm	0.550	2.14×10^6	6.22	983	986	1.455	378	5661
Lam 72 cm	0.550	2.14×10^6	6.21	983	986	1.459	377	5671
82 cm	0.550	2.26×10^6	6.32	1050	1054	1.403	392	5772
77 cm	0.550	2.23×10^6	6.17	990	1054	1.423	387	5762
72 cm	0.550	2.41×10^6	6.60	1050	1054	1.387	397	5966
67 cm	0.550	2.36×10^6	6.73	1059	1054	1.364	403	5862
62 cm	0.550	2.29×10^6	6.55	1050	1054	1.395	394	5809
Frozen 72 cm	0.550	2.41×10^6	6.60	1050	1054	1.387	397	5966

Table B.32: Boundary layer stability characteristics at experimentally observed transition location, shot 2778
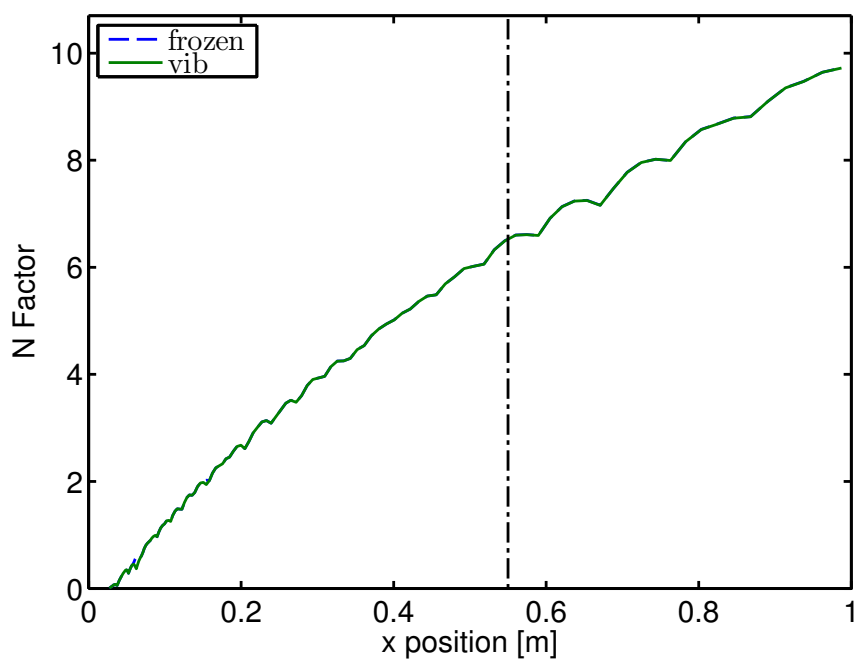
Figure B.22: N factor curves as a function of distance for realistic vibration and no vibration/frozen vibrational energy transfer, shot 2778. The dot-dashed line indicates the experimentally measured transition onset location. For the N_2 cases, the equilibrium case does not behave correctly due to the large amount of thermal nonequilibrium and is therefore omitted.
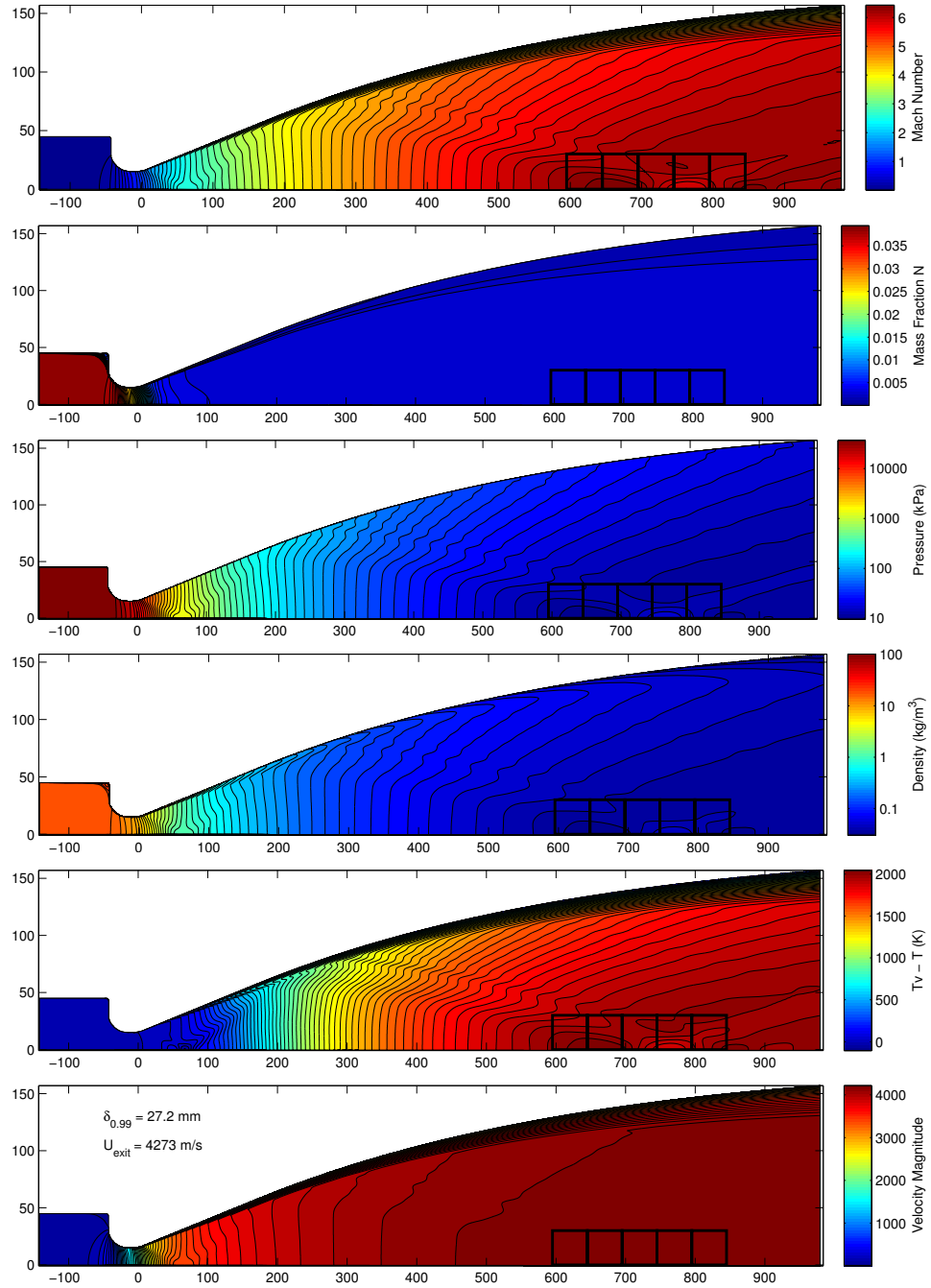
Figure B.23: Nozzle flow computed with the Spalart-Allmaras turbulence model for the wall, shot 2778. The black boxes highlight the averaged regions used to create STABL/DPLR inputs.

295
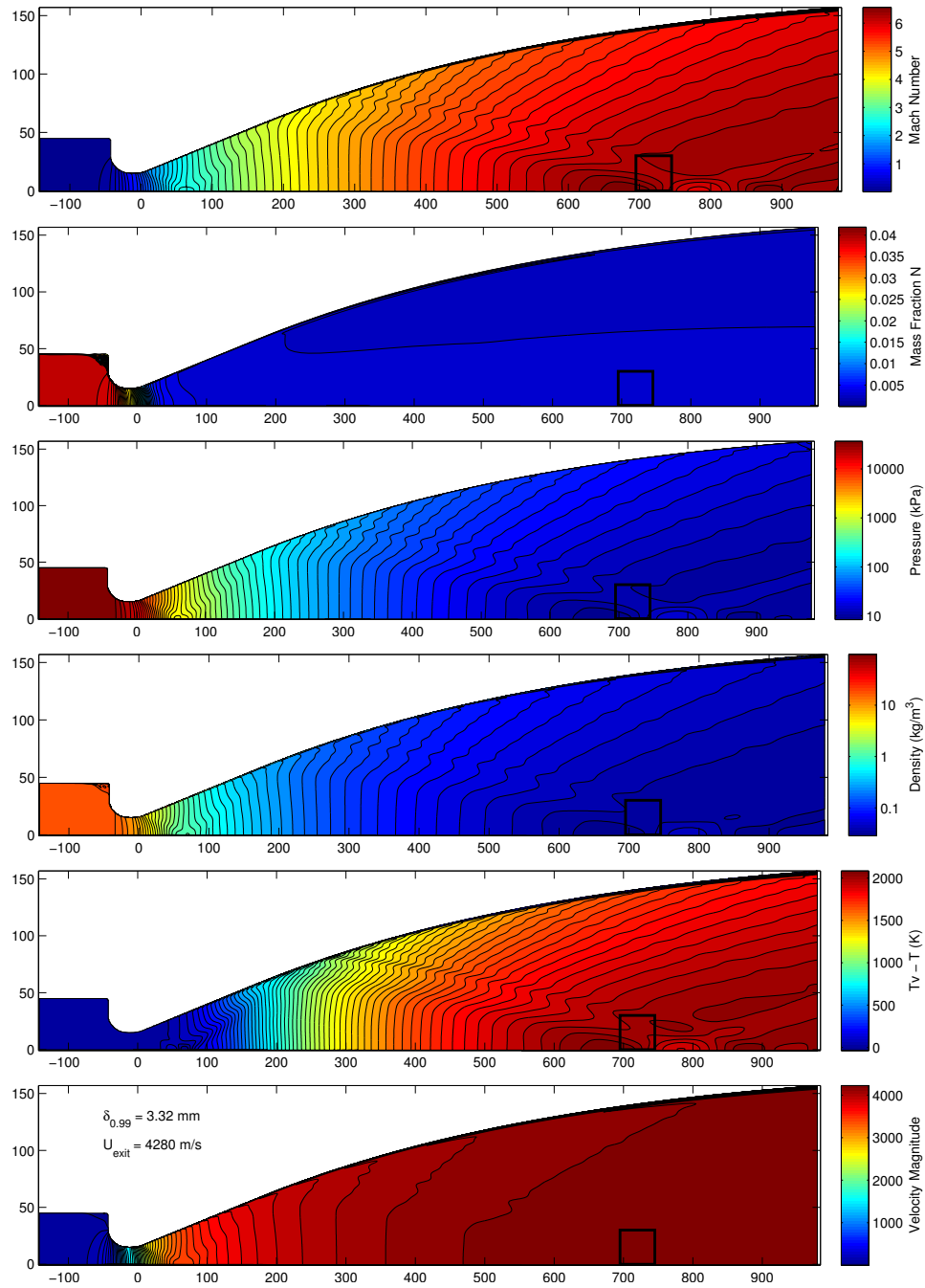
Figure B.24: Nozzle flow computed with laminar boundary layer growth for the wall, shot 2778. The black box highlights the averaged region used to create STABL/DPLR inputs.
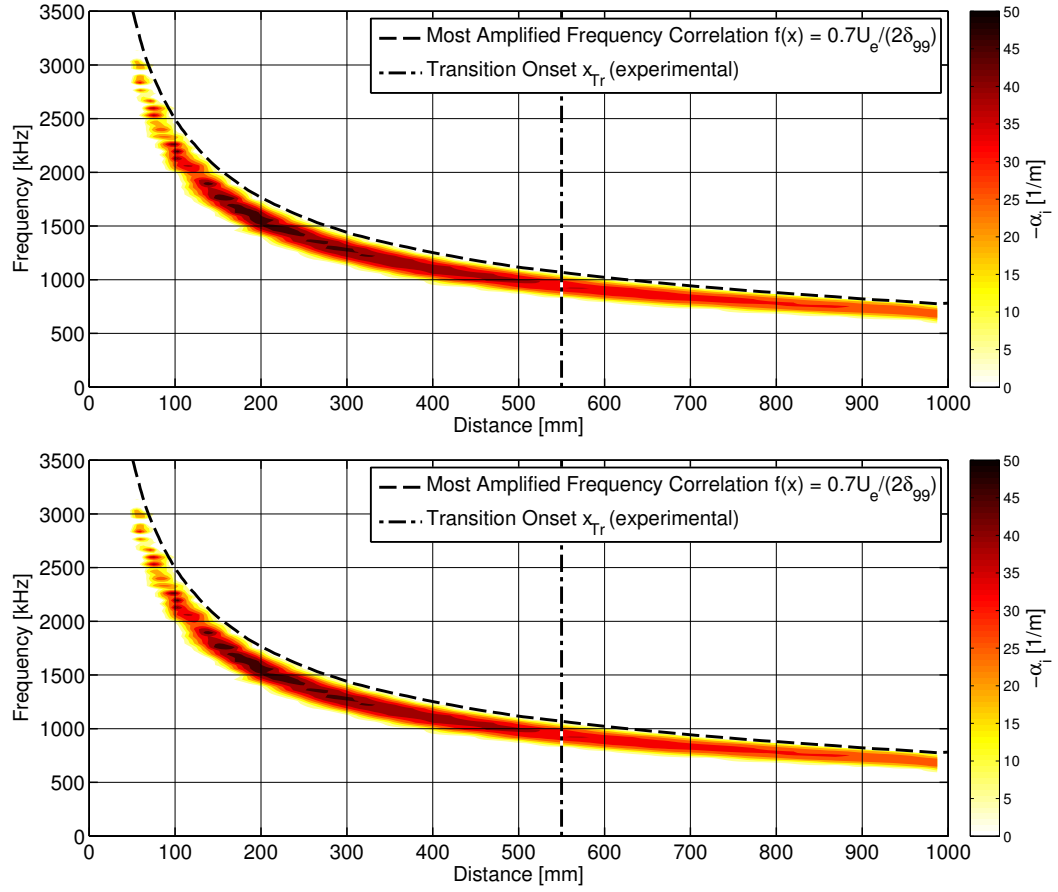
Figure B.25: Stability diagram with vibration (top) and no vibration/frozen (bottom) vibrational energy transfer, shot 2778. Dashed line indicates $0.7U_{\mathrm{e}}/(2\delta_{99})$; dot-dashed line is the transition location.
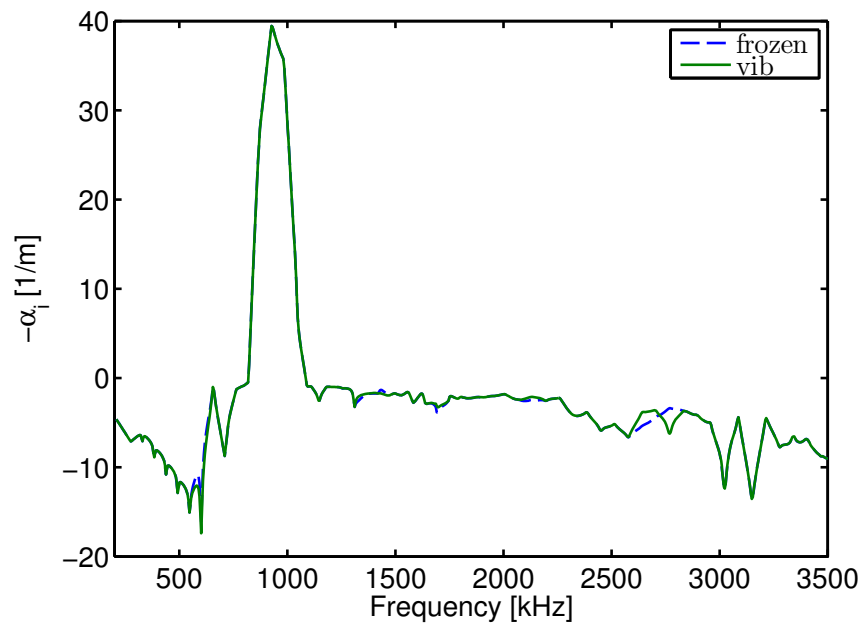
Figure B.26: Spatial amplification rate $-\alpha_i$ across frequencies calculated at x_{Tr}, with vibration and no vibration/frozen vibrational energy transfer, shot 2778.
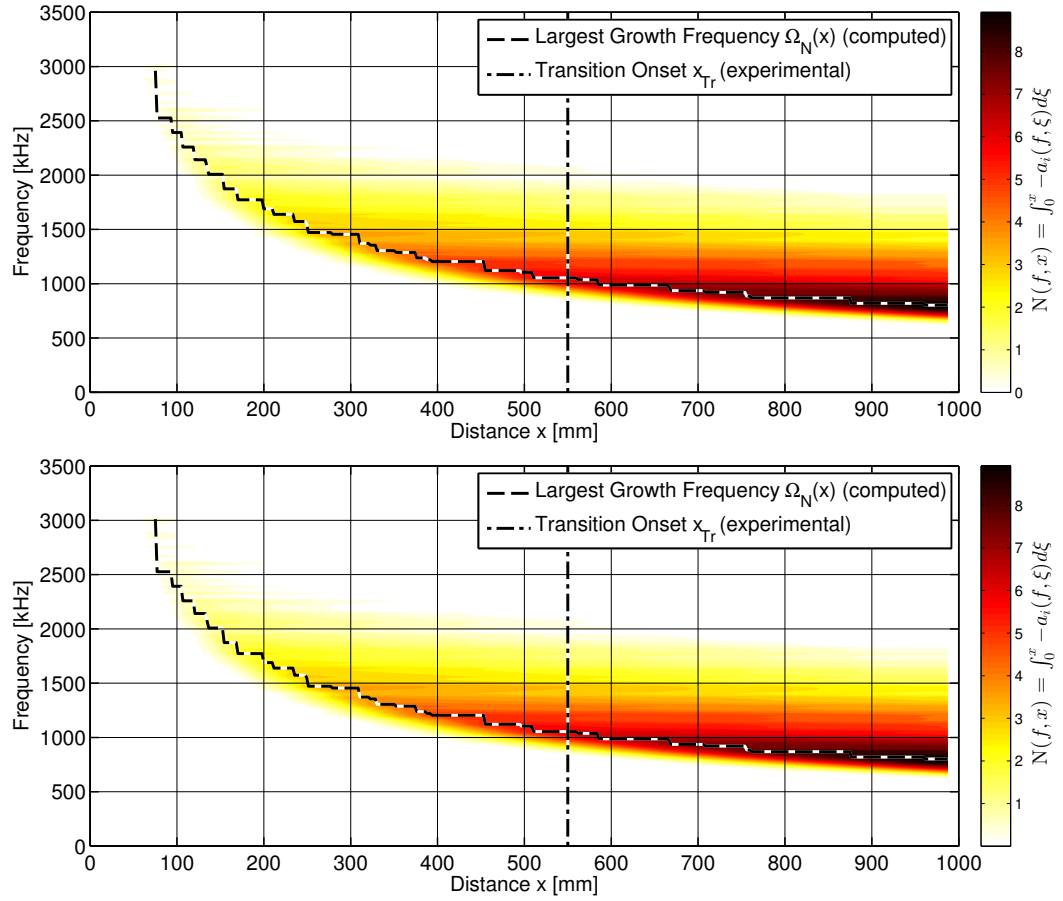
Figure B.27: Largest (integrated) growth frequency diagram with vibration (top) and no vibration/frozen (bottom) vibrational energy transfer, shot 2778. Dashed line indicates the computed frequency of largest growth at each x-location; dot-dashed line is the transition x-location.
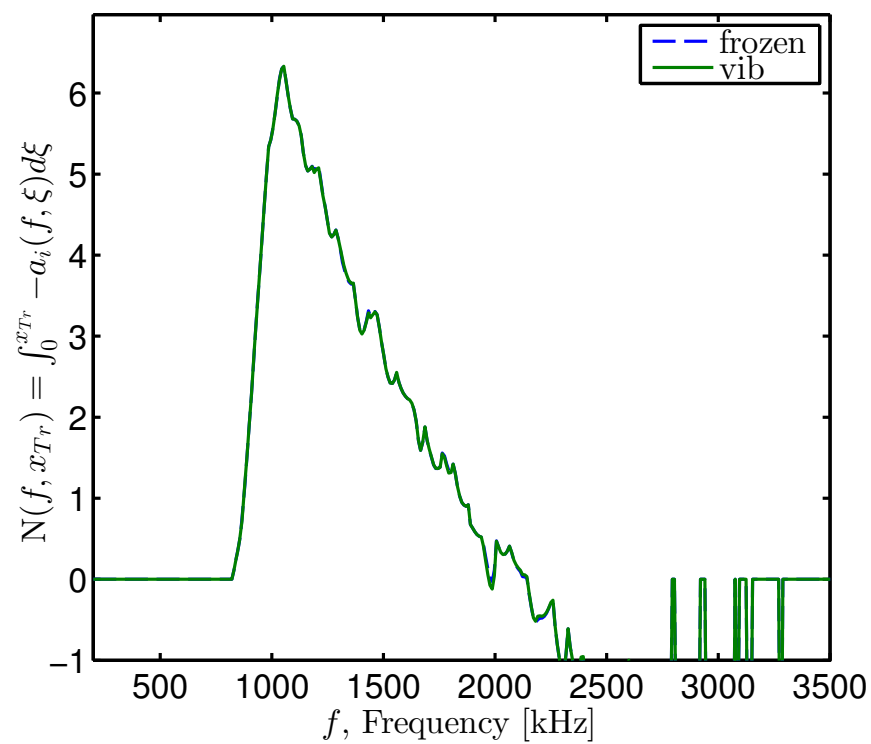
Figure B.28: $N(f, x) = \int_0^x -a_i(f, \xi)d\xi$ calculated at x_{Tr}, with vibration and no vibration/frozen vibrational energy transfer, shot 2778.

B.5   Shot 2793

Experiment 2793 was performed in T5 on 24 January 2013.

B.5.1   Geometry

The test article was a 1 m 5-degree half-angle cone with a sharp tip. The initial shock tube composition was 100% CO_2 by mass. Reservoir temperature, density, and composition are computed from the measured shock speed and shock tube initial conditions using a Cantera-based reflected-shock model adjusted for measured reservoir pressure.

B.5.2   Measured Quantities

Measurement	Symbol	Value	Units
Shock Speed	U_{s}	2220	m/s
Shock Tube Fill Pressure	P_1	50.00	kPa
Reservoir Pressure	P_{res}	22.7	MPa

Table B.33: Measured quantities, shot 2793

B.5.3   Computed Reservoir Conditions

Computed Quantity	Symbol	Value	Units
Reservoir Temperature	T_{res}	3179	K
Reservoir Density	ρ_{res}	35.28	kg/m^3
Reservoir Enthalpy	h_{res}	4.61	MJ/kg

Table B.34: Computed reservoir conditions, shot 2793

$Y_{\mathrm{N_2}}$	$Y_{\mathrm{O_2}}$	$Y_{\mathrm{CO_2}}$	Y_{NO}	Y_{CO}	Y_{N}	Y_{O}
0	4.94×10^{-2}	8.60×10^{-1}	0	8.88×10^{-2}	0	1.32×10^{-3}

Table B.35: Computed reservoir species mass fractions, shot 2793

B.5.4 Nozzle Position, Transition, and Chemistry Assumptions

These quantities are computed using the UMNAEM nozzle code with turbulent (unless otherwise stated) and laminar nozzle boundary layer assumptions, and the DPLR/STABL suite taking input freestream conditions at five different positions in the nozzle, and with and without the inclusion of chemical and vibrational rate processes. The results are compared to the results of a 1-D Cantera-based nozzle code with a Taylor-Maccoll shock and boundary layer similarity solution with conditions calculated from the nozzle exit, 100 cm downstream of the throat. The position 72 cm from the nozzle throat matches the best measurement of the experimental geometry, and the laminar-nozzle, frozen, and equilibrium cases are computed at this position.

| | U_∞ | T_∞ | Tv_∞ | M_∞ | P_∞ | ρ_∞ | Unit Re_∞ |
	m/s	K	K	-	kPa	kg/m^3	1/m
1D 100 cm	2449	1141.0	1141.0	4.71	15.4	0.068	4.18×10^6
100 cm	2457	1131.4	1131.3	4.38	15.1	0.067	4.46×10^6
Lam 72 cm	2443	1157.9	1159.2	4.31	17.6	0.076	4.96×10^6
82 cm	2423	1195.6	1197.3	4.20	21.5	0.091	5.70×10^6
77 cm	2432	1177.4	1179.9	4.25	19.6	0.084	5.34×10^6
72 cm	2440	1163.8	1164.8	4.29	18.1	0.078	4.78×10^6
67 cm	2444	1156.3	1157.8	4.31	17.4	0.076	4.93×10^6
62 cm	2449	1146.9	1148.1	4.34	16.5	0.073	4.75×10^6

Table B.36: Computed freestream conditions, shot 2793

	Y_{N_2}	Y_{O_2}	Y_{CO_2}	Y_{NO}	Y_{CO}	Y_N	Y_O
1D 100 cm	0	3.88×10^{-2}	8.93×10^{-1}	0	6.80×10^{-2}	0	4.87×10^{-5}
100 cm	0	3.68×10^{-2}	8.99×10^{-1}	0	6.44×10^{-2}	0	1.81×10^{-5}
Lam 72 cm	0	3.68×10^{-2}	8.99×10^{-1}	0	6.45×10^{-2}	0	1.83×10^{-5}
82 cm	0	3.68×10^{-2}	8.99×10^{-1}	0	6.45×10^{-2}	0	1.84×10^{-5}
77 cm	0	3.68×10^{-2}	8.99×10^{-1}	0	6.45×10^{-2}	0	1.83×10^{-5}
72 cm	0	3.68×10^{-2}	8.99×10^{-1}	0	6.45×10^{-2}	0	1.83×10^{-5}
67 cm	0	3.68×10^{-2}	8.99×10^{-1}	0	6.45×10^{-2}	0	1.82×10^{-5}
62 cm	0	3.68×10^{-2}	8.99×10^{-1}	0	6.45×10^{-2}	0	1.82×10^{-5}

Table B.37: Computed freestream species mass fractions, shot 2793

	U_e	T_e	Tv_e	M_e	P_e	ρ_e	Unit Re_e
	m/s	K	K	-	kPa	kg/m^3	1/m
1D 100 cm	2423	1191.1	1191.1	4.57	20.2	0.085	5.09×10^6
100 cm	2418	1192.7	1192.7	4.20	19.8	0.084	5.24×10^6
Lam 72 cm	2404	1218.8	1218.8	4.13	22.9	0.095	5.79×10^6
82 cm	2385	1255.2	1255.2	4.04	27.9	0.112	6.63×10^6
77 cm	2394	1238.1	1238.1	4.08	25.4	0.104	6.23×10^6
72 cm	2401	1224.3	1224.3	4.12	23.6	0.097	5.70×10^6
67 cm	2405	1217.6	1217.5	4.13	22.7	0.094	5.76×10^6
62 cm	2410	1208.2	1208.2	4.16	21.6	0.090	5.56×10^6

Table B.38: Computed boundary layer edge conditions, shot 2793

	Y_{N_2}	Y_{O_2}	Y_{CO_2}	Y_{NO}	Y_{CO}	Y_N	Y_O
1D 100 cm	0	3.88×10^{-2}	8.93×10^{-1}	0	6.80×10^{-2}	0	4.87×10^{-5}
100 cm	0	3.68×10^{-2}	8.99×10^{-1}	0	6.44×10^{-2}	0	1.71×10^{-5}
Lam 72 cm	0	3.68×10^{-2}	8.99×10^{-1}	0	6.45×10^{-2}	0	1.70×10^{-5}
82 cm	0	3.68×10^{-2}	8.99×10^{-1}	0	6.45×10^{-2}	0	1.67×10^{-5}
77 cm	0	3.68×10^{-2}	8.99×10^{-1}	0	6.45×10^{-2}	0	1.68×10^{-5}
72 cm	0	3.68×10^{-2}	8.99×10^{-1}	0	6.45×10^{-2}	0	1.69×10^{-5}
67 cm	0	3.68×10^{-2}	8.99×10^{-1}	0	6.45×10^{-2}	0	1.69×10^{-5}
62 cm	0	3.68×10^{-2}	8.99×10^{-1}	0	6.45×10^{-2}	0	1.70×10^{-5}

Table B.39: Computed boundary layer edge species mass fractions, shot 2793

	x_{Tr}	Re_{Tr}	N_{Tr}	Ω_{Tr}	Ω_{NTr}	δ_{99Tr}	$(x/\delta_{99})_{Tr}$	$Re_{\delta_{99}Tr}$
	m	-	-	kHz	kHz	mm	-	-
100 cm	0.601	3.15×10^6	9.14	1093	1093	1.001	601	5240
Lam 72 cm	0.601	3.48×10^6	9.33	1158	1180	0.945	636	5473
82 cm	0.601	3.99×10^6	9.73	1308	1307	0.874	688	5794
77 cm	0.601	3.74×10^6	9.59	1233	1248	0.907	663	5648
72 cm	0.601	3.45×10^6	9.42	1233	1180	0.934	644	5325
67 cm	0.601	3.46×10^6	9.37	1162	1180	0.947	634	5454
62 cm	0.601	3.34×10^6	9.31	1158	1180	0.967	622	5376
Frozen 72 cm	0.601	3.45×10^6	14.81	1273	1248	0.934	644	5325
Equil. 72 cm	0.601	3.45×10^6	13.18	1158	1122	0.934	644	5325

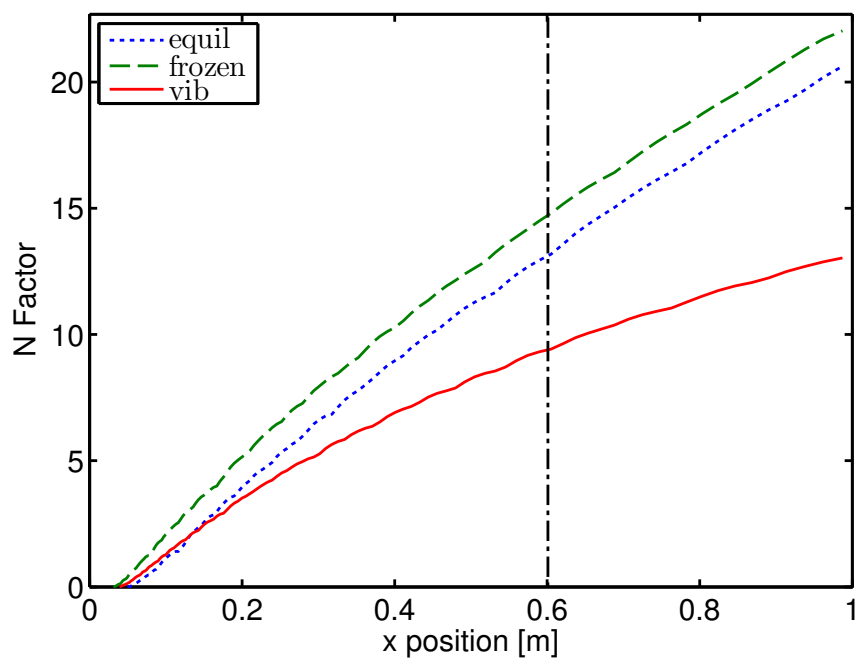Table B.40: Boundary layer stability characteristics at experimentally observed transition location, shot 2793

Figure B.29: N factor curves as a function of distance for realistic, frozen, and equilibrium vibrational energy transfer, shot 2793. The dot-dashed line indicates the experimentally measured transition onset location.
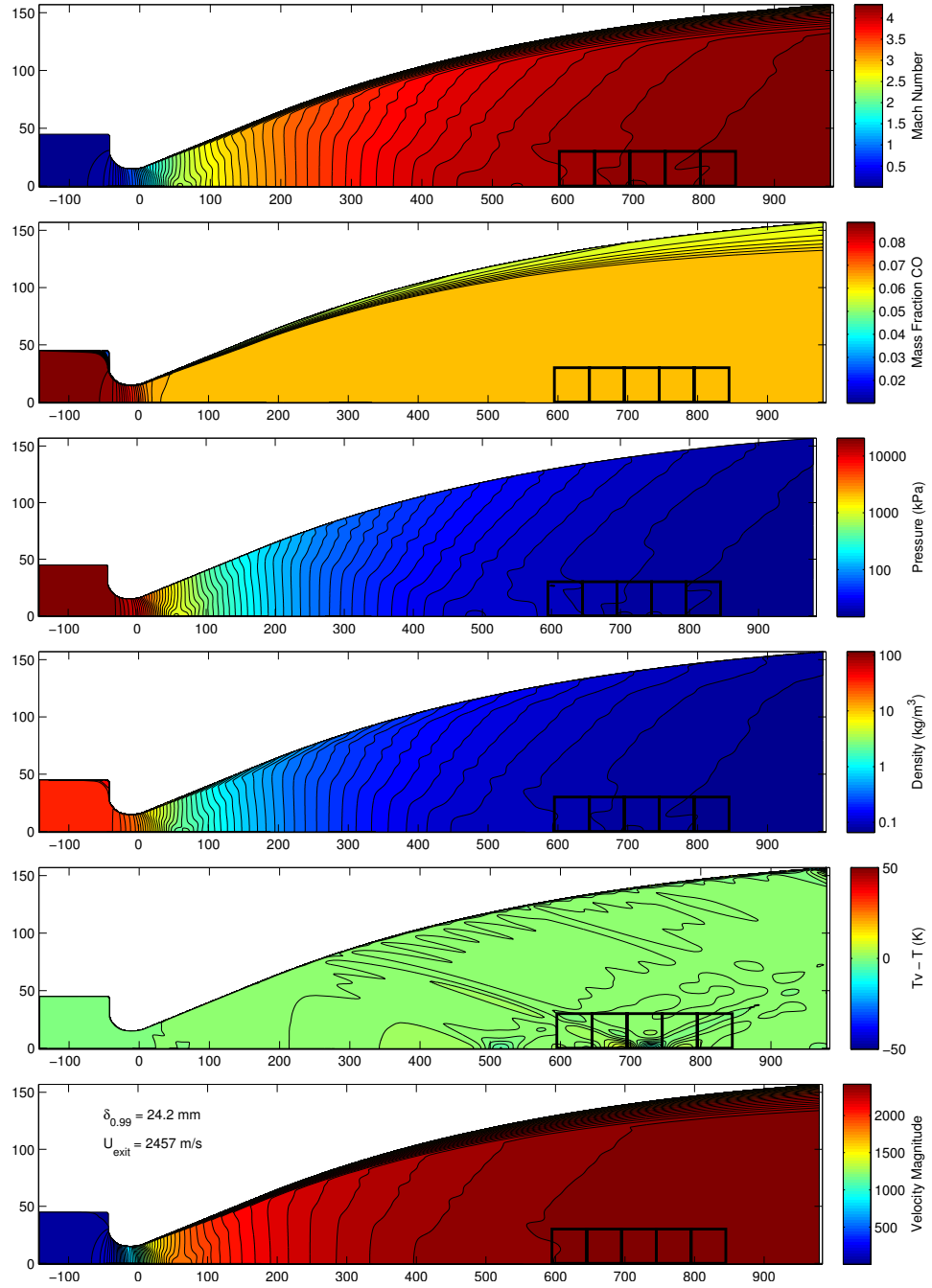
Figure B.30: Nozzle flow computed with the Spalart-Allmaras turbulence model for the wall, shot 2793. The black boxes highlight the averaged regions used to create STABL/DPLR inputs.
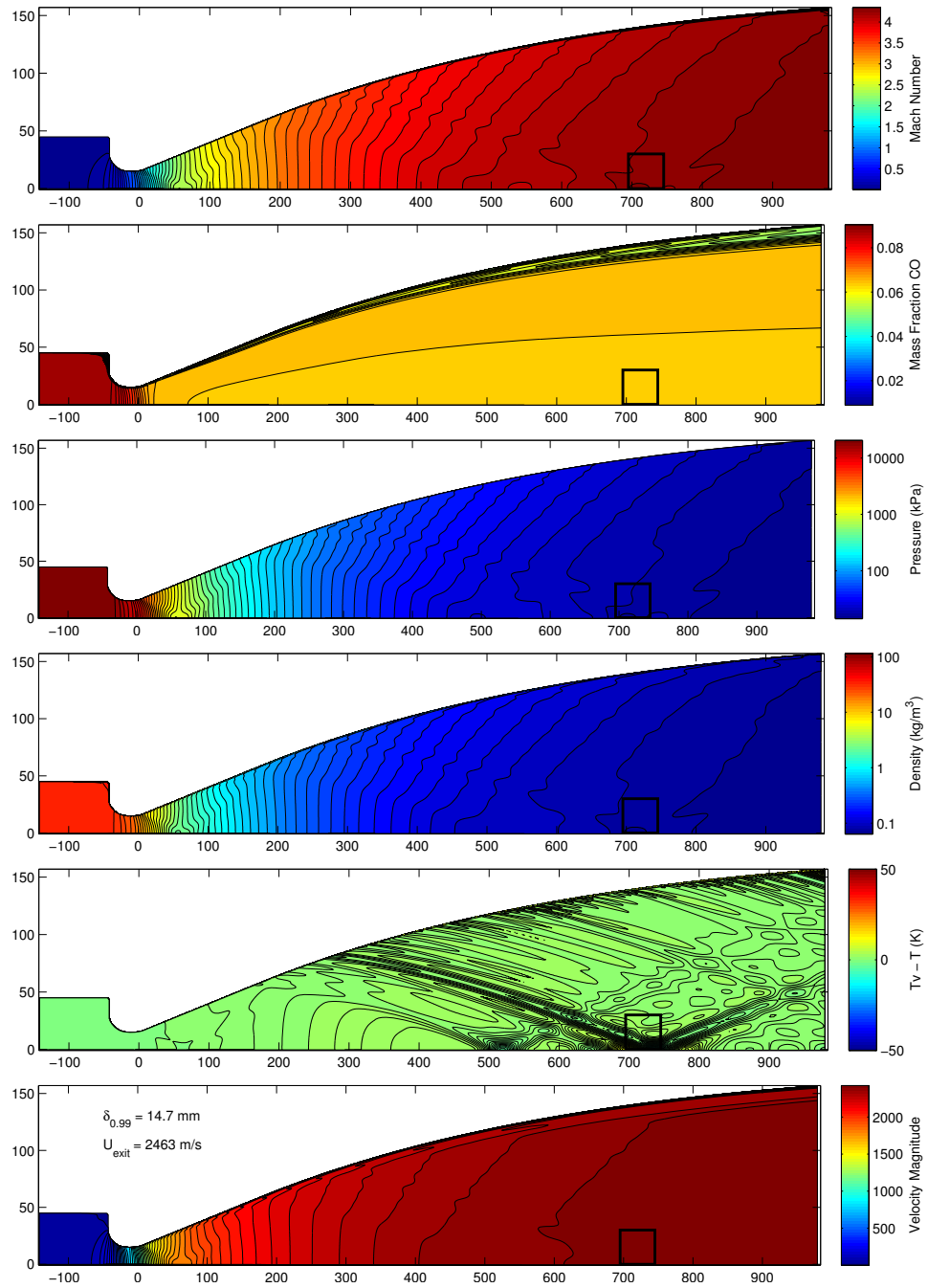
Figure B.31: Nozzle flow computed with laminar boundary layer growth for the wall, shot 2793. The black box highlights the averaged region used to create STABL/DPLR inputs.

Figure B.32: Stability diagram with physical (top), frozen (middle), and equilibrium (bottom) vibrational energy transfer, shot 2793. Dashed line indicates $0.7U_{\mathrm{e}}/(2\delta_{99})$; dot-dashed line is the transition location.
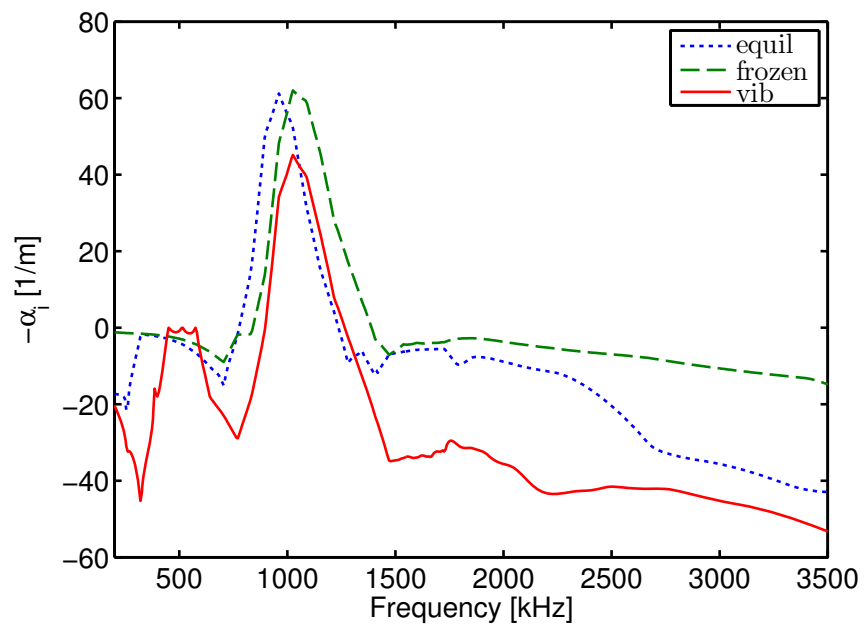
Figure B.33: Spatial amplification rate $-\alpha_i$ across frequencies calculated at x_{Tr}, with physical, frozen, and equilibrium vibrational energy transfer, shot 2793.

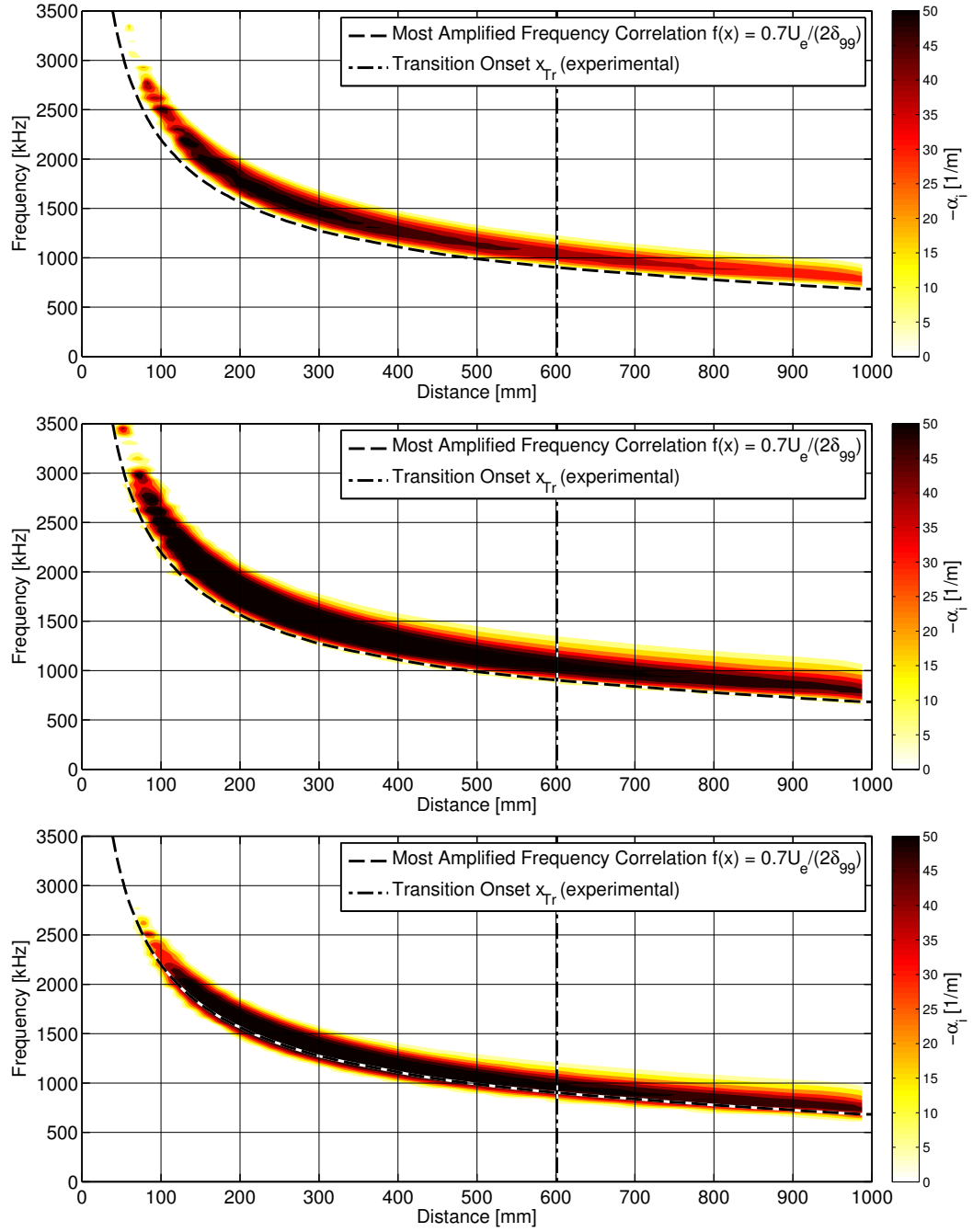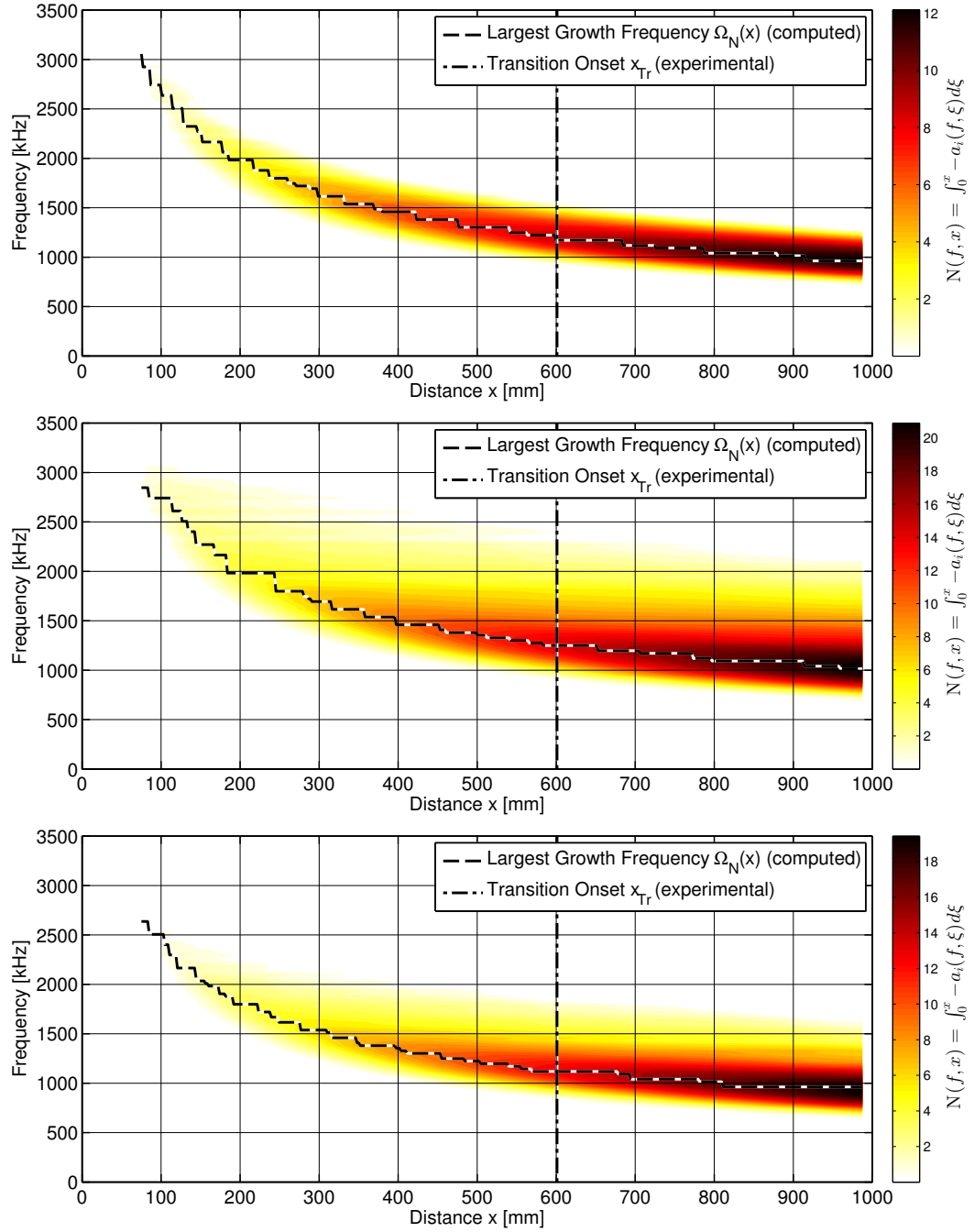Figure B.34: Largest (integrated) growth frequency diagram with physical (top), frozen (middle), and equilibrium (bottom) vibrational energy transfer, shot 2793. Dashed line indicates the computed frequency of largest growth at each x-location; dot-dashed line is the transition x-location.

Figure B.35: $N(f, x) = \int_0^x -a_i(f, \xi)d\xi$ calculated at x_{Tr}, with physical, frozen, and equilibrium vibrational energy transfer, shot 2793.

B.6   Shot 2808

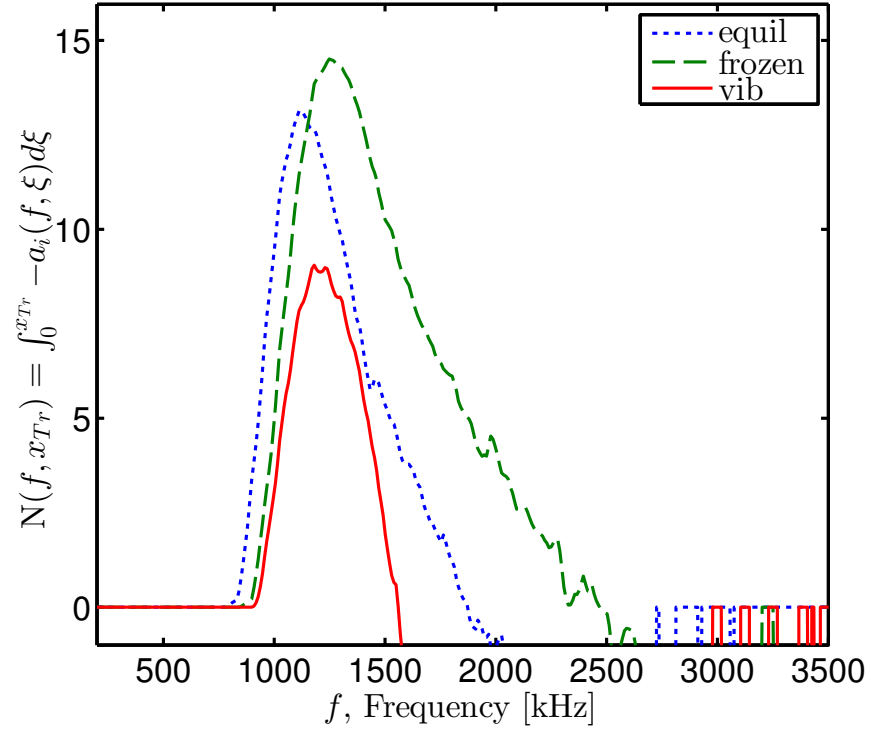Experiment 2808 was performed in T5 on 7 June 2013.

B.6.1   Geometry

The test article was a 1 m 5-degree half-angle cone with a sharp tip. The initial shock tube composition was 100% CO_2 by mass. Reservoir temperature, density, and composition are computed from the measured shock speed and shock tube initial conditions using a Cantera-based reflected-shock model adjusted for measured reservoir pressure.

B.6.2   Measured Quantities

Measurement	Symbol	Value	Units
Shock Speed	U_s	2460	m/s
Shock Tube Fill Pressure	P_1	99.55	kPa
Reservoir Pressure	P_{res}	54.5	MPa

Table B.41: Measured quantities, shot 2808

B.6.3   Computed Reservoir Conditions

Computed Quantity	Symbol	Value	Units
Reservoir Temperature	T_{res}	3567	K
Reservoir Density	ρ_{res}	72.96	kg/m^3
Reservoir Enthalpy	h_{res}	5.62	MJ/kg

Table B.42: Computed reservoir conditions, shot 2808

Y_{N_2}	Y_{O_2}	Y_{CO_2}	Y_{NO}	Y_{CO}	Y_N	Y_O
0	7.35×10^{-2}	7.89×10^{-1}	0	1.34×10^{-1}	0	3.05×10^{-3}

Table B.43: Computed reservoir species mass fractions, shot 2808

B.6.4 Nozzle Position, Transition, and Chemistry Assumptions

These quantities are computed using the UMNAEM nozzle code with turbulent (unless otherwise stated) and laminar nozzle boundary layer assumptions, and the DPLR/STABL suite taking input freestream conditions at five different positions in the nozzle, and with and without the inclusion of chemical and vibrational rate processes. The results are compared to the results of a 1-D Cantera-based nozzle code with a Taylor-Maccoll shock and boundary layer similarity solution with conditions calculated from the nozzle exit, 100 cm downstream of the throat. The position 72 cm from the nozzle throat matches the best measurement of the experimental geometry, and the laminar-nozzle, frozen, and equilibrium cases are computed at this position.

	U_∞	T_∞	Tv_∞	M_∞	P_∞	ρ_∞	Unit Re$_\infty$
	m/s	K	K	-	kPa	kg/m^3	1/m
1D 100 cm	2665	1382.0	1382.0	4.65	38.1	0.137	8.42×10^6
100 cm	2685	1363.8	1363.6	4.34	38.3	0.140	8.79×10^6
Lam 72 cm	2672	1395.8	1396.1	4.27	44.5	0.159	9.76×10^6
82 cm	2649	1439.1	1439.8	4.17	54.2	0.188	1.12×10^7
77 cm	2659	1418.3	1419.3	4.21	49.4	0.174	1.05×10^7
72 cm	2667	1403.1	1403.3	4.25	46.0	0.163	9.98×10^6
67 cm	2671	1394.0	1394.6	4.27	44.1	0.158	9.70×10^6
62 cm	2677	1382.3	1382.7	4.30	41.8	0.151	9.34×10^6

Table B.44: Computed freestream conditions, shot 2808

	Y_{N_2}	Y_{O_2}	Y_{CO_2}	Y_{NO}	Y_{CO}	Y_N	Y_O
1D 100 cm	0	4.66×10^{-2}	8.72×10^{-1}	0	8.16×10^{-2}	0	5.09×10^{-5}
100 cm	0	4.45×10^{-2}	8.77×10^{-1}	0	7.80×10^{-2}	0	3.16×10^{-5}
Lam 72 cm	0	4.45×10^{-2}	8.78×10^{-1}	0	7.79×10^{-2}	0	3.37×10^{-5}
82 cm	0	4.45×10^{-2}	8.78×10^{-1}	0	7.79×10^{-2}	0	3.45×10^{-5}
77 cm	0	4.45×10^{-2}	8.78×10^{-1}	0	7.79×10^{-2}	0	3.39×10^{-5}
72 cm	0	4.45×10^{-2}	8.78×10^{-1}	0	7.79×10^{-2}	0	3.35×10^{-5}
67 cm	0	4.45×10^{-2}	8.78×10^{-1}	0	7.79×10^{-2}	0	3.31×10^{-5}
62 cm	0	4.45×10^{-2}	8.78×10^{-1}	0	7.80×10^{-2}	0	3.27×10^{-5}

Table B.45: Computed freestream species mass fractions, shot 2808

	U_e	T_e	T_{v_e}	M_e	P_e	ρ_e	Unit Re_e
	m/s	K	K	-	kPa	kg/m^3	1/m
1D 100 cm	2637	1439.7	1439.7	4.51	49.6	0.171	1.01×10^7
100 cm	2643	1433.9	1433.9	4.17	50.1	0.174	1.03×10^7
Lam 72 cm	2630	1464.9	1464.9	4.10	57.9	0.197	1.14×10^7
82 cm	2607	1506.9	1506.9	4.01	69.9	0.231	1.30×10^7
77 cm	2618	1486.8	1486.8	4.05	64.0	0.215	1.22×10^7
72 cm	2625	1471.8	1471.7	4.08	59.7	0.202	1.17×10^7
67 cm	2629	1463.3	1463.3	4.10	57.4	0.196	1.13×10^7
62 cm	2635	1451.9	1451.9	4.13	54.5	0.187	1.09×10^7

Table B.46: Computed boundary layer edge conditions, shot 2808

	Y_{N_2}	Y_{O_2}	Y_{CO_2}	Y_{NO}	Y_{CO}	Y_N	Y_O
1D 100 cm	0	4.66×10^{-2}	8.72×10^{-1}	0	8.16×10^{-2}	0	5.09×10^{-5}
100 cm	0	4.45×10^{-2}	8.77×10^{-1}	0	7.80×10^{-2}	0	2.53×10^{-5}
Lam 72 cm	0	4.45×10^{-2}	8.78×10^{-1}	0	7.79×10^{-2}	0	2.56×10^{-5}
82 cm	0	4.45×10^{-2}	8.78×10^{-1}	0	7.79×10^{-2}	0	2.40×10^{-5}
77 cm	0	4.45×10^{-2}	8.78×10^{-1}	0	7.79×10^{-2}	0	2.47×10^{-5}
72 cm	0	4.45×10^{-2}	8.78×10^{-1}	0	7.79×10^{-2}	0	2.51×10^{-5}
67 cm	0	4.45×10^{-2}	8.78×10^{-1}	0	7.79×10^{-2}	0	2.52×10^{-5}
62 cm	0	4.45×10^{-2}	8.78×10^{-1}	0	7.79×10^{-2}	0	2.54×10^{-5}

Table B.47: Computed boundary layer edge species mass fractions, shot 2808

	x_{Tr}	Re_{Tr}	N_{Tr}	Ω_{Tr}	Ω_{NTr}	δ_{99Tr}	$(x/\delta_{99})_{Tr}$	$Re_{\delta_{99}Tr}$
	m	-	-	kHz	kHz	mm	-	-
100 cm	0.532	5.48×10^6	11.03	1833	1909	0.665	800	6854
Lam 72 cm	0.532	6.07×10^6	11.02	1984	2026	0.629	845	7180
82 cm	0.532	6.92×10^6	10.59	2188	2191	0.584	912	7588
77 cm	0.532	6.50×10^6	10.82	2104	2104	0.608	875	7430
72 cm	0.532	6.41×10^6	10.91	1984	2055	0.620	858	7281
67 cm	0.532	6.03×10^6	11.02	1984	2026	0.633	840	7176
62 cm	0.532	5.81×10^6	11.00	1908	1909	0.646	824	7059
Frozen 72 cm	0.532	6.41×10^6	24.88	2243	2279	0.620	858	7281
Equil. 72 cm	0.532	6.41×10^6	23.76	2059	2133	0.620	858	7281

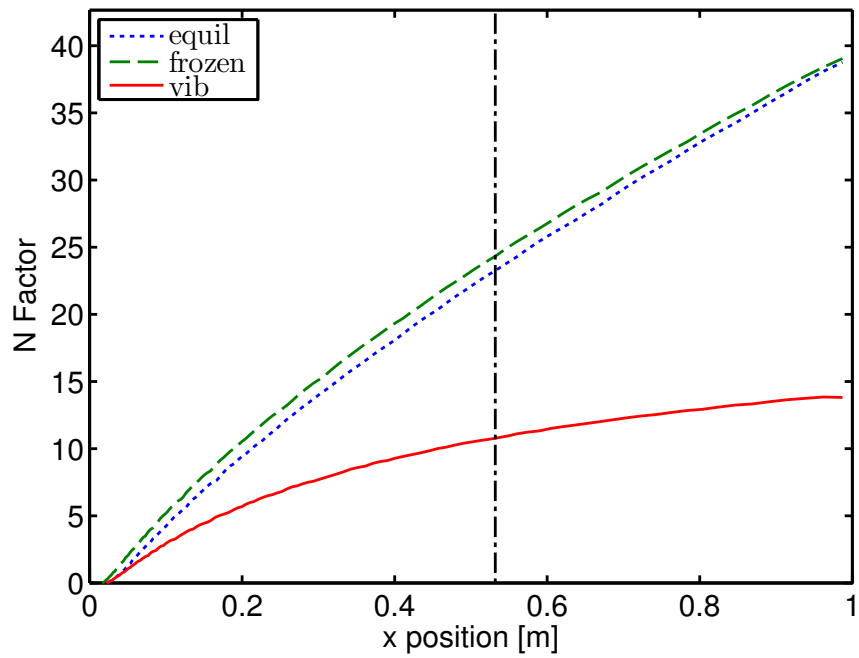Table B.48: Boundary layer stability characteristics at experimentally observed transition location, shot 2808

Figure B.36: N factor curves as a function of distance for realistic, frozen, and equilibrium vibrational energy transfer, shot 2808. The dot-dashed line indicates the experimentally measured transition onset location.
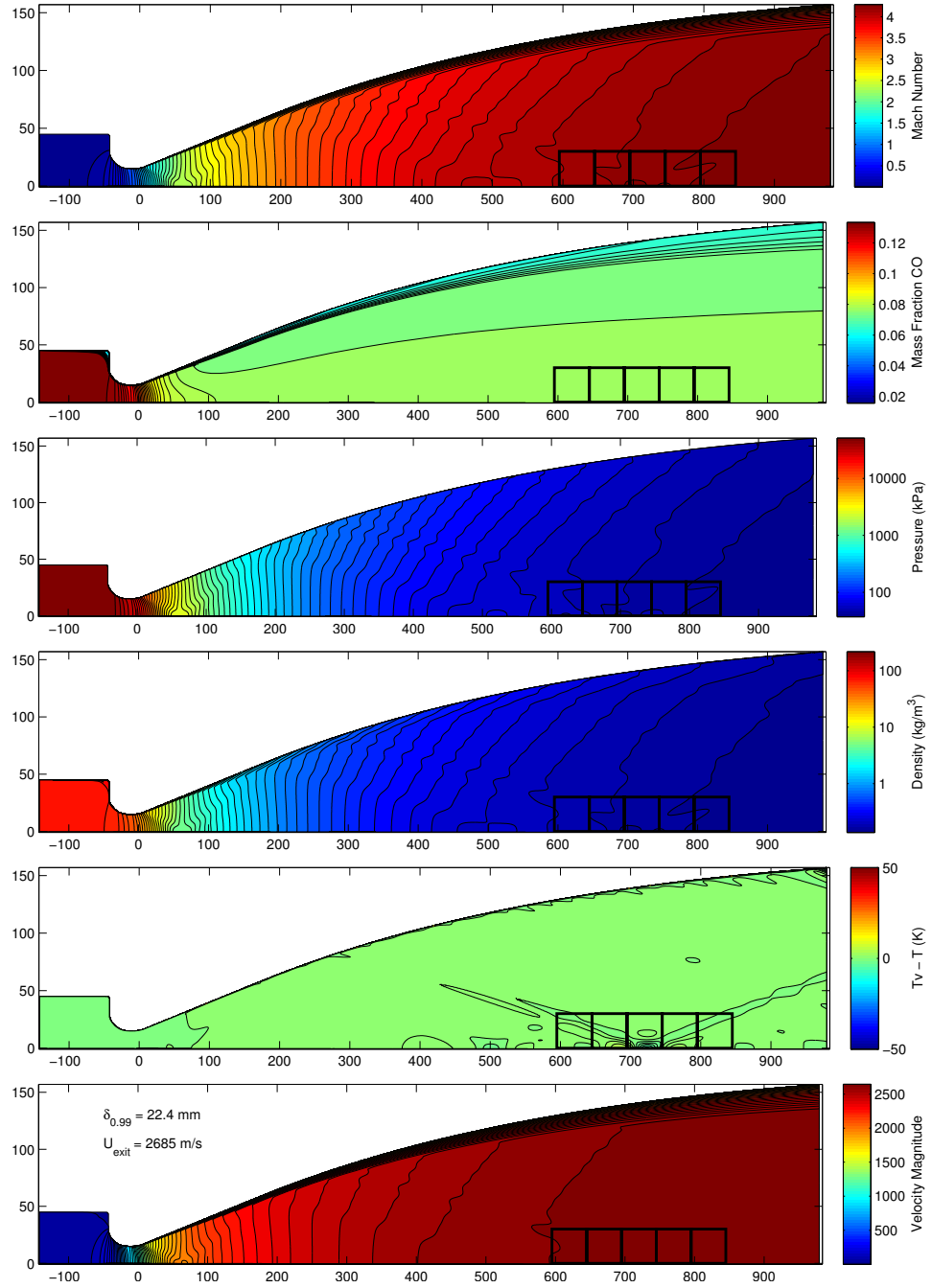
Figure B.37: Nozzle flow computed with the Spalart-Allmaras turbulence model for the wall, shot 2808. The black boxes highlight the averaged regions used to create STABL/DPLR inputs.
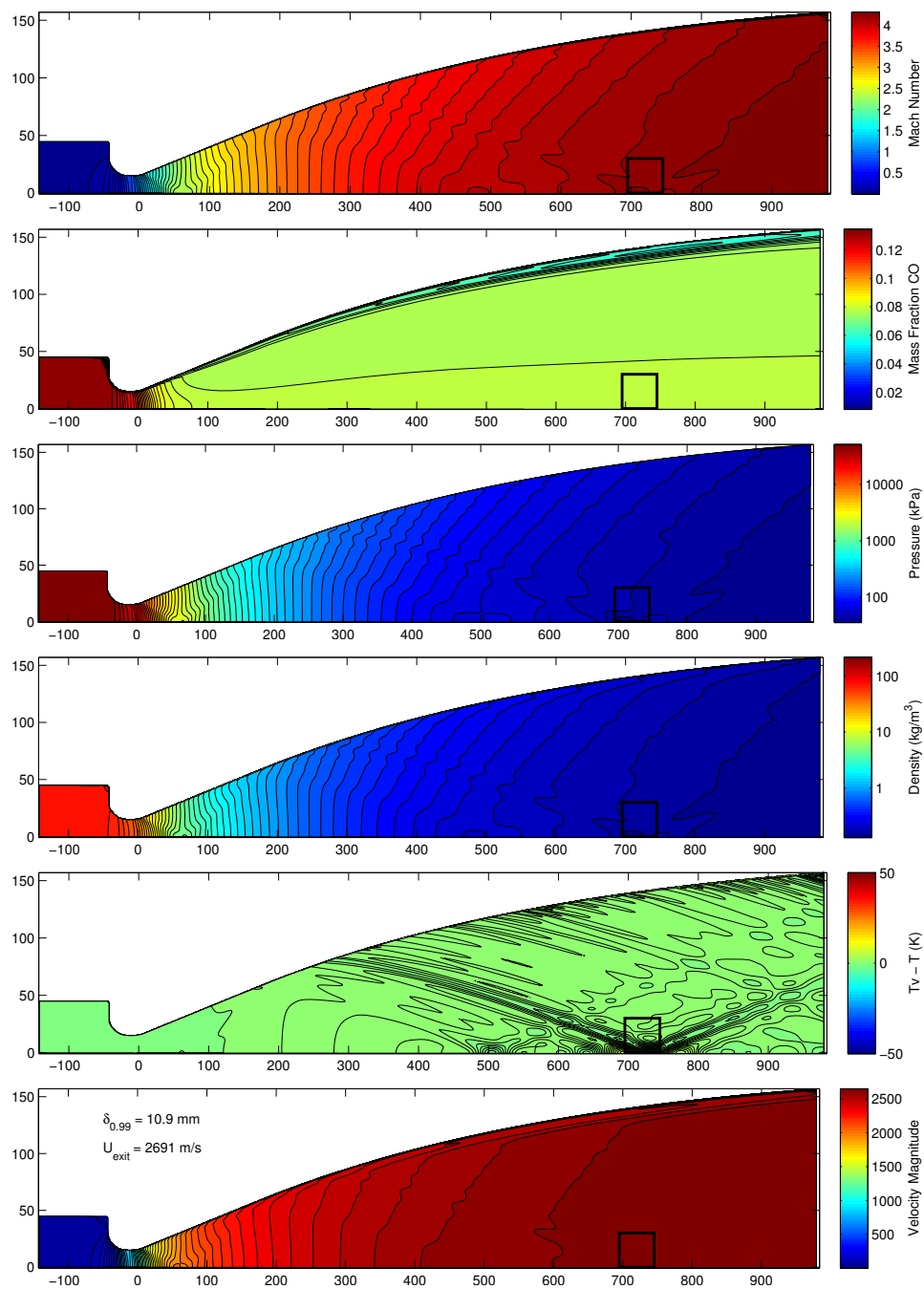
Figure B.38: Nozzle flow computed with laminar boundary layer growth for the wall, shot 2808. The black box highlights the averaged region used to create STABL/DPLR inputs.
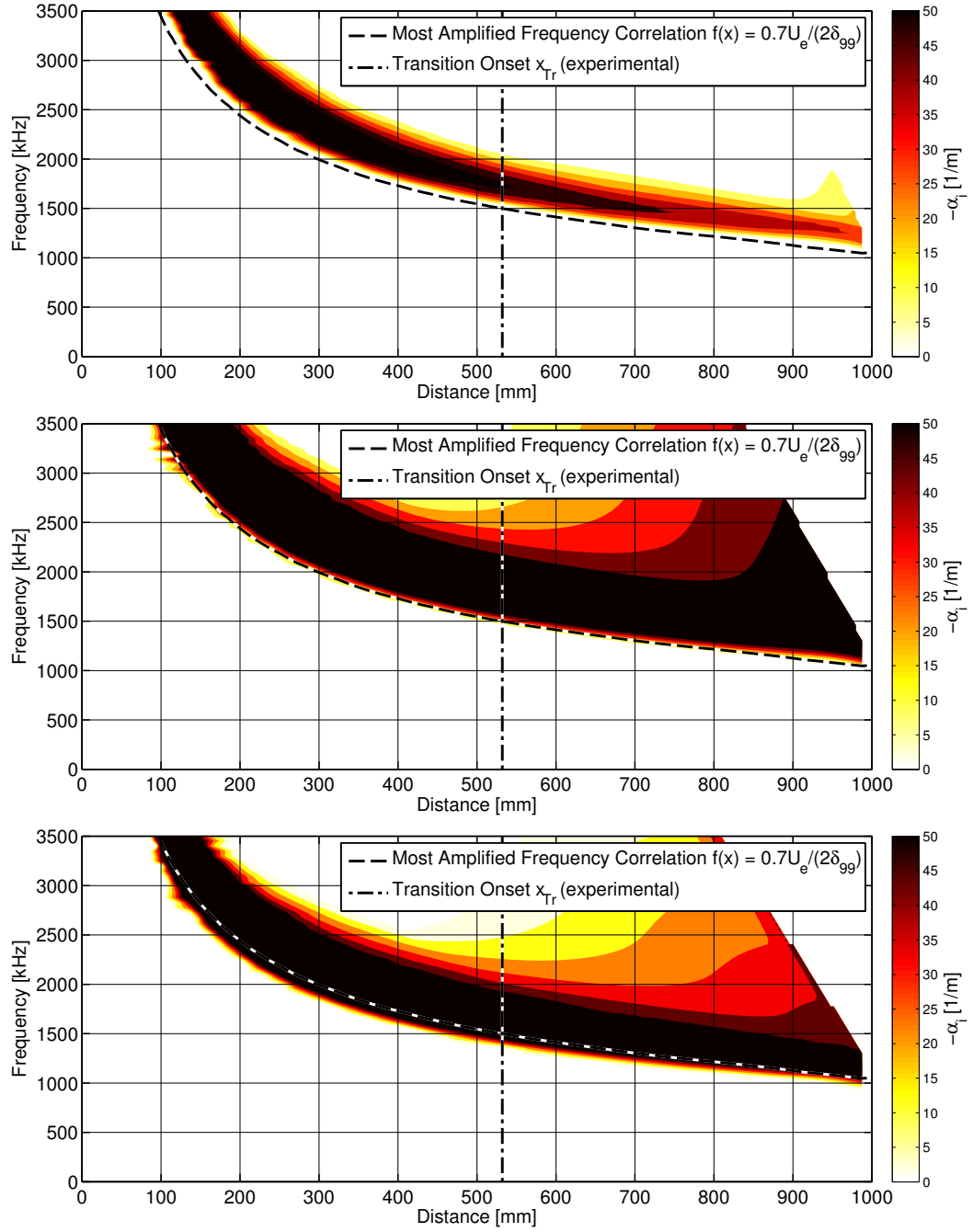
Figure B.39: Stability diagram with physical (top), frozen (middle), and equilibrium (bottom) vibrational energy transfer, shot 2808. Dashed line indicates $0.7U_{\mathrm{e}}/(2\delta_{99})$; dot-dashed line is the transition location.
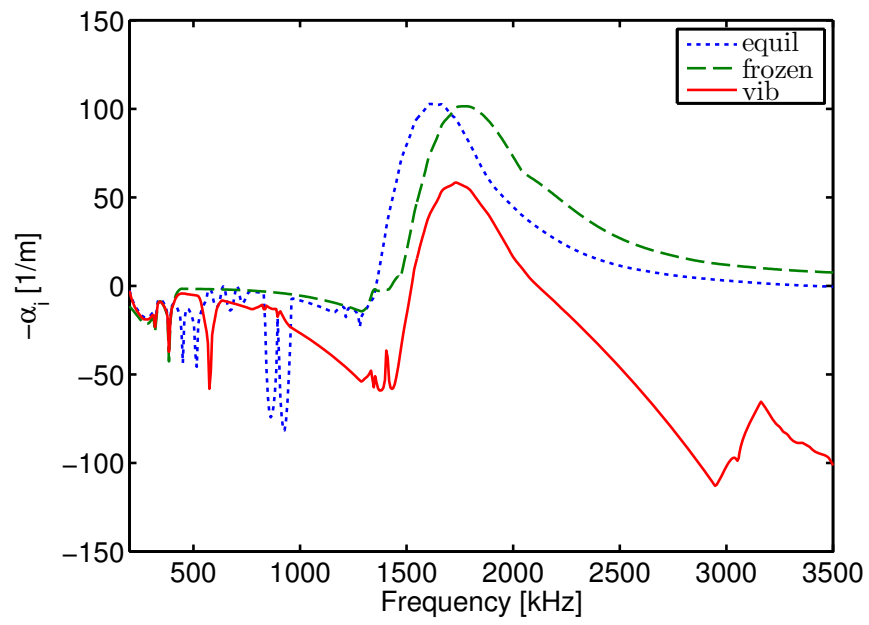
Figure B.40: Spatial amplification rate $-\alpha_i$ across frequencies calculated at x_{Tr}, with physical, frozen, and equilibrium vibrational energy transfer, shot 2808.

Figure B.41: Largest (integrated) growth frequency diagram with physical (top), frozen (middle), and equilibrium (bottom) vibrational energy transfer, shot 2808. Dashed line indicates the computed frequency of largest growth at each x-location; dot-dashed line is the transition x-location.

Figure B.42: $N(f, x) = \int_0^x -a_i(f, \xi)d\xi$ calculated at x_{Tr}, with physical, frozen, and equilibrium vibrational energy transfer, shot 2808.

B.7 Shot 2817

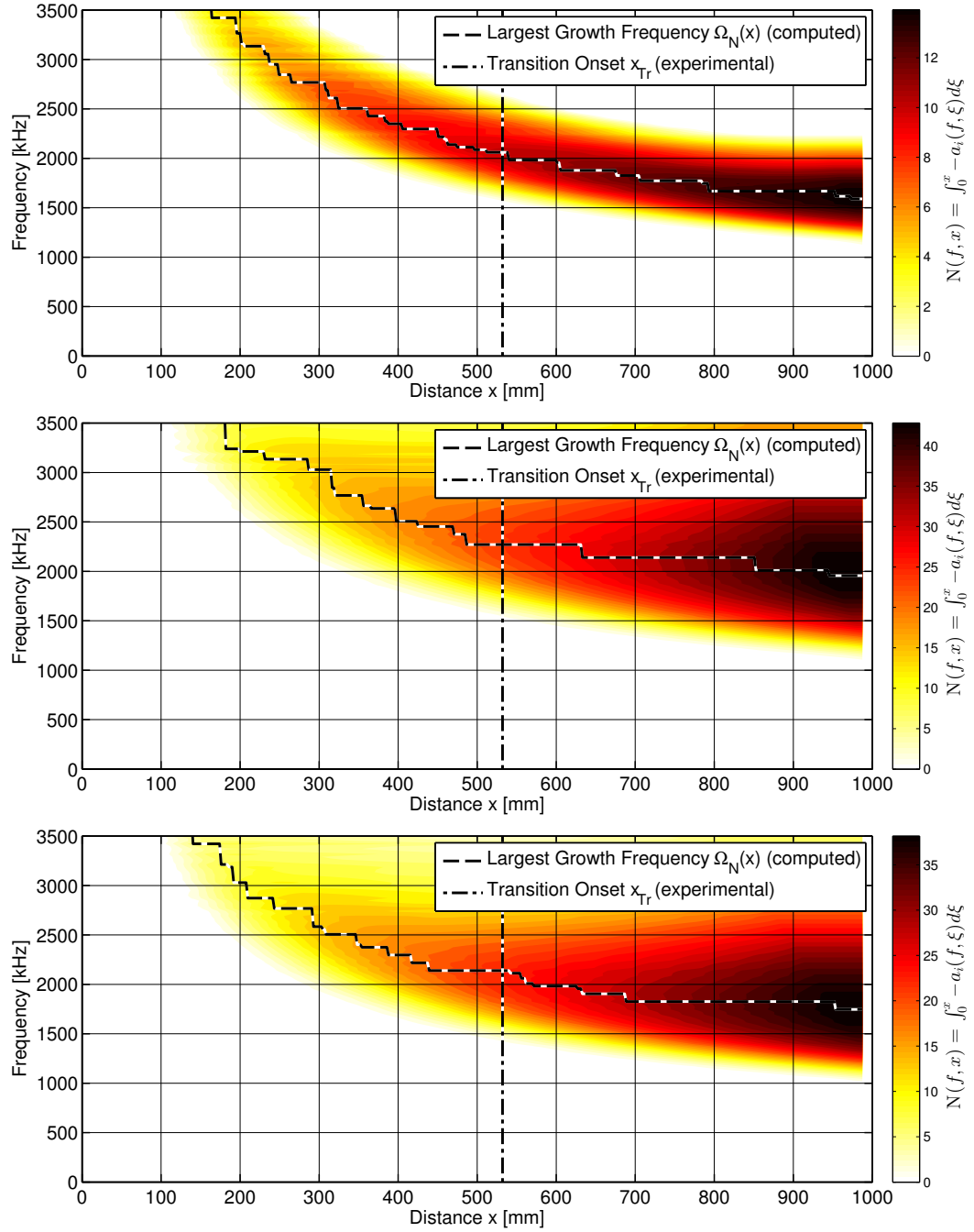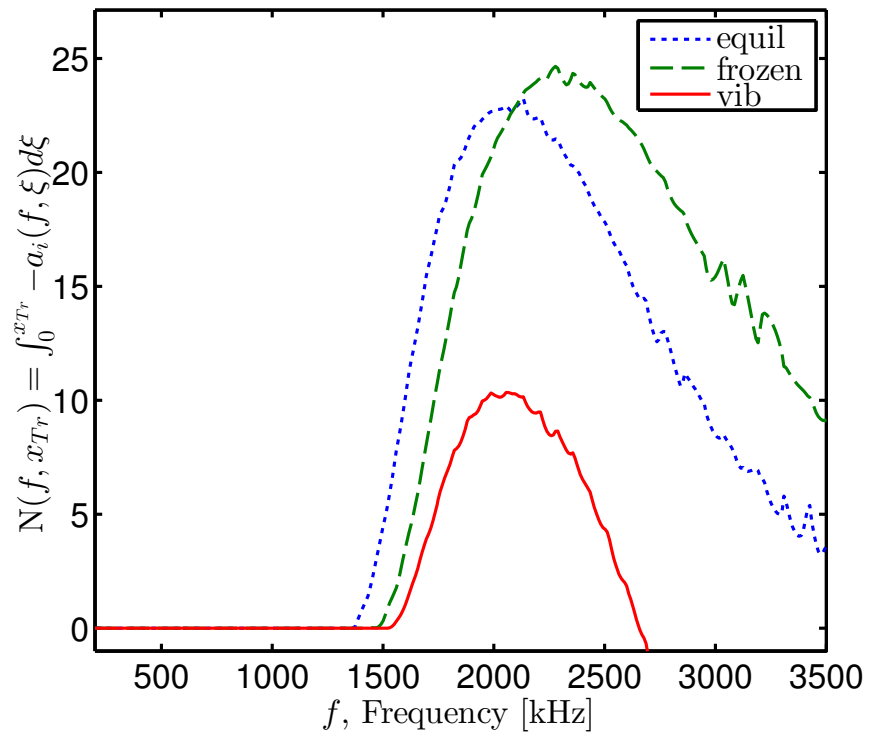Experiment 2817 was performed in T5 on 26 June 2013.

B.7.1 Geometry

The test article was a 1 m 5-degree half-angle cone with a sharp tip. The initial shock tube composition was 50% air, 50% CO_2 by mass. Reservoir temperature, density, and composition are computed from the measured shock speed and shock tube initial conditions using a Cantera-based reflected-shock model adjusted for measured reservoir pressure.

B.7.2 Measured Quantities

Measurement	Symbol	Value	Units
Shock Speed	U_s	2180	m/s
Shock Tube Fill Pressure	P_1	120.00	kPa
Reservoir Pressure	P_{res}	23.3	MPa

Table B.49: Measured quantities, shot 2817

B.7.3 Computed Reservoir Conditions

Computed Quantity	Symbol	Value	Units
Reservoir Temperature	T_{res}	3193	K
Reservoir Density	ρ_{res}	29.93	kg/m³
Reservoir Enthalpy	h_{res}	4.08	MJ/kg

Table B.50: Computed reservoir conditions, shot 2817

Y_{N_2}	Y_{O_2}	Y_{CO_2}	Y_{NO}	Y_{CO}	Y_N	Y_O
3.69×10^{-1}	1.17×10^{-1}	4.47×10^{-1}	3.05×10^{-2}	3.40×10^{-2}	8.13×10^{-7}	2.30×10^{-3}

Table B.51: Computed reservoir species mass fractions, shot 2817

B.7.4 Nozzle Position, Transition, and Chemistry Assumptions

These quantities are computed using the UMNAEM nozzle code with turbulent (unless otherwise stated) and laminar nozzle boundary layer assumptions, and the DPLR/STABL suite taking input freestream conditions at five different positions in the nozzle, and with and without the inclusion of chemical and vibrational rate processes. The results are compared to the results of a 1-D Cantera-based nozzle code with a Taylor-Maccoll shock and boundary layer similarity solution with conditions calculated from the nozzle exit, 100 cm downstream of the throat. The position 72 cm from the nozzle throat matches the best measurement of the experimental geometry, and the laminar-nozzle, frozen, and equilibrium cases are computed at this position.

	U_∞	T_∞	Tv_∞	M_∞	P_∞	ρ_∞	Unit Re$_\infty$
	m/s	K	K	-	kPa	kg/m^3	1/m
1D 100 cm	2577	792.0	792.0	5.23	11.7	0.061	4.52×10^6
100 cm	2578	774.3	775.8	5.04	11.2	0.060	5.11×10^6
Lam 72 cm	2565	802.3	805.5	4.93	13.4	0.069	5.69×10^6
82 cm	2556	823.6	822.5	4.85	15.0	0.076	6.09×10^6
77 cm	2556	823.4	824.3	4.85	15.1	0.076	6.11×10^6
72 cm	2561	809.9	813.2	4.90	14.0	0.072	5.18×10^6
67 cm	2568	796.2	798.5	4.96	12.9	0.067	5.56×10^6
62 cm	2571	789.5	791.2	4.98	12.3	0.065	5.42×10^6

Table B.52: Computed freestream conditions, shot 2817

	Y_{N_2}	Y_{O_2}	Y_{CO_2}	Y_{NO}	Y_{CO}	Y_N	Y_O
1D 100 cm	3.73×10^{-1}	1.14×10^{-1}	4.70×10^{-1}	2.34×10^{-2}	1.90×10^{-2}	0	3.25×10^{-4}
100 cm	3.70×10^{-1}	1.09×10^{-1}	4.75×10^{-1}	2.97×10^{-2}	1.56×10^{-2}	0	6.20×10^{-5}
Lam 72 cm	3.70×10^{-1}	1.09×10^{-1}	4.75×10^{-1}	2.97×10^{-2}	1.56×10^{-2}	0	6.23×10^{-5}
82 cm	3.70×10^{-1}	1.09×10^{-1}	4.75×10^{-1}	2.97×10^{-2}	1.56×10^{-2}	0	6.22×10^{-5}
77 cm	3.70×10^{-1}	1.09×10^{-1}	4.75×10^{-1}	2.97×10^{-2}	1.56×10^{-2}	0	6.21×10^{-5}
72 cm	3.70×10^{-1}	1.09×10^{-1}	4.75×10^{-1}	2.97×10^{-2}	1.56×10^{-2}	0	6.20×10^{-5}
67 cm	3.70×10^{-1}	1.09×10^{-1}	4.75×10^{-1}	2.97×10^{-2}	1.56×10^{-2}	0	6.20×10^{-5}
62 cm	3.70×10^{-1}	1.09×10^{-1}	4.75×10^{-1}	2.97×10^{-2}	1.56×10^{-2}	0	6.19×10^{-5}

Table B.53: Computed freestream species mass fractions, shot 2817

	U_e	T_e	$T\mathrm{v_e}$	$\mathrm{M_e}$	P_e	ρ_e	Unit $\mathrm{Re_e}$
	m/s	K	K	-	kPa	kg/m^3	1/m
1D 100 cm	2551	849.9	849.9	5.00	16.3	0.079	5.59×10^6
100 cm	2534	857.8	857.6	4.71	15.8	0.076	5.61×10^6
Lam 72 cm	2523	884.0	883.8	4.62	18.5	0.087	6.24×10^6
82 cm	2514	903.1	903.0	4.55	20.7	0.095	6.69×10^6
77 cm	2513	904.0	903.8	4.55	20.8	0.095	6.70×10^6
72 cm	2519	891.6	891.5	4.59	19.3	0.090	6.10×10^6
67 cm	2524	879.2	879.0	4.64	17.9	0.085	6.08×10^6
62 cm	2528	872.1	871.9	4.66	17.2	0.082	5.94×10^6

Table B.54: Computed boundary layer edge conditions, shot 2817

	$Y_{\mathrm{N_2}}$	$Y_{\mathrm{O_2}}$	$Y_{\mathrm{CO_2}}$	Y_{NO}	Y_{CO}	Y_{N}	Y_{O}
1D 100 cm	3.73×10^{-1}	1.14×10^{-1}	4.70×10^{-1}	2.34×10^{-2}	1.90×10^{-2}	0	3.25×10^{-4}
100 cm	3.70×10^{-1}	1.09×10^{-1}	4.75×10^{-1}	2.97×10^{-2}	1.56×10^{-2}	0	6.05×10^{-5}
Lam 72 cm	3.70×10^{-1}	1.09×10^{-1}	4.75×10^{-1}	2.97×10^{-2}	1.56×10^{-2}	0	6.05×10^{-5}
82 cm	3.70×10^{-1}	1.09×10^{-1}	4.75×10^{-1}	2.97×10^{-2}	1.56×10^{-2}	0	6.01×10^{-5}
77 cm	3.70×10^{-1}	1.09×10^{-1}	4.75×10^{-1}	2.97×10^{-2}	1.56×10^{-2}	0	6.00×10^{-5}
72 cm	3.70×10^{-1}	1.09×10^{-1}	4.75×10^{-1}	2.97×10^{-2}	1.56×10^{-2}	0	6.01×10^{-5}
67 cm	3.70×10^{-1}	1.09×10^{-1}	4.75×10^{-1}	2.97×10^{-2}	1.56×10^{-2}	0	6.02×10^{-5}
62 cm	3.70×10^{-1}	1.09×10^{-1}	4.75×10^{-1}	2.97×10^{-2}	1.56×10^{-2}	0	6.02×10^{-5}

Table B.55: Computed boundary layer edge species mass fractions, shot 2817

	x_{Tr}	$\mathrm{Re_{Tr}}$	$\mathrm{N_{Tr}}$	Ω_{Tr}	Ω_{NTr}	$\delta_{99\mathrm{Tr}}$	$(x/\delta_{99})_{\mathrm{Tr}}$	$\mathrm{Re}_{\delta_{99}\mathrm{Tr}}$
	m	-	-	kHz	kHz	mm	-	-
100 cm	0.502	2.82×10^6	8.82	993	996	0.975	515	5468
Lam 72 cm	0.502	3.13×10^6	9.50	1083	1064	0.916	548	5719
82 cm	0.502	3.36×10^6	9.90	1165	1161	0.876	573	5861
77 cm	0.502	3.36×10^6	9.93	1165	1161	0.873	575	5854
72 cm	0.502	3.08×10^6	9.59	1132	1122	0.901	557	5492
67 cm	0.502	3.05×10^6	9.30	1083	1083	0.927	542	5638
62 cm	0.502	2.98×10^6	9.12	1055	1054	0.942	533	5600
Frozen 72 cm	0.502	3.08×10^6	11.49	1158	1122	0.901	557	5492
Equil. 72 cm	0.502	3.08×10^6	10.60	1052	1054	0.901	557	5492

Table B.56: Boundary layer stability characteristics at experimentally observed transition location, shot 2817
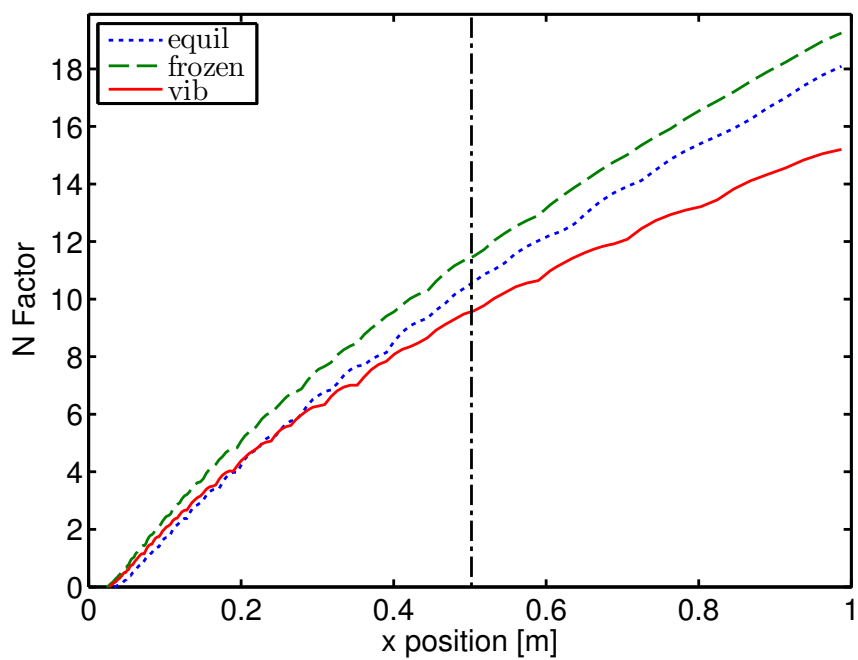
Figure B.43: N factor curves as a function of distance for realistic, frozen, and equilibrium vibrational energy transfer, shot 2817. The dot-dashed line indicates the experimentally measured transition onset location.
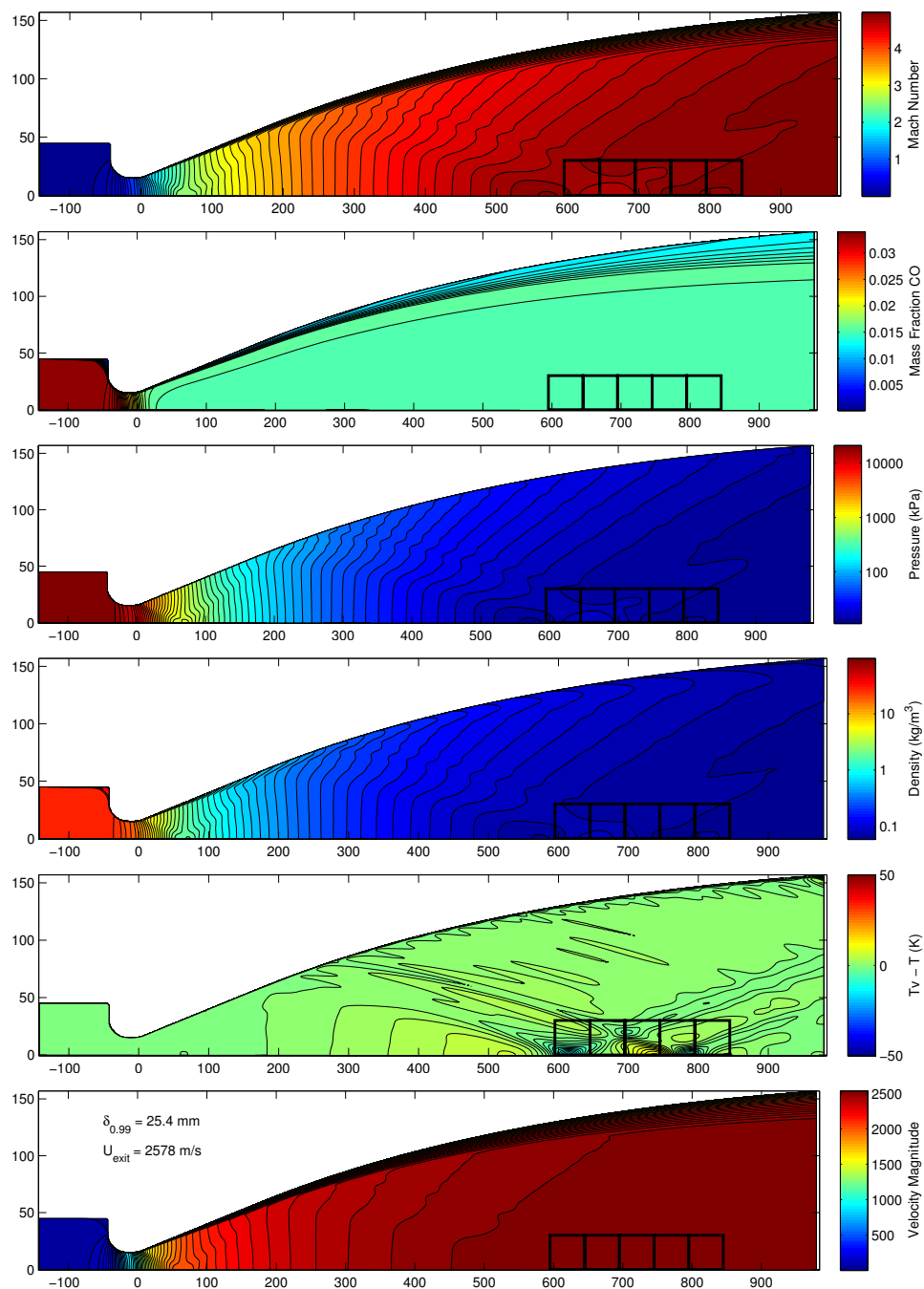
Figure B.44: Nozzle flow computed with the Spalart-Allmaras turbulence model for the wall, shot 2817. The black boxes highlight the averaged regions used to create STABL/DPLR inputs.
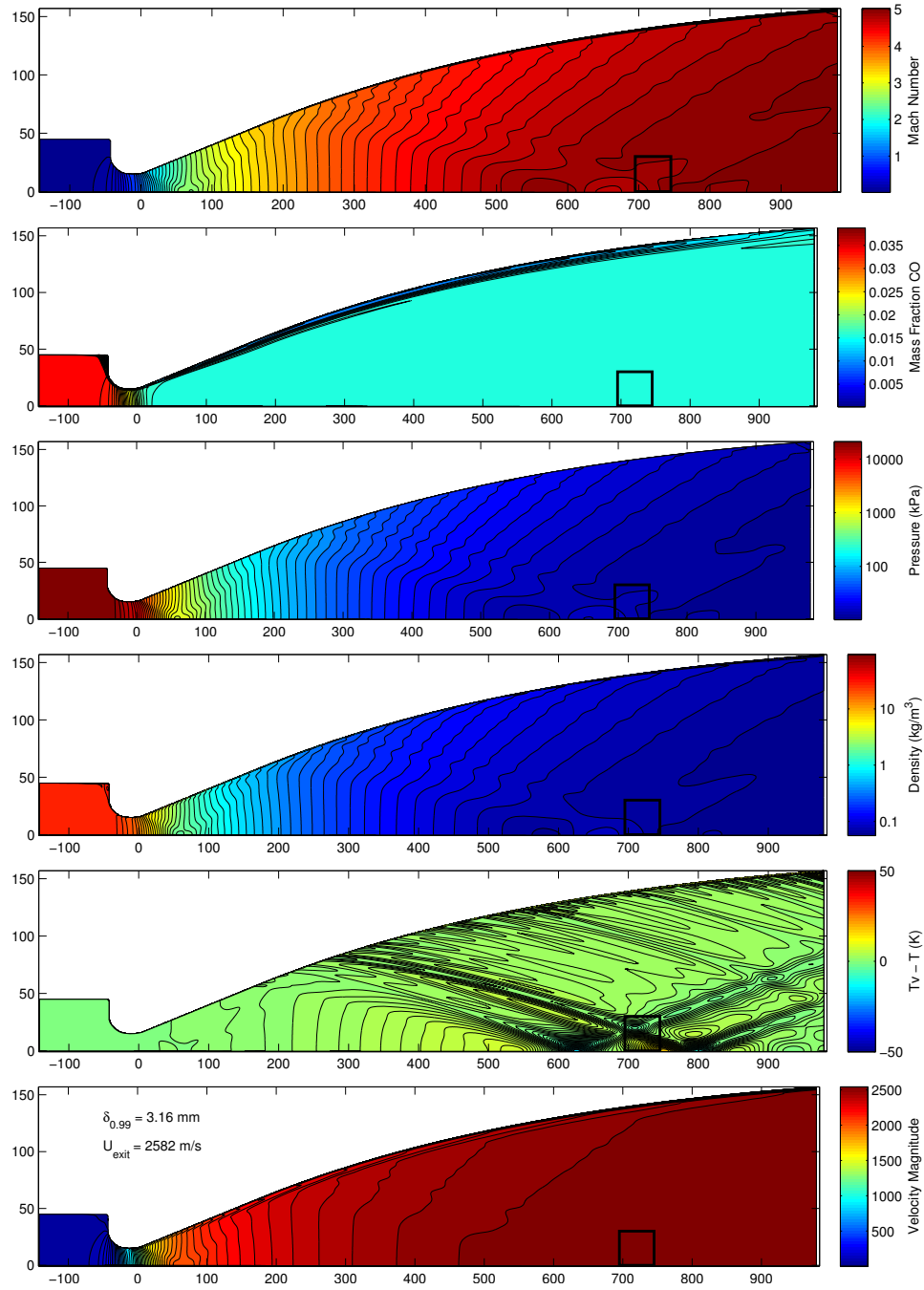
Figure B.45: Nozzle flow computed with laminar boundary layer growth for the wall, shot 2817. The black box highlights the averaged region used to create STABL/DPLR inputs.
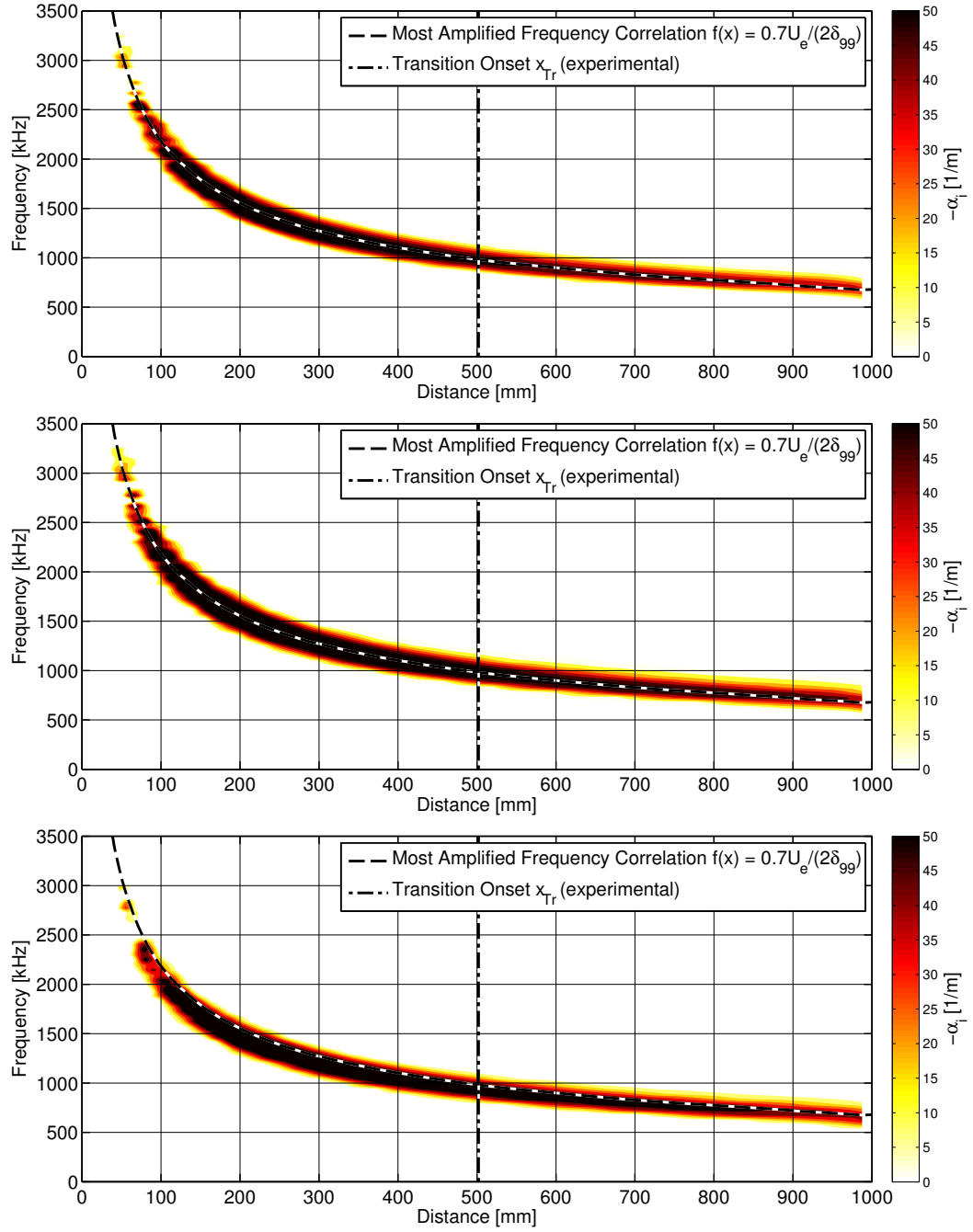
Figure B.46: Stability diagram with physical (top), frozen (middle), and equilibrium (bottom) vibrational energy transfer, shot 2817. Dashed line indicates $0.7U_{\mathrm{e}}/(2\delta_{99})$; dot-dashed line is the transition location.
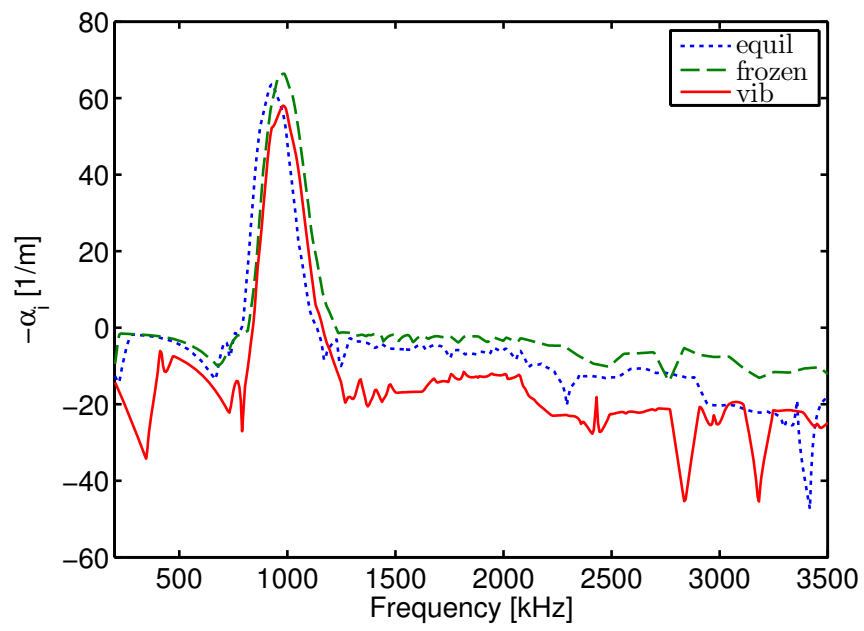
Figure B.47: Spatial amplification rate $-\alpha_i$ across frequencies calculated at x_{Tr}, with physical, frozen, and equilibrium vibrational energy transfer, shot 2817.
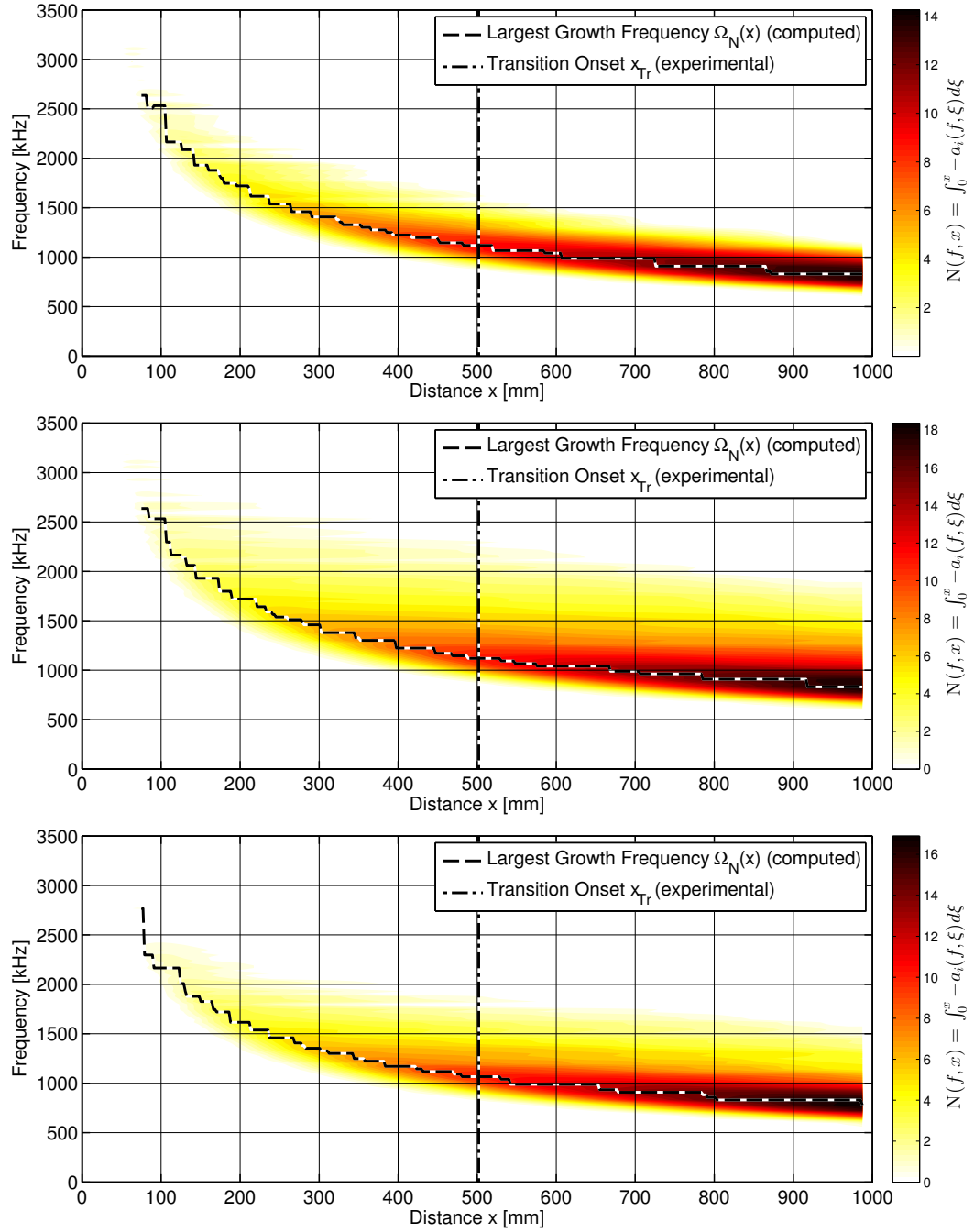
Figure B.48: Largest (integrated) growth frequency diagram with physical (top), frozen (middle), and equilibrium (bottom) vibrational energy transfer, shot 2817. Dashed line indicates the computed frequency of largest growth at each x-location; dot-dashed line is the transition x-location.
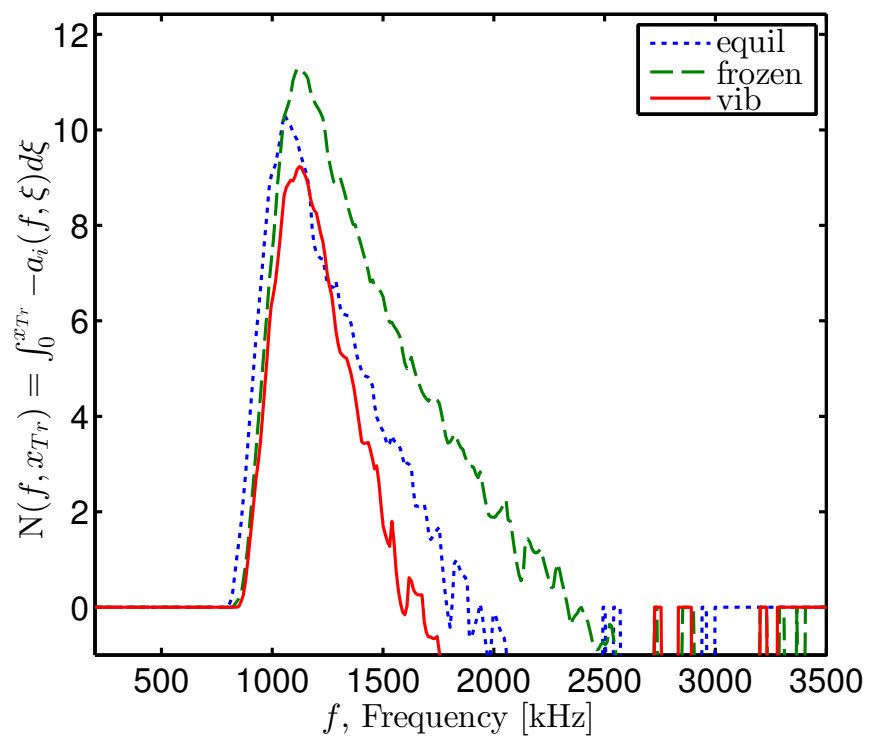
Figure B.49: $N(f, x) = \int_0^x -a_i(f, \xi)d\xi$ calculated at x_{Tr}, with physical, frozen, and equilibrium vibrational energy transfer, shot 2817.

B.8   Shot 2821

Experiment 2821 was performed in T5 on 3 July 2013.

B.8.1   Geometry

The test article was a 1 m 5-degree half-angle cone with a sharp tip. The initial shock tube composition was 50% air, 50% CO_2 by mass. Reservoir temperature, density, and composition are computed from the measured shock speed and shock tube initial conditions using a Cantera-based reflected-shock model adjusted for measured reservoir pressure.

B.8.2   Measured Quantities

Measurement	Symbol	Value	Units
Shock Speed	U_s	2720	m/s
Shock Tube Fill Pressure	P_1	100.00	kPa
Reservoir Pressure	P_{res}	42.5	MPa

Table B.57: Measured quantities, shot 2821

B.8.3   Computed Reservoir Conditions

Computed Quantity	Symbol	Value	Units
Reservoir Temperature	T_{res}	4102	K
Reservoir Density	ρ_{res}	39.23	kg/m^3
Reservoir Enthalpy	h_{res}	6.70	MJ/kg

Table B.58: Computed reservoir conditions, shot 2821

Y_{N_2}	Y_{O_2}	Y_{CO_2}	Y_{NO}	Y_{CO}	Y_N	Y_O
3.51×10^{-1}	1.43×10^{-1}	2.79×10^{-1}	6.97×10^{-2}	1.41×10^{-1}	3.48×10^{-5}	1.68×10^{-2}

Table B.59: Computed reservoir species mass fractions, shot 2821

B.8.4 Nozzle Position, Transition, and Chemistry Assumptions

These quantities are computed using the UMNAEM nozzle code with turbulent (unless otherwise stated) and laminar nozzle boundary layer assumptions, and the DPLR/STABL suite taking input freestream conditions at five different positions in the nozzle, and with and without the inclusion of chemical and vibrational rate processes. The results are compared to the results of a 1-D Cantera-based nozzle code with a Taylor-Maccoll shock and boundary layer similarity solution with conditions calculated from the nozzle exit, 100 cm downstream of the throat. The position 72 cm from the nozzle throat matches the best measurement of the experimental geometry, and the laminar-nozzle, frozen, and equilibrium cases are computed at this position.

	U_∞	T_∞	Tv_∞	M_∞	P_∞	ρ_∞	Unit Re_∞
	m/s	K	K	-	kPa	kg/m^3	1/m
1D 100 cm	3132	1266.0	1266.0	5.00	24.6	0.078	5.47×10^6
100 cm	3132	1207.0	1207.4	4.84	22.6	0.076	5.57×10^6
Lam 72 cm	3117	1244.7	1246.8	4.75	26.4	0.086	6.14×10^6
82 cm	3096	1298.2	1299.4	4.62	32.5	0.101	6.98×10^6
77 cm	3104	1278.6	1279.9	4.66	30.1	0.095	6.66×10^6
72 cm	3114	1253.3	1255.1	4.72	27.3	0.088	6.13×10^6
67 cm	3118	1242.7	1242.9	4.75	26.1	0.085	6.09×10^6
62 cm	3122	1232.4	1233.4	4.78	25.1	0.082	5.94×10^6

Table B.60: Computed freestream conditions, shot 2821

	Y_{N_2}	Y_{O_2}	Y_{CO_2}	Y_{NO}	Y_{CO}	Y_N	Y_O
1D 100 cm	3.66×10^{-1}	1.30×10^{-1}	4.04×10^{-1}	3.72×10^{-2}	6.14×10^{-2}	0	1.27×10^{-3}
100 cm	3.62×10^{-1}	1.25×10^{-1}	4.06×10^{-1}	4.57×10^{-2}	5.96×10^{-2}	0	7.42×10^{-4}
Lam 72 cm	3.62×10^{-1}	1.25×10^{-1}	4.07×10^{-1}	4.56×10^{-2}	5.95×10^{-2}	0	7.55×10^{-4}
82 cm	3.62×10^{-1}	1.25×10^{-1}	4.07×10^{-1}	4.57×10^{-2}	5.95×10^{-2}	1.22×10^{-10}	7.59×10^{-4}
77 cm	3.62×10^{-1}	1.25×10^{-1}	4.07×10^{-1}	4.57×10^{-2}	5.95×10^{-2}	0	7.55×10^{-4}
72 cm	3.62×10^{-1}	1.25×10^{-1}	4.07×10^{-1}	4.57×10^{-2}	5.95×10^{-2}	0	7.52×10^{-4}
67 cm	3.62×10^{-1}	1.25×10^{-1}	4.07×10^{-1}	4.57×10^{-2}	5.95×10^{-2}	0	7.49×10^{-4}
62 cm	3.62×10^{-1}	1.25×10^{-1}	4.07×10^{-1}	4.57×10^{-2}	5.95×10^{-2}	0	7.46×10^{-4}

Table B.61: Computed freestream species mass fractions, shot 2821

	U_e	T_e	$T v_e$	M_e	P_e	ρ_e	Unit Re_e
	m/s	K	K	-	kPa	kg/m^3	1/m
1D 100 cm	3100	1346.8	1346.8	4.79	33.4	0.100	6.69×10^6
100 cm	3081	1316.9	1316.8	4.56	31.1	0.095	6.30×10^6
Lam 72 cm	3066	1353.8	1353.7	4.48	36.0	0.107	6.93×10^6
82 cm	3045	1405.3	1405.2	4.36	43.8	0.126	7.86×10^6
77 cm	3053	1385.8	1385.8	4.41	40.8	0.119	7.51×10^6
72 cm	3063	1362.5	1362.4	4.46	37.2	0.110	7.23×10^6
67 cm	3068	1351.0	1351.0	4.48	35.6	0.106	6.88×10^6
62 cm	3071	1341.6	1341.6	4.50	34.3	0.103	6.71×10^6

Table B.62: Computed boundary layer edge conditions, shot 2821

	Y_{N_2}	Y_{O_2}	Y_{CO_2}	Y_{NO}	Y_{CO}	Y_N	Y_O
1D 100 cm	3.66×10^{-1}	1.30×10^{-1}	4.04×10^{-1}	3.72×10^{-2}	6.14×10^{-2}	6.79×10^{-11}	1.27×10^{-3}
100 cm	3.62×10^{-1}	1.25×10^{-1}	4.07×10^{-1}	4.57×10^{-2}	5.95×10^{-2}	1.32×10^{-10}	6.91×10^{-4}
Lam 72 cm	3.62×10^{-1}	1.25×10^{-1}	4.07×10^{-1}	4.56×10^{-2}	5.94×10^{-2}	1.90×10^{-10}	6.92×10^{-4}
82 cm	3.62×10^{-1}	1.25×10^{-1}	4.07×10^{-1}	4.57×10^{-2}	5.93×10^{-2}	2.98×10^{-10}	6.77×10^{-4}
77 cm	3.62×10^{-1}	1.25×10^{-1}	4.07×10^{-1}	4.57×10^{-2}	5.94×10^{-2}	2.52×10^{-10}	6.81×10^{-4}
72 cm	3.62×10^{-1}	1.25×10^{-1}	4.07×10^{-1}	4.57×10^{-2}	5.94×10^{-2}	2.04×10^{-10}	6.87×10^{-4}
67 cm	3.62×10^{-1}	1.25×10^{-1}	4.07×10^{-1}	4.57×10^{-2}	5.94×10^{-2}	1.83×10^{-10}	6.88×10^{-4}
62 cm	3.62×10^{-1}	1.25×10^{-1}	4.07×10^{-1}	4.57×10^{-2}	5.94×10^{-2}	1.68×10^{-10}	6.88×10^{-4}

Table B.63: Computed boundary layer edge species mass fractions, shot 2821

	x_{Tr}	Re_{Tr}	N_{Tr}	Ω_{Tr}	Ω_{NTr}	δ_{99Tr}	$(x/\delta_{99})_{Tr}$	$Re_{\delta_{99}Tr}$
	m	-	-	kHz	kHz	mm	-	-
100 cm	0.607	3.82×10^6	10.07	1293	1307	0.977	621	6159
Lam 72 cm	0.607	4.21×10^6	10.48	1383	1375	0.922	658	6391
82 cm	0.607	4.77×10^6	10.88	1516	1559	0.853	712	6705
77 cm	0.607	4.56×10^6	10.72	1458	1501	0.878	691	6597
72 cm	0.607	4.49×10^6	10.41	1383	1433	0.909	668	6575
67 cm	0.607	4.18×10^6	10.45	1372	1375	0.922	658	6348
62 cm	0.607	4.07×10^6	10.32	1358	1365	0.938	647	6298
Frozen 72 cm	0.607	4.49×10^6	15.98	1458	1501	0.909	668	6575
Equil. 72 cm	0.607	4.49×10^6	15.14	1383	1433	0.909	668	6575

Table B.64: Boundary layer stability characteristics at experimentally observed transition location, shot 2821
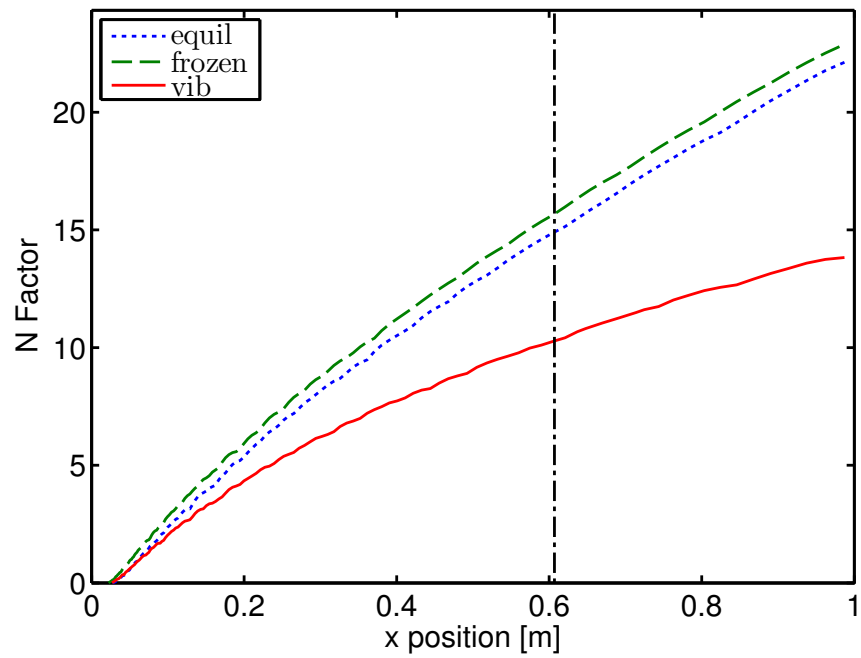
Figure B.50: N factor curves as a function of distance for realistic, frozen, and equilibrium vibrational energy transfer, shot 2821. The dot-dashed line indicates the experimentally measured transition onset location.
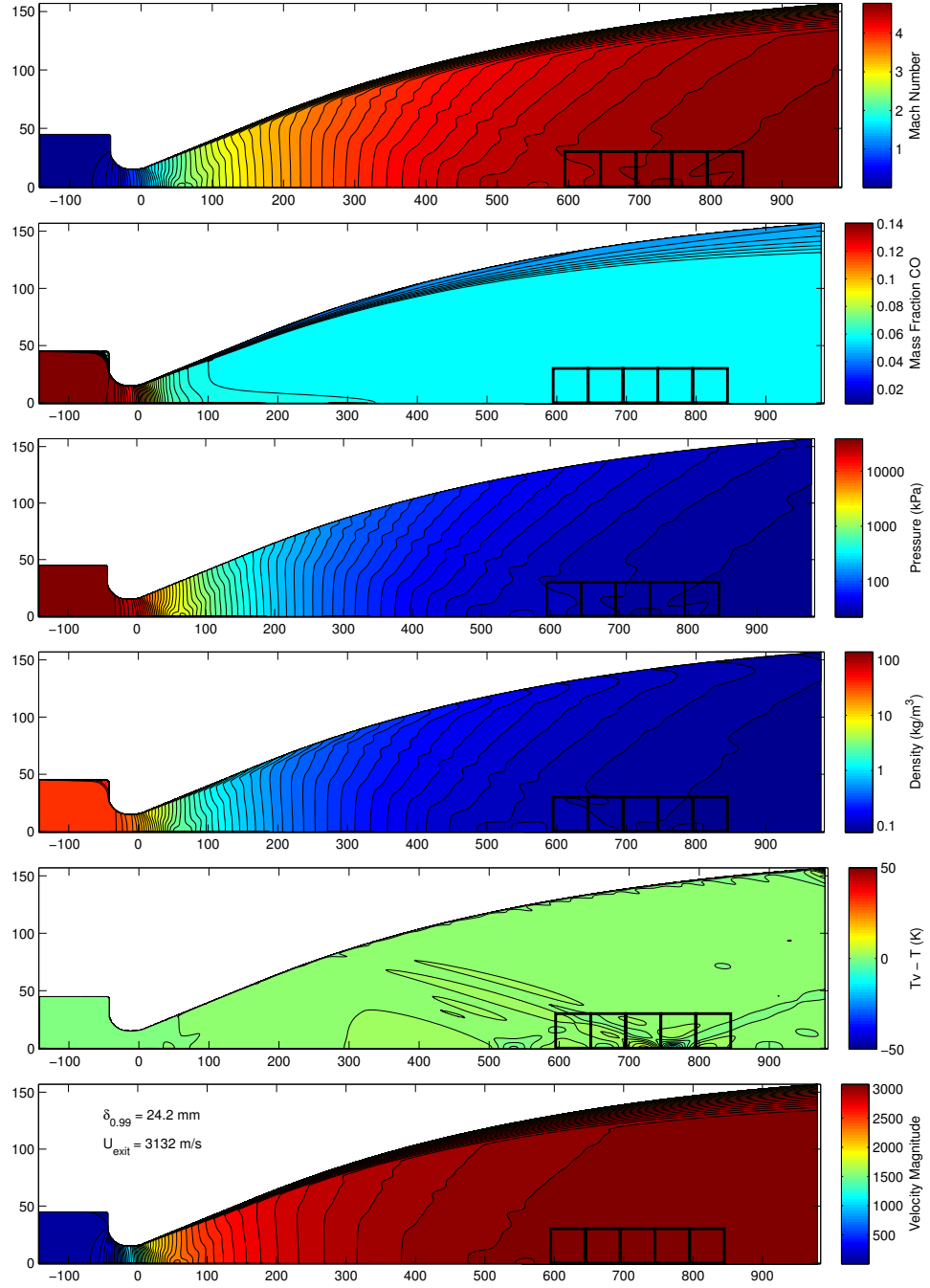
Figure B.51: Nozzle flow computed with the Spalart-Allmaras turbulence model for the wall, shot 2821. The black boxes highlight the averaged regions used to create STABL/DPLR inputs.
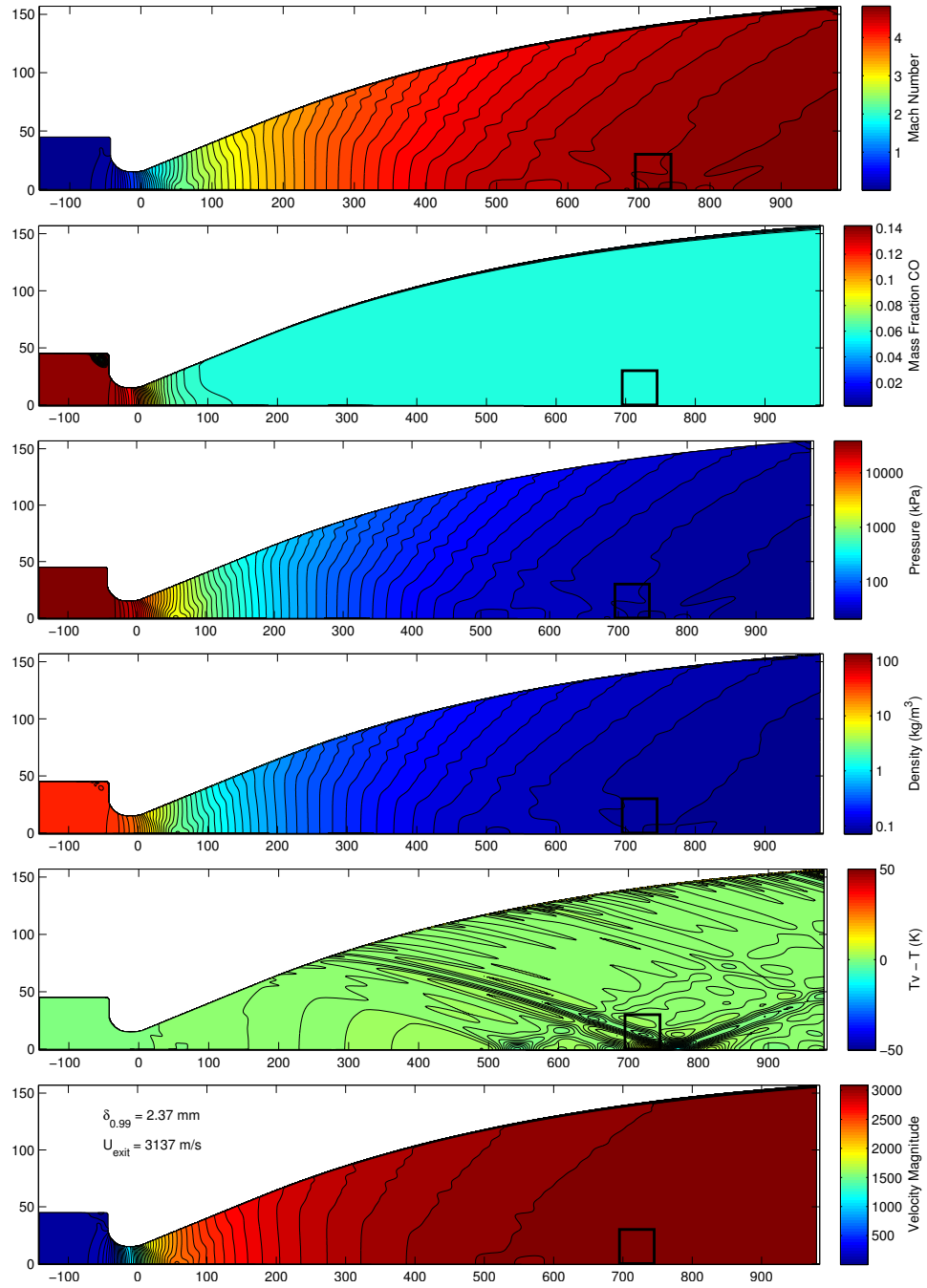
Figure B.52: Nozzle flow computed with laminar boundary layer growth for the wall, shot 2821. The black box highlights the averaged region used to create STABL/DPLR inputs.
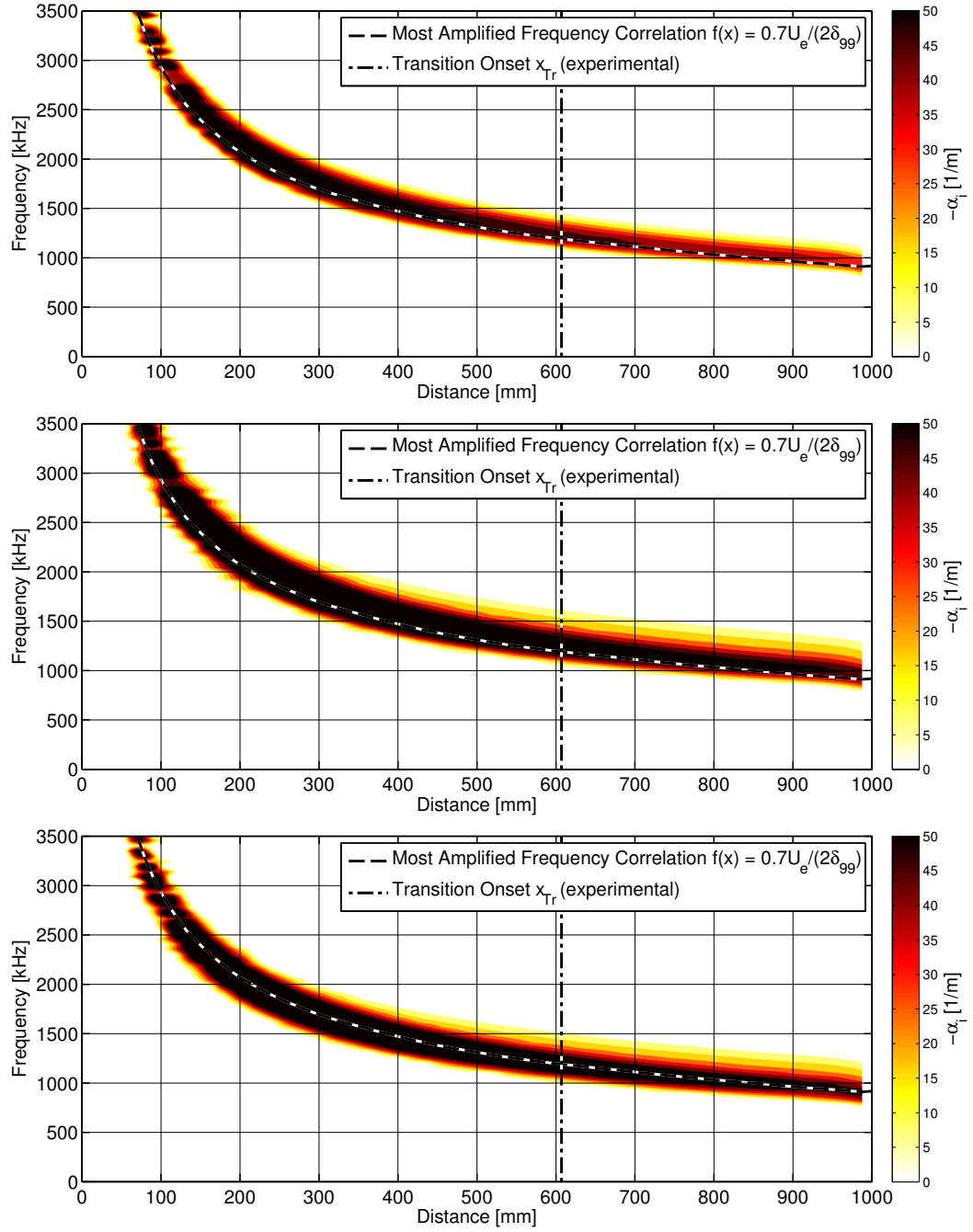
Figure B.53: Stability diagram with physical (top), frozen (middle), and equilibrium (bottom) vibrational energy transfer, shot 2821. Dashed line indicates $0.7U_\mathrm{e}/(2\delta_{99})$; dot-dashed line is the transition location.
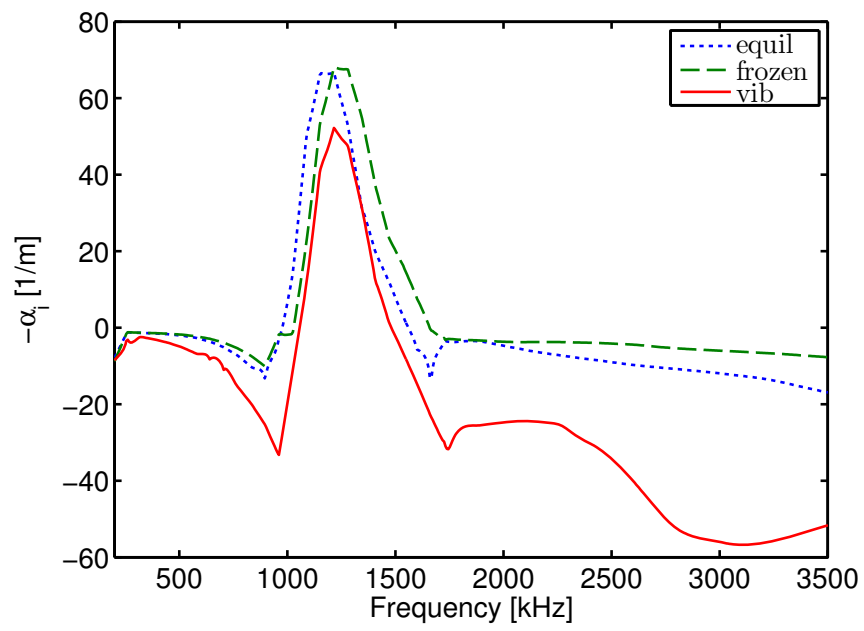
Figure B.54: Spatial amplification rate $-\alpha_i$ across frequencies calculated at x_{Tr}, with physical, frozen, and equilibrium vibrational energy transfer, shot 2821.
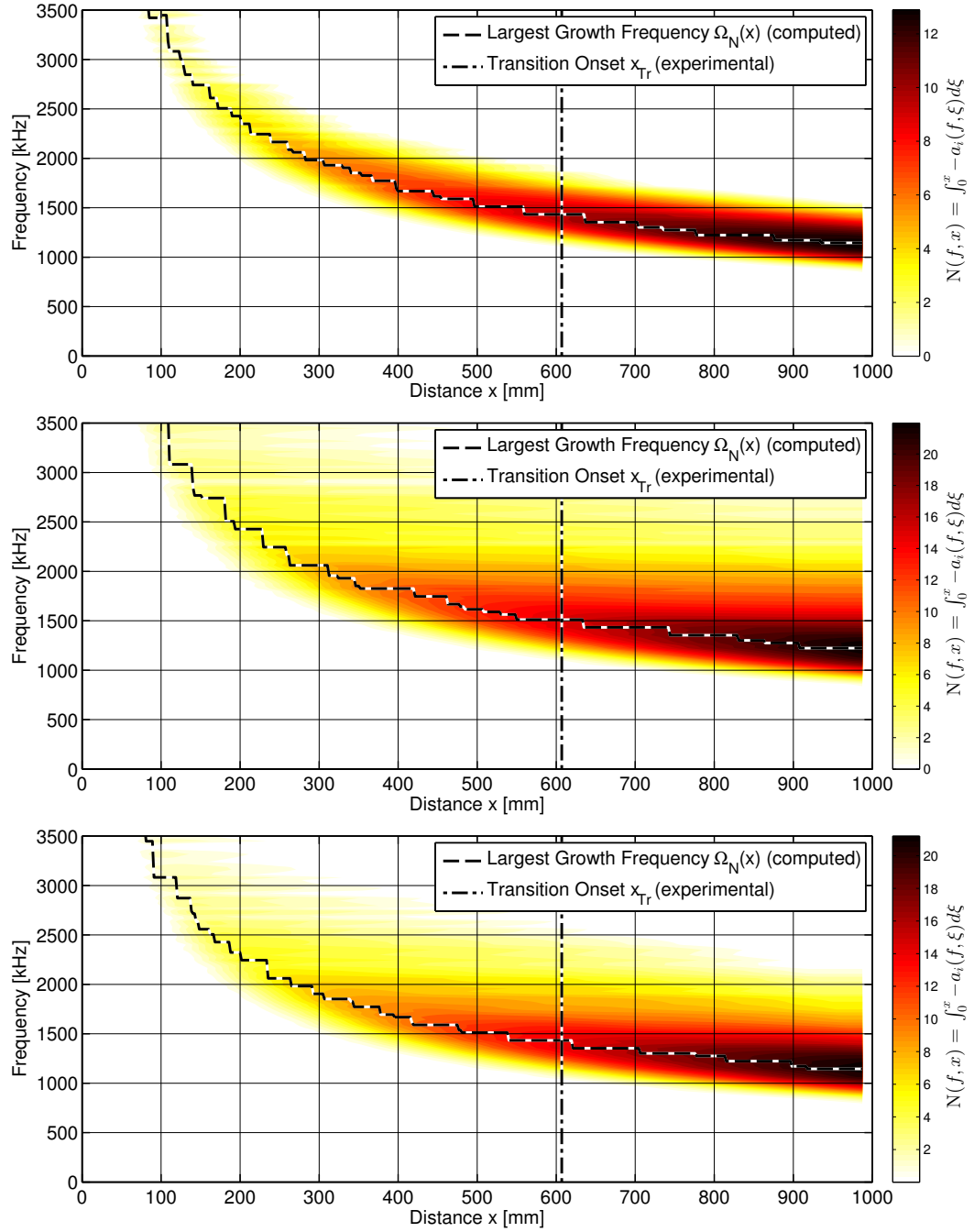
Figure B.55: Largest (integrated) growth frequency diagram with physical (top), frozen (middle), and equilibrium (bottom) vibrational energy transfer, shot 2821. Dashed line indicates the computed frequency of largest growth at each x-location; dot-dashed line is the transition x-location.
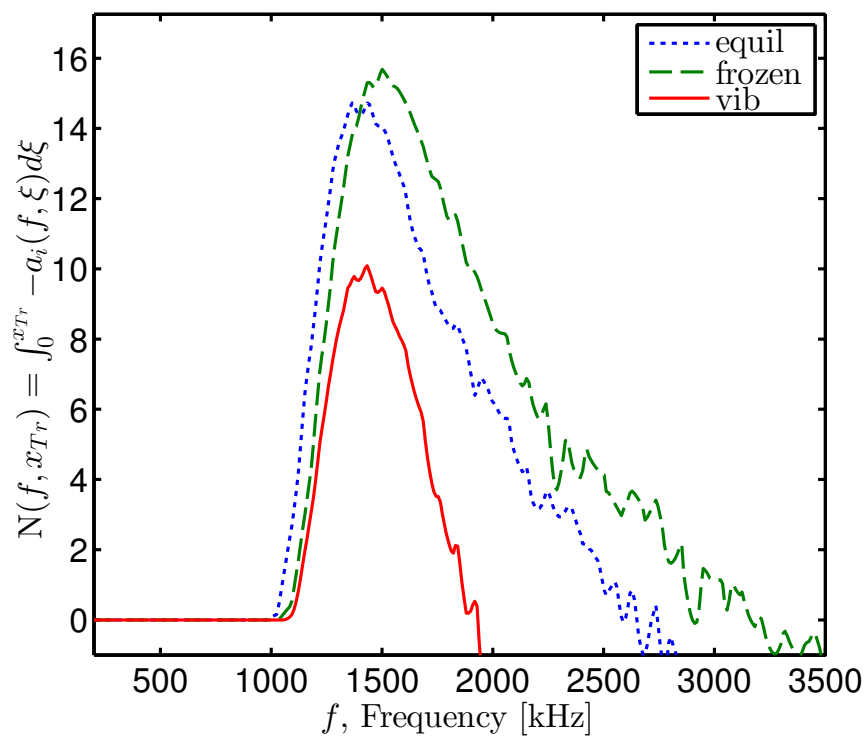
Figure B.56: $N(f, x) = \int_0^x -a_i(f, \xi)d\xi$ calculated at x_{Tr}, with physical, frozen, and equilibrium vibrational energy transfer, shot 2821.